In presenting the dissertation as a partial fulfillment of the requirements for an advanced degree from the Georgia Institute of Technology, I agree that the Library of the Institute shall make it available for inspection and circulation in accordance with its regulations governing materials of this type. I agree that permission to copy from, or to publish from, this dissertation may be granted by the professor under whose direction it was written, or, in his absence, by the Dean of the Graduate Division when such copying or publication is solely for scholarly purposes and does not involve potential financial gain. It is understood that any copying from, or publication of, this dissertation which involves potential financial gain will not be allowed without written permission.

7/25/68

EARLY STAGES IN THE INTERACTION OF CARBON MONOXIDE WITH IRON SINGLE CRYSTAL FILMS

A THESIS

Presented to

The Faculty of the Graduate Division

by

James Titus Ratliff

In Partial Fulfillment

of the Requirements for the Degree

Doctor of Philosophy in the School of Chemical Engineering

Georgia Institute of Technology

July, 1968

EARLY STAGES IN THE INTERACTION OF CARBON MONOXIDE WITH IRON SINGLE CRYSTAL FILMS

Approved:

Chairman:

Date approved by Chairman: 8/28/68

ACKNOWLEDGMENTS

I am indebted to Dr. R. F. Hochman for the guidance, encouragement, and support he gave me throughout my graduate studies; as my thesis advisor he was an invaluable ally. The genuine interest extended by Dr. W. M. Newton as well as Dr. Hochman was significant to my decision to remain in the graduate program at the Georgia Institute of Technology after the Master's degree. Both Dr. W. T. Ziegler and Dr. C. W. Gorton contributed materially to the successful completion of my thesis as members of my reading committee. The generous portions of time they spent appraising my work are very much appreciated.

Of particular value to my experimental work were the discussions I had with Dr. H. E. Grenga. My work benefited considerably from her experience at the University of Virginia on a similar problem of epitaxy and surface reaction under the direction of Dr. K. L. Lawless. It was on a trip to their laboratories prior to Dr. Grenga's move to the Georgia Institute of Technology that my program began to mature in definition. Consultations with both Dr. B. G. Lafevre of this institution and Dr. Brian Ralph of the University of Cambridge were also very beneficial by virtue of their broad experience in physical metallurgy and electron microscopy. A wealth of experience in electron microscopy was made available to me through discussions with Mr. K. D. Fike of the Lockheed-Georgia Company. The service of his counsel was invaluable to the success of the thesis.

I would like to express appreciation for a very pleasant working relationship with the faculty of the Georgia Institute of Technology and the

staff of the Engineering Experiment Station. There are at least two dozen of these people whom I could cite for valuable contributions to my work both by consultation and by means of their professional and vocational talents.

I am indebted to the Gulf Oil Company for the provision of a three-year fellowship. The personal attention and interest as expressed through the Gulf representative, Mr. F. B. Hamel, is very much appreciated. The National Association of Corrosion Engineers was also very helpful. The NACE extended me a scholarship, speaking engagements, and part-time employment at various times during my graduate work. The International Nickel Company is due thanks for research equipment funds. My appreciation is extended to Dr. H. V. Grubb for making these funds available to me and for his general interest in my work.

The unselfish consideration and encouragement of my wife, Elaine, through these several years of graduate study are deeply appreciated. She contributed not only to my morale but also to the editing and typing of the manuscript.

TABLE OF CONTENTS

TABLE OF CONTENTS (Continued)

TABLE OF CONTENTS (Continued)

LIST OF TABLES

LIST OF TABLES (Continued)

LIST OF TABLES (Continued)

LIST OF ILLUSTRATIONS

LIST OF ILLUSTRATIONS (Continued)

LIST OF ILLUSTRATIONS (Continued)

LIST OF ILLUSTRATIONS (Continued)

LIST OF ILLUSTRATIONS (Continued)

LIST OF ILLUSTRATIONS (Continued)

LIST OF ILLUSTRATIONS (Continued)

NOMENCLATURE

Å	= Angstrom unit, 1×10^{-10} meters
BF	= bright field electron micrograph
br	= broad diffracted beam
DF	= drak field electron micrograph
d-spacing	= interplanar spacing
d_{obs}	= interplanar spacing experimentally observed
hkℓ	= Miller indices for crystal plane notation
(hkℓ)	= the hkℓ plane
{hkℓ}	= the hkℓ family of planes
[hkℓ]	= the direction normal to the hkℓ plane
< hkℓ >	= the family of directions normal to the {hkℓ} planes
I	= intensity of a diffracted beam
I_o	= intensity of the undiffracted beam
m	= medium diffracted beam intensity
$\vec{R}_{(hk\ell)}$	= reciprocal lattice vector for the diffracted beam from the (hkℓ) plane
s	= strong diffracted beam intensity
SAD	= selected area diffraction
t_a^o	= time on initiating the annealing of an iron film; $t_a^o = 0$
t_a	= time at some point during the annealing of an iron film; $t_a^o < t_a < t_a^f$
t_a^f	= time at the termination of the annealing of an iron film; annealing period duration

t_e^o = time on initiating metal condensation on a NaCl substrate during the sublimation process for growing epitaxic single crystals of iron; $t_e^o = 0$

t_e = time at some point during the sublimation process; $t_e^o < t_e < t_e^f$

t_e^f = time at the termination of the iron sublimation during the process for forming iron single crystals; condensation duration

t_r^o = time on initiating a reaction; $t_r^o = 0$

t_r = time at some point during the reaction; $t_r^o < t_r < t_r^f$

t_r^f = time at the termination of a reaction; reaction duration

torr = unit of pressure, 1 mm Hg

vs = very strong diffracted beam intensity

vw = very weak diffracted beam intensity

w = weak diffracted beam intensity

α = symbol for alpha-iron

χ = symbol for Hägg carbide

ϵ = symbol for epsilon-carbide

μ = micron, 1×10^{-6} meters or unit of pressure, micron Hg

θ = symbol for cementite

SUMMARY

This dissertation treats the early effects of the catalytic decomposition of carbon monoxide on iron surfaces. To study the problem the system was simplified and the experimental analysis was conducted on a microscopic scale. The physical range of interest included crystallographic features such as dislocations on one end and product crystal distributions (over areas as large as 2,000 square microns) on the other. The electron microscope offers the versatility required to look at samples at the magnifications necessary to span this entire range. In addition, individual product crystals may be selected for electron diffraction analysis. In order to utilize the full capability of the electron microscope, metal samples cannot be much thicker than 1,000 Å. The experimental task was to develop the equipment and techniques to reproducibly grow thin, iron single crystal films and to expose these clean surfaces to high purity carbon monoxide at controlled temperatures.

The immediate goals of the thesis were to determine the nucleation sites for the first solid phase product, to identify it, and to study the effects of temperature and pressure on the reaction. Of more general significance, the reacted films were to be studied to characterize the early stages of the metal deterioration in CO environments. The collective information was to be used to establish the mechanism of the metal-CO interaction in its early stages. Success was achieved in the pursuit of these objectives.

The economic losses resulting from "metal dusting" provides the

motivation for research on the attack of metals by CO. Carbon monoxide decomposes on the surface of a catalyst to give carbon dioxide and elemental carbon. The decomposition reaction constitutes one of the more important reactions pertinent to metal dusting corrosion. The attack manifests itself on all the common alloys and base metals of Fe, Ni, Co, and their alloys resulting in embrittlement, pitting, and thinning of the metal. This type of attack is common to the petroleum and related chemical industries as well as many other applications dealing with high temperature carbonaceous environments. As a result of great deal of information related to and dealing directly with metal dusting and CO decomposition appears in the literature. The great amount of conflicting information and the even greater abundance of information for which no basis for comparison exists demand that more basic approaches be taken to solve the complex problem of metal dusting.

Several instances of the use of electron microscopy for studying reactions on metal films have been reported in the literature. On the basis of the success achieved in these studies, an experimental program was designed to explore the value of thin film studies for investigating the decomposition of CO on Fe, Ni, Co, and Cr. Polycrystalline films of these metals were made and reacted in a specially constructed tube furnace reactor. From this work it was evident that definite results could best be obtained from studies on virgin surfaces of single crystal iron films using high purity carbon monoxide and iron.

The general literature pertaining to the growth of epitaxic single crystal films of metals on alkali halides was very useful in providing the background necessary to ultimately develop the experimental techniques for

forming thin iron single crystals. The literature concerned with the growth of iron single crystals generally considered the process to be difficult, and few successful attempts have been reported.

From the literature it was learned that to prevent the formation of oxides on the surface of iron, a fresh surface would have to be prepared and maintained in a vacuum considerably better than 1×10^{-6} torr. The basic components of an Ultek TNB vacuum system (capable of vacuum in the 10^{-9} torr scale) were obtained to house the apparatus for making and reacting single crystal films of iron. The system was designed with a heater and substrate carrier assembly which could be moved through an arc at the end of an arm mounted on a rotary shaft. The substrate could, therefore, be positioned 1 inch away from an iron wire coil being sublimated electrically, and then positioned 1 inch beneath a radiant heater for annealing the deposited film. The latter position was also used for maintaining a controlled and definable temperature for reaction with carbon monoxide. The temperature of the film was defined by establishing a steady-state temperature for the substrate holder and bringing the temperature read by a thermocouple on the surface of the substrate to the same value. This was done by varying the power supplied to both the substrate heater and the overhead radiant heater.

Since the films were to be reacted without intermittent examination, the process for growing single crystals had to be reproducible. The successful development of the required techniques revealed that a rapid deposition rate and a high density of growth nuclei were more important than an exact temperature for the cleaved (001) face of the NaCl substrate. The corresponding film orientation had the (001) iron planes parallel to the film plane. It was determined that following the iron film deposition a

higher temperature annealing process was required before good quality single crystals were actually produced. Prior to annealing, the films were composed of a large number of crystallites of approximately the same orientation separated by low angle grain boundaries. Annealing the films resulted in the expulsion of the majority of the dislocations making up these grain boundaries. The resulting films contained a relatively low density of dislocation sub-boundaries. Attempts to make (110) and (111) plane single crystal films were not successful using the techniques developed for growing the (001) type crystals.

The (001) plane iron single crystal films were subjected to the surface decomposition of carbon monoxide at five different temperatures from 250° to 550°C and at four different pressures. Not all combinations of these conditions were used.

The investigations of the iron single crystal films in the electron microscope included the following: the crystallographic features of the iron films; the characterization of solid product nucleation sites; the morphology and size of precipitate particles; the precipitate particle population density; identification of the precipitate by electron diffraction; the orientation relationship between product crystals and the iron single crystal; the directional relationship between the precipitate growth directions and the crystal structure of the iron single crystal; and the interfacial character of the product-iron boundaries. The results showed the iron surfaces to be stepped and often faceted. The surface of high purity iron was demonstrated as a sufficient catalyst for the decomposition of carbon monoxide. Cementite was shown to be the first solid product to form. The cementite was found to nucleate at dislocation and dislocation

sub-boundaries. It was the only carbide identified under any of the reaction conditions used. Graphite was the only other product observed and it formed only after cementite began to decompose. Both products form by nucleation and growth processes. The growth rate for cementite particles was shown to be controlled by the diffusion of carbon in the iron lattice. The morphology of the cementite particles indicated the carbide to precipitate within the iron lattice. All these observations are explainable by the continuous precipitation process theory. No fixed orientation relationship exists between the cementite particles and the oriented iron lattice. Large crystals of cementite, suitable for structural studies can be produced by controlling the reaction by the techniques developed. Cementite was observed to decompose at a temperature as low as 450°C. Graphite, the product of cementite decomposition, has a tendency to precipitate from iron and/or cementite in special forms and orientations.

The results of this work and the general literature pertinent to the subject lead to the following postulate for the reaction mechanism in the early stages. Carbon monoxide adsorbs and decomposes relatively uniformly on the clean iron surfaces. This is indicated by the uniform density of the solid product particles. The nascent carbon dissolves in the ferrite matrix (a property which is proposed to distinguish a catalyst metal from a simple adsorber). If the metal is not capable of chemically accepting the nascent carbon then no CO decomposition will take place. The carbon eventually supersaturates the surface region of the lattice and cementite precipitates at local dislocations and dislocation networks. Thus, a continuous precipitation process is initiated for which iron and graphite are the equilibrium phases. The surface region may be supersaturated to some critical

value above which carbon penetration into the lattice ceases. The CO decomposition rate is, thus, a function of the carbon content of the iron as well as temperature and pressure. Therefore, the catalytic power of iron is a function of carbon content.

This mechanism may be obscured or even altered as the reaction develops. With the onset of cementite decomposition and a corresponding evolution of carbon and finely divided ferrite, a great increase in surface product formation seems a reasonable prediction due to the gain in surface area. This process would account for the many observations of increasing activity reported in the literature. However, actual mechanistic changes after long periods of reaction cannot be surmised from the present investigation.

CHAPTER I

BACKGROUND FOR THE STUDY

A. Introduction

This work treats the early development of the solid phase products resulting from the catalytic decomposition of carbon monoxide on iron surfaces. In order to expand the knowledge in this area, it was evident from the literature that rather sophisticated and basic experimental work was required. For this specific purpose equipment was designed and assembled to facilitate the *in situ* production and reaction of high quality single crystal thin films of iron. Such specimens were determined necessary in correlating and expanding the current information with the use of transmission electron microscopy and diffraction. The value and utility of the electron microscope in the analysis of this type of specimen is well recognized and constitutes a highly developed science. The theory and techniques of electron microscopy and diffraction applicable to this work are well treated in books by Thomas (1); Hirsch, Howie, Nicholson, Pashley, and Whelan (2); and Heidenreich (3). Therefore, when appropriate, descriptions of the techniques of electron microscopy used will be referenced rather than presenting them here.

The combined techniques of electron microscopy and electron diffraction have not been used before to study the effects of carbon monoxide decomposition on iron single crystal films. It is also the first program to use freshly prepared iron surfaces for the interaction studies. From a

review of the literature it is certain that such a basic approach is requisite to the full understanding of the complex counterpart encountered in industrial environments. The results of this research should also have a definite relevance to the continuing research on the heat treatment of steel.

B. Purpose

The specific goal of this research was to determine the nucleation sites of the first solid phase product formed in sufficient quantity to be detectable with the techniques of electron microscopy and electron diffraction. These techniques constitute the most sensitive methods of analysis available for the detection and characterization of reaction products precipitated within the metal matrix. The morphology of this first-formed product will be defined, the chemical compound determined, and its orientation habit with respect to the iron lattice established within the limitations of the above mentioned techniques. Secondary formation of other products will be investigated to a lesser extent. All the results will be discussed from the standpoint of their relation to the nature of the reaction process.

This research effort was limited to reaction temperatures below 550°C due to the high vapor pressure of the sodium chloride substrates. The temperature and pressure ranges actually studied were 250 to 550°C and 5 to 1,000 μ, respectively.

Although not the primary goal of this research, one of the more notable accomplishments was the prerequisite development of the techniques for the reproducible formation of high quality iron single crystal films.

C. Motivation

The immediate motivation for the research treated in this thesis is derived from the need to understand the basic factors in carbonaceous gas-metal corrosion phenomena occurring in a wide variety of large industries. "Metal dusting" is the general term ascribed to this phenomena which is manifested as metal deterioration and metal loss in high temperature carbonaceous environments (gas phases of pure components and combinations of CO, CO_2, and a large variety of hydrocarbons plus these same phases containing H_2O, H_2, and many other gases as minor constituents). All the common alloys and base metals of Fe, Ni, Co, and Cr are subject to attack under the right conditions. Vessels containing such atmospheres which are potentially carburizing and reducing may become brittle, pitted, and the walls may be uniformly thinned by metal wastage as a result of the attack. The reason for using "may" in the last sentence is because a subtle difference in atmosphere, physical variables, or material history can render metal dusting attack to one vessel while a similar one under essentially the same conditions may be spared. The petroleum, petrochemical, steel, and nuclear reactor industries as well as those making use of internal combustion engines are hurt economically by the occurrence of metal dusting.

In the petroleum and petrochemical industries, attack is known to occur in dehydrogenation units (4), waste heat boilers (5), fired heaters (6) and cracking units during operation and during regeneration of coke plugged lines, to mention just a few examples. Many other interesting and pressing problems exist as was demonstrated at the Refining Industry Symposium of the 15th Annual Conference of the National Association of Corrosion Engineers

in 1959 which was devoted entirely to metal dusting phenomena. Another extremely costly result of metal dusting in these industries is that of catalyst poisoning and fouling by metal dusting products. In the steel industry a major concern is the deterioration of fired clay, blast furnace linings due to the attack of so-called iron spot inclusions and other effects (7,8,9,10). Historically, the description by Pattinson (7) of the attack of blast furnace brickwork in Cleveland, England in 1876 was the first recognition of this type of deterioration as being the result of carbon monoxide decomposition. This reaction (the simplest reaction giving rise to metal dusting) is catalytic in nature and was given by Bell (11) and Boudouard (12) as $2CO = CO_2 + C$. Iron, nickel, cobalt, and their alloys and oxides have been reported as being the most active catalysts for this reaction (13-26).

The decomposition of CO stated to be the simplest case has received far and away the most attention of the metal dusting type reactions, and yet it proves to be complex enough with its side effects on the catalyst and its changing nature with gas mixtures to warrant continuing investigation. Some very good recent research on this topic has been reported by a team of scientists working in a nuclear reactor development program in England (26,27). In a steam generating High Temperature Gas Cooled Reactor (power reactor), inleakage of H_2O results in oxidation of the graphite core and production of partial pressures of CO and H_2 in the helium coolant. In the cooler parts of the helium circuit where the gas temperature ranges from 350 to 750°C, carbon monoxide is thermodynamically unstable. The gas can deposit carbon with regeneration of oxidizing H_2O and CO_2 impurities which can then further corrode the reactor core. On referring to the

literature relating to metal dusting, these workers found the information and data to be incomplete and often paradoxical. Therefore, a research program was initiated to solve their particular problem. Part of their work will be discussed in some detail later on in the thesis.

Another problem of current interest is the selection of materials for anti-smog devices for automobiles since these are subjected to atmospheres conducive to metal dusting (28).

Metal dusting is currently of such universal concern that the National Association of Corrosion Engineers (NACE), the American Petroleum Institute (API), the Atomic Energy Commission (AEC), and several individual companies are active in financing programs of research on topics related to the problem. The Engineering Experiment Station of the Georgia Institute of Technology was awarded a research contract from the NACE during the period 1965 to 1967. The purpose of the project was to define the products formed, the reactivity, and the reaction kinetics versus temperature for systems consisting of the common engineering alloys and the simpler metal dusting environments (gas phases of CO, CH_4, and their mixtures with H_2) for use in engineering design. This information has been published in project reports (29), periodicals (30,31), and presented at several conference symposia (32,33). These papers serve as good reviews of the current state of knowledge in the field. The largest and most current review compilation (soon to be published) is an annotated bibliography by Ratliff, et al. (34) covering the published material concerning metal dusting phenomena and related topics both applied and basic.

D. Literature Survey

A complete review of all the publications pertaining to metal dusting is beyond the scope of this work. This thesis is concerned with expanding the knowledge on the very early stages of the formations of solid phase products resulting from one metal dusting reaction ($2CO = CO_2 + C$) on iron. While this work stands unique to this system, there is obviously mutual relation between it and the rest of the literature. For completeness and logical introduction, a general summary of the reported phenomena occurring during CO decomposition on iron will be presented prior to a review of the literature specifically related to the research presented in this dissertation. Another review of the metal dusting literature may be found in the recent dissertation by Westerman (35).

1. General Summary

The carbon monoxide-carbon dioxide gas phase equilibrium is not independent of a carbon containing solid phase. The equilibrium was first studied by Bell (11) who formulated the chemical reaction as:

$$2CO = CO_2 + C \quad . \qquad (1)$$

As implied, however, it is not necessary for the carbon in this formulation to be present as amorphous or crystalline carbon (graphite). For example, it could be present as an interstitial solid solution in iron. Figure 1 represents the equilibrium composition of the gas phase over both iron (36,37) and graphite (11). It is evident from these graphs that there is a high potential (thermodynamic considerations are given in Appendix A) for carbon deposition at the low temperatures treated in this work (250 to 550°C).

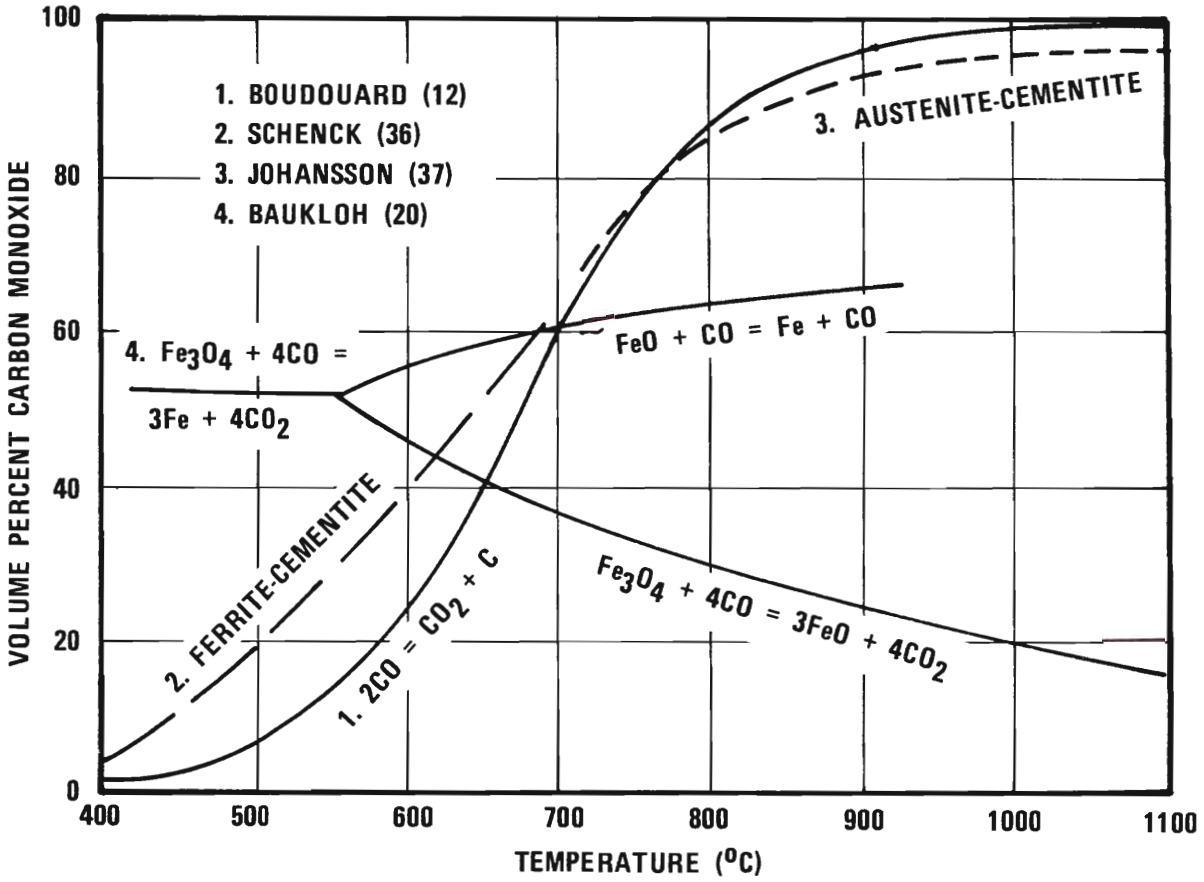

Figure 1. Equilibrium Diagram of the Fe-O-C System at One Atmosphere

Catalysts for this reaction exist which promote rapid carbon deposition in specific temperature ranges, characteristic of the catalyst present.

The reactivity of the decomposition of carbon monoxide over iron is found to be a complex function of temperature. This function is illustrated in Figure 2 which shows the reactivity (the slope of a weight gain curve of zone refined, 20 mil Fe wire in CO) plotted versus temperature. This information was taken from the work of Westerman (35) which represents the latest data of this type available. The peak in reactivity occurring between 450 to 650°C is a generally recognized phenomenon and characterizes the region showing maximum carbon deposition on the iron surfaces so often noted in the literature (10,15,38,39,40). Considerable uncertainty exists as to the phenomena producing this maximum which lies in the temperature region of most severe metal dusting. The theories postulated for the occurrence will be discussed later on in this section. It is important to note here that the temperature range of the investigation treated in this dissertation runs from 250 to 550°C which allows study of the phenomena creating the increasing reactivity.

a. Solid Phase Products. A variety of solid phase products has been reported by investigators of the phenomena accompanying the decomposition of carbon monoxide on iron-bearing materials:

Fe_2C-Hexagonal (also known as ϵ-carbide, $Fe_2C(H)$, and Fe_2C);

Fe_7C_3 (also known as FeC and Eckstrom and Adcock carbide);

Fe_5C_2 (also known as percarbide, χ-carbide, Fe_2C, Hägg carbide, X-carbide, and $Fe_{20}C_9$);

Fe_3C (also known as cementite and θ-carbide);

Fe_3O_4 (magnetite);

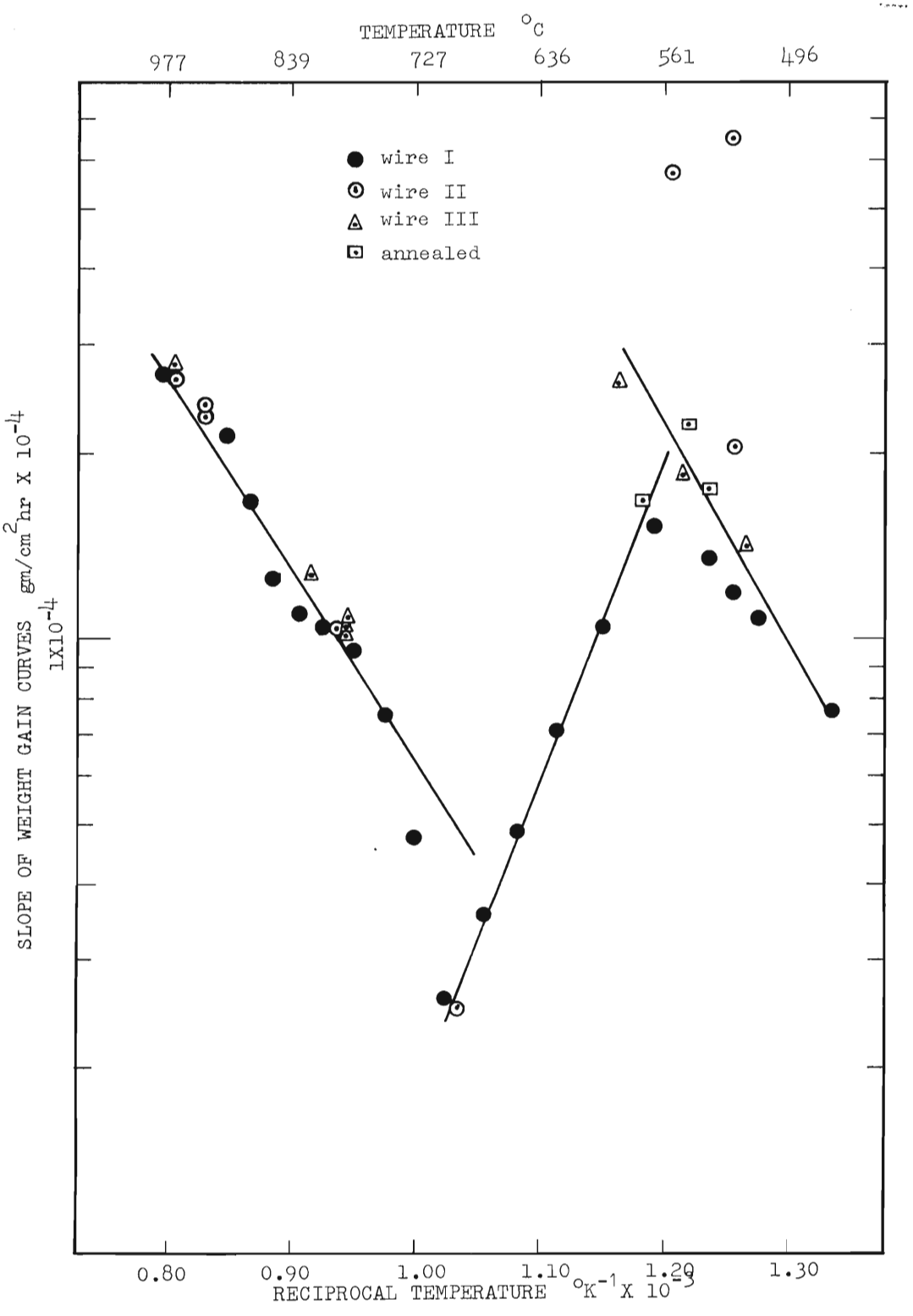

Figure 2. Reactivity at a Time of Incubation Plus Three Hours (35)

FeO (wüstite); and

$Fe(CO)_5$ (iron penta-carbonyl).

There is, however, contradiction over the occurrence of several of the products and more disagreement as to the range of existence and order of prevalence for each species. A summary of the literature pertaining to product identification is treated here by the tabulation of reported results and presented in Table 1.

Obviously from this information no definite conclusions can be drawn as to the existence and temperature ranges of all the products reported. Numerous forms of iron with varied histories were used for these examinations. In addition, the variety of treatments given the CO used in these studies makes it impossible to establish a basis for a systematic comparison of results. Although this tabulation does not represent all the literature related to CO decomposition, it does represent the major research efforts and those appearing to be the more carefully controlled.

In summation of Table 1, cementite (Fe_3C) has been observed after reaction on carbonyl Fe, Fe powder, vapor deposited thin films of Fe(single crystalline and polycrystalline), bulk single crystals (spheres and crystals with (001) faces exposed), Fe catalysts, zone refined Fe wire, electrolytic Fe (bulk and powder), Fe from reduced oxides, Fe_2O_3, Fe_3O_4, and blast furnace brick. There is not enough information on one type of iron to precisely determine the limits of stability of cementite and the other products. The temperature limits for each investigation often correspond to experimental design limits rather than a natural reaction range. On the whole, however, cementite has been found at temperatures as low as 250°C and as high as 1,000°C. Most of the observations lie in the range of 350 to 700°C.

Table 1. Products Observed for the Interaction of CO with Iron Bearing Phases

Year	Form of Iron Reactant	Reaction Products	Temperature °C	Gas Phase	References
1914	Fe Powder	$Fe(CO)_5$	RT	CO (1 atm)	41
		Decomposes	60-70		
1915	Fe_2O_3	Fe, C*	950	CO	42
		Fe Carbon, C	≤ 850		
1928	Fe	C_{gr}	400-700	CO	43
		X=Carbide	400		
1930	Carbonyl Fe	C_{gr}, Fe_3O_4, Fe*, Fe_3C*	≤ 450	CO (O_2 free)	44
		C_{gr}, FeO, Fe_3C*, Fe*, Fe_3O_4*	450-650		
		C_{gr}, Fe_3C, Fe			
	Fe_2O_3	Fe_3O_4, Fe_3C, Fe_2C	275 & 320		
1931	Fe_3O_4	Fe_2C(H) & Fe_3C mix with the	280-320	CO	45
		Fe_3C content inc. with temp.			
		$Fe_2C \rightarrow Fe_3C + C$	450		
1933	Fe	Mix of Fe_2C and Fe_3C	230-400	CO	46
		Fe_3C only	> 400		
1943	Fe Powder	Fe_3C, no higher carbides or oxides formed	to 500	CO	38
1949	Electrolytic Fe	Fe_3C first, then C_{gr}	500	CO	47

Table 1. Products Observed for the Interaction of CO on Iron Bearing Phases (continued)

Year	Form of Iron Reactant	Reaction Products	Temperature °C	Gas Phase	References
1950	Fe films stripped from rock salt	Fe_3C, C_{gr}, (Fe_3O_4*)	500-820	CO	48
1951	Fe films stripped from rock salt	Fe_3C, Fe_3O_4	350-400	CO	49
		Fe_3C*, Fe_2C(H)	350	CO & H_2	
		Fe_3C (1 hr), Fe_2C(H) (2-3 hr)	400		
		Fe_3C	> 400		
1951	Fe single crystals rock salt epitaxy	Fe_3C	500	Equal vols of CO & H_2	50
1952	Fe	Carbon filaments & Fe carbides	600	CO	51
1953	Fe from reduced Fe_2O_3	Graphite, Fe_3C (intermediate carbonyl)	500	CO	23
1953	Blast furnace brick	Filaments of C_{am} Fe_3C, $Fe_{20}C_9$	300-650	Furnace gas rich in CO	9
1954	Fe single crystal spheres	Fe_3O_4	250	CO	24
		Fe_3O_4, $Fe_{20}C_9$	350		
		Fe_3C, C	450		
		Fe_3C, C	550		
1955	Fe	Carbon filaments (0.01-0.2 μdia.)	390	CO	25

Table 1. Products Observed for the Interaction of CO on Iron Bearing Phases (continued)

Year	Form of Iron Reactant	Reaction Products	Temperature °C	Gas Phase	References
1955	Fe	Carbon filaments with Fe (0.01-0.2 μ dia.); $Fe_2C(H)$	450-600	CO	52
1955	Fe Powder	ε-carbide & carbon ε-transforms to χ then to θ	250-450	CO	53
1956	Fe_2O_3 of two history types	Fe_3O_4, $Fe_{20}C_9$, C	400-500	CO	39
		Fe_3C, Fe, C	500-1000		
1956	Fe_2O_3	Fe_3O_4	< 400		10
		C, $Fe_{20}C_9$, Fe_3O_4	400-565		
		C, Fe_3C, Fe_3O_4	565-700		
		Fe, no carbide nor C	> 700		
1957	Cast iron	Fe_3O_4	375-525	CO_2	54
		Fe_3O_4	375-525	CO/CO_2 equ.mix	
1959	Carbonyl Fe	Carbon & Fe_3C	500-700	CO + H_2	40
1959	Fe Cataylst	Carbon & Fe_2C	240-410	CO	55
1962	Reduced Fe	Fe_2C	250-300	CO	56
		Fe_3C	360-550		
1963	Fe Film	$Fe_{20}C$, C filaments (0.02-0.1 μ dia.)	649 (1200°F)	CO	57

Table 1. Products Observed for the Interaction of CO on Iron Bearing Phases (continued)

Year	Form of Iron Reactant	Reaction Products	Temperature °C	Gas Phase	References
1964	Fe Powder	Hägg carbide, Fe_3C, C	250-550	CO	58
1966	Electrolytic Fe (single and polycrystalline)	Fe_3C, Fe_7C_3, C lamellar, C whisker form	550	CO	26
1967	Fe wire (zone refined)	Fe_3C and C flakes and C filaments	500-700	CO	35

* - small quantity

C_{gr} - graphitic carbon

C_{am} - amorphous carbon

Hofmann and Groll (44) and Hägg (59) reported that temperatures as low as 200 to 300°C must be used to minimize the possibility of cementite formation.

Percarbide (Hägg carbide) has been observed as a result of CO action on Fe powder, Fe films (polycrystalline), single crystal spheres of Fe, Fe catalysts, Fe_2O_3, Fe_3O_4, and blast furnace brick. The temperature of formation has been reported as low as 230°C and as high as 850°C. However, several of the publications used in this tabulation indicated that percarbide does not form but decomposes rapidly above 400 to 450°C (45,46,49,53). On the other hand, Taylor (39) reported that in one instance, when graphite was produced in quantity over oxidized iron wire at 850°C, percarbide was formed. It should be noted that mixtures of cementite particles and percarbide particles have been reported in the temperature range of 275 to 400°C (44,45,46,49).

The higher carbides, ε-carbide (53) and Fe_7C_3 (26), were noted in iron powder attack at 250 to 450°C and in bulk electrolytic iron attack at 550°C, respectively. In the first case whole grains, though small, were converted to ε-carbide. The carbide was then observed to transform into Hägg carbide and then into cementite. In the second case the Fe_7C_3 formed as very small crystallites on the surface of the iron and on surface cementite. This carbide was also postulated as the nuclei for the growth of carbon filaments. This article will be reviewed in more detail a little later on in this chapter.

Carbon formation has been noted to occur in considerable quantity generally from 450 to 650°C and again above 800°C (29,35). In the 450 to 650°C range the carbon was observed in two typical forms, lamellae and filaments. The filaments were reported to have diameters in the range of

0.01 to 0.5 microns (9,25,26,35,52,57). Both types of carbon were generally graphitic in form and were believed to result from carbide decomposition as a consequence of this fact (26,43,47). Akamatsu and Sato (47) stated that diffraction patterns of amorphous carbon actually show d-spacings corresponding to (hk0) and (001), but since the carbon resulting from decomposition of CO showed (101) and (112) spacings, it proved to be graphitic. Since amorphous carbon must be heated to over 2,500°C to be graphitized, they concluded that the carbon deposit must have resulted from carbide decomposition.

The products contained oxides in several of the investigations listed. A few of these were from experiments using an oxide of iron as the initial reactant. Bahr (46) has said that products obtained by means of carburizing iron oxides always contain some oxide. Bauklow (15) found H_2O vapors to retard CO decomposition on oxides by preventing the formation of metallic iron surfaces. Thus, if oxides are initially present it is likely that an oxide will appear in the products. The most obvious reason for such an occurrence, of course, is that the reaction was not of sufficient duration to completely reduce the initial oxide phase.

In the case of an initially oxide-free iron sample, oxidation might occur from reaction with CO_2 in a CO_2-CO mixture if the composition of the gas mixture approaches the equilibrium ratio corresponding to the gas phase equilibrium. The ratio range affording this possibility is shown in Figure 1 illustrating the equilibrium relations for Fe_3O_4 (20). Billington (54) has described severe oxidation of cast iron in an equilibrium mixture at 375 to 450°C.

At low temperatures evidence indicates that the activation energy

must be relatively high for oxide reduction by CO. In Fischer-Tropsch catalysts, basically iron carbide, gradual oxidation to Fe_3O_4 has been ascribed to water vapor contamination in the feed stream of CO plus H_2 (60) (reactor temperatures of 225 to 400°C). A few of the tabulated examples showing oxide formation at low temperatures indicate the absence of an oxide at temperatures higher than 350 to 400°C.

It is difficult to effectively purify tank CO and CO produced by mixing sulfuric acid with formic acid. Berry, et al. (10) have analyzed commercially pure tank CO and CO made with formic-sulfuric acid with a mass spectrometer and have found air, CO_2, water vapor, benzene, H_2, SO_2, COS, and acetaldehyde as typical contaminants. They found in their investigation of carbon deposition on Fe_2O_3 that the sulfur-bearing contaminants were particularly troublesome. Their preliminary results were very erratic from run to run with the same tank as well as in comparison with runs using different tanks. Elimination of contaminants resulted in consistent results. Others have shown that the addition of small amounts of sulfur compounds to the CO decreases or stops decomposition over iron (15,19,61, 62,63). Nitrogen compounds such as cyanogen and ammonia are also effective inhibitors to the CO decomposition (15,25,62), while H_2 on the other hand is a well known carburizing promoter (25,62,64,65). Mention is made of these impurity effects in order to present the total setting in which the experimental findings were given. Before leaving this point it should be noted that impurities in the solid phase can also be effective in masking the true interaction relationship between carbon monoxide and the iron containing phase. Berry, et al. (10), for example, found that of two bottles of reagent grade Fe_2O_3 from the same manufacturer, one sample promoted

carbon formation, and the other failed to produce any carbon under the same reaction conditions with CO. Analysis of the contents of the two bottles indicated that in the carbon producing sample, 0.008 per cent sulfur was present and in the other, 0.2 per cent.

In summation, the phenomena governing the occurrence of each product constitutes a complex set of selection rules for real situations.

b. General Carbide Review. There are only four well characterized carbides of iron. Cementite (Fe_3C) was the first carbide structurally defined (66). The physical and chemical characteristics are well established for Fe_3C (67,68). This carbide is the familiar constituent of white cast iron and steels. As shown in the foregoing literature survey, it can be produced from ferrite by direct carburization with CO at appropriate temperatures. It has an orthorhombic crystal structure of lattice parameters a = 4.52 Å, b = 5.09 Å, and c = 6.74 Å. The crystal lattice spacings are given in Appendix B.

The next carbide discovered was the Hägg carbide in 1934 (59). It has been known as percarbide and as $Fe_{20}C_9$. Recently, Jack and Wild (69) definitely established this carbide to be Fe_5C_2 with the positions of the carbon atoms well defined. The monoclinic demensions are given with a = 11.562 Å, b = 4.573 Å, c = 5.060 Å, and $\beta = 97.74^{\circ}$. Hägg carbide may be formed by carburizing ferrite and is thought to be an intermediate in the tempering of martensite to cementite in high-carbon martensitic steels. The lattice parameters are given in Appendix B.

Epsilon-carbide was first characterized in the literature by Hofer and associates (68,70,71). Its structure has been established as hexagonal close-packed with lattice parameter a = 2.54 Å and c = 4.349 Å. Its com-

position is considered (72) very close to that of Fe_2C. As noted in the literature, it has been observed as a result of low temperature carburization of finely divided iron. It was conspicuous in the report of this observation that a promoted synthetic NH_3 type catalyst was used. Percarbide is also well established as the first intermediate in the decomposition of martensite. The lattice parameters for this carbide are given in Appendix B.

The current nomenclature for these three carbides is θ, χ, and ϵ, respectively (72). The literature indicated that the latter two are a result of precipitation from lattices highly saturated with carbon, but the temperature range of their stability has not been completely defined.

The fourth carbide was discovered by Eckstrom and Adcock (73) in 1950 in the catalyst charge of a fluidized-bed, hydrocarbon synthesis plant. It was tentatively characterized as FeC but has recently been found to be isomorphous with the well known M_7C_3 group (74). The substance Fe_7C_3 occurs among the reaction products of diamond synthesis when iron is used as the solvent for carbon. It does not lend itself to normal methods of laboratory synthesis. The lattice parameters are given in Appendix B.

c. Catalysts and Mechanisms. In this section discussion will be limited to the most important articles proposing mechanisms for the decomposition of CO over solids containing iron, excluding the great amount of information pertaining to intermetallic alloys. The development will be chronological so that the background available to the later investigators will be apparent since this knowledge had a bearing on their work and conclusions.

Hilpert and Dieckmann (42) studying the action of CO on Fe_2O_3 in 1915 found the oxide to be reduced after 10 hours at 950°C to 99.8 per cent

Fe without the separation of carbon. At 850°C and below carbide and carbon were found to form rapidly and led them to conclude that a carbide acts as the catalyst. They proposed that Fe_3C is broken down by CO with the formation of higher carbides (possibly Fe_2C and FeC) which then decompose to carbon and Fe_3C which is then available for further action.

Tropsch and Von Philippovich (13) in 1925 found great differences in the catalytic activities of irons produced by various oxide reductions. They studied the reactivity of CO with a large number of contact substances by measuring the CO_2 content in the product gas stream at 400°C.

In the period 1927 to 1931, Schenck (36,75), Hofmann and Groll (43,44) and Tutiya were major contributors to the research on CO decomposition in the presence of iron compounds. Schenck carried out extensive investigations of Fe-C-O equilibria and assumed metallic iron to be the catalyst. Hofmann and Groll held similar views of the catalyst, and their collective works indicate carbon deposits to result from carbide decomposition. Tutiya (76,77) on the other hand, proposed that the reaction is autocatalytic resulting from direct Fe_3C formation which subsequently catalyzes the reaction $2CO = CO_2 + C$. He stated that the carbon has no catalytic properties and further, that the Fe_3C becomes densely packed with the carbon and thereby isolates itself to the extent that it can no longer promote decomposition. A later interesting observation of his was that at 270°C percarbide can be formed.

The work of Baukloh and his associates Hieber, Spetzler, Henke, Chatterjee, and Das over the years 1936 to 1955 constitutes one of the largest and most comprehensive research programs carried out on the CO decomposition on metals and their compounds (14,16,19,20,65,78,79,80,81). Much of their work was specifically directed at determing the catalysts for

the reaction. They found that the oxides have practically no effect on the decomposition; the metal itself being the catalytic agent. Further, they noted that the decomposition occurred in the adsorption layer and was proportional to the amount of CO adsorbed. The temperature range studied was 300 to 900°C and the maximum rate of decomposition of CO at 1 atm was found to occur at 500°C whether the iron was initially present as Fe, Fe_2O_3, FeO, or Fe_3O_4. The generally noted decrease in reaction speed was attributed to the formation of metal carbides. The possibility of Fe_3C acting as a catalyst was explored and the conclusion was negative. Treatment of deactivated catalysts and Fe_3C separated from white cast iron with H_2 was found to produce a catalytic material owing to reduction of the carbides to the metal.

Olmer in 1942 (17),studying the catalytic decomposition of CO by ferromagnetic metals below 1,000°C, found catalysis to be limited to Fe, Ni, and Co. The activity was specifically attributed to the metals and not their compounds. He related the maxima in the activity curve for iron at 580 to 590°C to the agglomeration of the catalyst particles which thereby reduced the effective surface area.

Chufarov in 1947 (19) found the decomposition of CO on an "Fe catalyst" to be a first-order reaction in the pressure range 2 to 200 torr CO and in the temperature range 350 to 450°C. The reaction obeys the equation: $-dp/dt = k \cdot p$ where p is the pressure of CO. The reaction rate "v" was found to change according to the Arrhenius equation: $v = A \cdot \exp -E/RT$ where E, the activation energy, is 34 kcal/mole.

In 1948 Juliard, et al. (82) published their findings on a study of the dissociation of carbon monoxide in the presence of metallic oxides.

They observed in the case of iron that no carbon deposition occurred until the oxides had been reduced and an interface of iron-cementite had formed. Subsequently, the interface was considered to be the catalyst for the Boudouard reaction, Equation (1), rather than the pure metal.

In some carefully controlled experiments by Akamatsu in 1949 (47), iron was assumed to be the catalyst with carbon deposit formation resulting from carbide decomposition. Fleureau in 1953 (23), on the other hand, suggested as the first step of the reaction the chemisorption of CO forming a carbonyl on the surface. The volatility of the iron carbonyl, he stated, accounts for the presence of iron within the bulk of the carbon deposit. Further, Fleureau concluded that carbon and cementite are formed in two parallel reactions from the decomposing carbonyl. McKinney (18) was another proponent of a carbonyl intermediate in the reaction mechanism.

In the period 1948 to 1950, Kummer, et al. (83) and later Podgurski, Kummer, et al. (84) reported some interesting findings from their studies of Fischer-Tropsch synthesis catalysts. Radioactive tracer techniques and adsorption studies showed that the carburization of synthetic ammonia caralysts (iron base) with CO results in carbide formation at active surface sites rather than forming uniformly over the entire catalyst surface (the temperature range of carburization being 200 to 325°C). It was theorized that carbon could diffuse rapidly through the iron and deposit deep within the iron matrix on a carbide precipitate interface. Epsilon-carbide was observed to form by carbiding the fine grained ammonia synthesis catalyst at a temperature of 215°C without the presence of Cu as a promotor. The adsorption experiments showed that carbides do not adsorb CO. It is important to note that they postulated that oxygen in small amounts could stabilize

cementite. This hypothesis was based on stability comparisons between cementite formed by CO carburization versus hydrocarbon carburization; cementite from the latter process decomposing after only a few hours at 500°C. Longer times and higher temperatures were required to decompose cementite resulting from the former process which was also noted to always produce small amounts of oxide. Articles by these investigators, although comprehensive, failed to give a complete formulation of carburization.

Kehrer and Leidheiser (24) made a study of the catalytic properties of the various crystal surfaces of a number of metals. The decomposition of CO was the selected reaction and the crystals used were in the form of spheres so that all planes would be exposed in a single run. For iron in carbon monoxide they found the first darkening of the sphere at 550°C in regions neighboring the three major crystal faces. These crystal faces showing highest reactivity were planes of unequal indices and generally of high index. Second in order of reactivity were the crystal faces of type (211), (311), (411), etc.; third in order of reactivity were crystal faces of type (221), (331), (441), etc.; fourth in order of reactivity were crystal faces of type (210), (310), (410), etc.; fifth in order were type (111) and (110) faces; and sixth were (100) faces. Cementite in fine needle form was the first product to form on each face and was followed by the appearance of carbon deposits. The reaction sequence for both products when related to crystal faces followed the activity guide above. The cementite needles were observed to increase in size with time and to cover practically the entire crystal surface before the carbon deposits began to appear. The carbon deposit was characterized, using the electron microscope, as being made up of long coiled threads. Similar results were observed at lower temperatures with Fe_3C being replaced by $Fe_{20}C_9$ (350°C and below).

In 1955 Royen and Blumrich (53) and MacIver and Emmett (52) found metallic iron to catalyze the decomposition of carbon monoxide in the temperature ranges 250 to 450°C and 450 to 600°C, respectively. On the other hand, Berry and his associates (10) claimed the catalyst to be provided by the conversion of the oxide (Fe_2O_3 being the iron-bearing phase investigated) to a carbide. They reported Hägg-carbide to be the catalyst from 400 to 565°C; from 565 to 700°C the catalyst was stated to be cementite having an abnormally low Curie temperature range. Further, they stated definitely that cementite does not catalyze the reaction between 400 and 565°C and that metallic iron, magnetite (Fe_3O_4), and carbon are not catalysts. The reaction maxima was found to occur in the same temperature interval as that found by the majority of other researchers, 500 to 600°C.

Taylor (39) in 1956 introduced a new idea to the list of proposed catalyst mechanisms. While studying the decomposition of CO over iron and iron-oxide powders in the temperature range 400 to 1,000°C, he found carbon deposition to take place below 723°C only when there was some Fe_3O_4 present. At the higher temperatures nascent carbon was viewed to penetrate and supersaturate the iron lattice with subsequent graphite and carbide precipitation. At the lower temperatures, Taylor doubted the ability of the carbon to migrate into the lattice fast enough to result in the high reaction rates observed. Since the iron atoms are more widely spaced both in the oxide lattice and at the oxide-iron interface than in α-iron, he suggested that carbon atoms could enter the iron lattice more easily at the oxide-iron interface or by exchange with oxygen ions during reduction. Further, the supersaturated solution formed tends to precipitate graphite and iron carbide. According to this scheme, carbon deposition is catalyzed

by the Fe_3O_4-Fe interface which can result from partial oxide reduction or from reoxidation of iron. They attributed deactivation to complete conversion to iron and iron carbide. Reaction rate was suggested as determining the proportion of graphite to carbidic carbon formed (cementite and percarbide at low temperatures). The higher rates were reported more favorable to carbide formation. The appearance of percarbide at 500°C instead of cementite was explained by the occurrence of accelerated carburization due to a "rate promoting pretreatment" of the oxide. In summation of his section on the preparation of iron carbides, it is also interesting to note that he stated "evidently, temperature is by no means the only factor in determining which carbide shall form." The generally noted reactivity decrease above 550°C he attributed to the more rapid reduction of Fe_3O_4.

Kagan and associates (55) in 1959 reported a study of the reaction kinetics of carbon monoxide in the presence of iron catalysts. The temperature range was 240 to 410°C, and the catalyst was formed by reducing a mixture of 100 Fe_3O_4 + 6 Al_2O_3 + 4.2 SiO_2 + 1.2 K_2O + 0.5 Cr in hydrogen at 800°C. Although this particular CO-catalyst system is not of interest, certain points in the results should be noted. It was shown that in the presence of this catalyst, curves relating the rate of the carbon deposition with time pass through a maximum during the initial stages. It was determined that this resulted from an autocatalytic phenomena in the reaction concurrent with carbide formation (percarbide at lower temperatures). The following mechanism for the formation of iron carbide was then suggested. Initially, crystal nuclei of the new carbide phase form and grow, increasing the area of the carbide-iron interface. The reaction apparently occurs by an autocatalytic process as do a great many reactions involving solid phases.

During the second stage, following the maximum rate of reaction, the nuclei of the new phase were explained to begin to coalesce. They form a layer of carbide which advances to the center of the granule. The phase boundaries contract and access of carbon monoxide to these boundaries and migration of carbon are retarded. The reaction rate decreases with time, and the reaction proceeds by diffusion. Carbon deposits as described are noted to form only after the maximum rate of carbide formation is reached.

Extensive investigations by Walker, et al. (40) of the decomposition of CO on carbonyl iron in the presence of hydrogen indicated the catalyst to be metallic iron. They assumed that CO chemisorbs on iron but not on cementite. The carbon atoms produced on decomposition were said to have a high mobility and migrate across the surface to a nucleating center (probably a dislocation) where they begin forming concurrently both free carbon and carbide (cementite). The production of free carbon was said to stop when the catalyst has been completely carbided to cementite, since the chemisorption of carbon monoxide will also stop. This work was done in 1959 and covered the temperature range 450 to 700°C.

During the period 1962 to 1964, Cox (57), Hui and Boulle (56), and Schmitt (58) found that metallic iron acts as a catalyst in the decomposition of CO.

The Bureau of Mines Bulletin 631 (72), published in 1966, analyzed and summarized research at the Bureau of Mines dealing with the preparation, properties, and reactions of iron carbides in the period 1948 to 1960. This work was compiled under the direction of L. J. E. Hofer. The major objective of the program was to develop better catalysts for the synthesis of hydrocarbons from hydrogen and carbon monoxide. The investi-

gations resulted in the characterization of epsilon-carbide, which has also proved to be an important intermediate in the tempering of martensite in steel. It was observed that the carbon from CO reacts nearly completely with finely divided alpha-iron to form ε-carbide in which the metal atoms are arranged in a hexagonal, close-packed configuration. Epsilon-carbide was observed to have a composition within 2 atomic per cent of that for Fe_2C and had a Curie point of about 370°C. This carbide was convertible to percarbide by thermal treatment at 343°C for approximately 70 hours. The latter had a Curie point of 247°C and could also be synthesized from CO at 240°C. The resulting carbide had a carbon content within 7 atomic per cent of Fe_2C. Percarbide was noted to transform and produce cementite at 550°C in about 315 minutes. Pure percarbide was found to decompose to form cementite with the elimination of free carbon. The Curie point of the cementite formed was 210°C. In the presence of an excess of free iron (percarbide and iron being in intimate contact), percarbide was found to react with the α-iron to form cementite. The latter reaction proceeded at an appreciable rate at 320°C. It was stated that the ease of the reaction in the presence of free iron suggests percarbide to be an intermediate in the tempering of epsilon-carbide to cementite.

It was noted that carbiding α-iron to near completion at 240°C over a period of approximately 300 hours resulted in a preparation containing no measurable amount of epsilon-carbide. However, brief periods of the order of a minute resulted in the formation of detectable epsilon-carbide even at temperatures as high as 325°C. The data was then said to indicate that epsilon iron carbide is an intermediate in the formation of percarbide.

The detailed mechanism of the carbiding of alpha-iron is somewhat

uncertain, Hofer admitted, but the main features, he suggested, may be summarized in the illustration given in Figure 3 taken from his report. Hofer used the following line of reasoning in his account of the reaction scheme. At temperatures below 100°C and at CO pressures of several atmospheres, the iron carbonyl may form. For the standard pressure of 1 atm, a surface carbide results at higher temperatures subsequent to CO dissociation and CO_2 formation and desorption. The surface carbide atoms can combine to form free carbon, or in a competing process, the surface carbon atoms can penetrate the lattice and form an interstitial solid solution in the iron. The free energy of the surface carbide atoms was stated to be sufficiently high so that the solution may become supersaturated with respect to the three known carbides. Which particular carbide is precipitated was noted to be a function of temperature. Therefore, in view of the proposed ϵ to χ to θ sequence, Hofer proposed that by choosing the correct temperature the reaction can be halted at any desired stage. Alternately, the various iron carbides may form directly from a solid solution (85) as indicated by the dotted lines in Figure 3. The carbon concentration values, determined by Roberts, Averbach, and Cohen (86) and given in Figure 3, indicate the concentration limits giving rise to ϵ-carbide and cementite precipitation.

It should be pointed out that the emphasis of the work by Hofer, et al. was the study of carbides in bulk (the determination of the temperature range of their formation and thermodynamic stability). They sought to carburize the whole sample or a large percentage of it. As a result, they used methods which accelerated iron carburization and completely bypassed the study of the initial carbide precipitation in high purity iron

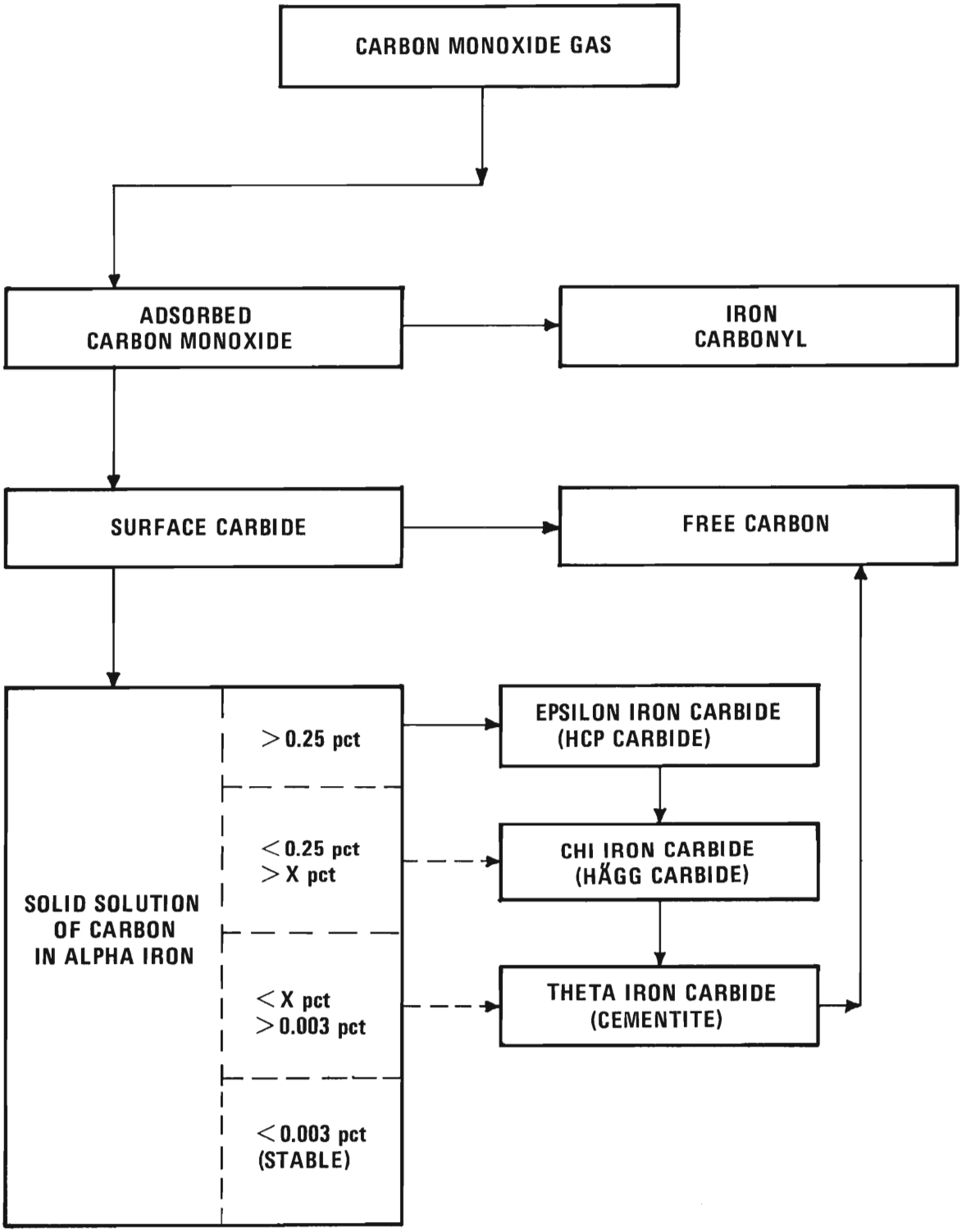

Figure 3. Hofer's (72) Concept of the Process of Direct Carburization of Alpha-Iron. Heavy Arrows Indicated the Most Probable Sequence

at relatively slow rates of carburization. This is the area covered by the present research.

Ruston, et al. (26) in 1966 reported iron to catalytically decompose carbon monoxide. High purity, electrolytic iron samples of single crystal and polycrystal plate configuration were used at 550°C. They found that the various partial pressures of CO used in argon mixtures served only to effect the rate of the reaction and not the mechanism. The nacent carbon produced in the CO decomposition was proposed to carburize the metal bulk by interstitial diffusion with subsequent precipitation of cementite after the solution became supersaturated. The surface cementite was observed to take the shape of simple or composite pyramids with varying geometries at their base. These were said to have grown epitaxially on the surface (relation not given) and were dendritic in structure. The locations of cementite precipitates were transgranular and intergranular, and each precipitate particle was considered to be a single crystal. After a period of time dependent on the CO partial pressure, a carbon deposit appeared in the central region of the cementite pyramids. The carbon formations (lamellar graphite flakes)were found to grow in size with time along with their number.

The selective effect of metal crystal orientation was noted to disappear after long periods of exposure. Concurrent with cementite formation and decomposition, small crystals of Fe_7C_3 were observed to grow epitaxially (relations not given) and to be uniformly distributed over a single metal grain. These were noted to vary in population density from one grain to another. These crystals were reported to act as growth centers for the second type of carbon deposit observed, whiskers (the commonly ob-

served filamentary carbon). In the later stages of reaction the whiskers were said to lift the Fe_7C_3 crystals from the surface which continue to function as the growth centers.

2. Literature Specifically Related to the Present Research

There have been published approximately a dozen articles relating to research quite similar to that treated in this dissertation. It is pertinent to examine these investigations separately and in more detail than the general literature reviewed thus far. Jean J. Trillat is one of the pioneers in the use of electron diffraction as a tool in the investigation of metallurgical phase transitions, solid state reactions, and surface reactions. As early as 1950 he and his associates were investigating the CO attack on thin iron films. Their efforts were directed primarily at the development of the utility of their research technique rather than being specifically aimed at complete solutions of the physical problems investigated. The early articles were short and lacking in detail. The latter studies were taken up by Oketani and his co-workers as a direct result of his association with Trillat. The research effort changed under their direction to a study of the carbide phases as a consequence of CO carburization rather than a study of the process of carburization.

The first reports (48,87) described the results of carburizing thin polycrystalline films of iron and mild steel. The films were prepared by thermally evaporating the metal in a vacuum system and condensing it on freshly cleaved rock salt (single crystal NaCl blocks) at the temperature of the system. The films were stripped by dissolving the salt in water, and the films were then collected on nickel grids. These specimens were then submitted to cementation in a separate reactor and later examined by elec-

tron diffraction. The results at 540°C revealed the presence of orthorhombic Fe_3C. The carbide formation was noted not to occur at lower temperatures, and higher temperatures resulted in graphite formation as well as cementite. Above 820°C the diffraction patterns of cementite and iron were masked by the carbon. Oriented maganetite (Fe_3O_4) was observed to form either as a result of the reaction or spontaneously on exposure of the samples to air. From the text of the discussion, excessive Fe_3O_4 was produced if fresh CO was not continuously supplied to the reactor. The fine-line character of the diffraction patterns indicate that very fine and randomly distributed crystallites of both iron and cementite formed.

The next article in this group by Trillat and Oketani (88) treated the same subject with the addition of a study using CO and H_2 mixtures (equal volumes). The iron film thickness was stated to be 500 to 1,000 Å and the reactions were carried out for 1 to 3 hours. In pure CO the only products noted at temperatures of 350 and 400°C were Fe_3C and Fe_3O_4. In the H_2 mixtures no oxide was formed. At 350°C in the gas mixture Fe_2C (Hägg-carbide) was observed as well as a trace of Fe_3C. At 400°C after 1 hour of reaction (in the gas mixture) only Fe and Fe_3C were detected; after 2 to 3 hours Fe_2C began to appear. As a result of these findings, H_2 was determined to promote carburization and Fe_3C was proposed as a precursor to Fe_2C. Also, Fe_2C was said to decompose to Fe_3C and carbon at 450°C.

Their next publications (50,88) concerned the cementation of single crystals of iron. The only changes in procedure over those previously used were the heating of the freshly cleaved substrate to 600°C before depositing the iron and the annealing of the freshly stripped film in H_2 at 700°C for 1 hour. The result of cementing the films at 500°C in an equal volume mix-

ture of CO and H_2 (the only atmosphere used) for 1 hour was the formation of cementite particles with an estimated mean dimension of 1 to 10 μ. The crystal face of the iron which was exposed was said to be the (001). The Fe_3C was observed to be oriented such that Fe_3C (111) ‖ Fe (111) and Fe_3C ($1\bar{2}1$) ‖ Fe (110). The orientation of the cementite was said to deviate ± 5° around the [111] of Fe_3C. On prolonging the reaction (2 or more hours) the diffraction patterns took on the appearance observed for the polycrystalline reactions.

From the diffraction patterns given in the article, it is evident from iron reflection arcing that continuous iron crystals of near perfect orientation were not obtained in these experiments; only a highly oriented film of many iron crystallites. The disorientation of the cementite is further evidence of the discontinuity of the original iron film.

The latest article of interest by Trillat (89) showed a shift of emphasis. Electron microscopy and diffraction studies were reported for the carburization of iron by the heat treatment of iron-carbon layers. He observed that up to 350°C only iron and carbon were present as a result of heating an iron layer (200 Å thick) vapor deposited on a layer of carbon (100 Å thick). Above this temperature a new (unidentified) ring appeared growing in intensity with temperature. Cementite first appeared at 500°C and remained visible to 700°C where it began to decompose to iron and graphite.

In 1955 the work of Oketani and Nagakura began to appear and continued to be published through 1961 (90,91,92,93,94). The publication in 1959 (93) by Nagakura covers their work on iron and is available in English. The substance of their work was the study of the temperature range of stability and

the nature of the phase transformations of iron carbides. The samples used were polycrystalline and single crystal films produced by the techniques developed under Trillat. However, the temperature of the rock salt was held at 500°C for the epitaxial growth of single crystals. These films were reported to be 200 to 300 Å thick, and the polycrystalline films had an estimated mean crystallite size of 50 Å. The carburizing atmosphere was carbon monoxide but the iron films were oxidized to Fe_3O_4 at temperatures lower than about 350°C. It was found, however, that the specimen films were carburized without oxidation even below 350°C if they were covered by fine iron powder. Using this technique for the polycrystalline films the carbides ϵ, χ, and θ were found to be formed in the temperature ranges: below 250°C, from 250 to 350°C, and above 350°C, respectively. At temperatures above 350°C, amorphous carbon was observed along with the other products. Cementation for several hours was observed to convert the films completely to carbide.

It was found difficult to form carbides from the single crystal films. Epsilon-carbide could not be produced even after treatment for 20 hours. For temperatures below 250°C, oxidation of the film could not be prevented. Above 250°C the χ- and θ-carbons formed in the same temperature intervals as before. Epitaxial relations of the carbides to the iron were noted on the single crystals of iron although that for the χ-carbide was not defined. Cementite was determined to have either the orientation relation Fe_3C $(1\bar{2}1)$ [111] $\parallel$ Fe (110) [001] or Fe_3C (111) $[\bar{2}11]$ $\parallel$ Fe (001) $[0\bar{1}0]$. They pointed out that the orientation relation given by Trillat and Oketani is not internally consistent.

Phase transitions from ϵ to χ and from χ to θ took place irreversibly

at 380 to 400°C and at about 550°C, respectively. This occurred in the span of only a few minutes. Cementite was observed to partially decompose at 600°C to Fe and graphitic carbon. The absence of detectable carbon resulting from the ϵ to χ and χ to θ transitions was said to indicate the lack of an appreciable composition difference between the carbides.

It was proposed that for the formation ϵ-carbide imperfections in the iron matrix play an important role by accelerating the diffusion of carbon and forming the nuclei of carbide crystals. This idea was based on the resistance of the single crystals to form ϵ-carbide in comparison to the ease of its formation on polycrystalline films of high fault density, i.e., grain boundaries. Also, ϵ-carbide crystals were noted to be approximately the same size as the original iron grains, suggesting a one for one relation with no recrystallization. The χ- and θ-carbides, on the other hand, formed on both types of iron films and resulted in crystals much larger than the iron grains in the polycrystalline specimens. The nuclei were said to form on the surface of the iron and grow gradually. Thus, it was proposed that the imperfections in the iron lattice do not play an essential role in χ- and θ-carbide formation. These statements were made without the aid of micrographic information. The character of the iron reflections in the diffraction patterns given in their work does not suggest that the films were continuous iron monocrystals of nearly perfect orientation, but films of highly oriented iron crystallites.

The chemical preparation of stable iron carbides has met with success in only a few special cases. Hermann Schenck, et al. (95) in their investigations of the time and temperature stability relations of the iron carbides utilized the method of high vacuum vapor deposition for preparing samples

which can be studied in the electron microscope. They stated that high vacuum deposition is the only method for production of thin foils under varied but controlled conditions. In this work Schenck reported how reproducible layers of Fe and C can be made by successive depositions on a suitable substrate. He outlined the procedure for heat treatments to obtain the thin carbide layers of interest. The evaporation of iron and carbon were made after the system had been evacuated to a pressure of 8×10^{-6} torr. The total sample thickness was limited to 1,000 Å for best electron transmission. The thickness was monitored by a photoelectric device. The heat treatment of the samples was effected immediately following deposition in a special device inside the evacuated chamber.

On 215 Å carbon foils which covered a perforated screen (microscope grid), 500 Å of Fe was deposited. Individual specimens were heat-treated at 200 to 900°C for times ranging from several seconds to 10 hours. Cementite and Hägg carbide were identified. In one electron diffractograph of a specimen heated above 750°C, using a heated specimen holder, the decomposition of cementite was observed.

In order to make an investigation with limited amounts of C, pieces of NaCl were used as condensing and heating surfaces. Using a ratio of 600 Å of Fe to 130 Å of C, special attention was given to the conversion of Hägg carbide into cementite. In successive experiments the distinction of the structures was made on the basis of lattice spacings. From the electron micrographs he stated that it was obvious the transformation of Hägg carbide into cementite proceeded by decomposition of $Fe_{20}C_9$ and simultaneous formation of Fe_3C.

It was also observed that the formation of carbides could be affected

by the manner in which the iron film was condensed. After deposition of Fe on freshly cleaved NaCl crystal at 400°C, a two-fold orientation of Fe to salt occurred. A strong lattice disorder of the Fe matrix resulted from this orientation. After carbon was evaporated on such an Fe foil, hexagonal ε-carbide was found following heat treatment between 180 and 280°C. The high degree of disorder of the Fe lattice, they stated, seemed to promote diffusion of C and increased reaction rates. According to the electron micrographs, α-Fe carried its particle form and size into ε-carbide. At lower temperatures the ε-carbide was specifically oriented relative to the iron lattice. The ε-carbide transformed into cementite through an intermediate Hägg carbide stage. The ranges found for the existence of the carbides are given in the Time-Temperature diagram of Figure 4.

The question in view of the above summary of the literature is whether or not the general phenomenon of CO attack is complex enough to consider as legitimate, all the superficially contradictory findings. A closer look at the work of these investigators reveals the merit of their observations and postulates and justifies the assumption that a complex problem exists in studying the carbon monoxide reaction and its effect on the iron bearing phase.

It should be evident that in order to fully understand the phenomena involved, a systematic approach starting with the simplest system possible and designing in step by step the complications involved is necessary to understanding the real problems confronted in practice. Only by so doing can a basis be formulated for systematic comparisons and extensions of the work on the overall problem. The present work is the most basic approach to date and can serve as the nucleus for the development of planned research

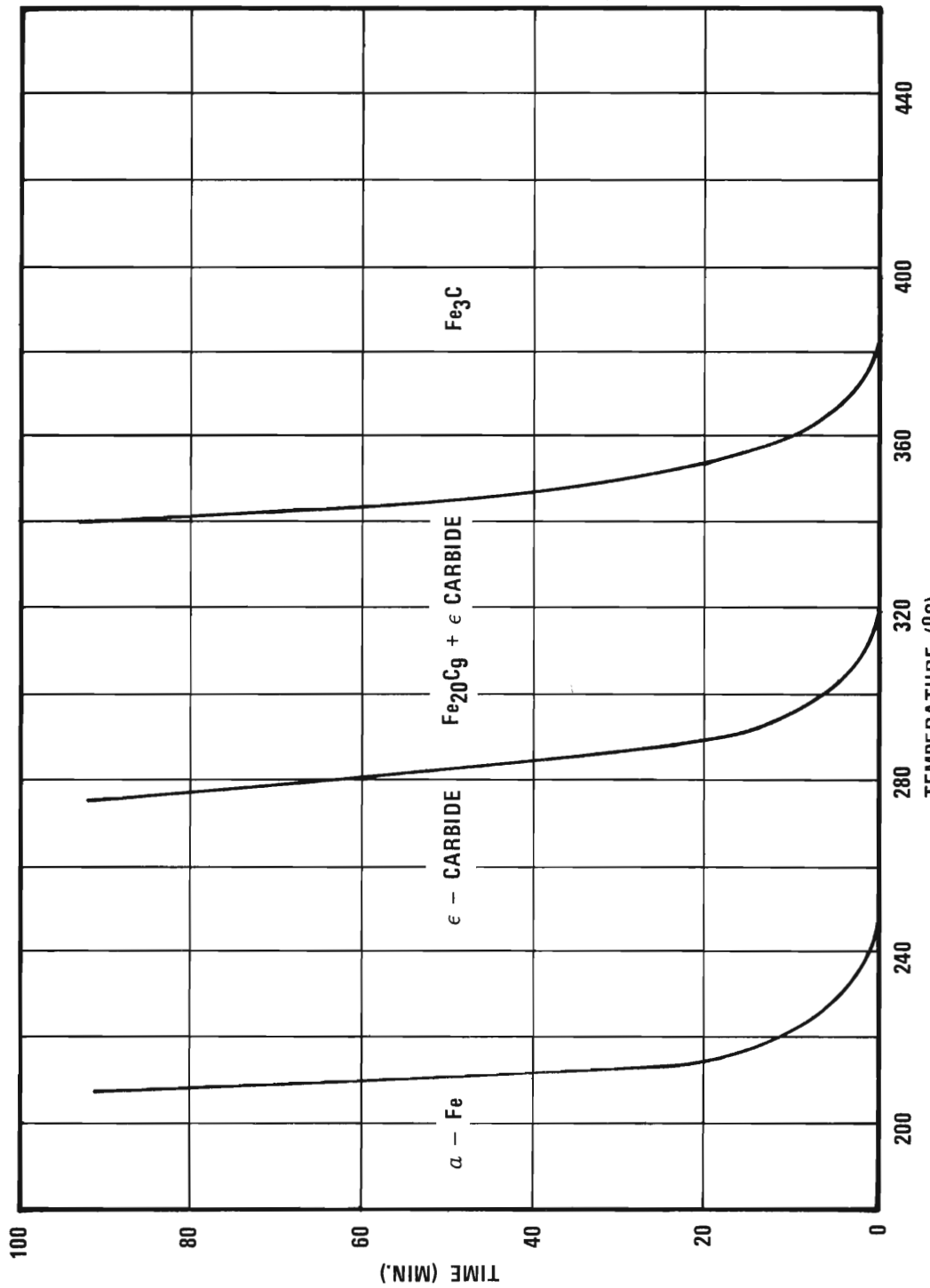

Figure 4. Schenck's (95) Time-Temperature Diagram for Carbide Formation

on the total problem.

The next section will contain a description of preliminary work performed in the development of the techniques and experimental background ultimately used in this research program.

E. Background Investigation

The substance of this thesis represents not only the information obtained in this work but also the capability for determining much more basic knowledge by use of the equipment and techniques developed. A whole vista is opened for the study of the early stages of solid phase product formation resulting from catalyzed heterogeneous reaction. The development of the research program was, of course, a step-wise process, and it is instructive to examine here the implications of the first experiments carried out.

Prior to the present work at this institution, Cox (57) performed a series of preliminary experiments on CO decomposition on thin vapor deposited films of iron. His work was confined to reactions at 1,200°F followed by electron microscopic examinations. Since this was not the major subject of his thesis, the experiments were of an introductory nature. Consequently, it was decided to expand this work to include more temperatures and to look at films of cobalt, chromium, and nickel as well as iron. The metal-CO system corresponding to a single stainless steel constituent being perhaps most responsible for metal dusting susceptibility and offering interesting and studiable characteristics was sought. The successful performance of similar research by Trillat and Oketani (48,49,50) and analogous investigations on the oxidation of thin copper single crystals by Marcus and

Brockway (96) helped justify the thin film approach. It allows the use of the powerful techniques of transmission electron microscopy and diffraction.

Detailed reports of the work done on the thin films of Ni, Cr, Co, and Fe have been presented in papers given at two of the regional meetings of the National Association of Corrosion Engineers (97,98). In view of this and since the work reported in this thesis makes use of these results only as a guide for more precise programming rather than using them for the foundation of thesis conclusions, only a brief summary is considered pertinent here.

The polycrystalline (crystal size of the order of 0.01 to 0.1 μ mean diameter by 500 to 1,000 Å thick) were prepared by vapor deposition onto amorphous substrates in a vacuum system at 1×10^{-6} torr. The evaporator source was stranded W wire. The geometry for evaporation placed the source beneath the substrate at a distance of approximately 4 inches. The substrates were previously prepared by vapor depositing a layer of SiO on parlodion film covered electron microscope grids (3 mm diameter, 200 mesh, copper screens). The purities of the source metals were 99.7 per cent for Ni and Fe and unspecified (reagent grade materials) for Co and Cr. Thirty-five specimens were prepared per evaporation. Several were reserved of this number for unreacted standards, and the others were reacted in multiple specimen runs at various temperatures for different durations. The specimens had to be exposed briefly to air upon removal from the evaporator. Consequently, storage in a desiccator was the only means of contamination control. The samples were all reacted within 48 hours of their deposition and restored in the desiccator. Analysis normally followed within 24 hours after reaction using a Phillips 200 electron microscope with an 80 KV

accelerating potential for both micrographs and selected area diffraction.

The samples were reacted in the apparatus illustrated in Figures 5 and 6. The laboratory furnace and temperature controller incorporated into this system was previously described by Cox (57). Chemically pure carbon monoxide or argon was supplied from commercial cylinders and was metered at approximately 0.5 cfh through the 1-inch ID quartz reactor tube. Exhaust gases were expelled into a hood either through an oil trap bubbling station or through a mechanical vacuum pump. The general procedure for a reaction run was to purge the system repeatedly with argon using the mechanical vacuum pump for successive evacuations and then to heat the system to reaction temperature under a vacuum. The CO was then admitted to the reaction chamber. The termination of a run was carried out by evacuating the system and removing the furnace to freeze the reaction for final analysis.

In the case of nickel, an unreacted film was taken directly from the vacuum evaporator and examined in the electron microscope. The film displayed a uniform grain size and gave an electron diffraction pattern for pure nickel. There were no extra diffraction rings or spots. This same sample was then reacted for 1 hour at 649°C (1,200°F). A specific account was kept of this sample and its analysis.

The temperatures used in these experiments were in the more reactive range of metal dusting and followed the precedents set by Seagraves (99) and Cox (57). Ten runs were made on Ni films at the three temperatures, 594°C (1,100°F), 649°C (1,200°F), and 760°C (1,400°F) for durations of 2 to 60 minutes. The diffraction patterns for all runs indicated graphite to be the only reaction product which formed. This was noted under all the conditions used.

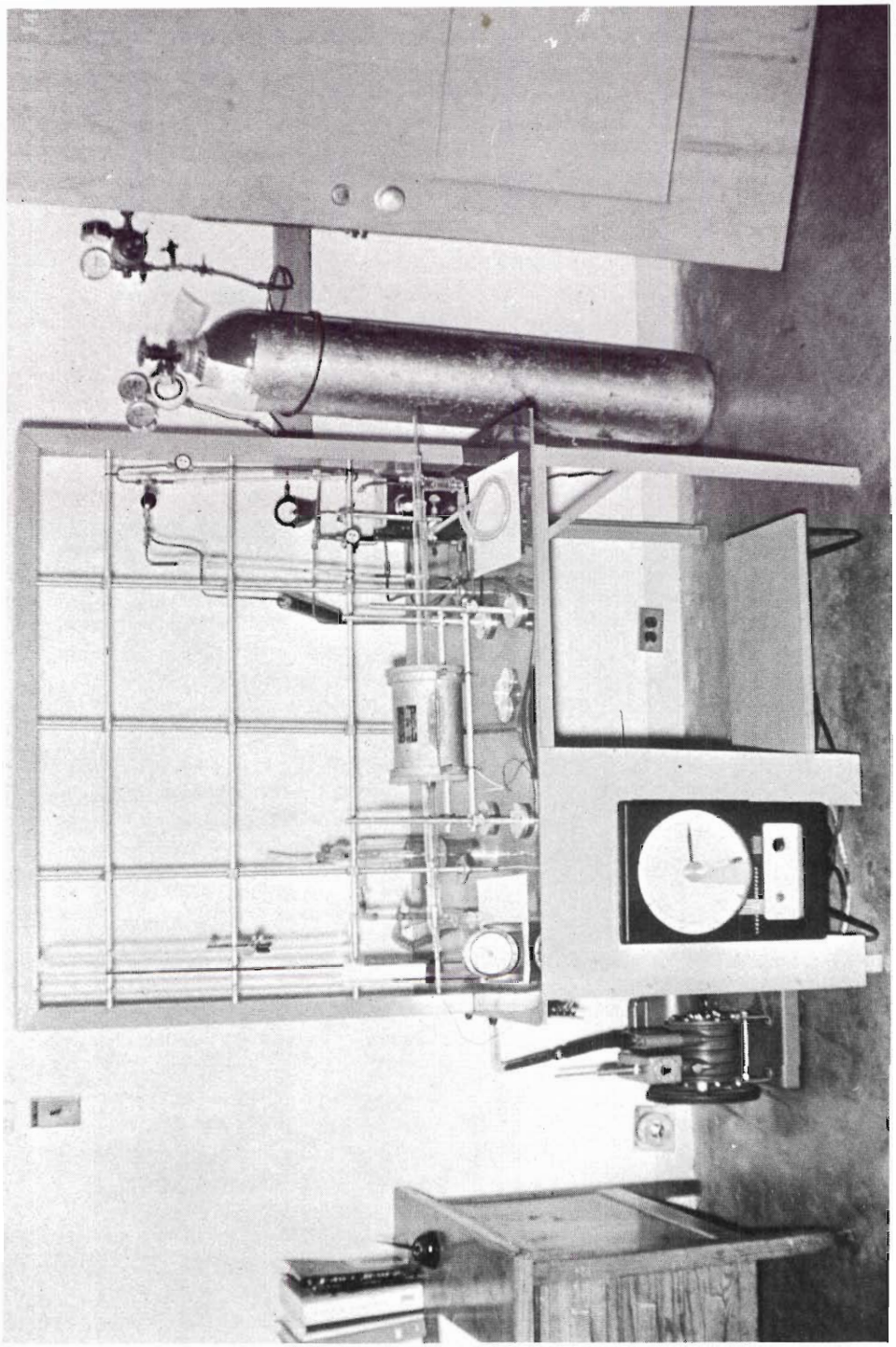

Figure 5. Atmospheric Pressure Reactor for Polycrystalline Film Experiments

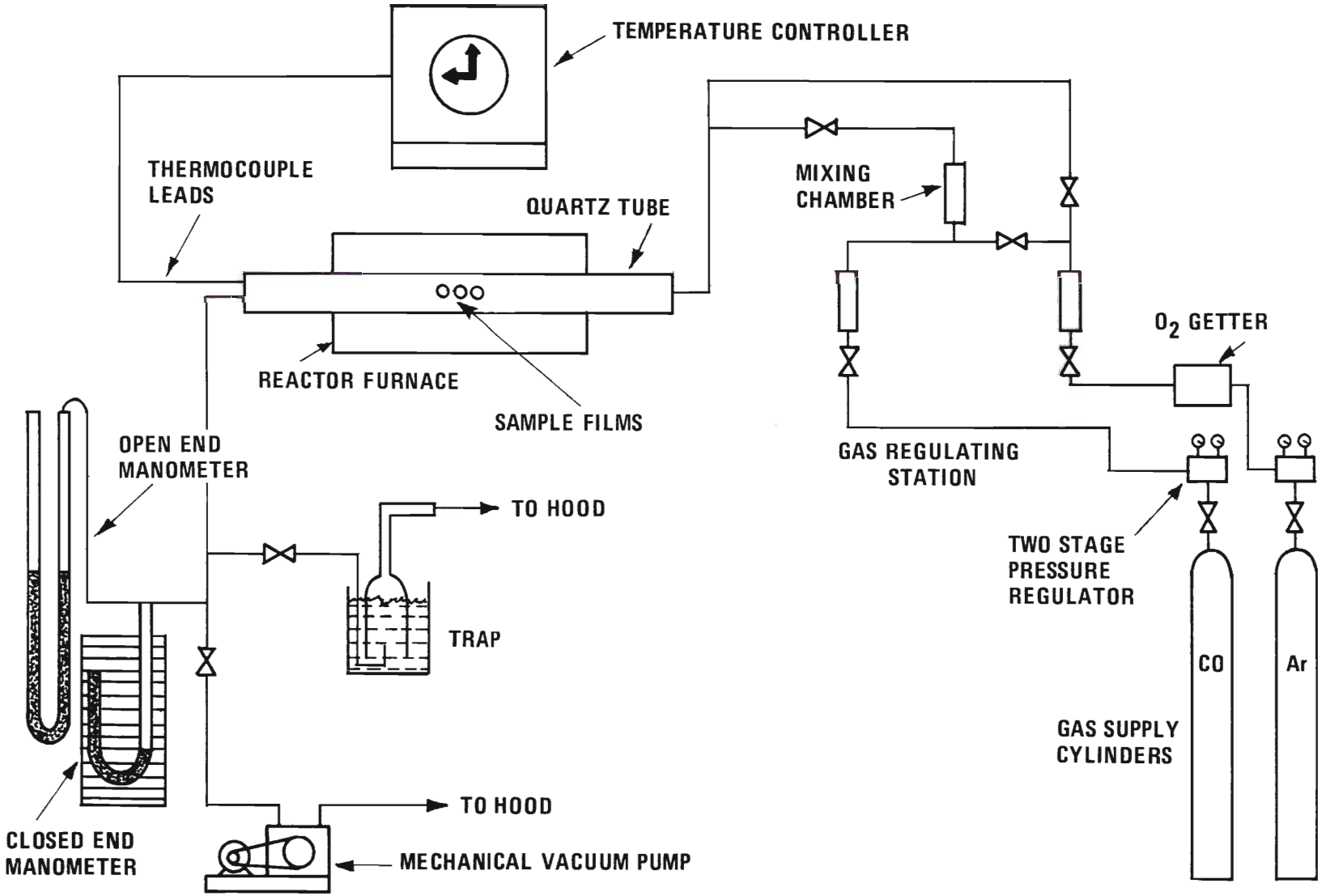

Figure 6. Schematic Diagram of the Reactor System for Exposing Polycrystalline Metal Films

Combining the information contained in the micrographs and their corresponding selected area diffraction patterns (noted as SAD patterns henceforth), carbon formation appeared to cluster on selected grains. Likely filament formations were also noted in a few instances and appeared to be attached to specific grains. Nickel, it was noted, tends to agglomerate on the substrate surface and in some instances to form regular patterns. This implied a preference in crystallographic orientation for the crystallites of nickel. The agglomeration of films of this thickness is not an uncommon effect. Agglomeration is an undesirable phenomena for this type of investigation since the crystallographic features of grain boundaries, dislocations, etc., disappear or are masked by the process.

Concurrently, Grenga (100) at the University of Virginia was reacting expitaxially grown single crystal thin films of nickel with CO. The general procedure for preparation of nickel single crystals by Grenga was the vapor deposition of nickel onto heated rock salt in a vacuum system with the subsequent removal by water stripping. The films were then dried and stored in a desiccator. Before exposing the films to CO they were annealed in hydrogen in the reactor. Her results showed that the catalytic activity of nickel varied from one major plane face to another. The order of decreasing activity was (111) > (110) > (100). Graphite was the reaction product forming at surface steps on the (111) and (110) faces. Only on the (001) face did she notice a carbide to form. This phase was not identifiable as one of the well-known carbides and was suspected to decompose to give graphite. A possible correlation existed between the graphite deposits and dislocations in the film.

Difficulty was encountered in preparing chromium films of good elec-

tron optical quality. Experimental runs were made, however, reacting Cr films at 649°C for 1, 3, 6, and 10 minutes. The micrographs contained very little comprehendible information regarding the reaction. The electron diffraction patterns showed the chromium to rapidly undergo carburization. However, in a preoxidized condition the chromium was not subject to carburization. After 1 hour at 649°C, cobalt remained unreactive. Based on this result, experiments on cobalt were terminated.

Iron was studied in considerable detail and the results were interesting. Prior to the experimental work, all the reactions devisable between CO, CO_2, C, and Fe were checked for thermodynamic feasibility. This treatment is presented in Appendix A. The study was made in order to clarify the thinking on possible reaction phenomena taking place.

One of the freshly deposited iron films was examined in the electron microscope immediately upon its removal from the vacuum evaporator. The microstructure of this specimen is shown in Figure 7 along with the corresponding SAD pattern. The rings observable in this picture are characteristic of iron only. However, there are some very faint rings present which did not show up in the print, corresponding to Fe_3O_4. Groups of the other Fe films were reacted in a total of ten runs at the following temperatures and times: 594°C - 60, 10, and 4 minutes; 649°C - 60, 20, 10, 4, and 2 minutes; 705°C - 16 and 2 minutes. In all cases an Fe_3O_4 pattern was present mixed in with the other product patterns. The quantity of Fe_3O_4 was observed to increase with reaction time. The character of the pattern indicated the presence of an exceedingly fine-grained oxide material which probably covered the entire specimen. The small amount of oxide observed on the unreacted standard iron film is not an uncommon occurrence, and

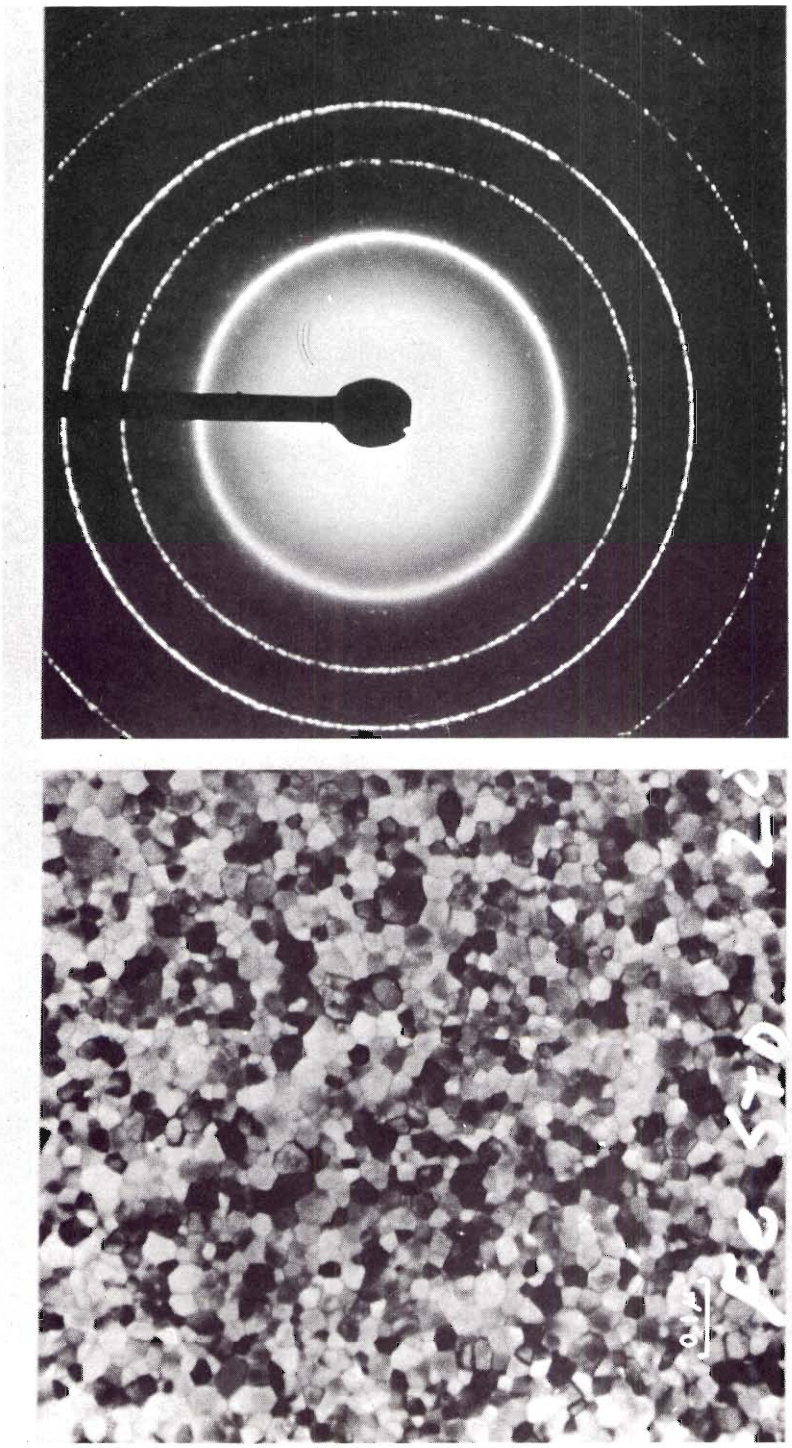

Figure 7. Micrograph and SAD Pattern of a Freshly Deposited Iron Film

similar effects have been found by Schenck (95). It appears that a pure iron film is immediately oxidized upon exposure to air. This results in a thin film of Fe_3O_4 perceptible only with electron diffraction.

In the shorter runs the products of the reaction appeared to be carbides with graphite appearing only after 1 hour of reaction. The carbide reflections were absent when graphite reflections were observed. Figure 8 shows the diffraction pattern of a sample reacted for 2 minutes at 705°C and a specimen reacted for 1 hour at 649°C. The diffraction pattern shows that the iron of the first specimen is being depleted as the oxide (characterized by the new rings) and carbide (characterized by the reflection spots) form. The pattern of the second specimen is typical of the 1 hour runs at higher temperatures. Here the oxide rings are visible with the graphite reflections just perceptible in the negative. The left frame of Figure 9 is a SAD pattern of a sample reacted for 1 hour at 594°C. The major reflection of graphite, (002), appears as the bright center-most ring. Accompanying the SAD pattern is a micrograph of the sample. It is evident that the original metal matrix has been destroyed and replaced with a disoriented mass of reaction products. The left frame in Figure 10 shows a micrograph of a sample reacted for 2 minutes at 649°C. A definite morphology is observed for the relatively large crystalline product. The SAD pattern on the right was taken of a similar area of a sample reacted in the same run. The relatively small number of reflection spots attests to the large crystallite size of the carbide. It was not possible to determine whether more than one type of iron carbide was present. The difficulty may be attributed to the similarities of the different carbide patterns and to the lack of resolvable ring reflections which would have allowed the comparison of

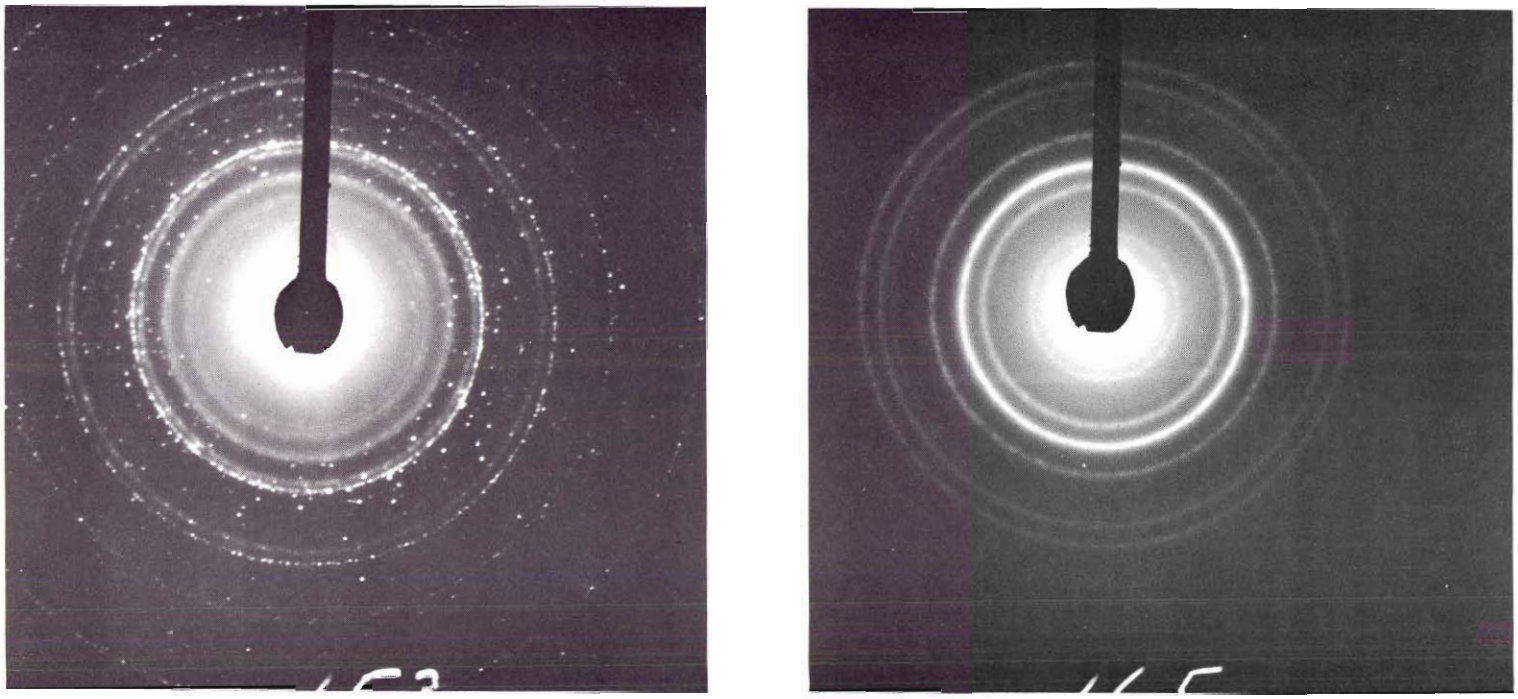

Figure 8. SAD Patterns of Iron Films Exposed to Carbon Monoxide: 2 min. at 1300°F (705°C)(Left) and 1 hr. at 1200°F (649°C)(Right)

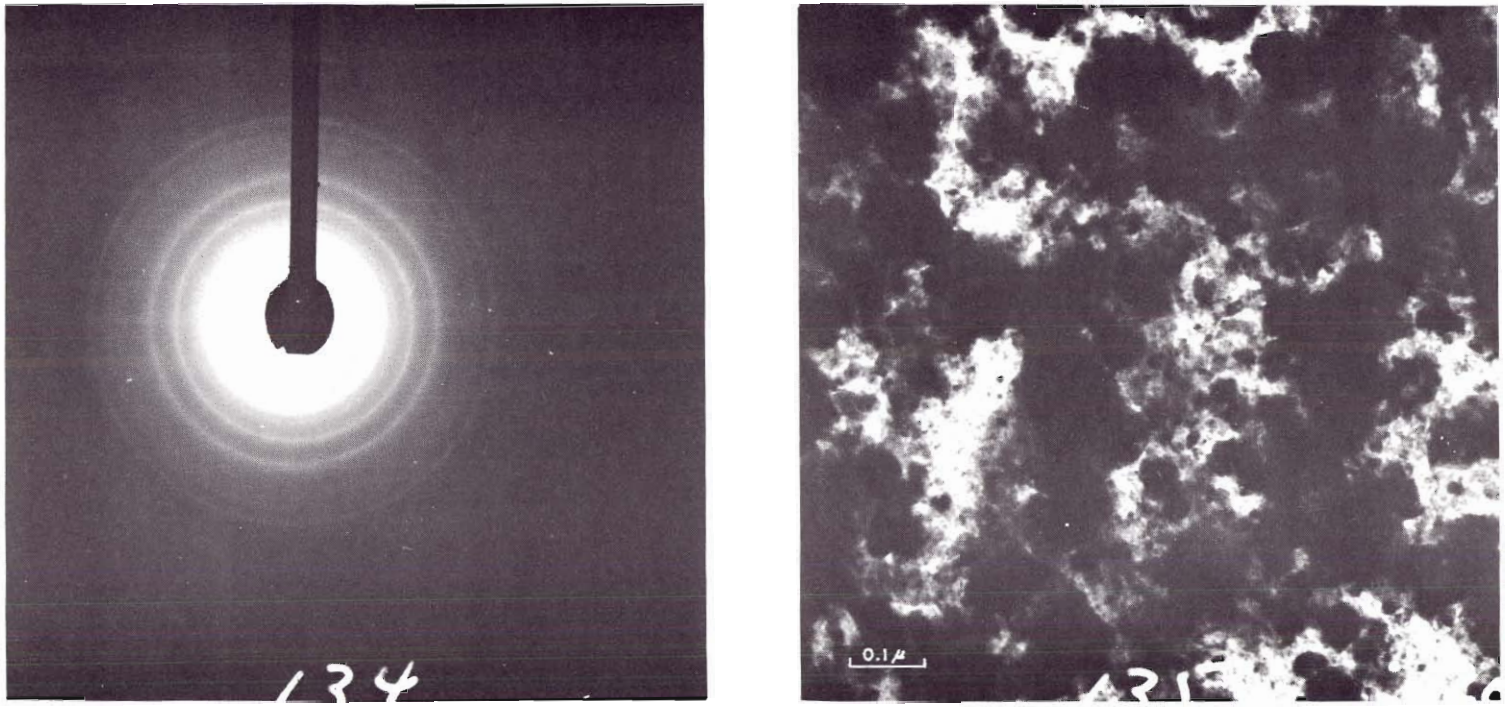

Figure 9. SAD Pattern and Micrograph of an Iron Film Exposed to Carbon Monoxide for 1 hr. at 1100°F (594°C)

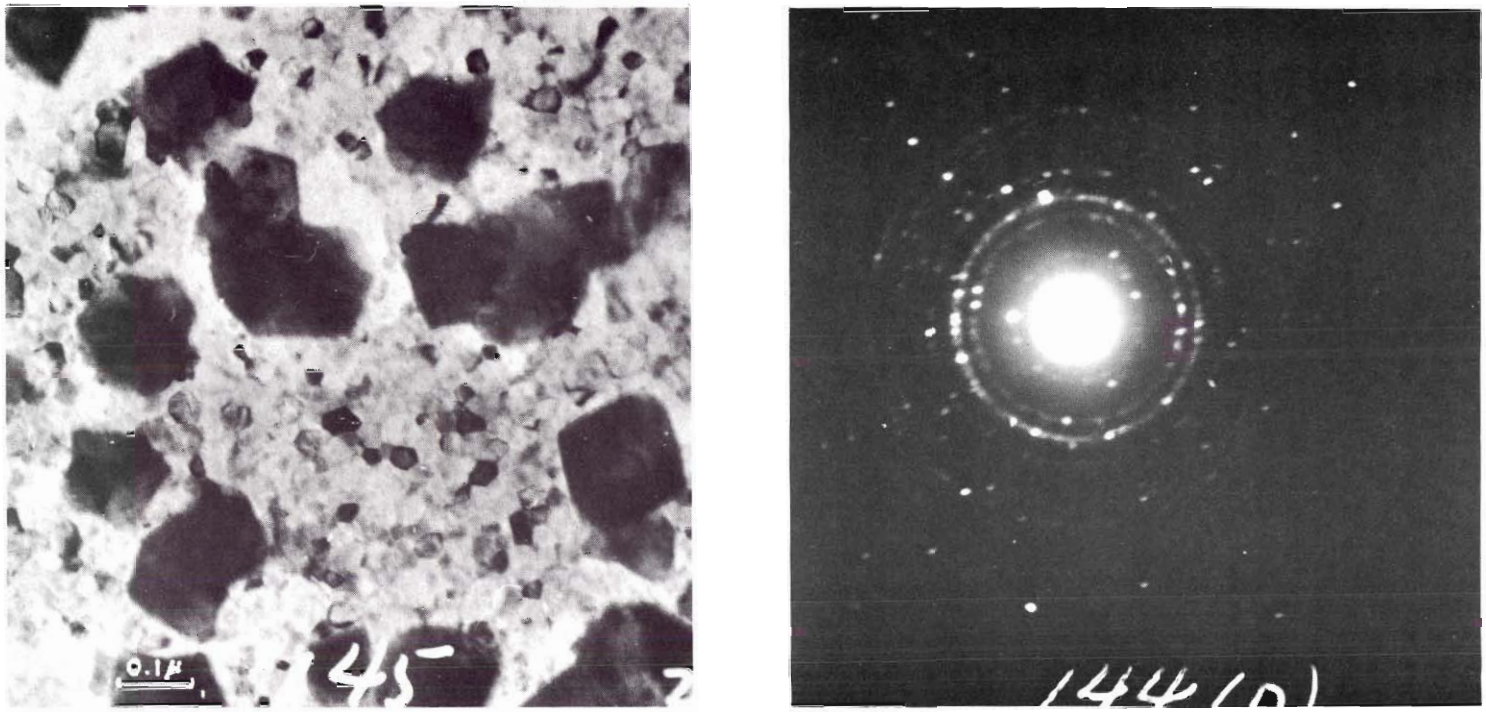

Figure 10. Typical Micrograph and SAD Pattern of Iron Film Exposed to Carbon Monoxide for 2 min. at 1200°F (649°C)

ring intensities and accurate diameter measurements. On the other hand, a single crystal pattern from an individual product particle could have been used to define the product if such had been available.

In Figure 11 products formed after 20 minutes of reaction at 649°C are shown at low and high magnifications. This product appears to be a decomposed version of a crystal of the type illustrated for the product after 2 minutes of reaction. The configuration of these deposits suggest that they may be the nuclei for the filament formations referenced in the metal dusting literature.

Small regular crystals of carbide were found for short reactions on iron at all the temperatures investigated. Figure 12 shows two micrographs picturing the relative placement of the product crystals with respect to the large grains of iron. The grain size increase resulted from grain growth during the time required to attain thermal equilibrium at 705°C (reaction time was 2 minutes for this run).

The degree of reaction in the temperature range used was determined to be too great for a good morphological study of the solid phase product development. It was observed after 4 minutes of reaction that the metal matrix had been consumed. Therefore, no relationship could be found between the product and parent crystals. Even after 2 minutes the crystalline product was so large with respect to the metal grains that little information could be obtained concerning the location of nucleation and the crystallographic relationships between the product and metal grains. Specific crystals and grain boundaries were observed to be more susceptible to attack. However, the phenomena could not be thoroughly investigated due to the metal's abnormally small grain size. Such small crystals are known to have an

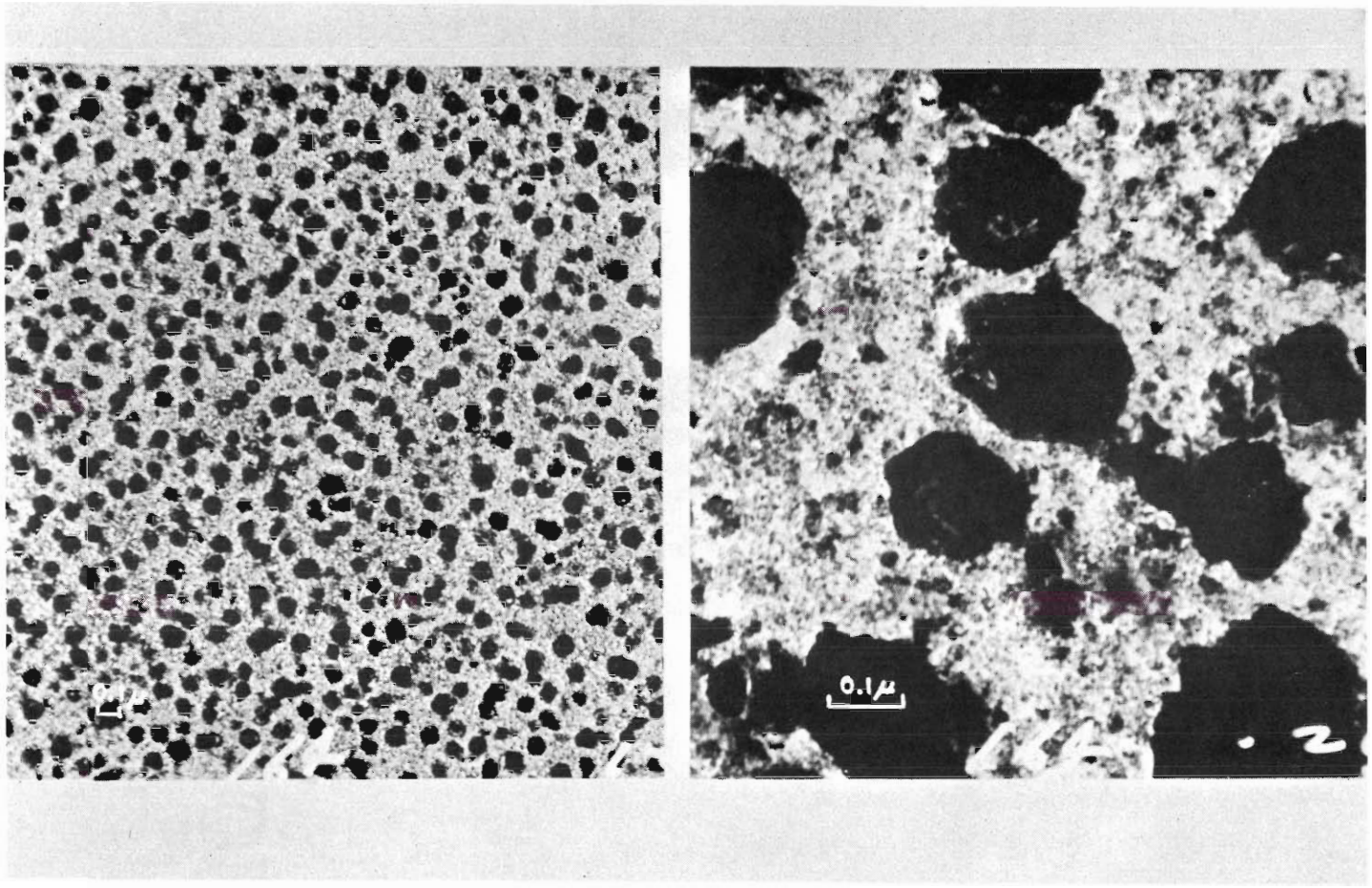

Figure 11. Micrographs of an Iron Film Exposed to Carbon Monoxide for 20 min. at 1200°F (649°C)

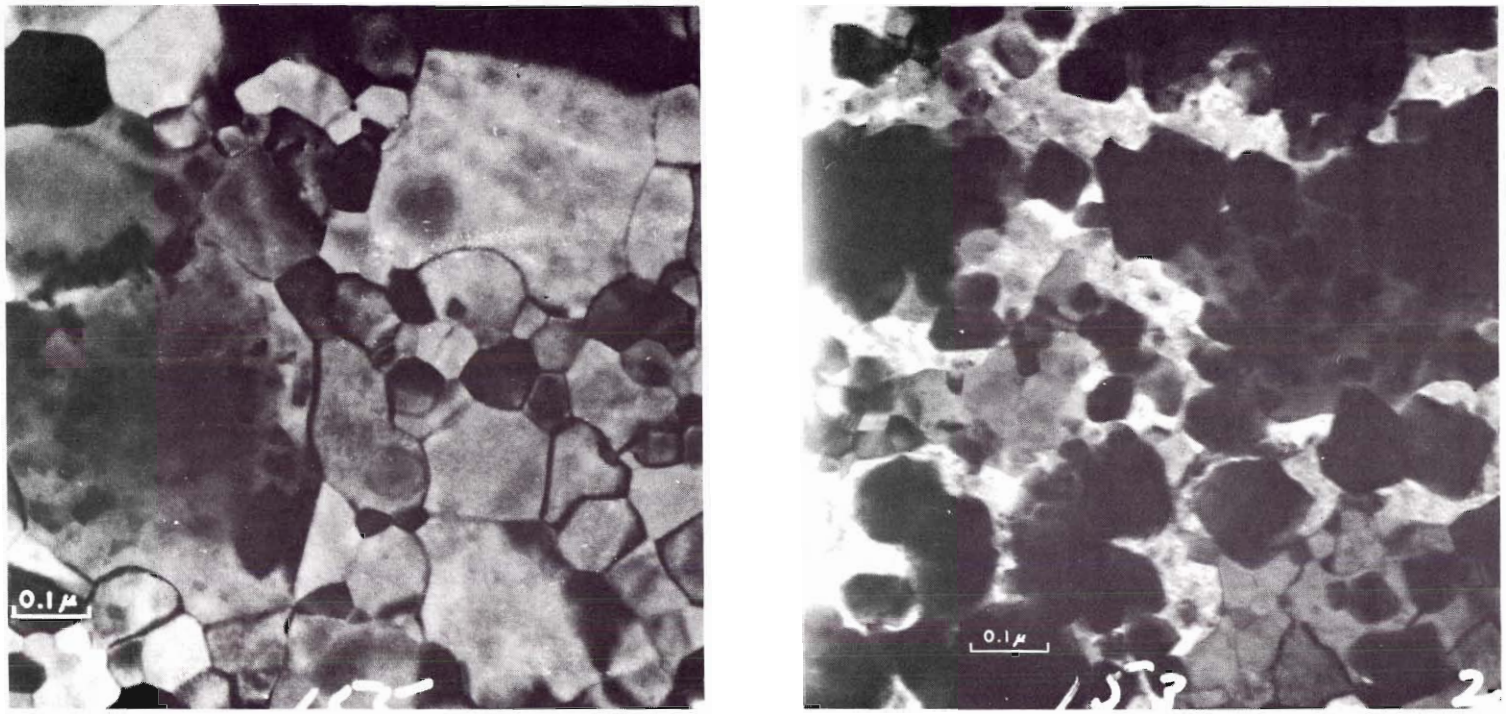

Figure 12. Micrographs of Iron Film Exposed to Carbon Monoxide for 2 min. at 1300°F (705°C)

abnormally high degree of internal lattice order. As a result, the reactions were unduly influenced by grain boundary phenomena in comparison with bulk metal. A greater density of precipitate crystals on iron crystal faces adjacent to grain boundaries was noted to some extent. This effect may have implied a reaction relationship with dislocations which are known to pile up against grain boundaries.

As a result of this work, the literature survey on the iron-CO interaction and the recent successful reaction studies with epitaxicly grown metal films, it was decided to build a system for the reproducible production of iron single crystals. The system was also to have the capability of in situ reaction of the freshly formed films. A study was proposed for the investigation of the product nucleation sites, precipitate morphology, crystal analysis, and the orientation relationship of the solid phase precipitate to the parent metal. Due to the great affinity of iron for oxygen, an ultra high vacuum system for evaporation and in situ reaction was mandatory. Reaction at low pressure was thought necessary to slow the reaction rate allowing products to form of substantial size without destruction of the delicate metal film. In order to carry out this program, equipment and techniques had to be developed. Although this work is not the first report of single crystal iron film formation, the process is still as much an art as a science and techniques vary from system to system. The following section will review the technological background for growing single crystal films.

F. Thin Film Technology

During the past ten to fifteen years, the efforts to produce miniature

electronic components have generated a great deal of research on thin film properties and the theories relating to film formation. Vacuum vaporization and subsequent condensation on suitable substrates is the method of thin metal film production which has received the majority of the attention. Several excellent review articles (101,102,103,104) and books (105,106,107, 108,109) on the state of the science are available. The most notable studies on the epitaxic growth of metal single crystal films have been reported since 1960. The more important parameters effecting the epitaxic phenomena have been established, but as yet no set of rules have been defined to ensure epitaxial growth in every attempt. Epitaxy as originally defined by Royer refers to the oriented growth of one substance on the crystal surface of another (103).

The 1967 volume of Physics of Thin Films contains an excellent review of the present knowledge of evaporated single crystal films by J. W. Matthews (104). This text is a complete, concisely written report and obviates such a thorough treatment here. Only a summary of some of the more important ideas from this review and others will be presented. The parameters affecting epitaxy are substrate character, temperature, deposition rate, residual gas pressure, and evaporant source (102,104,110), and each will be briefly discussed in the following section.

Film formation on a substrate surface by vacuum evaporation generally occurs by the generation of nuclei and their three-dimensional growth. The process passes through a stage of coalescence on peripheral contact, subsequent channel formation, and closure resulting in a continuous film (103,104). The thickness of the film as it becomes a hole-free layer is dependent on the materials involved, substrate temperature, the contamination present (sur-

face energy considerations), and deposition rate (104,110). From the very nature of the closure process, the films formed contain dislocations, double-positioning boundaries, stacking faults, and twins. These are typical lattice defects created by the accommodation of rotation and displacement misfits of coalescing neighbors and accommodation between overgrowth and substrate (103,104). The occurrence of each defect type is characteristic of the metal being deposited and results in a sample differing significantly from the bulk only in surface to volume ratio and defect density (111). The influence of the substrate is to generate epitaxy if the temperature of the substrate is sufficient to afford mobility to the depositing material allowing atomic ordering to occur (112). It has been well established that lattice misfit between the overgrowth and the substrate is not the primary factor determining the epitaxial relation (103). It has been proposed that the tendency is toward preservation of the normal co-ordination of the atoms at the interface (112). If the lattice misfit is very large (20 per cent to 30 per cent) incomplete or no orientation relation to the substrate is likely (112). Substrate imperfections such as the monatomic step have been predicted to enhance the nucleation rate of films. Macroscopic surface defects should also enhance film formation if the defect increases the area of the substrate-condensate interface for the critical nuclei (110). The presence of a layer of adsorbed impurities has several effects on the nucleation rate of a film. Impurities generally decrease the binding energy of the vacuum deposited species and, therefore, decrease the activation energies for both desorption and surface diffusion. The former effect decreases the film nucleation rate and the latter enhances it (110). Of course, the surface nucleation sites may also be "poisoned"

by impurity adsorption which results in a decrease in the formation rate (110). The character of the individual metal-substrate system will determine whether good epitaxy is achieved in the presence of contamination. Contamination has been observed both to hinder and promote epitaxy in different instances (104, 113).

The effect of higher substrate temperature is to afford surface mobility to condensing metal atoms to facilitate formation of an ordered atomic array (112). In the majority of systems it has been found that preference for a specific nucleus orientation increases with substrate temperature. Thus, higher substrate temperatures screen out less desirably oriented nuclei and promote the formation of a singly oriented film. However, high temperatures tend to deter the formation of a continuous film by aglomerating the deposit.

The proper deposition rate is also dependent on conflicting phenomena. Epitaxy of growth nuclei is favored by a slow rate which allows time for unhampered ordering of the newly arriving atoms (102,104,110). On the other hand, a rapid deposition of material is often necessary for the formation of a continuous film (102). An increase of deposition rate is also known to increase the number of nuclei formed per unit area (104). This allows the faster growing, preferentially oriented nuclei to predominate at an early stage of deposition. Reorientation and early coalescence can occur before their mass has become prohibitive (103,104). These processes thus promote singly continuous films.

The presence of gas molecules in the deposition system will obviously effect the structure of the crystal film to some extent (103,104). Adsorbed gas in quantity may react with the deposit. Reaction of gas

molecules with the deposit atoms in transit from the vapor source to the substrate may also occur (103). Adsorbed layers also tend to shield the deposit material from the attractive forces of the substrate and thereby disturb the normal epitaxic processes (110). It has been observed in numerous instances that the epitaxic temperature (minimum temperature resulting in epitaxy for the system involved) is lowered by improving the vacuum and by cleaving the substrate in the deposition chamber (104,113). Recent investigations have shown differences in the growth nuclei generated in ultra high vacuum (10^{-6} to 10^{-10} torr) on air cleaved versus vacuum cleaved NaCl. The effect on nuclei orientation was slight but there was a very significant change in nuclei density. The density of nuclei was found to be greater for air contaminated substrates (104). The density of lattice imperfections in evaporated films has been observed to be reduced by improving the vacuum and by using freshly formed substrate surfaces (104).

The evaporant source must also be carefully considered as a contamination source during evaporation; otherwise, the quality of the vacuum prior to deposition is of little consequence (102).

Pignocco and Pellissier (114) have exposed atomically clean iron surfaces to 55 x 10^{-6} torr-sec of oxygen and subsequently annealed them at 550°C. Low-energy electron diffraction techniques showed that FeO formed on the surface. It is apparent that numerous difficulties arise when dealing with highly reactive materials.

G. Review of Thin Iron Single Crystal Preparations

One of the major tasks of this research was the development of techniques for the reproducible formation of high quality thin single crystal

iron films for well defined reaction studies. It is, therefore, pertinent to review the attempts reported in the literature to make such crystals.

It is apparent that continuous films of near perfect orientation are difficult to form. Investigators prior to 1960 (112,115,116,117) found that above the epitaxic temperature more than one three-dimensional orientation of the deposited iron usually occurred. At thicknesses of approximately 1,000 to 1,200 Å, practically continuous films were formed for which the density was close to that for bulk iron. The epitaxic temperatures reported for iron lay in the range 440 to 540°C with a variety of alkali halides substrates (sodium chloride, potassium chloride, potassium bromide, and potassium iodide). The pressure range for the reported experiments was of the order of 10^{-5} to 10^{-4} torr. The substrates generally were cube faces cleaved in air or occasionally polished surfaces which were thermally etched prior to deposition. The rates of deposition were of the order of 50 Å per second.

The orientations reported of the iron matrix with respect to the exposed (001) rock salt substrate surfaces were as follows:

a) Fe (001) [100] || NaCl (001) [100];

b) Fe (001) [110] || NaCl (001) [100];

c) Fe (111) [11$\bar{2}$] || NaCl (001) [$\bar{1}$10]; and,

d) Fe (210) || NaCl (001) ,

with four equivalent orientations in which [112] type directions lie along NaCl [100]. The a) and b) type relations were most common and generally mixed. For films grown on (110) rock salt, two orientations were observed:

a) Fe (110) [001] || NaCl (110) [001], and

b) Fe (111) [$\bar{1}$10] || NaCl (110) [001].

On (111) rock salt surfaces the following orientations have been observed:

a) Fe (110) [001] || NaCl (111) [$\bar{1}$10];

b) Fe (111) [$\bar{1}$10] || NaCl (111) [$\bar{1}$10]; and,

c) Fe (111) [$\bar{2}$11] || NaCl (111) [$\bar{1}$10].

Collins and Heavens (110) pointed out that when epitaxial growth occurs on a monocrystal substrate, the orientation primarily observed is governed by a tendency to continue the substrate structure across the boundary. This results in the normal co-ordination of the atoms across the interface. They stated that lattice misfit is of less importance than the co-ordination condition, which is in agreement with the proposals based on most other studies of epitaxy.

In 1962, Belser and Woolf (118) reported on extensive studies of general epitaxy. They found that iron single crystals while prepared readily on MgO, were not grown on the cube-face of NaCl. However, stripping the film from the M_gO substrate for transmission electron microscopic examination is a problem.

Sakata and Funaki (111) prepared continuous films of iron monocrystal on cube cleavage faces of NaCl, although they reported that their results were difficult to reproduce. Their method for producing an iron vapor consisted of the electron bombardment of electrolytic iron. The source to substrate distance was 10 mm and the vacuum prior to deposition was about 2×10^{-5} torr. The cleavage of the NaCl single crystals was carried out in air. From the diffraction patterns, they observed the nature of the orientation of the film to change from place to place on a single sample. The film was found to be monocrystalline in some areas, a mixture of two orientations in others (the second orientation being 45^{o} to the first), and

polycrystalline in others having yet a high orientation preference. Anomalous spots were noted in all the diffraction patterns published. One set was located "at a position half of {200}." The others consisted of "four diffraction spots around spots {110}." They related the former type to dislocations; the latter were undefined. It is important to note that they observed the latter spots quite strongly with the film inclined about a < 200 > rotation axis. Spots analogous to all these are discussed and defined in Chapter III of this dissertation. The micrographs published in their report show continuous films with high densities of dislocations and sub-boundaries as well as undefinable contrast effects of the order of 0.01 μ across. The NaCl was removed from the films by sublimation chosen to prevent oxidation. They concluded that the evaporated film is "structurally analogous to the thin film of iron formed through the electrolytic polishing method," and should be useful to fundamental research of iron and steel.

In 1963, Heavens (119), as part of a general paper on the properties of ferromagnetic materials, reported renewed efforts to produce a single-position orientation of iron films on rock salt. The diffraction pattern reproduced in the text indicated the attempts were successful. Polished and thermally etched (100) and (110) faces of NaCl were used. The substrates were held at a temperature of 325°C during the evaporation of iron. An evaporation rate of 800 Å per minute was used and the vacuum is assumed to have been of the order of 10^{-7} torr. Heavens reported that well-oriented (111) films may be grown at this temperature on the (110) face of NaCl.

Cahoreau and Gillet (120) have grown (001) oriented films of iron of good quality on (001) surfaces of gold films. The details of their procedure were not reported. This technique is of no great interest to this study

since either the removal of the gold in KCN or the superposition of diffraction patterns from the combination foil, introduces intolerable complications to analysis.

In 1965, Shinozaki and Sato (121) published an interesting report on extensive studies of the phenomena affecting the epitaxic growth of iron on rock salt. This work was done in an effort to develop a reproducible method of preparing samples for magnetic domain studies in the electron microscope. A systematic study was made of appropriate epitaxic conditions for depositing iron on "in air," cleavage faces of NaCl in a conventional vacuum system (capable of vacuums of the order of 10^{-6} torr). A deposition rate of 50 to 100 Å per minute (using a heated alumina crucible for evaporating the iron) was found to be best for producing films up to 1,000 Å in thickness. They found statistically that substrate baking at 500°C for 30 minutes and subsequently establishing a substrate temperature of 400°C resulted in the best deposits. In general, they found that epitaxy was very sensitive to minor differences in the evaporation conditions but was not very sensitive to minor differences in the substrates produced in cleaving. The results, however, generally showed some mixing of two orientations as well as faint superpositions of polycrystalline rings in the absence of the following substrate treatment.

They discovered that good single crystal films could be produced consistently if the substrates were slightly contaminated. Before making the iron deposition, the substrates were exposed to a vapor (presumed to be primarily H_2O) raising the vacuum system pressure momentarily to 1×10^{-4} torr. The evaporation was then begun a few seconds after this peak pressure had been attained. A mechanistic explanation of this phenomenon was not given.

Matthews (122) described a technique for preparing single crystal films of iron on clean sodium chloride substrates. In his paper he confirmed the growth of polycrystalline iron films on clean salt (vacuum cleaved) in ultra-high vacuum by conventional techniques. He went on to say that exposure of the substrate to air at 1 atm has essentially the same effect as the contamination used by Shinozaki and Sato. Studies to characterize the role played by the contaminants indicated that the effects of air exposure were: (1) to increase the number of growth nuclei generated per unit area, and (2) to increase the fraction of the substrate surface covered by the iron. The phenomena, he reported, are similar to those observed for gold epitaxy. Therefore, good iron films should be produced by a technique analogous to the one he developed (123) for growing single crystal gold films. In essence, this requires a rapid initial deposition of metal to generate a high density of growth nuclei on the substrate surface. This is followed by slow deposition allowing realignment and annealing to accompany film growth. The deposition is continued until enough material has been deposited to form a continuous film. The details of the technique are important and are reproduced as follows. He stated:

> A sodium chloride crystal (of optical quality from Harshaw Chemical Company) was heated in ultra-high vacuum (10^{-9} torr) and cleaved to expose a fresh, uncontaminated (001) surface. Shortly thereafter roughly 20 Å of iron was deposited onto this surface by vaporizing a 99.9 per cent iron wire positioned 0.6 cm from the surface. The rate of metal deposition during this process is not accurately known but probably exceeded 1,000 Å/sec. The rapid deposition was followed, about one minute later, by deposition of 500 to 1,000 Å of iron at approximately 2 Å/sec. Slow deposition was achieved by sublimation of an iron wire helix. The pressure in the chamber during rapid film growth was about 10^{-6} torr; during slow growth it was less than 5×10^{-8} torr. The temperature of the substrate was 410°C.
>
> A transmission electron diffraction pattern reproduced in Matthews

paper showed the film was a high quality single crystal with (001) parallel to the plane of the foil.

In 1966, Heavens (124) again reported on studies of the epitaxial growth of iron single crystals on a number of alkali halides. By choice of a suitable substrate, deposition temperature, and rate of deposition he found it possible to grow films of iron in single orientation. Potassium chloride or potassium iodide were found to be particularly suitable at 330°C using a deposition rate of the order of 300 Å per minute. Sodium chloride was useful with rates in excess of 300 Å per minute. He pointed out the errors reported in previous measurements of the epitaxic temperature and maintained this temperature to be close to 320°C for air cleaved surfaces and close to 260°C for in situ vacuum cleavages.

In 1966 Tagawa, Ino, and Ogawa (125) studied the epitaxy of iron on NaCl cube faces to determine the effect of vacuum cleavage of the NaCl substrate. The deposition rate was reported as 3 to 10 Å per second and was carried out at a pressure of 1 to 5 x 10^{-5} torr. They reported that single crystals of iron were very difficult to form at temperatures up to 500°C. Very little difference was observed between the results from both types of substrate preparations. Three orientations of iron were observed on the (001) NaCl faces with the following two being most common and mixed:

a) Fe (001) [100] || NaCl (001) [110], and

b) Fe (001) [100] || NaCl (001) [100].

It should be noted in reflecting on the results presented in these articles that only one presented electron micrographs of the iron films produced. Therefore, a good critical judgment of the quality of the crystals reported in the other articles was not possible. The electron micrograph is

a more sensitive basis on which to judge the ultimate quality of an epitaxially grown film than the electron diffraction pattern. Both types of information are required for a rigorous analysis (1,2,3). A good pattern may be obtained from a film made up of fine grains which are slightly misoriented with respect to each other. The failure of electron diffraction to detect this film characteristic is partly due to the normal resolution obtained in photographing the diffraction pattern. In addition, the shape of diffracting crystals influences the size and shape of the reciprocal lattice reflections and, thereby introduces analytical uncertainties (1,2,3). The difficulty in obtaining single crystals of good quality as opposed to producing films of well oriented crystallites will be discussed again in Chapter III.

CHAPTER II

APPARATUS AND EXPERIMENTAL TECHNIQUES

A. Apparatus

From the literature and the preliminary studies of metal films reacted in carbon monoxide, it was apparent that an ultra-high vacuum system in which iron single crystal films could be made and reacted would be required to obtain necessary information for a better understanding of the metal dusting phenomena. The growth and reaction of thin iron single crystals was chosen for this research program to allow the use of the electron microscope for high magnification transmission examination and for electron diffraction crystallographic analysis. Ultra-high purity iron wire and the cleanest carbon monoxide commercially available were used for the studies in order that as fundamental an approach as practicable might be maintained. The analyses of the iron and CO are presented in Appendix C.

1. Design Requirements

As demonstrated in Chapter I, iron is extremely reactive with oxygen even at very low partial pressures. It was, therefore, a necessary criterion that the iron single crystals be prepared in a vacuum of the order of the 10^{-8} torr to low 10^{-7} torr scales. From the literature, pressures of this order should prevent the formation of oxide compounds on the iron surface.

The basic vacuum system selected to give the vacuums required on a routine basis was the Ultek TNB system. The principle of pumping combines

cold-cathode ion pumping with titanium getter pumping. The titanium getter pumping is achieved by resistence-heating a titanium filament to sublime titanium onto the walls of a stainless steel well at room temperature. At the surface of the fresh film, the active gases combine chemically with the titanium to form stable compounds. Some of the more important gases which are pumped are nitrogen, oxygen, hydrogen, water vapor, carbon dioxide, and carbon monoxide. The cold-cathode ion pump provides pumping action for both getterable and non-getterable gases. The pumping speed for air of the ion pump section of the equipment was rated at 50 liters/second while the pumping speed of the titanium sublimation system was rated at 3,600 liters/second.

Figure 13 shows an overall view of the apparatus assembled for developing the techniques used for growing the iron single crystal films. This apparatus was slightly modified later according to procedural developments for making single crystals and for the in situ reaction of the freshly grown films. The key to the component designation system used in Figures 13 through 17 of the apparatus is presented in Table 2.

The basic vacuum system vessel consisted of a stainless steel well mounted on three bracket type feet. The stainless steel well was fitted with a 16" O.D. - 11" I.D. baseplate on which was mounted a 12" x 12" Pyrex belljar. A few inches below the baseplate 10 feedthrough ports of the metal-to-metal seal type were mounted 36° apart in the well wall. The axes of the port nipples were normal to the axis of the well. Nine of the ports were supplied with blank flanges. The tenth supported the foreline pumping manifold. The foreline manifold was equipped with a thermocouple pressure gage element, a 1-inch system-isolation valve, a foreline trap, and a gas

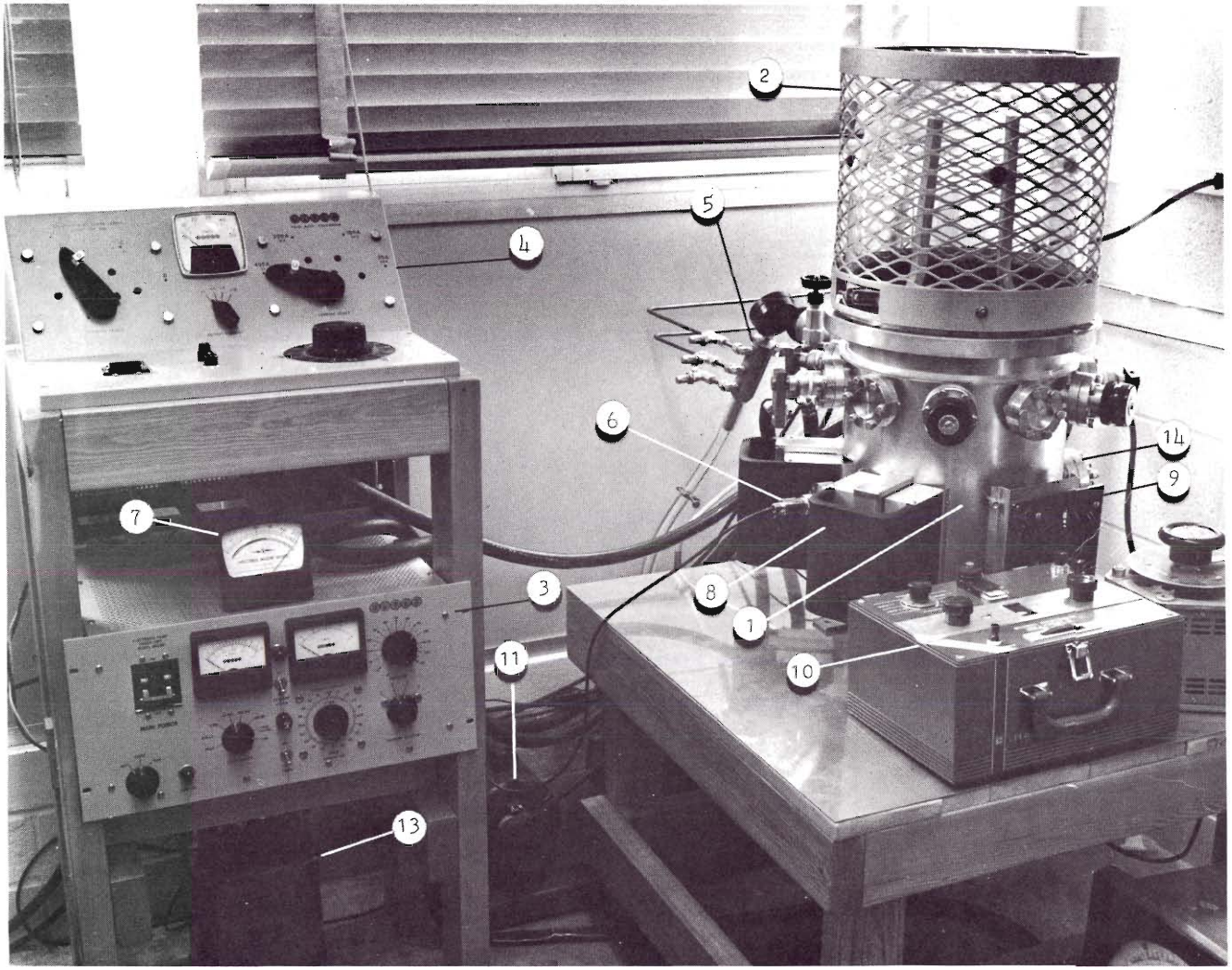

Figure 13. An Overall View of the Vacuum System Components

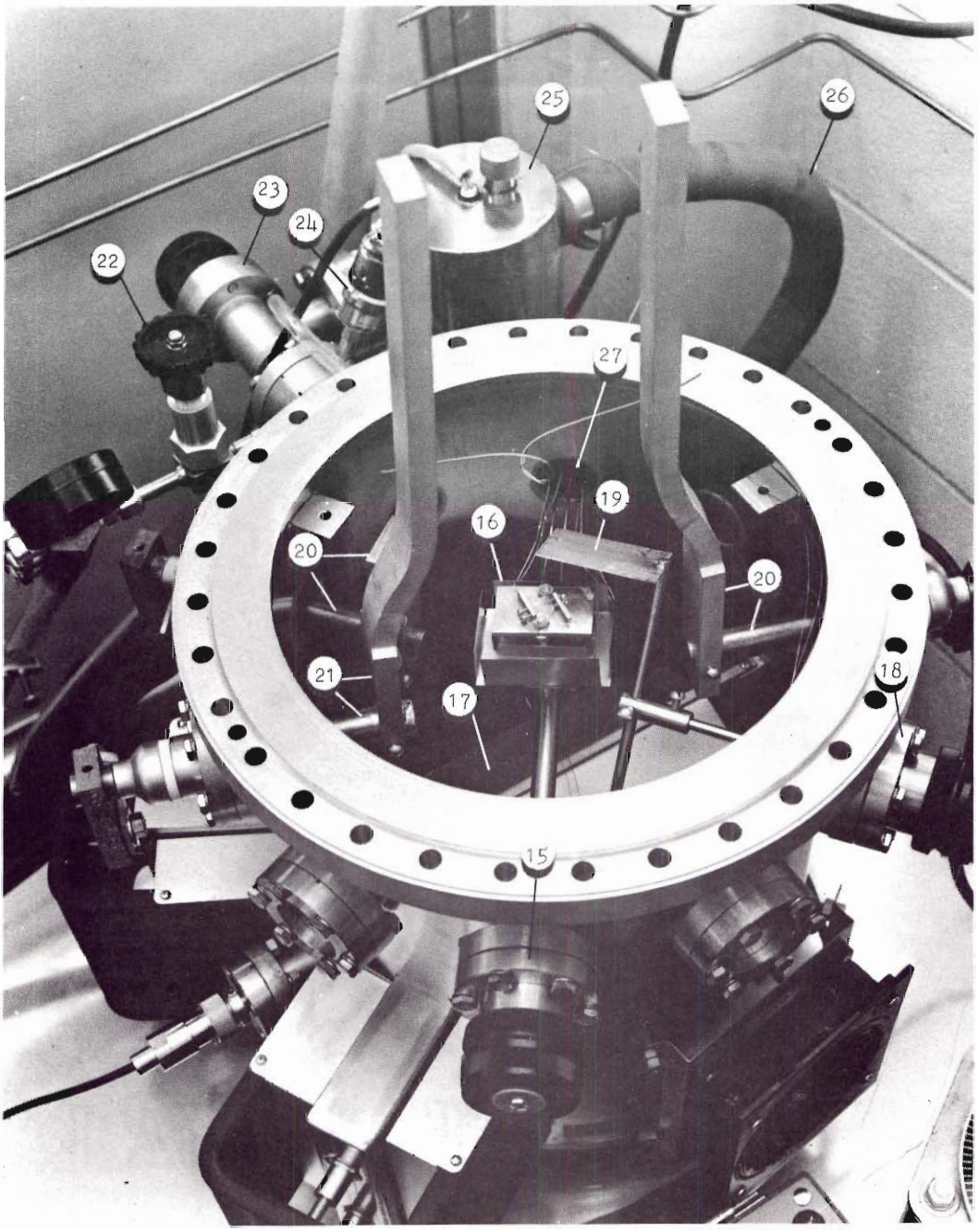

Figure 14. Plan View of the Apparatus Showing the Feedthrough Layout

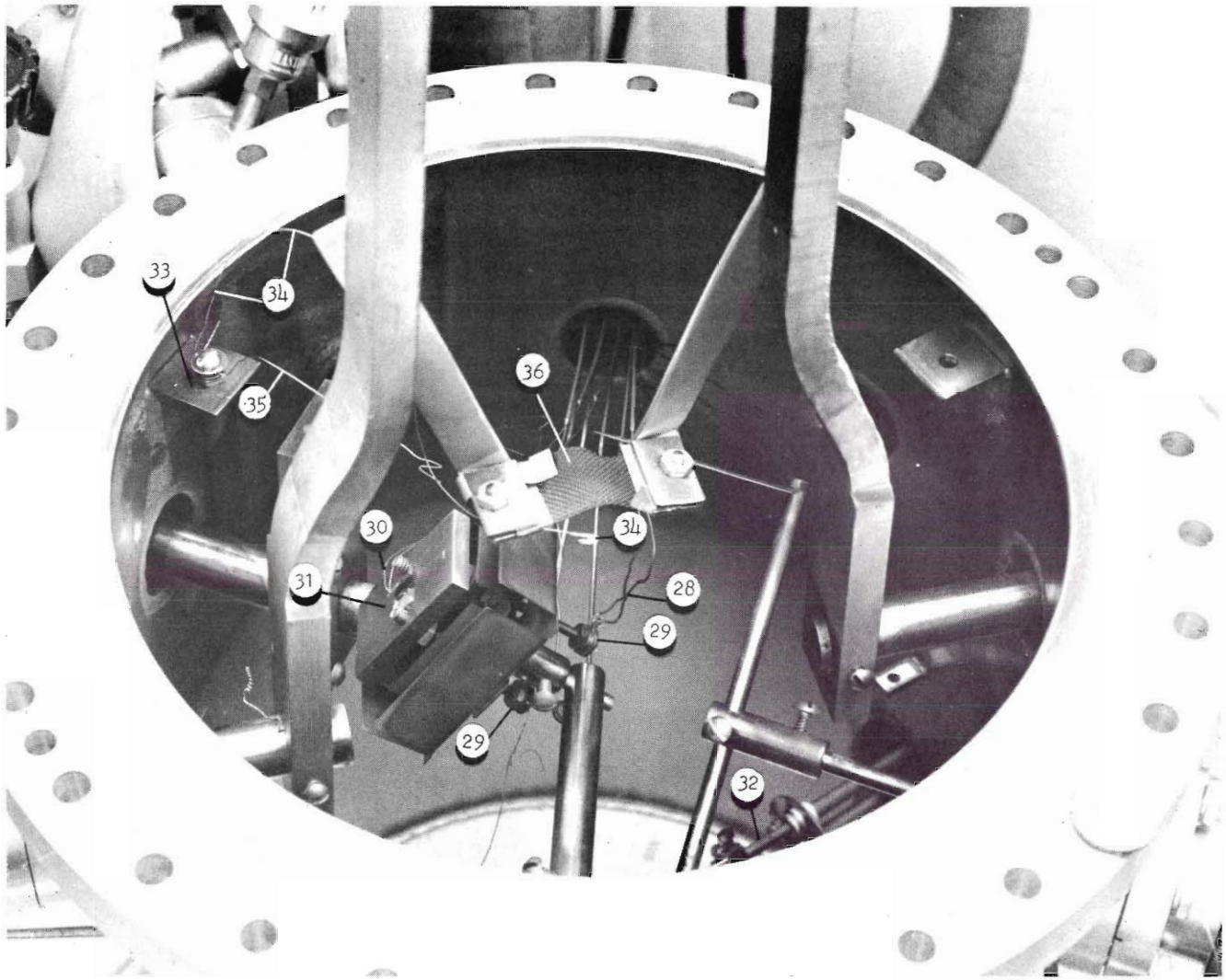

Figure 15. A View of the Apparatus Showing the Position of the Substrates During the Deposition of Iron

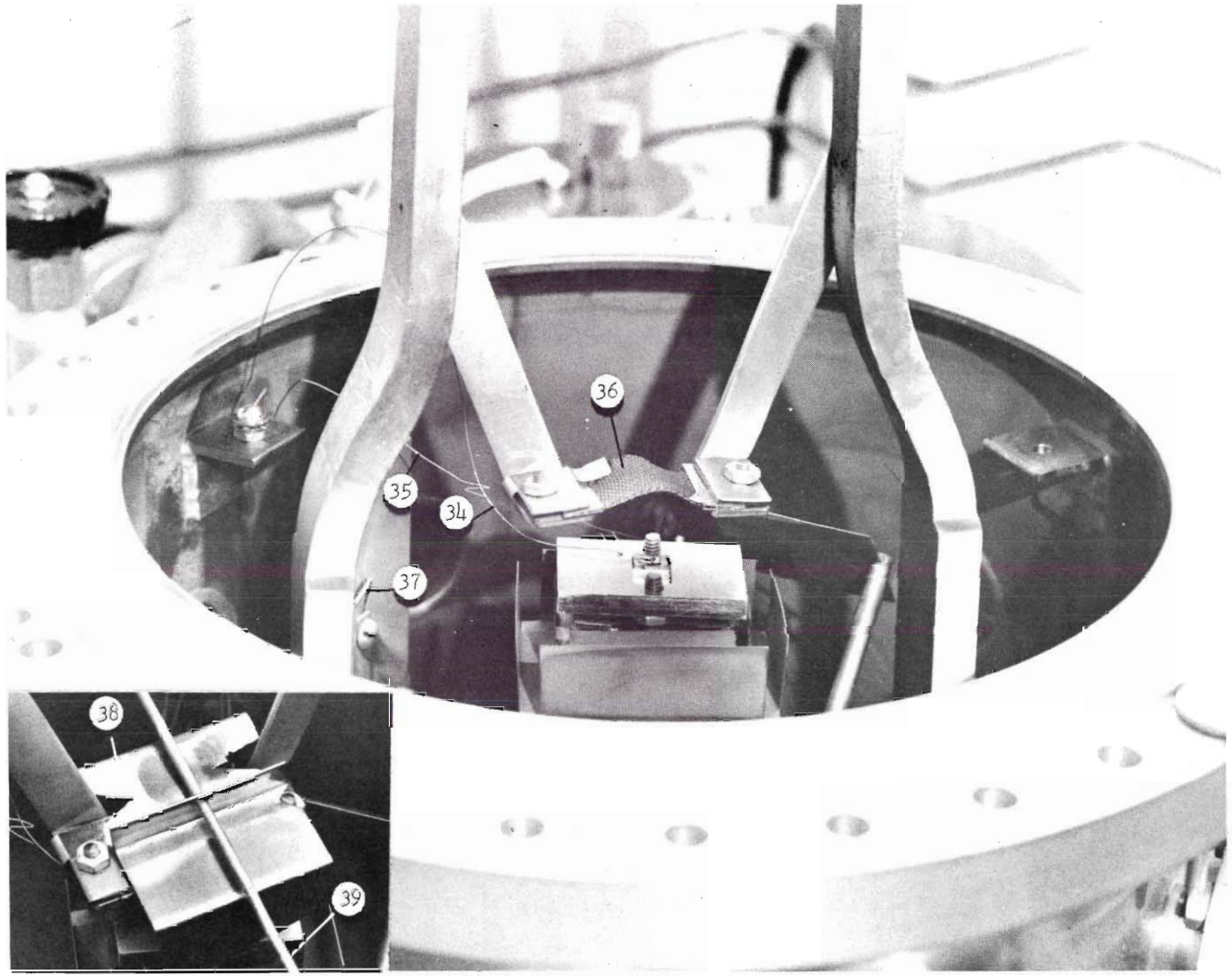

Figure 16. A View of the Apparatus Showing the Position of the Substrate During the Reaction of Film Specimens

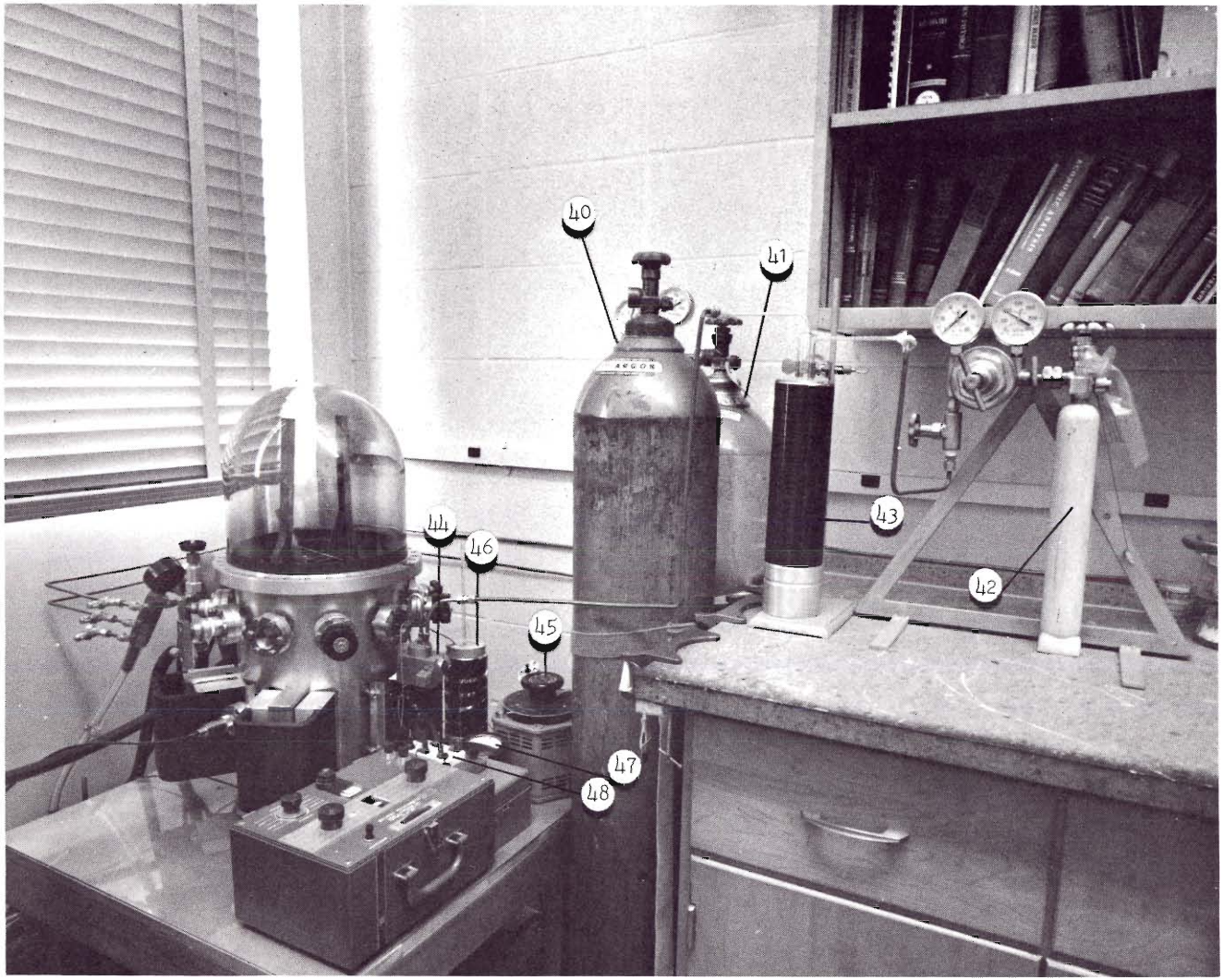

Figure 17. An Overall View of the Apparatus as Set Up for Reacting Specimens

Table 2. Tabulation of the Apparatus Components Illustrated in Figures 13 Through 17

1. Vacuum System Well (housing the ion and titanium sublimation pumps)
2. 12" x 12" Pyrex Belljar and Guard
3. Electronic Pump Power Unit - Ultek Model 60-656
4. Filament Power Supply - Ultek Model 60-300
5. Backfilling Gas Manifold
6. Ion Pump Power Connection
7. Thermocouple Vacuum Gauge - Hastings Model VT-6
8. Ion Pump External Magnet
9. Fan (for cooling well wall)
10. Potentiometer - Leeds and Northrup Model 8691
11. 5 cfm Mechanical Pump - Welch Model 1405 (motor shown)
12. 15 cfm Mechanical Pump - Welch Model 1402 (not shown)
13. Transformer - Hevi-Duty Type S1 (110 V, 20 A, to 220 V, 10 A)
14. Power Feedthrough for titanium sublimation pump
15. Rotary Motion Feedthrough - Ultek Model 80-324 (substrate heater support)
16. Substrate Heater
17. Titanium Vapor Shield
18. Rotary Motion Feedthrough (shutter support)
19. Shutter
20. Electrode and High Current Feedthrough - Ultek Model 80-354
21. Electrode and High Current Feedthrough (common pole)

(continued)

Table 2. Tabulation of the Apparatus Components Illustrated in Figures 13 Through 17 (continued)

22. System Up-To-Air Valve - Hoke Type 440

23. System Isolation Valve - 1 inch, right angle valve - Ultek Model 40-131

24. Element for Thermocouple Pressure Gauge - Hastings Model DV-6M

25. Foreline Trap - Ultek Model 50-005

26. Hose to Roughing Pump

27. Octal Conductor Feedthrough Port - Ultek Feedthrough; Model 80-333

28. Substrate Heater Current Leads

29. Substrate Heater Electrode Terminal

30. Thermocouple Wire

31. Substrate Carrier Block (position of copper block thermocouple, a bare sample substrate, and the auxiliary substrate with an overgrown film shown in Figure 15)

32. Exposed Titanium Sublimator Electrodes

33. Bracket (supporting the iron-constantan thermocouple)

34. Iron-Constantan Thermocouple (for reading the film temperature of the auxiliary substrate)

35. Thermocouple Guide Wire

36. Radiant Heater Element - 1 inch carbon cloth ribbon

37. Iron Sublimation Filament

38. Heat Shield for overhead radiant heater

39. Support Rod (the ends rest on lip of base plate inside the belljar)

40. Cylinder of Argon (for leak detection)

41. Cylinder of Nitrogen

(continued)

Table 2. Tabulation of the Apparatus Components Illustrated in Figures 13 Through 17 (continued)

42.	Cylinder of High Purity CO
43.	Cold Trap Station (surge vessel)
44.	Leak Valve - Granville-Phillips variable leak
45.	Variable Transformer for the substrate heater circuit - Standard Electrical Products Type 1500B
46.	Ice Bath for thermocouple cold junction
47.	Volt Meter for substrate heater circuit - Marion Electric Model H-53
48.	Double-Throw Knife Switch (for potentiometer-thermocouple circuits)

inlet valve. A special manifold was fabricated and installed on the air side of the gas-inlet valve in order to incorporate the option of back-filling of the system with more than one gas. The manifold was equipped with a mechanical vacuum gage to facilitate backfilling regulation and with a 5 cfm mechanical pump to allow vacuum purging. Pre-purified grade nitrogen was selected as the normal backfilling medium to minimize contamination of the system with materials difficult to pump. Forepumping of the vacuum chamber was done with a 15 cfm, two-stage mechanical pump.

Through the walls of the lower section of the stainless steel well were inserted the ion pump and the electrodes carrying the titanium for sublimation. Two fans were also attached to the lower section of the well for the purpose of cooling the walls during Ti sublimation and condensation.

Power to the pumps was supplied by an Ultek power unit, Model 60-655. The instrumentation for the ion pump power supply was used to indicate vacuum by correlating the current drawn by the cold-cathode discharge with the system pressure. The sublimator portion of the power supply had a filament current meter and variable transformer for accurate power settings. A variable cycle timer permitted proper choice of on-to-off time for filament conservation. The only utility requirement for the entire system was a 115 V, 60 cycle, single phase electrical power supply with a 20 A capacity.

The experiments performed in the IMB system were carried out in the upper portion of the vacuum chamber above a baffle preventing Ti contamination. The geometry is illustrated in the equipment plan views of Figures 14 and 15. In Figure 14 the baffle is visible below the experimental apparatus while in Figure 15 the system is pictured with the baffle removed and the sublimator electrodes and well bottom showing. One of the most important

features of the BoostiVac principle (Ultek's designation for the pumping principle) is that the backstreaming of pump oils for conventional vacuum systems has been by-passed. This feature is considered critical to the production of single crystal films and catalyst investigations. Prepumping of the system with the mechanical pump was required before the BoostiVac operation could be started. This procedure could afford an opportunity for pump oil backstreaming contamination. To prevent such an occurrence, an Ultek trap was placed in the foreline to the system. The trap contained a charge of Linde 13X Molecular Sieve. Ultek Technical Report D 1144 describes a study of the residual gases by mass spectrometry during forepumping with and without a foreline trap. The results indicate backstreaming of hydrocarbons from mechanical pump oils to be virtually eliminated by the trap.

The apparatus built into a vacuum system for the production of single crystal films is fairly complicated. As discussed in Chapter I, a single crystal substrate (in this case rock salt) must be heated to a prescribed temperature before the deposit material is condensed on it. Also, multiple evaporations may be required as indicated by Matthews (122) for some deposit materials. The present system was built to facilitate multiple evaporations onto a heated substrate. The components to be discussed in the following description of the apparatus have been numbered in Figures 13 through 17 and a key to their identity is presented in Table 2.

For making the unobstructed evaporations required in the technique development, movement of the substrate and heating assembly was chosen as the method for positioning the substrate directly beneath each evaporating filament. The substrate heater and holder assembly was mounted on an arm normal to the axis of a rotational mechanical feedthrough introduced through

one of the ports described earlier. The placement and movement are indicated in Figures 14 and 15. The mechanical feedthrough was magnetically coupled so that no moving seal was introduced. Figure 15 is a good illustration of the positions assumed by the electrical leads to the substrate heater electrodes. The electrical leads and thermocouple wires were introduced into the system by sealing them in the tubes of an octal conductor feedthrough located directly opposite the shaft carrying the substrate heater. During positioning of the substrate the wire leads were readily able to follow the short arc path of the heater without shorting. A detailed description of the substrate heater and carrier will be presented later.

The technique finally developed for reproducibly making single crystal films did not incorporate double evaporation. However, it was still necessary to move the substrate during the course of the process. It was determined that sublimation of the iron from a small coil of iron heated resistively at a source to substrate distance of 1 inch was required. After deposition the film had to be annealed. The most efficient method of annealing the film on the surface of the NaCl substrate was to heat the film radiantly from above as well as by conduction through the NaCl block. To supply the radiant heat a 1-inch wide carbon cloth was placed 1 inch above the substrate. To facilitate the proximate sublimation and heating it was necessary to move the substrate. The two positions of the substrate relative to the iron source and radiant heater are shown in Figures 15 and 16, respectively. Unfortunately, the view of the iron wire coil is blocked in Figure 15. However, the coil may be seen in Figure 16 although the substrate is not positioned normal to it.

The iron coil was formed by wrapping a piece of 20 mil wire tightly around a 35-mil tungsten wire form. The length of the iron wire used was 5 inches, and the number of turns used was 15. The coil was pushed off the form and stretched to a length of 9/16-inch. The leads to the coil, of essentially equal lengths, were bent 90° to the coil in positions cis to each other. The leads were then clamped between two copper electrodes as indicated in Figure 16. (The electrode positioned three ports from the mechanical feedthrough carrying the substrate heater is partially blocked from view.) The coil in this position lies perpendicular to the arc of the substrate movement. By adhering closely to this procedure for making the iron filaments for each experiment, the variable transformer setting for producing a predetermined sublimation rate was nearly the same from one run to another. The proper deposition rate was roughly 400 Å/min. as determined from film thickness measurements made on films deposited on glass slides.

The high ampere feedthroughs supporting the electrodes for sublimation are clearly visible in Figure 14. A third high ampere feedthrough and electrode in prominent view was positioned on the other side of the system. The function of the two prominent electrodes was to carry the current and mechanically support the radiant heater. The large electrode on the left in Figure 15 acted as a common pole for both the evaporator circuit and the radiant heater circuit. Power for both circuits was supplied by a 2KVA power supply shown in Figure 13. This power supply was capable of energizing four circuits using a common pole from a four-tap transformer. Power to the external circuits was regulated by a variable transformer in the unit.

Before the substrate or the iron film was exposed to the radiant heater, it was necessary to degas the heater in high vacuum. To facilitate shielding of the substrate during the degasing operation, a shutter was installed in the vacuum chamber. Figure 14 gives a good view of the shutter which was mounted on an arm perpendicular to the axis of a second magnetically coupled mechanical feedthrough. The port used for the installation was 72° counterclockwise to that containing the shaft supporting the substrate heater. With the substrate and shutter in the raised positions, the shutter also acts as a heat shield for the substrate heating assembly in the absence of overhead radiant heater operation. A heat shield positioned over the radiant heater was also part of the normal operating apparatus. A picture of the heat shield is given in the insert of Figure 16.

The substrate holder shown in Figures 15 and 16 was the design used for these studies rather than the one shown in Figure 14. Figure 14 was included for the excellent view of the feedthrough layout. The substrate carrier block was made of copper plate with two mounting holes and two symmetrically positioned recesses to accommodate rectangular solids of NaCl substrate. The dimensions of the substrates were shaped by cleaving single crystals of NaCl (optical crystal blanks from the Harshaw Company) along {100} planes with single edge, stainless steel safety-razor blades. The temperature of the copper block was determined with a chromel-alumel thermocouple. The thermocouple hot junction was fitted securely in a hole in the upper face of the block near a substrate as shown in Figures 15 and 16. The thermocouple wires exited the system through the tubes of the octal conductor feedthrough described earlier. The thermocouple used an ice bath cold junction, and the potential was read with a potentiometer.

Measuring and regulating the temperature of the deposited iron film on the NaCl surface was difficult. NaCl has poor properties of thermal conduction, and the quality of thermal contact between the NaCl substrates and the copper block was questionable. Measuring the temperature of a heated NaCl block can be uncertain due to the relative transparency of the NaCl to infrared radiation. For this reason, the temperature measurement of the bare surface of a NaCl substrate before iron deposition was not attempted. Such measurements would have been required to define the epitaxic temperature for iron in the system studied. Reasonable measurements of the iron film temperature were, however, made during the film annealing and reaction processes using the following technique.

Many of the more conventional techniques of film temperature measurement were not applicable to this system due to the importance of immediate reaction following film deposition and due to the necessity of moving the substrate. The surface of the substrate carrying the single crystal film for study could not be perturbed by clamps nor covered by temperature measuring devices without spoiling the experiment. Therefore, an indirect measurement was necessary. Two single crystal specimens were made simultaneously in each experiment. Two NaCl substrates were mounted in the carrier block in symmetrically similar positions for evaporation and heating. One of the substrates carried the film to be examined and the other carried a film to be used for temperature measurements. A thermocouple was designed which would contact the face of the film on the auxiliary substrate. This thermocouple had to be capable of supporting its own weight when the substrate was moved from the raised position to the position required for iron deposition. Figure 15 shows the attitude assumed by the thermcouple

when the substrate is positioned for deposition. Figure 16 illustrates the location of the thermocouple on the auxiliary substrate with the apparatus set for annealing or reaction. The auxiliary substrate is pictured with a film on it while the specimen substrate is bare. It is obvious that the thermocouple must be able to repeatedly slide across the substrate and copper block during movement of the apparatus and return to the same position on the auxiliary crystal. To do this a thermocouple was made from a length of 20 mil iron wire to which a 5-mil constantan wire was spot welded. The iron wire was attached at one end to a bracket on the chamber wall and shaped into a configuration which would allow the hot junction to follow the proper path. The thermocouple is pictured in Figures 15 and 16. The hot junction end of the wire was flattened to simulate the configuration of a film on the substrate. The constantan wire was connected to one of the tubes of the octal conductor feedthrough. The exterior end of this tube was connected to another portion of constantan wire which was run to the potentiometer. The system wall (stainless steel) was required as a section in the iron wire portion of the thermocouple leading to the cold junction. Although the thermocouple used could not be checked in situ, a very similar setup was checked against boiling water as a standard and was found to indicate a temperature well within 1° of the actual value.

Similar calibration tests were made to check the chromel-alumel couple with both freezing zinc and boiling water. The readings for several determinations were within 4°C of the standard values. The chromel-alumel couple as built into the system did not make use of insert or lead conductors in its circuit. In a test of temperature measurement consistency between the two thermocouples set up in the apparatus, a temperature differ-

ence of 0° to 7°C was observed for several readings around 400°C. However, the most common difference in the temperature reading was less than 1°C. The tests were conducted as follows: Both radiant and substrate heaters were used; the two couples were clamped together with a silver C-clamp of relatively large mass; the clamp and couples were electrically insulated from the substrate carrier block with mica sheets; and the thermocouple potentials were measured alternately.

To establish the temperature for the iron films, the power to both the substrate heater and the radiant heater was adjusted to give the same steady-state indications for both the thermocouple in the copper block and the iron-constantan thermocouple in contact with the auxiliary substrate. Only temperatures measured in this manner were considered truly representative of the iron film and substrate temperature. These temperatures were probably within 10°C of the actual film temperature. Exact knowledge of the film temperature was not critical to this work since reaction product identification and characteristics in various temperature regions were the points of study and not transition point phenomena.

The substrate heater assembly consisted of a double-walled reflector box in which a heater element was mounted. The walls of the reflectors were short with open edges to allow the free passage of gas. The substrate carrier block was mounted on two bolts which also supported the inside heater box. These bolts were secured in the bottom of the outer reflector. The outer box was supported by a tube of Monel which was attached to the mechanical feedthrough shaft. The heating element was a 1/2-inch wide carbon cloth ribbon held between two bolts acting as electrodes. The bolts were supported by and insulated from the inner reflector box by nuts spaced

with mica washers. The electrodes extended through the outer box passing through oversized holes to prevent shorting. Outside the heater assembly the bolts were fastened to lead wires entering the system through the octal conductor feedthrough. Power was supplied to this heater by reducing the standard 110-volt source with a transformer to 11 volts and regulating the voltage supplied to the heater with a variable transformer. A voltmeter was installed across the leads to the heater to facilitate reproducible power input.

The overall picture of the equipment as set up for reaction is given in Figure 16. A lecture bottle of the carbon monoxide was connected to a two-stage pressure regulator equipped with a diffusion resistent diaphragm. The gas was conducted through refrigeration grade copper tubing to a pyrex glass cold trap. Due to the small quantity of gas actually used per experiment, the trap was not used as a purifying device but rather served as a surge tank. From the trap the gas was conducted through more copper tube to a leak valve. The valve was coupled to the vacuum system by a stainless steel tube silver soldered into a hole drilled in one of the blank flanges of a feedthrough port. Soldering was done from the inside surface of the flange to prevent the creation of virtual leaks. The tubing connections were made with brass swagelok couplings. At glass tubing connections Teflon ferrules were incorporated into the swagelok couplings.

2. Special Equipment

Four electron microscopes were used at various times in the research program. Choice of the instrument used depended on the type of sample, instrument availability, and the quality of the results required. The instruments were a Japan Electron Optics Laboratory JEM 7, a Philips EM 200,

an RCA EMU 3, and an Akashi TR S-80. Micrographs and diffraction patterns of metal foils were made using 100 and 80 KV potentials (depending on the instrument used). Micrographs of replicas were made using 50 KV electrons.

A Kenney laboratory high vacuum evaporator was used for making specimen replicas. The replicas were of the direct platinum shadowed and carbon film type. The components in the vacuum system were arranged to evaporate platinum from a tungsten wire to give a shadowing angle of 15^{o}. Some of the components were arranged to make a second evaporation of carbon immediately following deposition of platinum. The carbon source was positioned normal to the specimen surface.

A multiple beam interferometer employing fringes of equal chromatic order was used for iron film thickness determinations.

Although not emphasized to great degree in the thesis, in situ studies of CO decomposition on bulk iron single crystals were also made. The program was not pursued extensively and the information obtained was correspondingly limited. However, it is worth mentioning that a Metioscope (secondary emission electron microscope) was employed for in situ investigations of the reacting samples. In order to expose the required crystal faces for study, a back reflection x-ray Laue Camera was used to orient a bulk iron single crystal and a spark machine employed to cut out specimens of crystal along the appropriate planes.

B. Experimental Procedures

The primary experiments in this research required the growth of single crystal films of iron and their reaction without an intermediate exposure to the atmosphere. The specimens were examined as quickly as possible

following reaction by electron microscopy. Their characteristic features were recorded photographically in electron micrographs and selected area diffraction patterns.

Supporting experiments included film thickness measurements by interferometry and sample surface characterization by direct carbon replication with subsequent electron micrographic recording of the surface features.

The time available for in situ studies in the metioscope was very limited and accordingly, the information obtained constitutes only a minor portion of the overall presentation. For this reason a detailed description of the experiments is not included. Useful information on the problem can be obtained only if an extensive research program is designed around the metioscope.

The following treatment will present the details of the experimental procedure used for making, reacting, and analyzing iron single crystal films.

1. Substrate Preparation

The substrate material was NaCl single crystals produced by the Harshaw Chemical Company and sold as optical crystal blanks. The dimensions were 1 cm x 1 cm x random lengths. The as-received crystals were washed quickly in a series of four distilled water baths to remove packing contamination and any impurity films. After this treatment the crystals were dried with dustless laboratory tissue. As needed, crystal blanks were chosen and heated in high vacuum at a temperature of 400°C for a period of 1 hour. The blanks were then stored in a desiccator. As required, substrate crystals were cleaved from the treated blanks to dimensions approximately 0.20" x 0.40" x 0.07". The actual dimensions were somewhat less so that the substrates would readily fit the recesses cut in the substrate

carrier block. Cleavage was done on the surface of fresh bond paper and the crystals were handled with methanol-cleaned tweezers. Immediately following cleavage, the substrate crystal surfaces were quickly and sharply blown with nitrogen and immediately placed in the reactor. The vacuum system was immediately closed and pumped down.

Prior to each experimental run a new iron wire filament was installed in the system. After forming, the filament was cleaned in successive solutions of trichloroethylene, acetone, and methanol to remove a grease coating applied to retard oxidation. Immediately following this treatment the filament was installed and a run initiated.

Before each experiment, it was found desirable to clean the belljar of the iron film formed in the previous experiment. The old iron films hindered the rapid achievement of ultra high vacuum due to sorbed gases. Also, it was convenient to have a clean belljar for use in checking the sublimation rate of iron at the previously determined power level. The check can be made since a few parts in the apparatus cast shadows on the belljar during sublimation. The film was removed using nitric acid fumes from a small pool of concentrated solution in the bottom of the inverted belljar. The treatment was followed by rinsing with water and drying in the hot air stream of a laboratory heat gun. In the meantime, the boot gasket for the belljar was wiped clean with a dustless laboratory tissue and a light coating of Apiezon Type L grease applied to the glass to Viton sealing surface. With the gasket back in place the system was ready for operation.

2. System Operation During the Deposition of Iron

After installing a new iron filament and NaCl substrates, the system was pumped down to 20 microns as read by a Hastings thermocouple vacuum

gage. At that point the titanium sublimator filaments were energized and degased at a power setting producing approximately 35 amperes in the filaments. The pumping was continued with the 15 cfm mechanical pump until the system pressure was 10 microns. The system was then isolated and pumping with both titanium sublimation and the ion pump was initiated. When a pressure of approximately 1×10^{-5} torr was attained, the radiant heater element (shutter in place to shield the substrates), the substrate heater element, and the iron filament were degased. Subsequently, the temperature of the substrate carrier block was raised to a temperature of approximately 500°C and baked for 15 minutes or more before cooling to approximately 445°C. The latter temperature was maintained for at least 30 minutes before iron was deposited on the substrates. The purpose of this procedure was to degas the substrates and to establish thermal equilibrium in the NaCl. The procedure to this point was conducted with the shutter in the raised position and in the absence of the overhead radiant heater operation. The variable transformer in the substrate heater circuit was set at approximately 59 per cent of full scale yielding a circuit voltage of 6.5 V in order to maintain the copper block temperature at 445°C. Exact setting and temperature were not critical to the results.

The iron filament was now heated slowly to a power level corresponding to a variable transformer setting of 60 per cent of full scale using the 400 A - 5 V tap of the transformer in the filament power supply. This action was taken to check the power level required for adequate sublimation of the iron wire and to clean the filament. The power to the filament was then decreased.

An initial pressure of 1×10^{-7} torr was considered to be the highest

pressure at which deposition should be conducted. The pressures actually used were generally in the low 10^{-8} torr to 10^{-9} torr range. Before lowering the substrates into the deposition position, the system pressure and copper block temperatures were recorded along with the substrate heater variable transformer setting.

After recording the data, deposition was initiated by turning the power to the filament up to approximately 65 per cent of full scale. The progress of the deposition was visually rated and corresponding adjustments made in the power supply. The substrates were observed to turn brown and darken during deposition before becoming metallic in color and optically dense. The proper deposition rate was determined empirically to bring about the metallic appearance of the deposit at approximately 45 seconds into the sublimation. The duration of the deposition was 3 minutes unless a little thicker or thinner film was considered more desirable for the experiment to be performed. The data pertinent to the sublimations, film anneals, and reactions are tabulated in Appendix D.

Following deposition of the iron film it was found necessary to anneal the deposit at higher temperatures in order to produce the best single crystal. The technique to be described was not considered optimum but it gave successful results. The substrate heater transformer setting was moved to 68 per cent of full scale, and the radiant heater was operated with a variable transformer setting of 54 per cent of full scale employing the 200 A - 10 V transformer tap of the filament power supply. The latter setting was approached slowly over a 15-minute interval using an initial setting of 35. Both settings were maintained for at least 15 more minutes to give a total annealing time of 30 minutes or more. The final copper block tempera-

ture was approximately 530°C, and the temperature indicated by the iron-constantan thermocouple on the auxiliary substrate was approximately 450°C. The 450°C value was established quickly after making the final radiant heater power adjustment and was maintained at a near constant value during the last 15 minutes. The exact film temperature was not defined. However, it is a reasonable assumption that an annealing time of 15 minutes at a temperature between 450°C and 500°C would be sufficient for a film of the purity employed.

3. System Operation During Film Reaction

Reaction of a single crystal film with CO was conducted by first establishing thermal equilibrium of the substrates and support apparatus at the temperature to be investigated. The temperature was equilibrated as soon as possible after the film annealing treatment. By setting the variable transformers of both heater circuits at predetermined power levels, the temperature of the copper block was brought into coincidence with that measured at the auxiliary substrate. This process established the iron film temperature as that indicated by the thermocouples.

Carbon monoxide was let into the system through the leak valve until the experimental pressure was established as indicated by the thermocouple vacuum gauge. The pressure was maintained approximately constant with mechanical adjustments of the valve as required.

Some temperature instability was encountered on introducing the CO. The effect was countered by adjustments of the heater power levels. The temperature deviations were small during the major portions of the reactions being of the order of ± 2°C. At the beginning, however, short-lived departures from the reactor temperature as large as 15°C were encountered. For-

tunately, the phenomena studied were not critically effected by these temperature deviations, and the results observed are representative of the average temperature. The temperature data for each reaction are given in Appendix D.

The duration of a reaction was normally 1 hour. However, several extended experiments were also conducted. The reaction portion of the experiment was terminated by evacuating the system and then shutting off the power to the heaters. The time required to pump the system down to 1 x 10^{-5} torr following a reaction was less than 5 minutes. Pumping was continued until a low 10^{-7} torr scale pressure was established. The power to the heaters was shut off approximately 5 minutes after the system evacuation was initiated. The cooling curves for the apparatus as established from both the substrate carrier block thermocouple and the thermocouple resting on the auxiliary substrate are given in Appendix E.

After a specimen had cooled to near room temperature (as indicated by the copper block temperature), the system was backfilled with pre-purified grade nitrogen to 1 atm of pressure.

A postreaction vacuum anneal of the film was performed in one experiment. The system was evacuated and the reaction temperature was maintained throughout the annealing period. The process was terminated by discontinuing the power to the heaters.

4. Specimen Preparation for Analysis

The substrate and single crystal films were removed from the system and placed in a closed petri dish. As quickly as possible the film was scored with a dissecting knife, and the pieces of crystal, approximately 2 mm^2, were floated from the substrate onto the surface of water. Three

baths of distilled and degased water (degasing accomplished with an aspirator) were prepared for the stripping and washing of the specimens prior to the removal of the substrate from the vacuum system. The pieces of iron crystal were transferred from one bath to another by picking them up on 3 mm, 75 mesh, copper grids. On removal of the specimens from the last bath, the excess water was removed by adsorption with filter paper, and the specimen resting on the support grid was placed under an infrared lamp for drying. Within 15 minutes of the opening of the vacuum system, the specimens could be stored in a desiccator. Within 1.5 hours the first specimen was generally in an electron microscope.

5. Analysis of the Specimens

The investigation of the specimen films in the electron microscope included the following: The crystallographic features of the iron films; the characterization of solid product nucleation sites; the morphology and size of product particles; the product particle population density; electron diffraction identification of individual particles; the orientation relationship between product crystals and the iron single-crystal; the directional relationship between product particle growth directions and the crystal structure of the iron; and the interfacial character of the product-iron boundaries.

6. Iron Film Replicas

Replicas of the surfaces of some of the reacted iron films were made. The purpose was to provide support information for the interpretation of the transmission electron microscopy. A portion of the substrate carrying the film was cleaved carrying a cleaved section of film with it. The portion of the sample to be investigated was placed in a laboratory evaporator

with the iron film side up. As described earlier, the apparatus was set up to evaporate platinum onto a specimen surface at an angle of 15° (shadowing the surface features) and to follow the first deposition with a deposit of carbon applied normal to the surface. The composite film was then removed from the NaCl in the manner previously described. Following the film stripping process, the specimens were placed in a nital etching solution to dissolve away the iron. The carbon-platinum replicas were then washed and mounted on electron microscope grids for examination. The points studied in the electron microscopy of the replicas were: The surface topography of both the iron crystals and the product crystals; the shapes of product crystals; and impressions left by decomposed product particles.

7. Substrate Preparations for Trials to Produce Single Crystals of (110) and (111) Film Planes

Attempts were made to produce iron single crystals having (110) and (111) film planes. The procedure was to produce NaCl plane faces of the corresponding orientation and to deposit iron on these in the same manner as that used for the (001) films. Depositions on these two new orientations were carried out at three different substrate temperatures. A temperature corresponding to that used for the (001) film deposits and temperatures 50° above and below that temperature were used.

The NaCl faces were prepared by cutting the optical crystal blanks with a jeweler's saw. The blanks were oriented and the cutting plane defined by placing them in specially prepared miter boxes. The faces were smoothed by polishing the surfaces on a nylon cloth wet in one region and dry in the others. The wet region was used for polishing. Etching during removal of the crystal from the cloth was prevented by quickly sliding the

crystal into the dry portion of the cloth. Final polishing of the surface was accomplished by placing a drop of water onto the surface of interest and very quickly blowing the surface dry again with a quick burst of nitrogen.

8. Interferometer Determinations of Film Thickness

The cleavage steps on the NaCl substrate surfaces prevented direct thickness determinations of the iron film overgrowth. Therefore, experiments were performed by depositing iron onto glass slides positioned identically with respect to the iron filament as the NaCl substrates. A sharp step was required at an edge of the iron film on the glass surface in order for a good interferometer measurement to be made. To facilitate the formation of the required step, the edge of a glass slide cover platelet was beveled and the sharp edge placed next to the base slide. The platelet was snugly fit to the slide with a very small amount of Apiezon L grease located as far from the edge as possible. The deposition of the iron was made at room temperature. The thickness measurements were made in the Physical Sciences Division of the Engineering Experiment Station. The determinations were made in a multiple-beam interferometer employing fringes of equal chromatic order.

CHAPTER III

RESULTS AND DISCUSSION

A. Introduction

Many studies have been made of the carbon monoxide decomposition on iron and iron-bearing materials, but none have studied the attack of the iron by the nascent carbon in the early stages of the reaction. A variety of products were reported to form at the onset or during the reaction. The nucleation centers for the solid products were not known, and the role of the metal in the process was not understood. These problems were the objects of this research. The approach was to simplify the system to a study of the interaction of high purity CO with virgin surfaces of high purity iron single crystals.

The electron microscope was chosen for the analytical tool. Although there are some analytical techniques more precise than electron microscopy, none is more versatile for studying the solid metal phase. With this instrument the first stages of formation of a solid phase product can be detected, the crystallographic location on or in the iron matrix can be determined, specific crystallographic analysis of individual phases can be made, and the mutual orientation between a product crystal and the metal matrix can be established.

Obviously, the metal has to be thin enough for electron transmission if the full potential of the technique is to be utilized (transmission microscopy as opposed to surface replica microscopy). Epitaxic single

crystal films of iron were, therefore, chosen for the specimens. Such a specimen provides a surface of known orientation for reaction. It also provides a matrix of low imperfection density in which products may develop without perturbation from grain boundaries. This matrix gives excellent standard reflections in the electron diffraction patterns from reacted films.

1. Experimental Program

To implement the objectives of this study, the research was carried out in the following manner.

The first step was the development of equipment and techniques for the reproducible production of single crystal iron films in ultra high vacuum. The films had the (001) plane of α-iron parallel to the film plane.

The technique for reacting the films in the same system in which they were grown was developed next. Without exposure to the air, the reaction could be studied in the absence of significant surface contamination which inevitably forms even in vacuum to 10^{-5} torr. Although the surfaces were not considered atomically clean, they were free of any significant surface compounds.

Finally, techniques for handling and analyzing the reacted films were developed.

The temperature range from 250 to 550°C was chosen for study because it covers the important region in which the macroscopic reactivity of the CO decomposition on iron is increasing. Also, the highest temperature 550°C corresponds to the maximum temperature experimentally feasible. The temperature limitation is due to the sublimation of the NaCl substrates.

A number of trial experiments were made at various pressures, times,

and temperatures to determine the combinations which would yield sufficient product for definite electron microscopic analysis. The trials also served in finalizing the experimental techniques. The first satisfactory run (Run 49) was made at 350°C for 1 hour under 1,000 μ (1 μ = 10^{-3} torr). The experiment indicated the presence of a single reaction product (a carbide) and proved in itself that pure iron is a catalyst for the decomposition of carbon monoxide. The CO had to decompose on the surface, and the nascent carbon had to diffuse to the interior of the matrix in order to form the carbide. The process is opposed to that of direct formation of a carbide molecule at an exposed iron surface. The observation is also contrary to the proposal that an iron compound must act as the catalyst since none was present prior to CO exposure. Iron has, of course, been postulated as a sufficient catalyst before, but iron has not previously been subjected to reaction in as clean a condition as that used for the present experiments. Many other compounds have been suggested as the catalyst in opposition to iron acting in a catalytic capacity. Much more will be said concerning the nature of the catalyst and the mechanism of the overall reaction through the course of the discussion.

The reaction program is outlined in Table 3. In retrospect, it is evident that extensive study using time as the single variable would be profitable. However, the occurrence of a uniform product particle size for individual runs had to be established before it could be surmised that time-varied reactions could yield reasonable kinetic data.

2. Form of the Experimental Data

The experimental parameters are tabulated in Appendix D. The tables contain the pertinent information for the temperatures and pressures at

Table 3. Reaction Scheaule

Reaction Number	Run	Temperature °C	Pressure μ CO	Reaction Period
1	60	250	1,000	1 hour
2	61	250	1,000	2 hours 30 minutes
3	63	320	1,000	1 hour
4	49	350	1,000	1 hour
5	62	350	500	1 hour
6	51	350	100	1 hour
7	48	350	5	1 hour
8	40	350	5	2 hours
9	52	450	1,000	1 hour
10	65	450	1,000	*1 hour
11	64	450	1,000	6 hours
12	55	450	5	1 hour
13	57	450	**Control Run	1 hour
14	66	450	**Control Run	6 hours 55 minutes
15	54	550	1,000	1 hour 5 minutes
16	39	Control film (as made and pre-treated for Run)		

*Reaction followed by an 8 hour annealing period at the reaction temperature

**Control Runs were made in the absence of CO.

points of time during the various phases of the experiments. A table is given for each run listed in the Reaction Schedule. In addition to the temperatures and pressures, summary data are given for the variable transformer settings used during the different phases of the process. From the information given in Chapter II and the data of Appendix D, the experiments could be duplicated. Further information about the less critical experimental parameters can be obtained from the laboratory record books for this project which are on file in the Metallurgy Department.

Electron micrographs and selected area diffraction patterns constitute the raw product data. The information is contained on 3" x 4" glass plate, photographic negatives. Interpretation of contrast effects in the electron micrographs can be complex. For extensive treatments of the subject, references 1, 2, and 3 should be consulted. The area of a sample examined on a micrograph ranged from 3.2 to 2,000 square microns. All the information contained in the micrographs concerning product particle size and distribution was reduced to numerical form and tabulated. This information along with sample micrographs for each reaction is presented in subsection C.1.

The selected area diffraction patterns contain the crystallographic data pertaining to that portion of the sample selected for analysis. The patterns represent a reciprocal lattice plane of the crystals analyzed. Many of the SAD patterns and their solutions are discussed in subsection C.2.

3. Accuracy of Selected Area Diffraction

The accuracy of the selected area electron diffraction technique has been discussed by Thomas (1), Hirsch, et al. (2), and Heidenreich (3). The principal error in the technique results from diffraction effects from peripheral areas outside the selector aperature. This error is caused by

spherical aberration in the objective lens. In the present investigation it was easy to circumvent this problem. The diffraction patterns selected for the present analysis were obtained from areas remote from complicating features. As a result, no diffraction anomalies were developed in the patterns.

The accuracy in the determination of interplanar spacings and angles using electron diffraction is less than that possible by x-ray measurements. Under nearly ideal conditions the accuracy for electron diffraction is 0.1 per cent (2). This value may readily degenerate to 1 per cent, and by using less than desirable specimens accuracies of only 2 to 5 per cent may not be unreasonable. With reasonable attention to machine maintenance, the greatest source of error is likely to be inherent in the sample itself.

Problems were encountered due to foil buckling and magnetic domain interference. The buckling changed the angle of the specimens with respect to the electron beam slightly and the magnetic domains tended to split diffraction spots. However, using the iron reflections in the diffraction patterns as standards, the accuracy of the d-spacings were determined within 2 per cent of the reported values and usually better than 1 per cent. This figure corresponds well to the variation in the values given by different authors as shown in the tables of Appendix B. Appendix B presents the electron and x-ray diffraction data used in the solution of the electron diffraction patterns.

The angles between the planes of cementite as observed in the present analysis were generally within 2^{o} of the reported values. Due to the unique character of a single crystal pattern for a specific compound, positive identification of a material is possible even when the accuracy of individual

measurements is no better than that described. The requirement is that the approximate solution found by measuring interplanar spacings be compatible with the corresponding interplanar angles for the proposed crystal. When there is doubt about the reliability of the machine constant, a third check can be made by comparing Relative Reciprocal Lattice Spacings. A computer program was written for the calculation of approximately 16,000 of these values for cementite. Fortunately, the quality of the electron diffraction patterns did not necessitate extensive use of this information. The program and generated data are not included in the thesis since they are quite voluminous. The program and data have been placed in permanent file in the Metallurgy Department.

B. Characterization of the Single Crystal Films

Considerable difficulty was experienced in developing the techniques for producing single crystal films of iron on a reproducible basis. Initially, the conventional technique of evaporating iron from a tungsten basket placed approximately 8 centimeters above a cleaved NaCl single crystal substrate was used. The results were discontinuous films of poor orientation. An orientation of the (001) iron plane parallel to the same plane of the substrate was sought.

The next technique tried was sublimation from tightly wound coils of 20 mil. iron wire heated by passing a current through them. The distance from the substrate to the evaporation source was again 8 centimeters. The results were promising and one very good single crystal was produced in this manner, but reproducibility was very poor. The chief problem lay in producing a continuous film. Changing the substrate temperature was not

beneficial. Making use of the suggested technique of Matthews (122), the sublimating iron coil technique was combined with the pre-evaporation of a short segment of iron wire at a substrate to source distance of 1 centimeter. Success was not achieved by this combination either. The films were generally discontinuous, and as a result the film segments were only moderately well oriented.

The results indicated that the growth of the film was not rapid enough to force the film to grow as a continuous layer. Based on this knowledge, sublimation of an iron wire coil placed 2.5 centimeters above the substrate was tried next. It was found that a continuous film could be produced in every trial following the procedures described in Chapter II. If the procedures for making the iron coil were closely followed, the current required to maintain a constant sublimation rate for each experiment was nearly constant. Therefore, the thickness of the film could be controlled reasonably well. Indirect interferometer measurements of the film thickness were described in Chapter II. The range of film thickness used in this research was approximately 650 to 1,300 Å. The majority of films had thicknesses estimated at 1,000 Å. The thinner films were used for reaction experiments at the lower temperatures, and the thicker films for the higher temperature runs. The thicker films maintained better film integrity at the higher temperature where even an initially continuous film tends to separate and agglomerate on prolonged treatment. The thicker films, however, give rise to poor diffraction patterns due to the greater inelastic scattering of electrons. This phenomenon introduces into the normal diffraction pattern Kikuchi lines as exhibited in Figure 18. A significant point to be made by presenting this figure is that the Kikuchi pattern of the film attests to

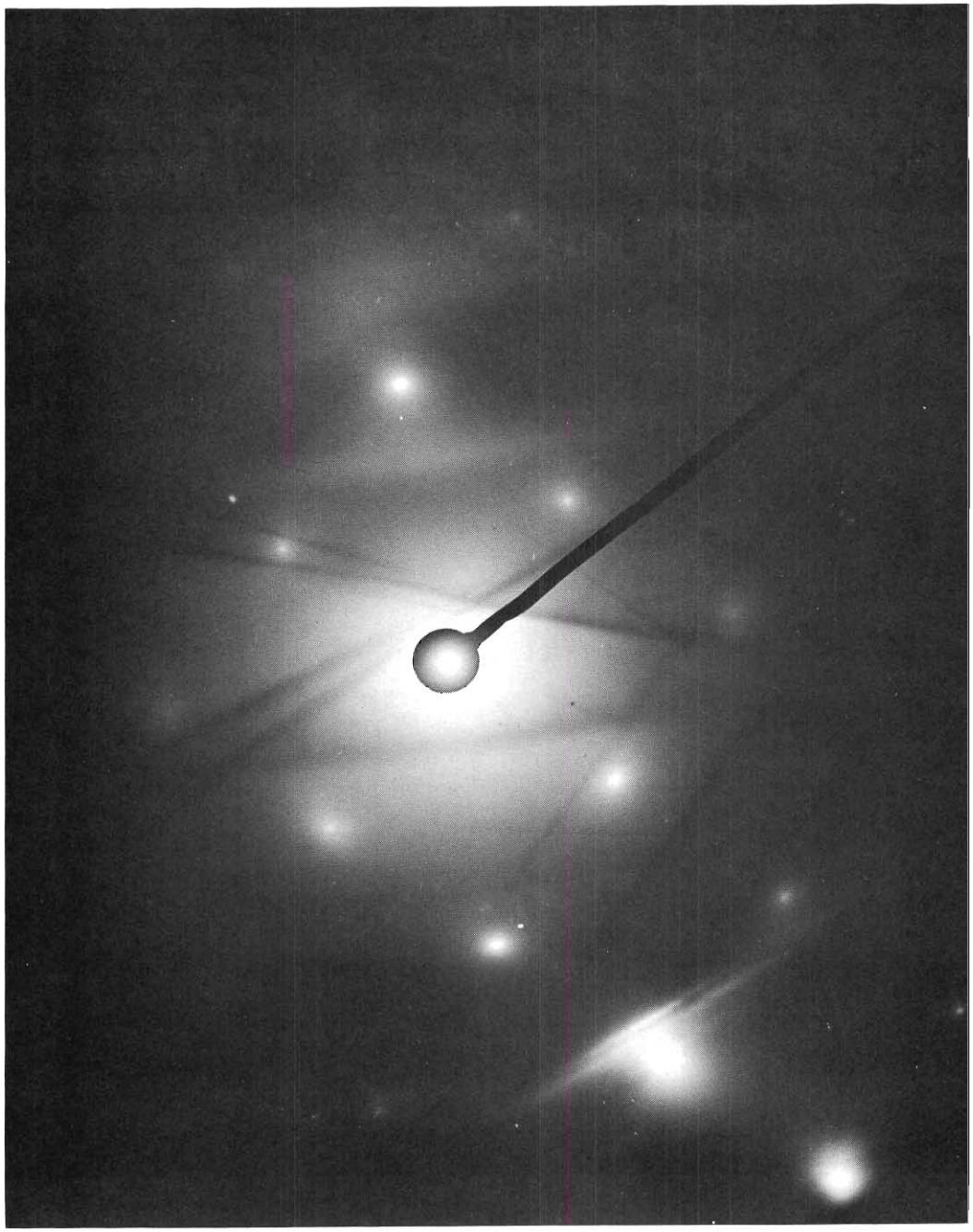

Figure 18. Kikuchi Pattern for an Iron Single Crystal Film

the good quality of the film's crystal structure. However, to facilitate the solution of patterns from reacted films the thinner foils were preferred.

It was not considered practical in the present investigation to obtain more precise information regarding the thickness of the films produced for several reasons. First, it was necessary to use films of different thickness. Second, the film thickness varies from one region to another. Third, there exist local variations in film thickness, as will be demonstrated shortly.

The exact temperature of the substrate surface during vapor deposition was not established in this investigation. It was not the purpose of this work to determine the epitaxic temperature. This could be a formidable problem in itself. For this investigation, the temperature of the copper block substrate carrier was monitored and that temperature used for deposition which was found by trial to give reproducible iron single crystals. The temperature was approximately 450°C and small variations were not found to be critical. Such a value is characteristic only of the particular system used. The variation in the reported epitaxic temperatures found in the literature was greater than 100°C. The differences are considered the result of using different methods for the measurement. The method developed for measuring the substrate and film temperature during annealing and reaction for this research was discussed in Chapter II.

After determining that rapid film formation ($\approx$ 400 Å/min.) was necessary to obtain continuous films reproducibly, work was still required to bring the orientation of the individual film grains into registry and to eliminate the majority of the lattice defects. It was found that annealing the films for half an hour at 450°C resulted in good quality single crystals

with their (001) planes parallel to the film plane. In the following few paragraphs an illustrated account will be presented of the formation of a single crystal iron film.

A single crystal film forms by the growth of initially isolated nuclei on a substrate surface. These nuclei impinge at an early stage if a good, continuous film is to be produced. Film development continues by the growth and impingement of composite islands of nuclei which results in a structure with many open channels. The channels are filled with depositing material by the growth of thin bridges and edge extensions. Imperfections are believed to be grown in, since in the channel structure adjacent segments may be slightly misoriented and unable to readjust before closure occurs.

Using the deposition techniques presented in Chapter II, the sequence of growth of iron single crystals may be pictured as follows. Figure 19 shows a micrograph of the nuclei formed after 5 seconds of sublimation. The fine dispersion of very small nuclei ($\approx$ 200 Å in diameter) is required for single crystal film formation as proposed by Matthews (122). Close examination reveals thin islets of iron already impinging. Figure 20 shows a typical diffraction pattern of the same film. A high degree of the proper orientation is indicated although many nuclei are obviously randomly oriented. Figure 21 is a lower magnification of the same film showing the decorating effect of the nuclei for the cleavage steps of the NaCl substrate. This is not a new observation and only shows the preference of the initial nuclei for formation at cleavage steps.

Figure 22 pictures a film after 15 seconds of evaporation. The film was in a stage of joining compound island chains to form the channel structure.

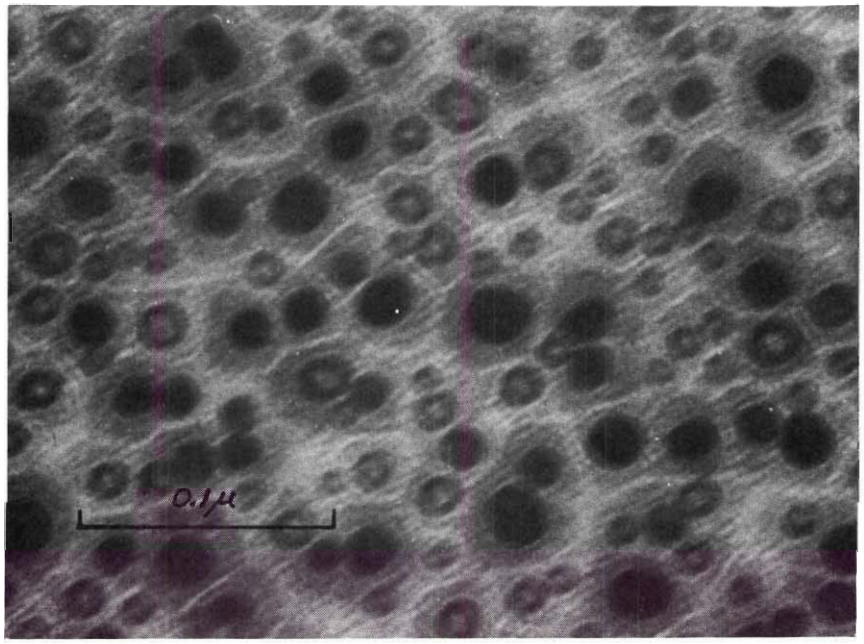

Figure 19. Iron Nuclei After 5 Seconds of Deposition

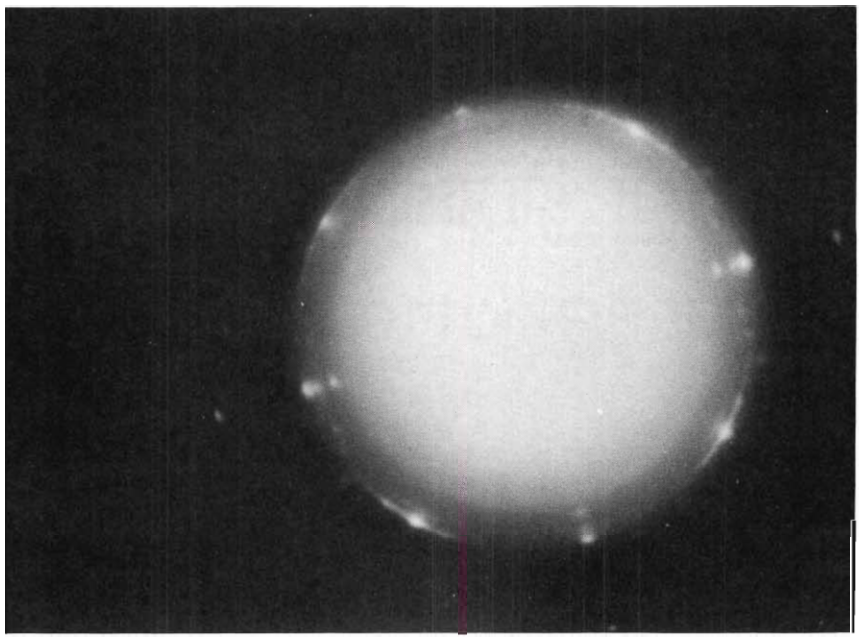

Figure 20. SAD Pattern from a Film of Iron Nuclei Formed After 5 Seconds of Deposition

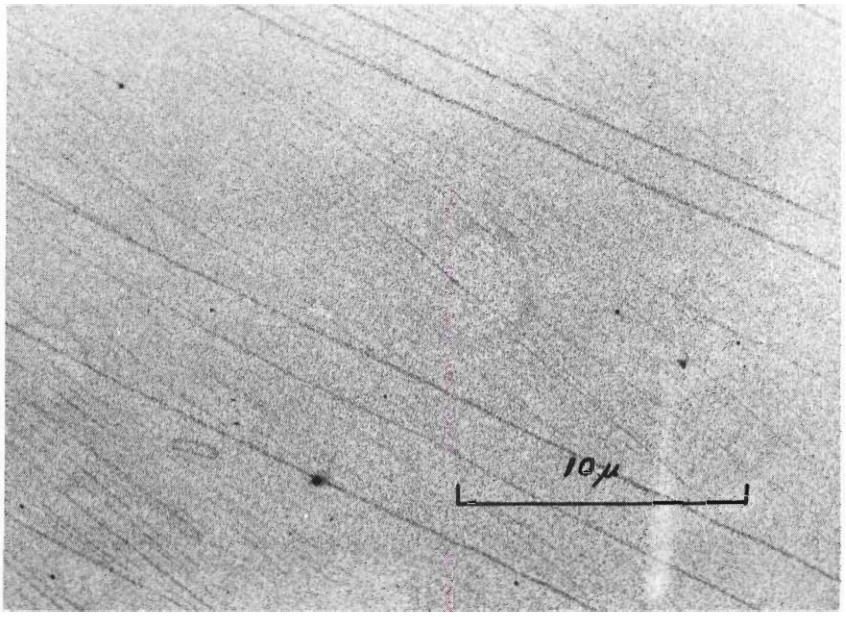

Figure 21. Substrate Decoration by Iron Nuclei After 5 Seconds of Deposition

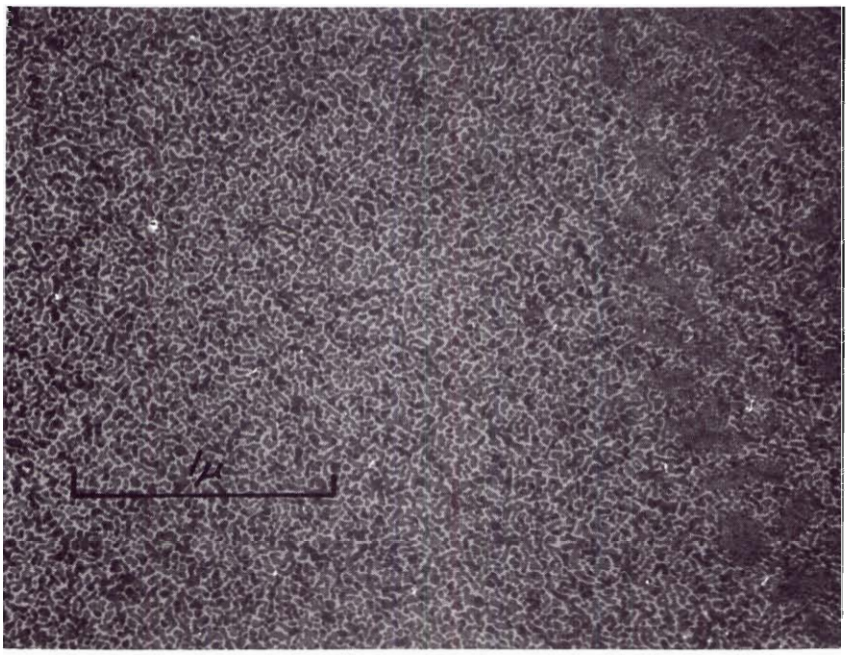

Figure 22. Iron Film After 15 Seconds of Deposition

The internal features of the complex islands are well illustrated in Figure 23. Figure 24 serves to illustrate the bridging between adjacent segments across the channels. It is significant to note the perfection of the matrix structure in each grain shown in Figure 24. This implies that lattice imperfections in the final film are introduced primarily during the closure process. The diffraction patterns of films in the complex island and channel structures show a considerable amount of perferred orientation, but still a great many grains are randomly oriented or exist in secondary orientations of lesser preference.

Figures 25 and 26 are typical examples of the micrographs and SAD patterns obtained from continuous films which had not been given the annealing treatment after deposition. The micrographs indicate the film to be made up of crystallites of questionable orientation. On tilting the specimen in the microscope, it was observed that the contrast between adjacent crystallites was readily reversed indicating the two crystallites to be of nearly identical orientation. In the RCA electron microscope, defocusing the objective lens allowed the magnetic domain structure to become distinguishable. A typical example is shown in Figure 27. Deviations in Bloch Wall traces at grain boundaries are observed to be slight, indicating the boundaries to be very low angle. The reflection spots in the SAD pattern (Figure 26) are observed to be slightly arced, indicating that the constituent crystals are only slightly misoriented.

The general appearance of a SAD pattern for a continuous unannealed film is close to that expected for a single crystal. Figure 26 is typical except for the reflections of a second orientation. The positions of these occasionally occurring reflections are illustrated in Figure 28 and marked

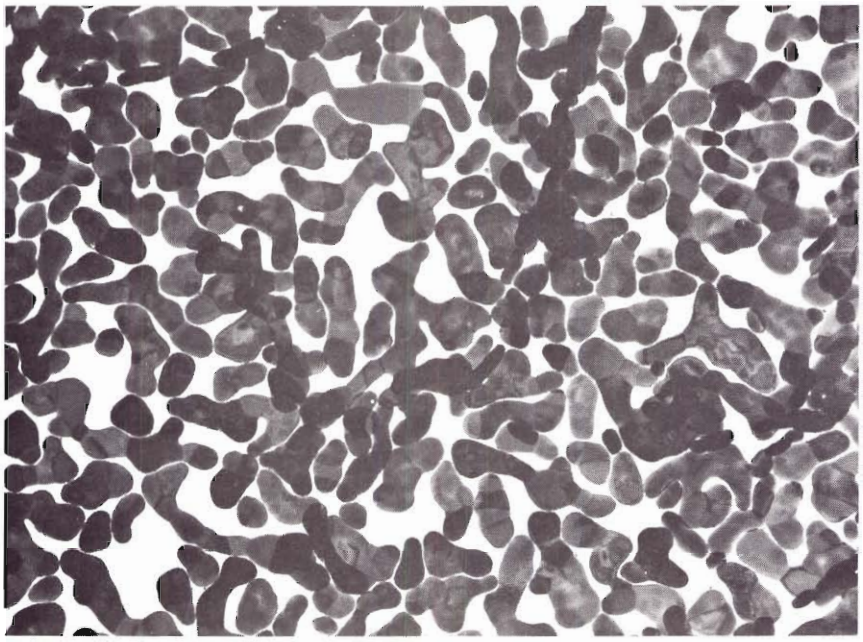

Figure 23. Complex Island Stage in the Development of an Epitaxic Iron Single Crystal

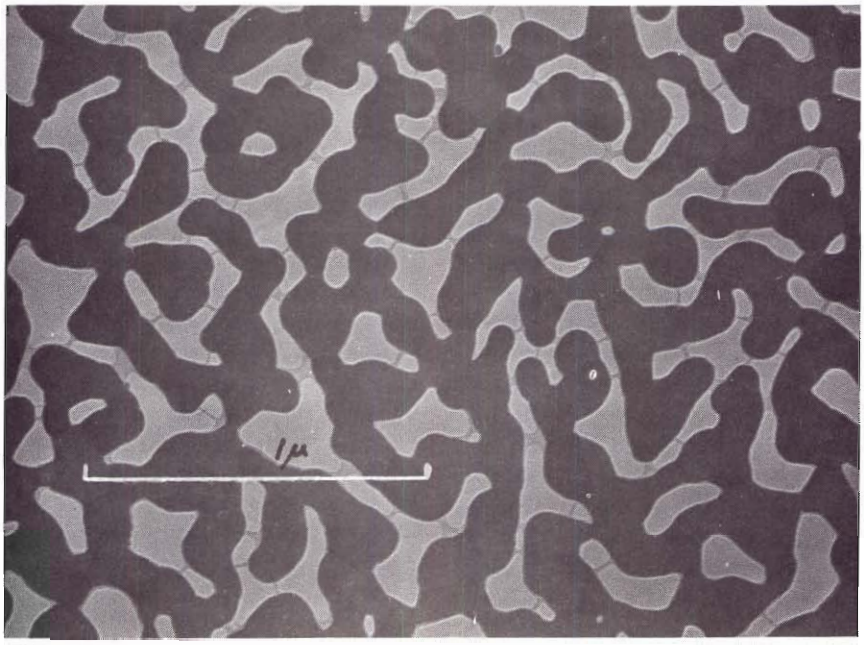

Figure 24. Channel Bridging

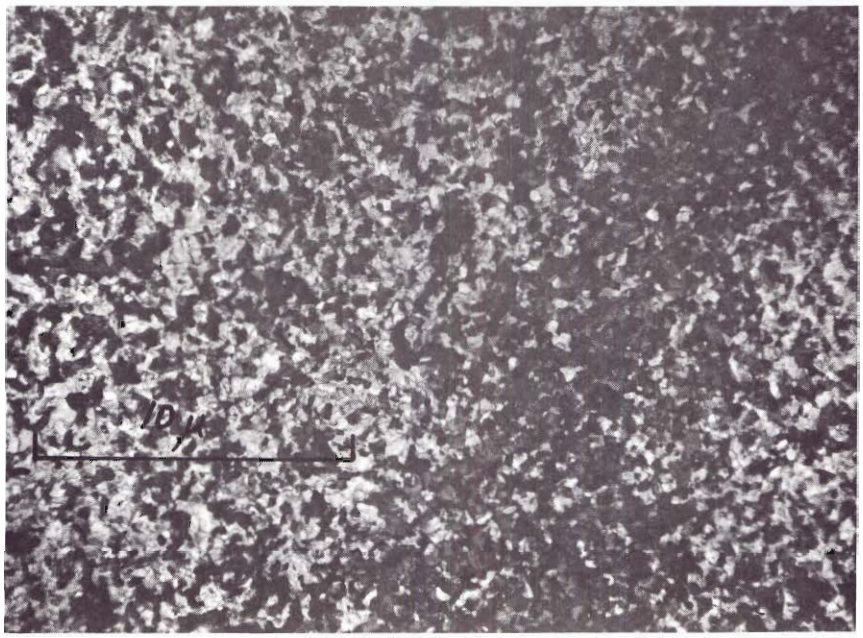

Figure 25. Micrograph of an Unannealed Iron Film

Figure 26. SAD Pattern from an Unannealed Iron Film

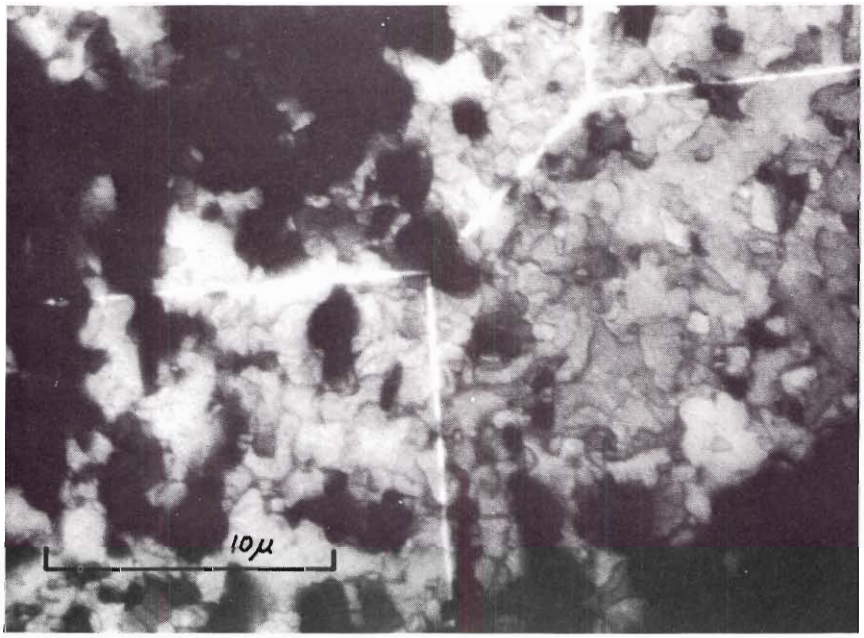

Figure 27. Over-Focused Micrograph Revealing the Magnetic Domains in the Iron Film

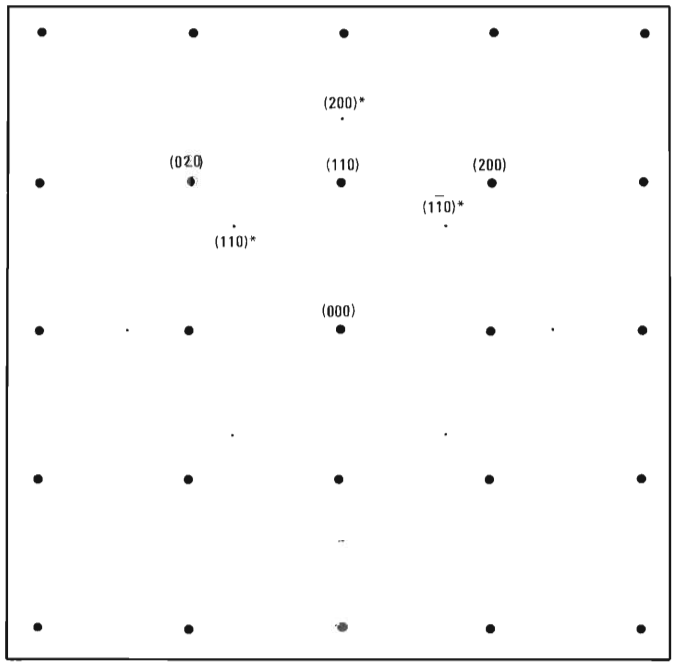

Figure 28. Constructed Diffraction Pattern of Two (001) Plane Oriented, Iron Film Crystals. The second orientation marked with an asterisk is rotated 45° to the first.

with an asterisk. The secondary orientation has an [001] zone axis as does the primary. The difference in the two is a 45° reotation about the [001] axis. The second orientation was never as abundant as the first and was not always present in the unannealed films. The annealing process apparently eliminates it along with the establishment of near perfect registry for the other subcrystals.

Figures 29, 30, and 31 are good examples of the film quality capable of being produced by the methods developed during the present research. From the micrographs it is evident that the film is singly oriented. The lattice imperfections observed are individual dislocations and dislocation sub-boundaries. The latter are exhibited only in Figure 31. After annealing the films, most dislocations present are tied up in networks such as the sub-boundaries.

Figure 32 presents a typical SAD pattern of a single crystal iron film. The sharp spots in the regions of the proper matrix reflections for iron are the actual iron reflections. The nearby diffuse spots located at slightly greater d-values are due to an epitaxic oxide film which forms on the iron immediately on exposure to the atmosphere. The sharp character of the matrix reflections is indicative of the absence of misoriented regions in the iron film. More will be added to the discussion of the surface oxide shortly.

The surface structure of the iron films are discernible in Figures 29, 30, and 31. A mottled feature of the surface is observable in all three figures. On a smaller scale, the surface is fine textured. Figure 33 is a micrograph of a surface replica of the film from Reaction 9 (Run 52). This figure shows the mottled features of the films to be the results of

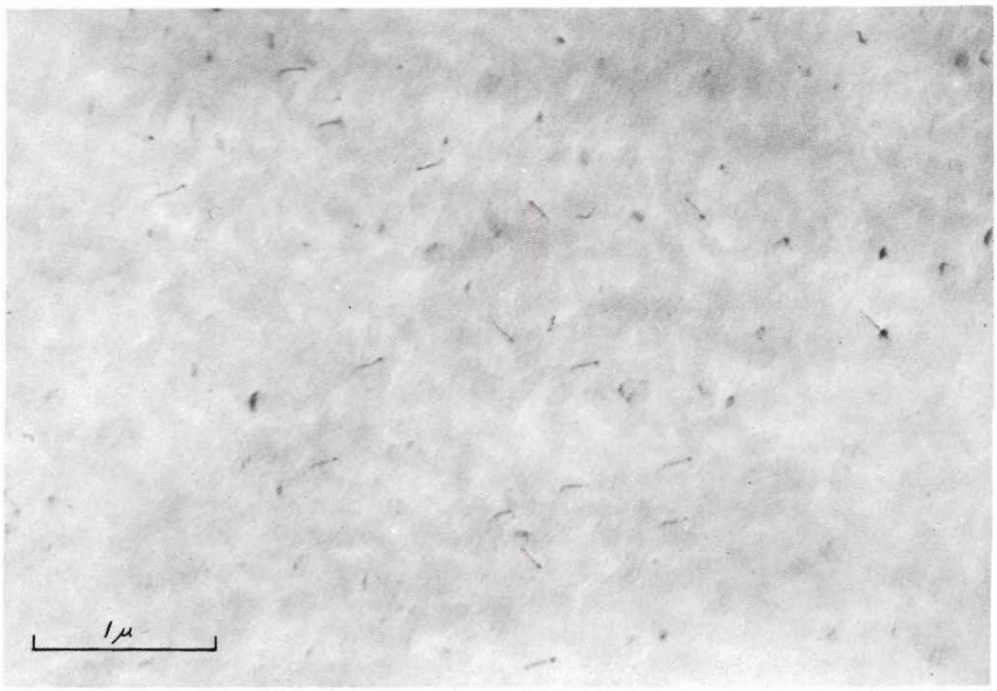

Figure 29. Micrograph of an (001) Iron Single Crystal Film of High Quality

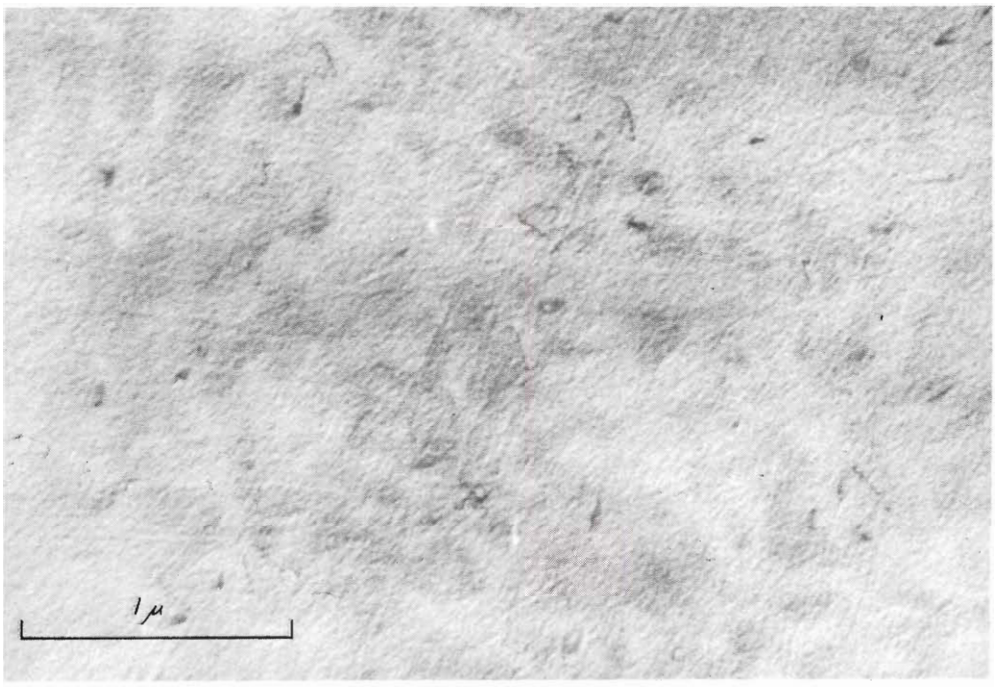

Figure 30. Micrograph of an (001) Iron Single Crystal Film of High Quality

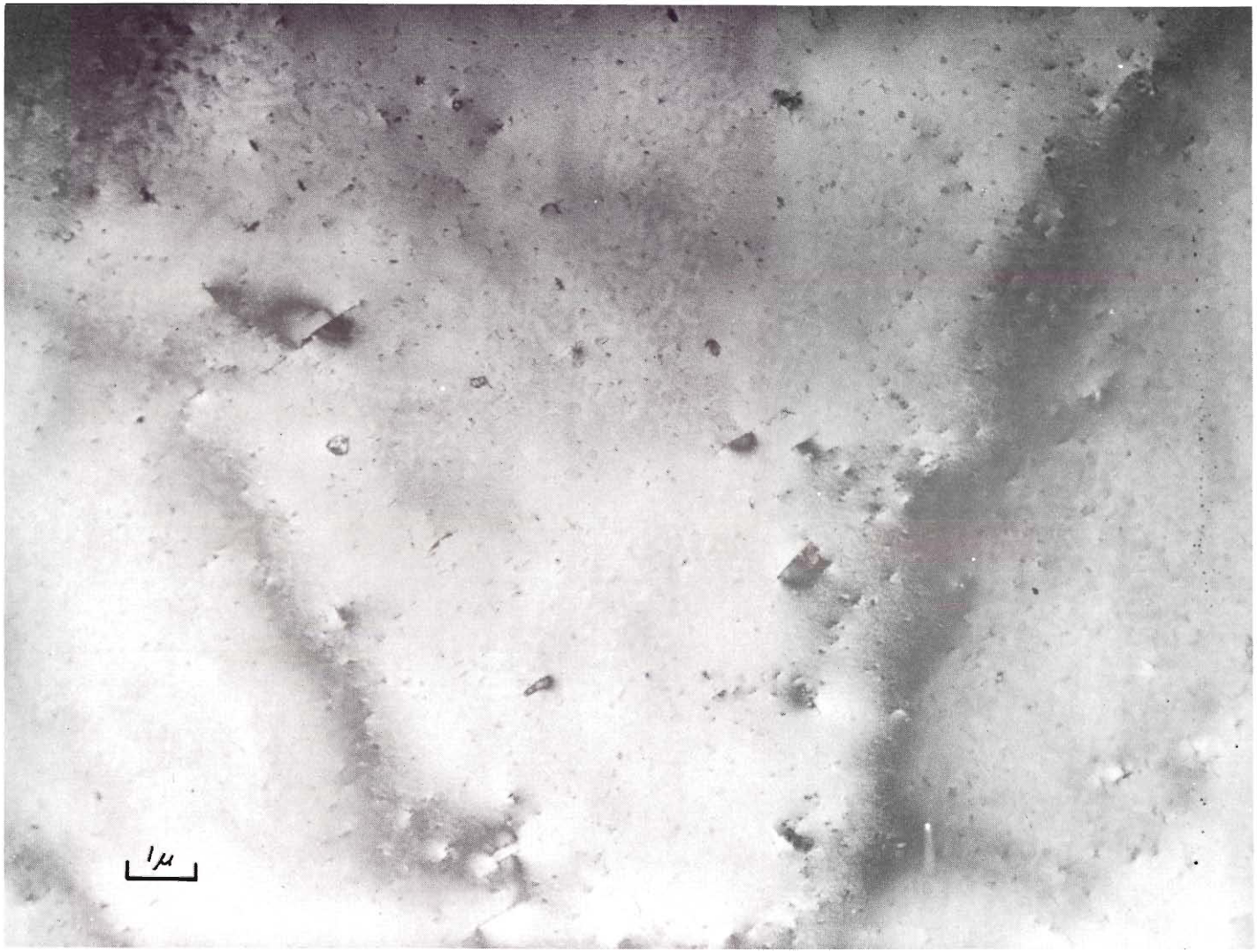

Figure 31. Micrograph of an (001) Iron Single Crystal Film of High Quality

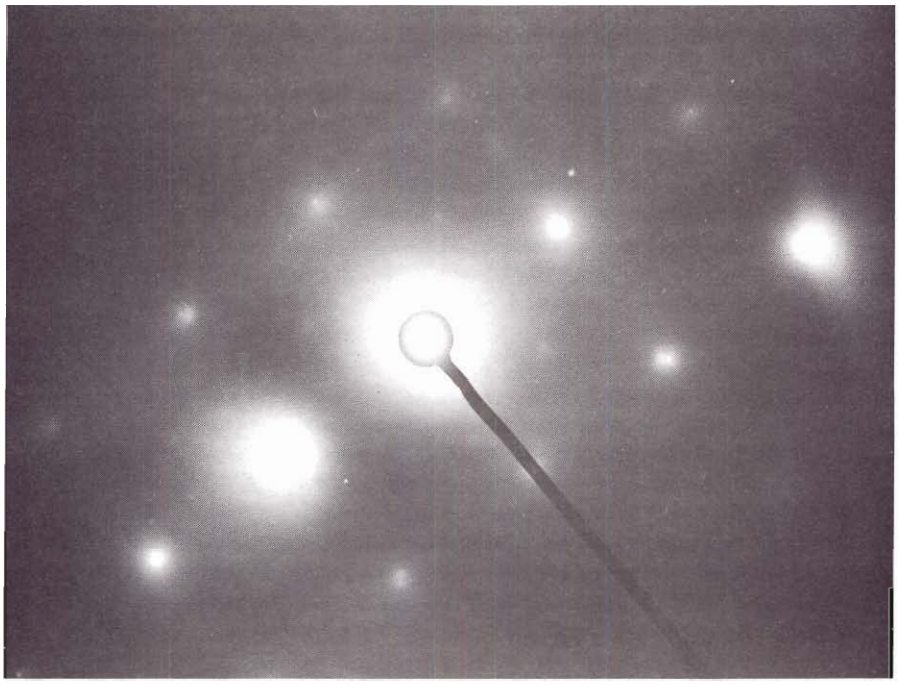

Figure 32. SAD Pattern of an (001) Iron Single Crystal Film of High Quality

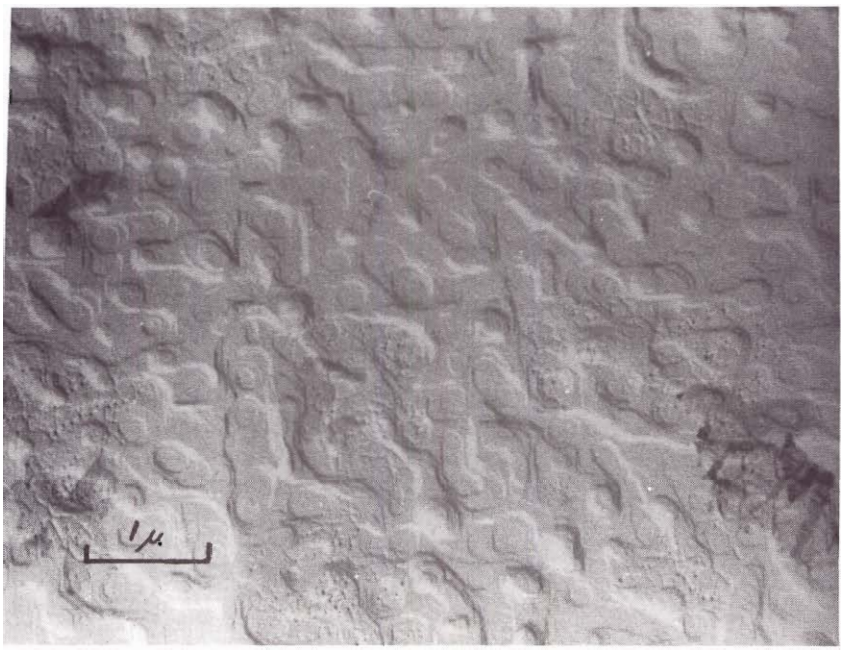

Figure 33. Micrograph of a Surface Replica on an Iron Single Crystal Film

stepped and faceted surface mounds. As noted in the transmission micrographs, the surface character of the iron appears to be approximately the same from one film to another after the initial annealing process.

The surface oxide referred to earlier has been observed by other investigators. Schenck and Nacken (95) in studies of iron films formed inside an electron diffractometer found an oxide (Fe_3O_4) film to form on the surfaces after the pressure in the system had been raised to atmospheric. Such a treatment was reported to immediately oxidize the films. Rasigni (126) also observed that iron films are not oxidized in high vacuum. Using the very sensitive technique of Low-Energy Electron Diffraction, Pignocco and Pellissier (114) found iron to form small quantities of oxide after exposures to oxygen of only 55×10^{-6} torr-sec. Less exposure generally resulted in only oxygen chemisorption. The point being made is that oxide forms immediately on exposure of iron to the atmosphere. This event is unavoidable in the practical procedures required to prepare specimens for electron microscopy.

The question then arises as to what effects the formation of the oxide film might have on the reacted specimens. In the first place, graphite and the carbides of iron will not be effected by exposure to air at room temperature. Since these were the only products of the CO reaction for which any evidence was found, exposure should not effect the reacted films except to oxidize the iron. None of the specimens can be definitely stated to have been oxide-free. However, the characteristic pattern of the oxide was frequently noted to be absent in some regions of the films. The quantity of the oxide present appeared to vary. The tendency seemed to be toward the formation of a passive layer of limited thickness. The oxide never became

thick enough to distort the structural features of the iron film nor was double diffraction ever observed. In fact, films were left in air for a period of approximately three months following examination without any perceptible increase in the oxide.

The oxide layer appears to form epitaxially as a very thin, closely adherent film on the iron surface. Figure 34 presents a diagram of the relative positions of the iron and oxide reflections. The orientation relationship between the oxide and iron lattices was Fe (001) [100] $\parallel$ Fe_3O_4 (001) [110] as has been previously reported by others (127,128). The four sets of four satellite reflections in the vicinity of the iron {110} spots do not lie in the same plane of reciprocal space as the other reflections. These spots are attributed to the Fe_3O_4 {311} and {511} planes whose reflections lie one-quarter of the reciprocal lattice cell dimension off the (001) reciprocal lattice plane of the oxide. If the oxide film is very thin, then the reciprocal lattice points are elongated parallel to the electron beam. This lengthening coupled with buckling of the iron film can quite easily account for satisfying the diffraction conditions for the {311} and {511} oxide reflections. Figure 35 shows a SAD pattern which includes the anomalous oxide reflections. These reflections show up very well and it is apparent from the incomplete iron pattern that the area of the sample giving rise to diffraction was tilted with respect to the incident electron beam.

The phenomenon just discussed gives a pattern similar to the twin patterns obtained from face centered cubic materials. The fact that the extra spots are not produced by an anomalous iron structure or by double diffraction can be proven geometrically. In order for the iron matrix to

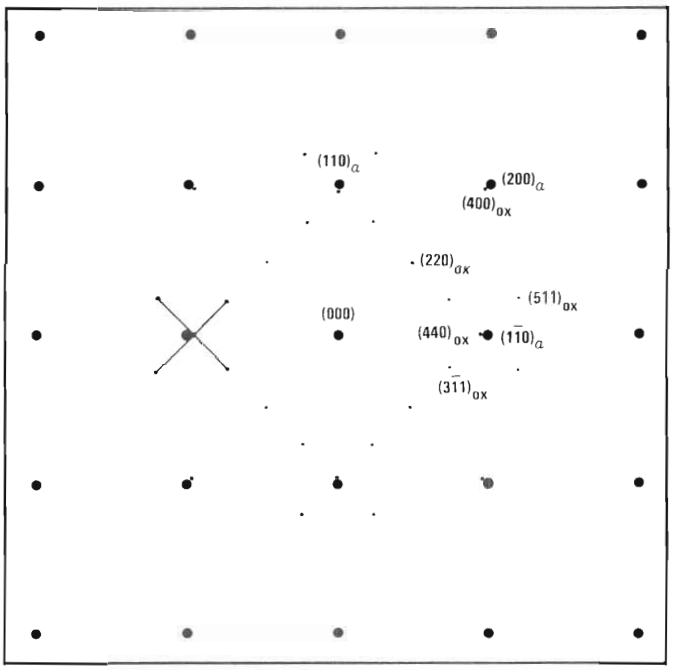

Figure 34. Constructed Compound Diffraction Pattern from an Oriented Fe_3O_4 Film Overgrowth on an (001) Single Crystal Iron Film

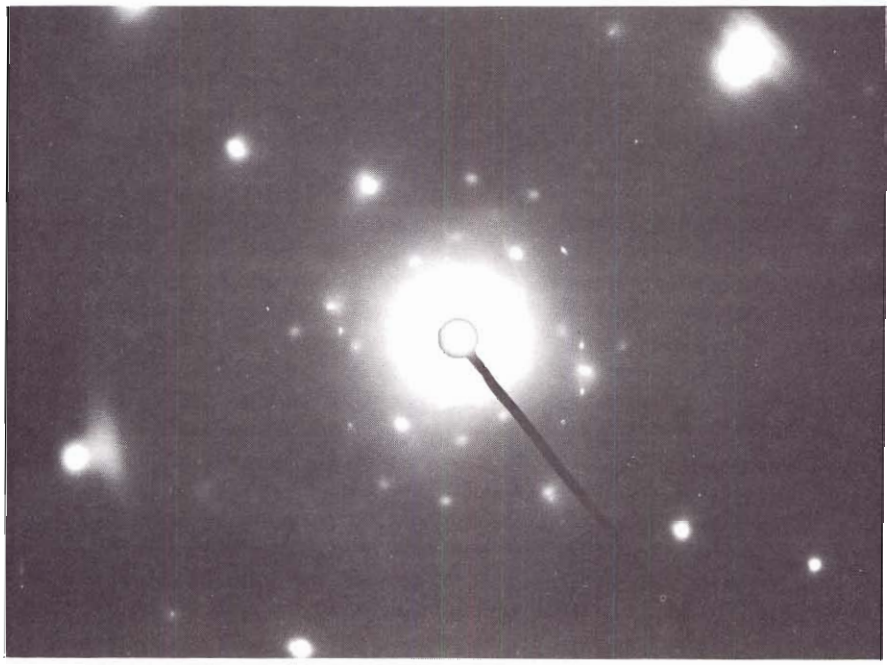

Figure 35. SAD Pattern Illustrating the Compound Pattern Resulting from the Overgrowth of Fe_3O_4 on the Iron Single Crystal Films

be instrumental in producing the sets of four satellite reflections, the diagonals of each set would have to cross at the {110} iron spots. Instead, the satellite spots are symmetrically placed about the {400} oxide reflections and are solely related to oxide diffraction effects.

The characterized diffraction effects introduced by the oxide film can be disregarded in the analysis of SAD patterns from reacted films.

The principal type of crystallographic defect present in the iron films during reaction was the dislocation sub-boundary. The majority of these boundaries tended to be straight and to have approximately < 110 > traces in the plane of the iron films. Generally, the individual dislocations making up these boundaries could not be resolved in the electron microscope without tilting the specimens through large angles. The dislocation lines overlapped and lay inclined to the film plane. The results were walls of dislocation lines which were perpendicular to the surface. In an effort to minimize the total dislocation energy, many of the original dislocations in a deposited film were annihilated by migration to the film surface during the annealing process.

A plausible explanation for the lining up of dislocations in the regularly spaced and directed sub-boundaries is minimization of the misfit strain between the lattices of the substrate and the overgrowth. In the absence of misfit, it might be expected that nearly all dislocations in the film would be eliminated during the annealing process. Analogous mechamisms for the relief of overgrowth strain have been reported (104).

Following the development of the equipment and procedures for producing the (001) iron films, attention was directed to growing (011) and (111) type films. The substrate preparation and sublimation techniques were

described in Chapter II. The only differences in the procedures used in the attempts to make (011) and (111) films from those used for (001) films were in the preparations of the substrates and in the substrate temperatures used during the depositions. Three different temperatures were used for each film orientation type. The results of these experiments are shown in Figures 36 and 37. Typical micrographs and SAD patterns were selected from the best experimental runs.

The experiments and the corresponding temperatures of the substrate carrier chosen to illustrate the results obtained for (011) type films were: Run 41 (434°C), Run 45 (489°C), and Run 46 (401°C). Similarly, for (111) type films, the experiments were: Run 50 (407°C), Run 58 (446°C), and Run 59 (489°C). The experimental details for these runs may be found in the research record books for this project which are on file in the Metallurgy Department. From the electron micrographs it was evident that the techniques used developed continuous films for all the conditions investigated. However, in no case was a good single crystal prepared of the orientation sought. On the basis of the results from these experiments, reasonable predictions may be made concerning the likelyhood of obtaining good quality iron single crystal films of the (011) and (111) orientations.

The results of the trials to form (011) films showed that a layer of deposit 1 grain thick formed which was composed of quite separate crystallites. The orientation of adjacent grains differed considerably. There appeared to be several preferred type orientations which formed on the (011) rock salt surfaces. Little random orientation existed among the grains. Surprisingly, the (111) type orientation was quite prevalent. The preferred orientations represented averages, and there was considerable scatter-

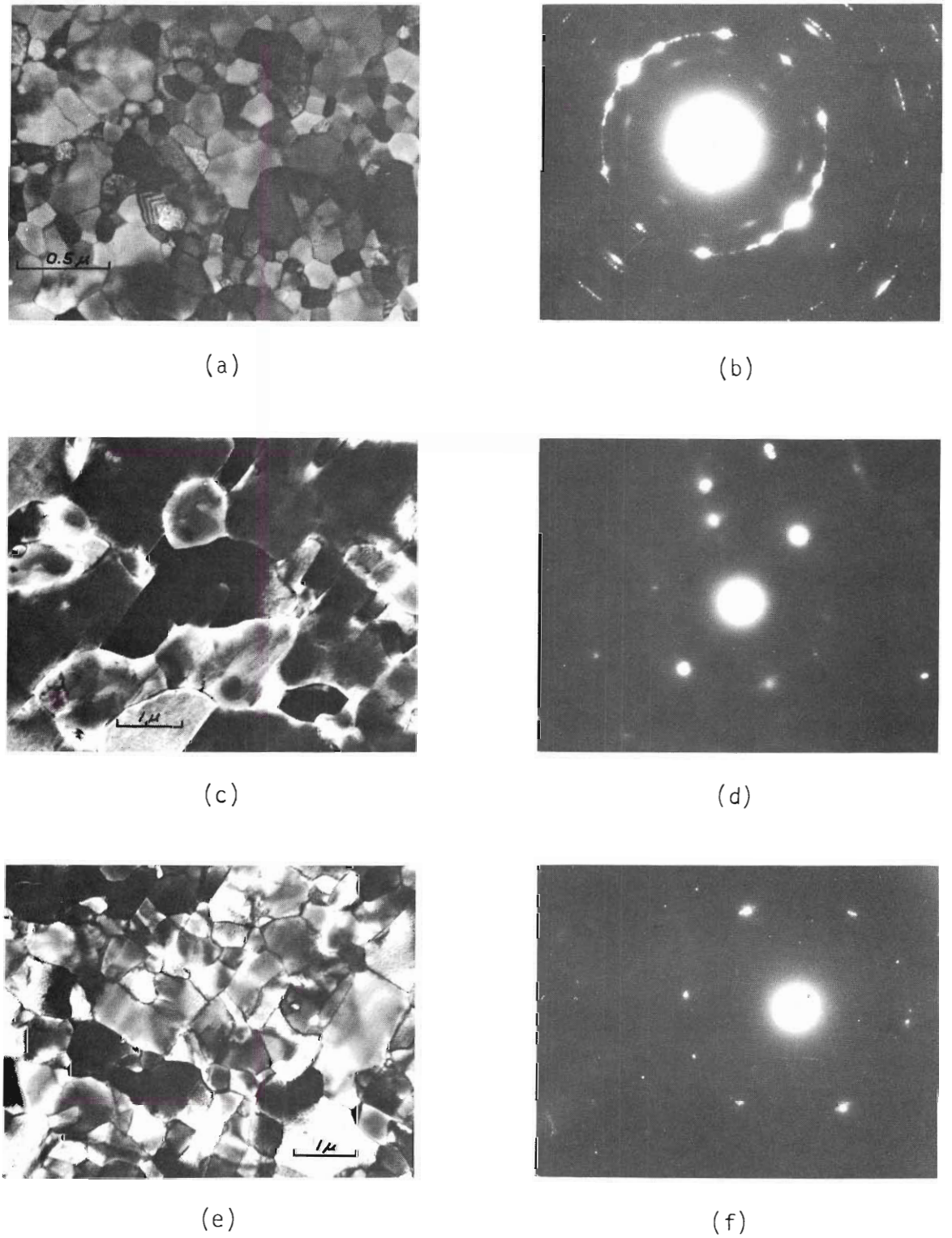

Figure 36. Typical Micrographs and SAD Patterns from Iron Films Formed on (011) Plane Faces of NaCl at Different Temperatures; (a) and (b) from Run 46 (401°C); (c) and (d) from Run 41 (434°C); (e) and (f) from Run 45 (489°C)

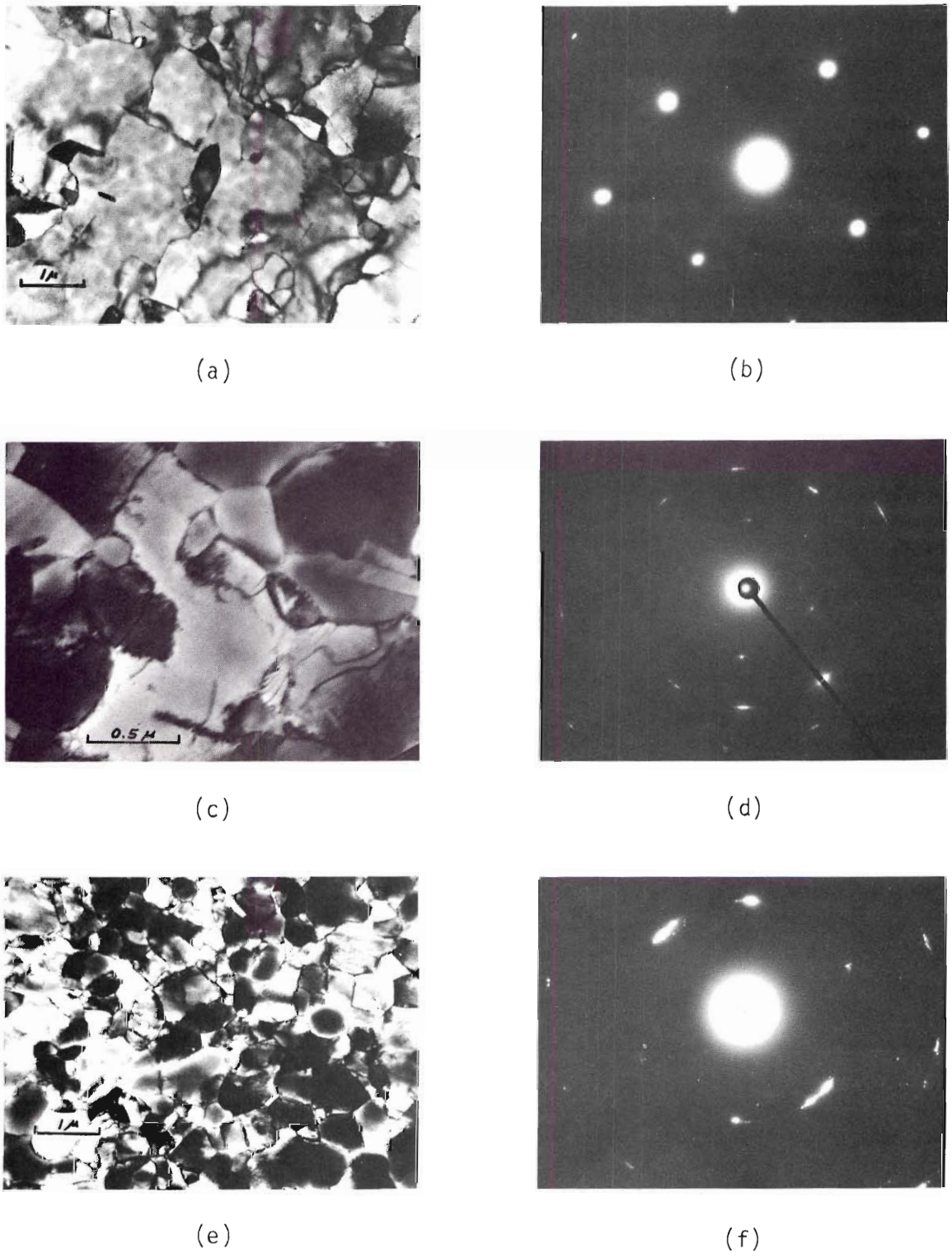

Figure 37. Typical Micrographs and SAD Patterns from Iron Films Formed on (111) Plane Faces of NaCl at Different Temperatures; (a) and (b) from Run 50 (407°C); (c) and (d) from Run 58 (446°C); (e) and (f) from Run 59 (489°C)

ing of grain orientations around the so-called preferred positions. The lowest temperature gave the best (011) epitaxy. However, it is doubtful that single crystals of the (011) type can be made without considerably more technique development. The results were much less promising than those found at the outset of the work to prepare (001) type films.

Some rather peculiar observations were made in the trials to form (111) type single crystals of iron. At the lowest substrate temperature a near single crystal film of the (001) type was formed instead of the (111) type expected on a (111) NaCl face. At the intermediate temperature, grains as large as 1 square micron of a (311) film plane orientation were formed in addition to the (111) type. The grains had a 10° angle of scatter around the two zone axes as evidenced by the arcing of the reflections in the SAD patterns. At the highest temperature, (120) plane oriented grains were common as well as the (111) type. Again the reflections were arced. The variety of readily formed crystal orientations on the (111) rock salt surfaces indicates that it would be extremely difficult to form a single crystal iron film of the (111) type.

C. Analysis of the Reacted Single Crystal Films

This section contains the experimental results and their discussion for the reactions and treatments given the iron single crystal films. The experiments were outlined in the Reaction Schedule of Table 3.

The physical picture of the reacted films will be presented first in subsection C.1. This subsection will contain typical micrographs from each experiment. It will also include summary tables and graphs which treat the data extracted from all the electron micrographs taken from reacted

specimens.

The next subsection (C.2) will treat all the electron diffraction data obtained from the reacted iron films. This topic will be covered prior to all other discussion in order to emphasize what reaction products do form and to simplify the later treatments. The remaining subjects will be covered in an order relating to their occurrence in the physical phenomena studied.

The nucleation of the first formed solid product will be considered in subsection C.3. The remaining subsections will discuss the following topics: the morphology of the growing precipitate particles, the mechanism of particle growth, the effect of CO pressure on the development of the solid phase reaction, the experiments of extended duration, and the additional information obtained from extraction replicas.

1. Electron Micrographs and Reduced Data

Typical electron micrographs have been selected to represent each Reaction listed in the schedule of Table 3. At the end of each group of micrographs a tabulation is presented containing the pertinent data regarding each micrograph and SAD pattern taken of the specimens for that reaction. A considerable amount of information is given in the tables for each plate. The entries in the tables warrant some explanation. The first column contains the assigned photographic plate number of the original negative. The next pair of columns contain the image magnifications on the original negative and on the 8" x 10" print actually used for making measurements. All the prints are on file in the Metallurgy Department. The next column gives the number of inches in the 8" x 10" print which corresponds to 1 micron on the sample surface. The following column indi-

cates the number of square inches corresponding to 1 square micron of the sample on the 8" x 10" print. This information is followed by the "Rotation Angle" specifing the number of degrees which the specimen image has been rotated with respect to the SAD pattern. The photographic plates were graded on an A through F scale based on the combined merits of the information contained in them and on their photographic quality. These grades are presented in column 7. Column 8 contains the values for the areas pictured in each micrograph in square microns. The next column lists the number of precipitate particles pictured in each micrograph. This information is followed by the precipitate density calculated as precipitates per square micron of the iron film examined. Column 11 lists the size range of the precipitates pictured in the micrograph as based on their projected areas. The last column presents the distance ranges between adjacent precipitate particles pictured in the micrographs.

Following the presentation of the micrographs and reduced data tables, summary tables and graphs are presented. These will facilitate later discussions.

Electron micrographic data from Reactions 14 and 16 are not included in the following presentation. The information regarding Reaction 16 was presented in Section B, and that for Reaction 14 will be treated in subsection C.7.

a. The Precipitate Size Measurement. All the precipitate crystals and the precipitate nuclei which were pictured in the electron micrographs of this work were measured. Since it was not possible to calculate a volume for the precipitates, the projected area of each particle in the plane of the film was measured. The purpose of this effort was to illustrate the

varying degrees of attack sustained by the iron single crystal films under the different reaction conditions. The iron films were very thin in comparison with the mean film plane dimension of the precipitate particles. The transmission micrographs indicated the precipitates to be platelets in the plane of the foil. The extraction replicas also indicated the particles to approximate plates embedded in the film matrix. The particle area should then be roughly proportional to the actual particle volume. The sizes of the particles for each individual run did vary approximately an order of magnitude. Therefore, an average of the sizes over a large number of particles per experiment was required to obtain a reasonable quantity for relative precipitate size comparisons from one experiment to another.

The precipitate sizes were measured by taking the average of three planimeter area measurements per particle made on the 8" x 10" micrograph prints. The average was reduced to the corresponding number of square microns and tabulated. For particles with sizes within the error of the planimeter measurement, the mean dimension of the precipitate was determined and the value squared and reduced to square microns.

b. The Precipitate Density Measurement. When relevant, the precipitate density was calculated for each electron micrograph taken. The operation was simply to divide the number of precipitates observed by the area of the sample pictured in each micrograph. The result then precipitates per square micron of projected area in the film plane. The "Typical" values given in the summary tabulations for each reaction do not necessarily represent the average calculated from all the micrograph values. These were not generally representative. Large areas are required for proper analysis.

Therefore, the "Typical" values represent judgments which were made based on extensive sample viewing in the electron microscope as well as the calculations from the micrographs. For the reactions in which only a few precipitates were observed and for reactions in which the precipitates were very small nuclei, considerable error may be expected.

c. Micrographs and Reduced Data Tables. The typical transmission electron micrographs of the iron single crystals examined in the reaction studies are presented in the following pages (Figures 38 through 100). The micrographs for individual experiments are grouped together. Each group will be preceded by a cover page stating the corresponding Reaction number and the experimental conditions. Also, each group is followed with the table of data extracted from all the micrographs taken of the samples from the experiment (Tables 4 through 17). The micrographs were made in a JEM 7 instrument using a 100 KV accelerating potential.

Reaction 1

(250°C, 1,000 μ CO, 1 hour)

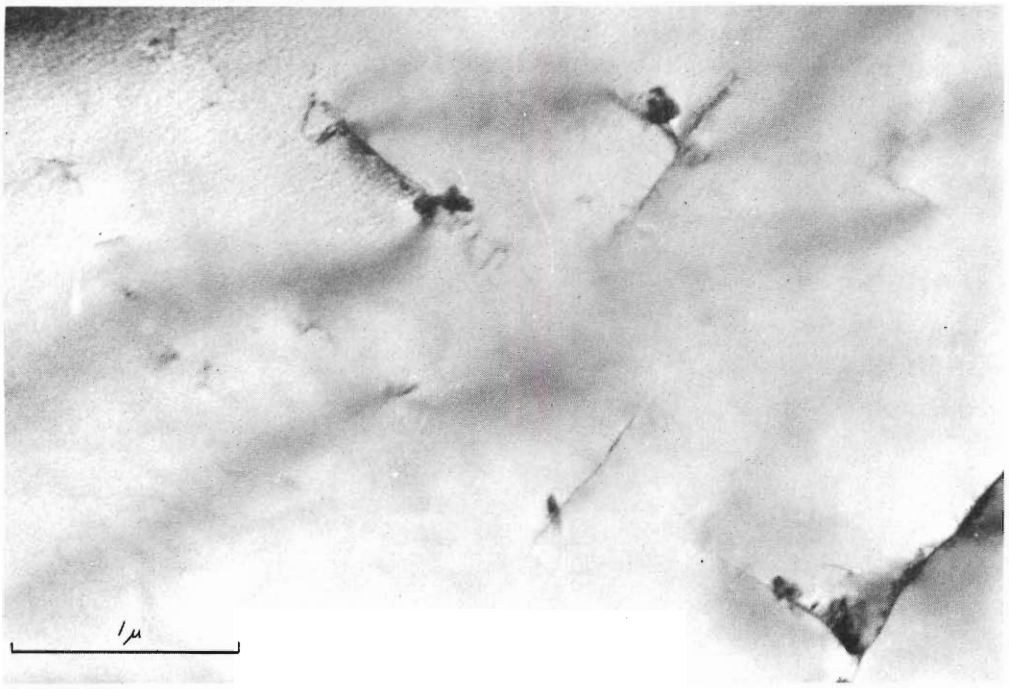

Figure 38. Reaction Product Nucleation Sites

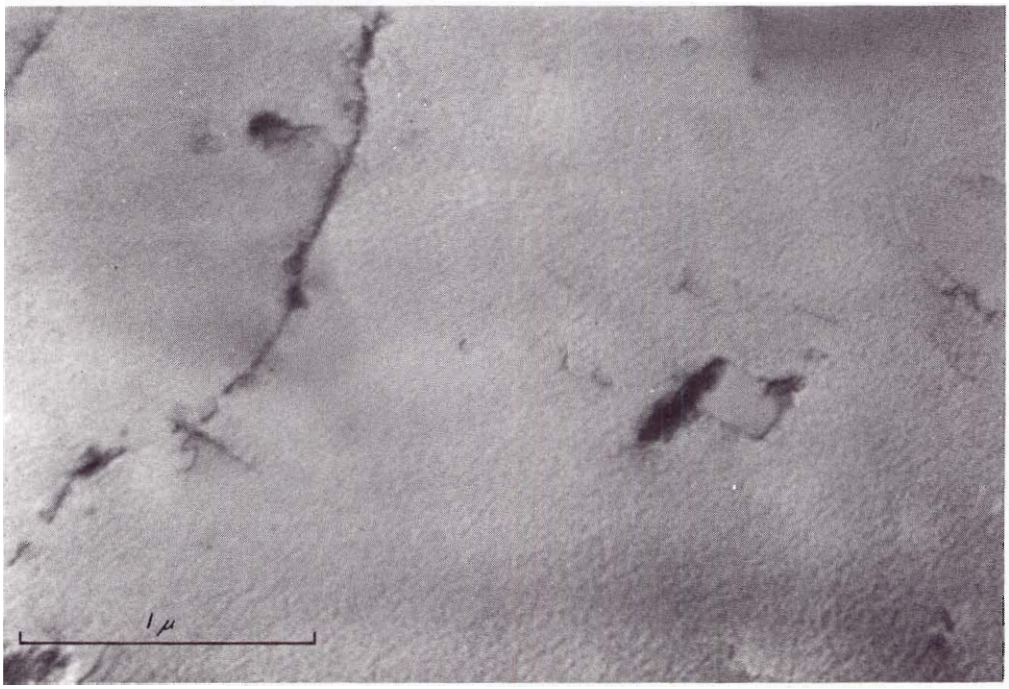

Figure 39. Reaction Product Nucleation Sites

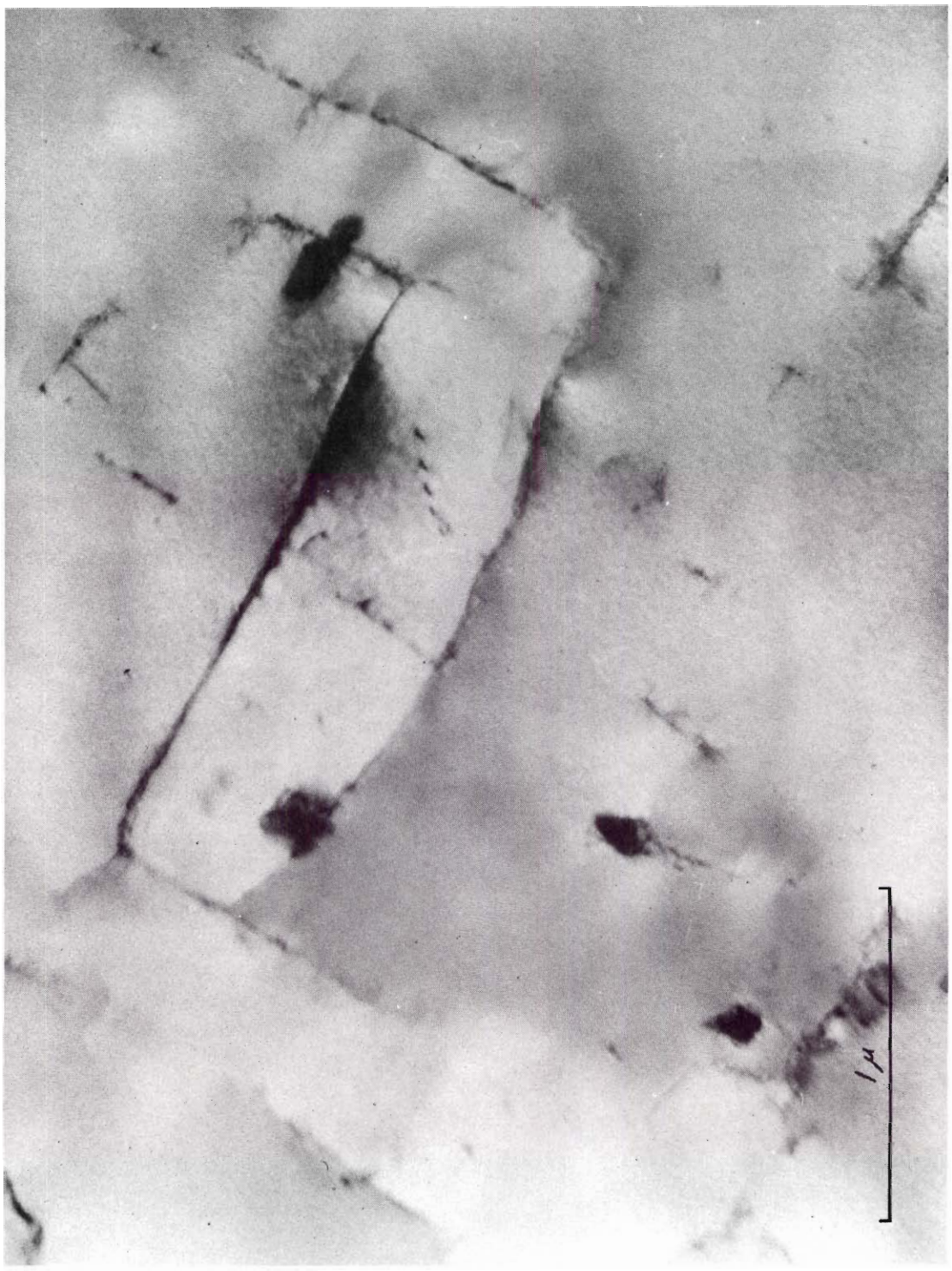

Figure 40. Reaction Product Nucleation Sites

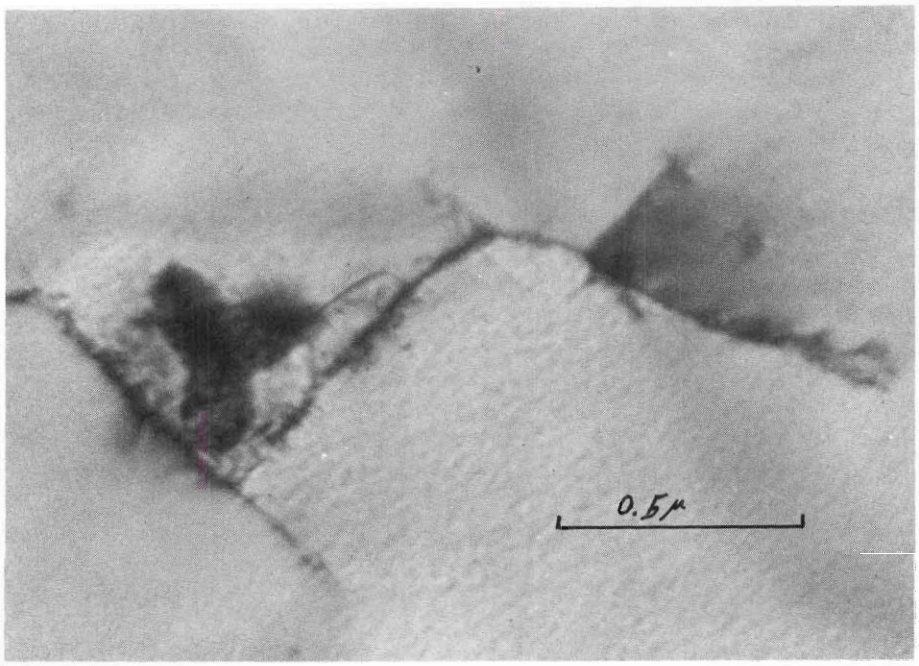

Figure 41. Reaction Product Nucleation Sites

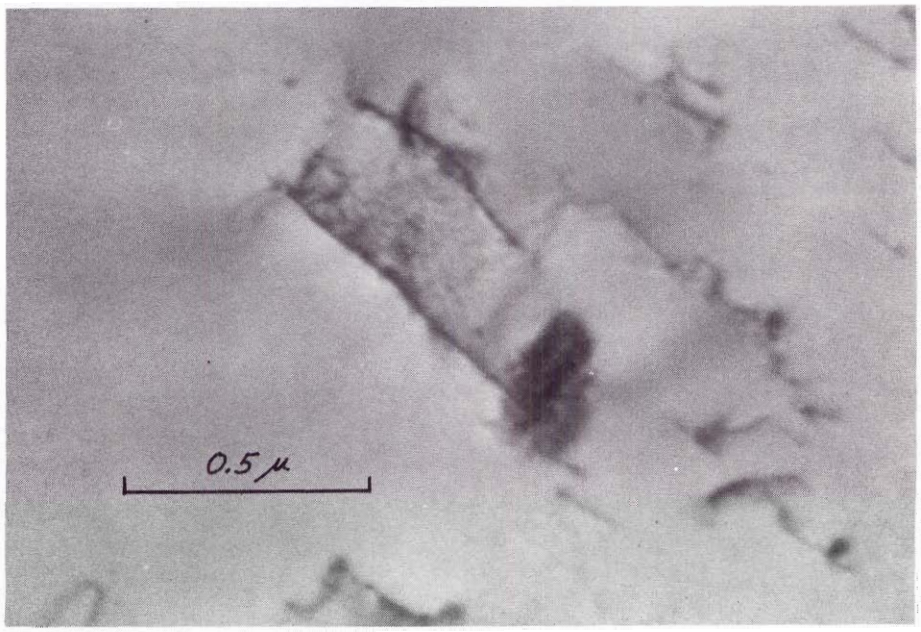

Figure 42. Reaction Product Nucleation Sites

Figure 43. Reaction Product Nucleation Sites

Table 4. Run at 250°C for One Hour at 1,000 μ CO (Run 60)

Plate No.	Magnification Plate	Magnification Print	1 μ (in)	1 μ^2 (in^2)	Rotation Angle (°cl/ccl)	Plate Grade	Plate Area (μ^2)	No. of Ppts.	Ppt. Density $\frac{\text{Ppts.}}{\mu^2}$	Ppt. Size Range (μ^2)	Distance Range Between Ppts. (μ)
5325	29,000	74,000	2.9	8.4	32.5 ccl	A+	7.7	3	0.39	0.006 to 0.065	0.50 to 1.0
5326	24,000	62,000	2.4	5.8	29.5 ccl	B	11	6	0.55	0.008 to 0.022	0.30 to 0.90
5327	24,000	62,000	2.4	5.8	29.5 ccl	A	11	4	0.36	0.009 to 0.034	0.60 to 1.4
5328	26,000	67,000	2.6	6.8	31 ccl	A	9.5	6	0.63	0.006 to 0.035	0.50 to 1.2
5329	29,000	74,000	2.9	8.4	32.5 ccl	B-	7.7	4	0.52	0.020	1.6
5330	24,000	62,000	2.4	5.8	29.5 ccl	B+	11	2	0.18	0.060	1.8
5331	20,000	51,000	2.0	4.0	27 ccl	A	16	6	0.38	0.005 to 0.027	0.15 to 1.3
5332	29,000	74,000	2.9	8.4	32.5 ccl	A-	7.7	1	0.13	0.014	0.80
5333	29,000	74,000	2.9	8.4	32.5 ccl	B+	7.7	5	0.65	0.003 to 0.014	0.50 to 0.90
5334	24,000	62,000	2.4	5.8	29.5 ccl	B	11	3	0.27	0.015 to 0.017	1.6
5335	29,000	74,000	2.9	8.4	32.5 ccl	B+	7.7	2	0.26	0.006	1.4
5336	5,900	15,000	0.59	0.35	4.3 cl	A	180	N*	--	--	1.6

Table 4. Run at 250°C for One Hour at 1,000 μ CO (Run 60) (Continued)

Plate No.	Magnification Plate	Magnification Print	1 μ (in)	1 μ^2 (in^2)	Rotation Angle (°cl/ccl)	Plate Grade	Plate Area (μ^2)	No. of Ppts.	Ppt. Density Ppts./μ^2	Ppt. Size Range (μ^2)	Distance Range Between Ppts. (μ)
5337	14,000	36,000	1.4	2.0	20.5 ccl	A	32	20	0.63	--	$\approx$1

*N - Numerous

Typical Precipitate Population Density = 0.4 ppts./μ^2
Average Precipitate Projected Area Size= 0.018 μ^2
Distance Range Between Precipitates = 0.15 to 1.8 μ

Reaction 2

(250°C, 1,000 μ CO, 2.5 hours)

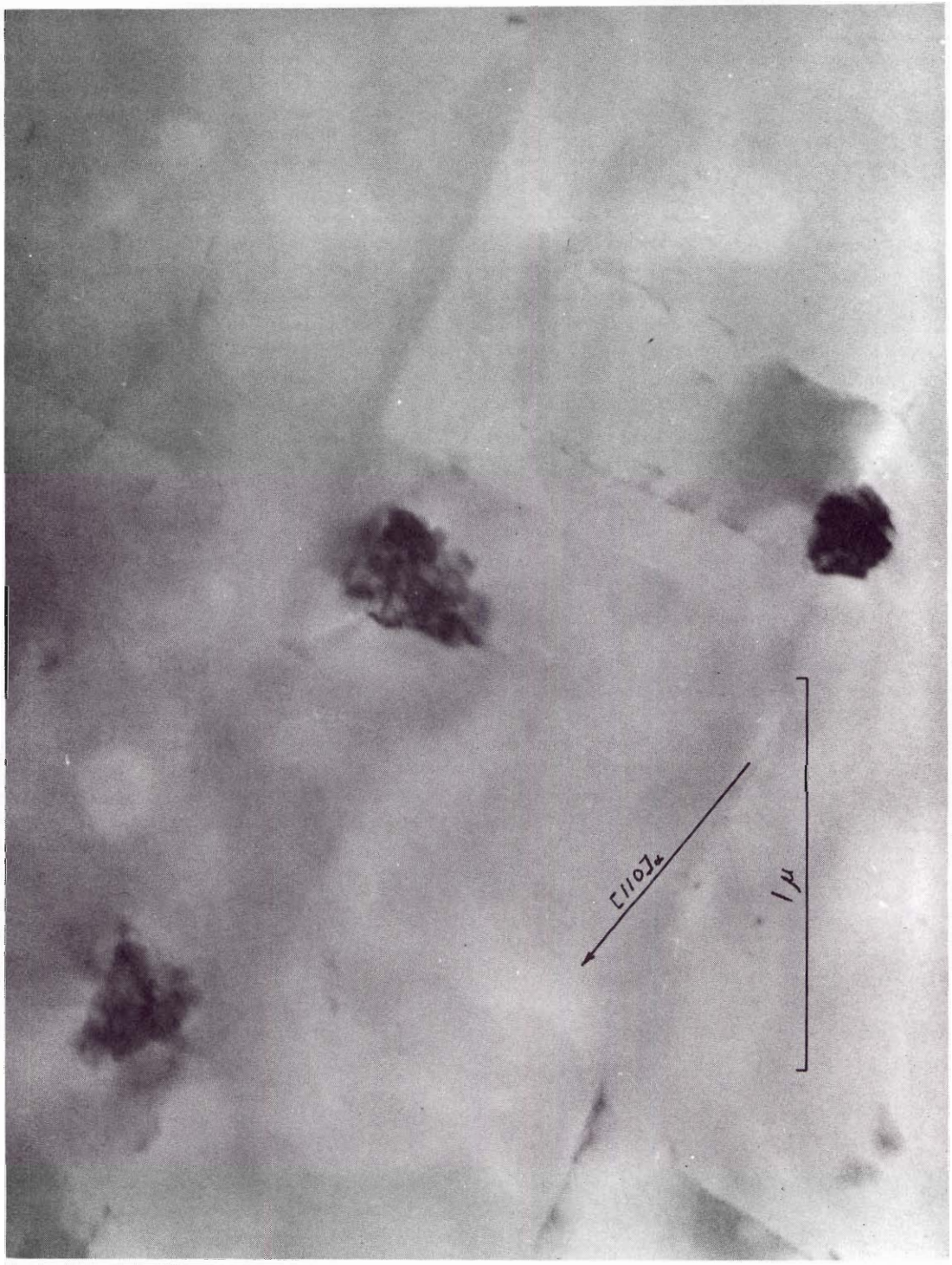

Figure 44. Cementite Nucleation Center

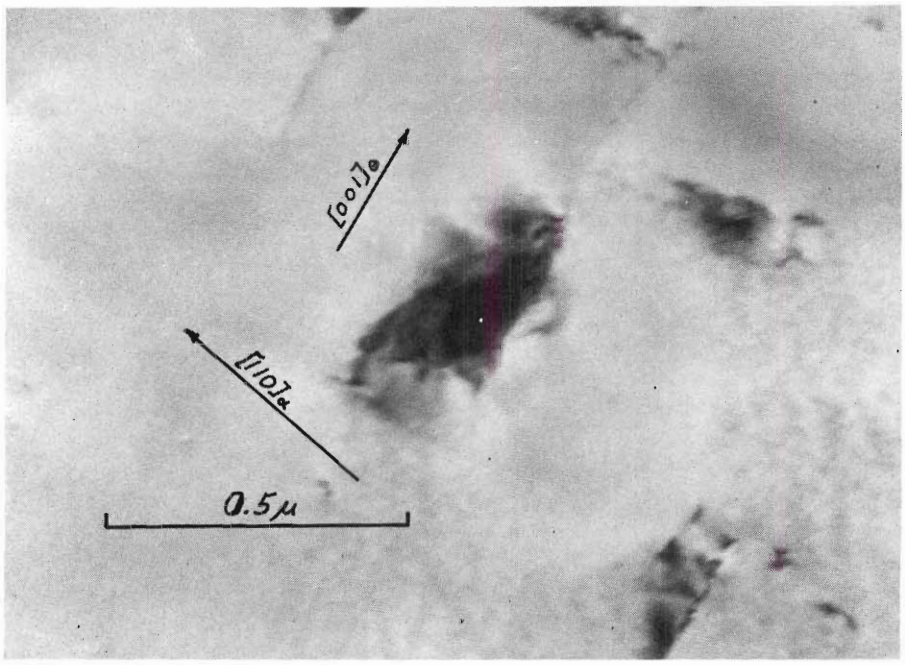

Figure 45. Cementite Nucleation Center

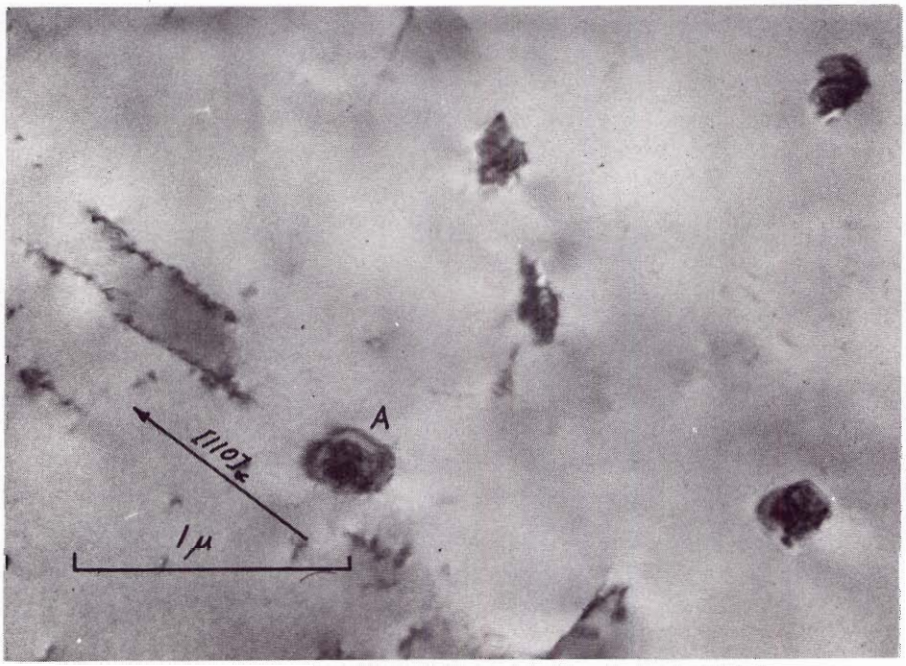

Figure 46. Cementite Nucleation Centers

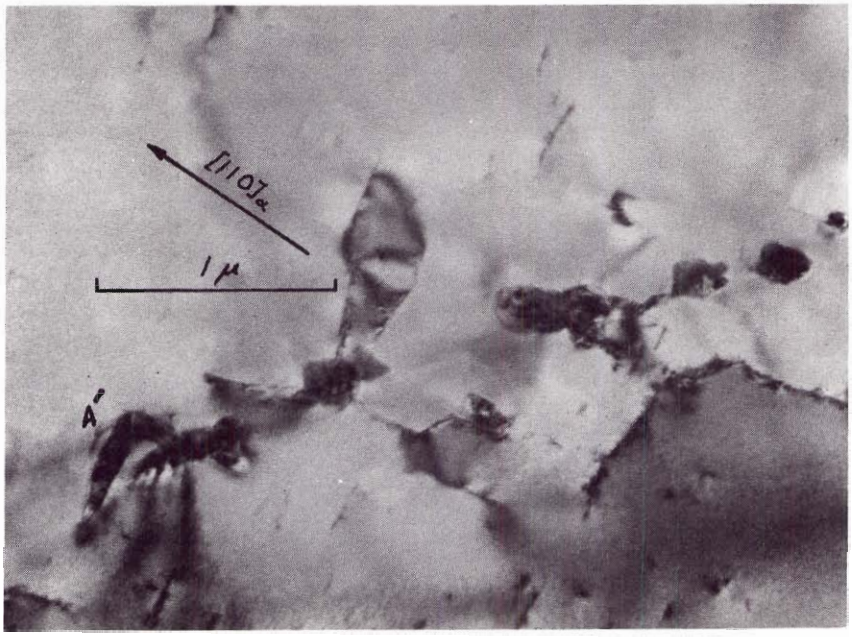

Figure 47. Cementite Nuclei

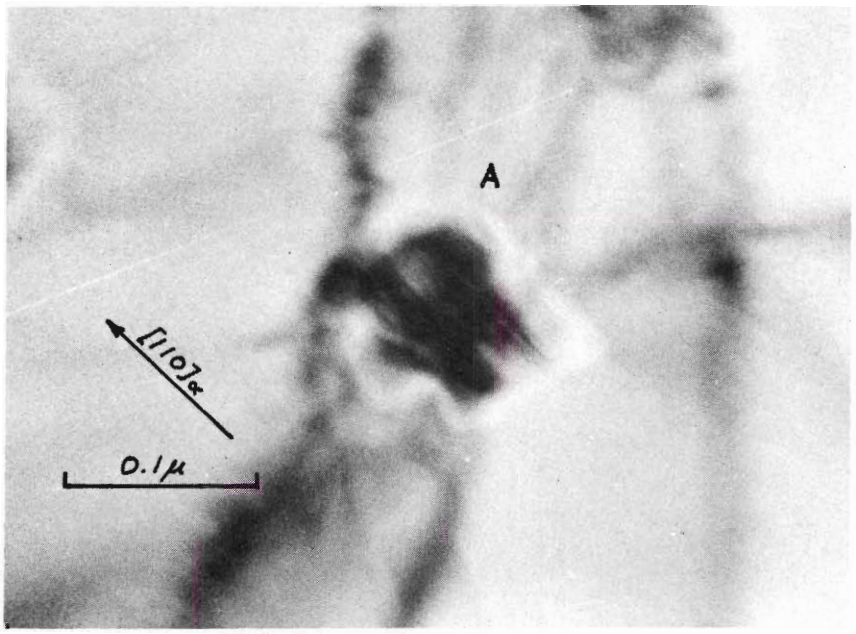

Figure 48. Cementite Nucleus

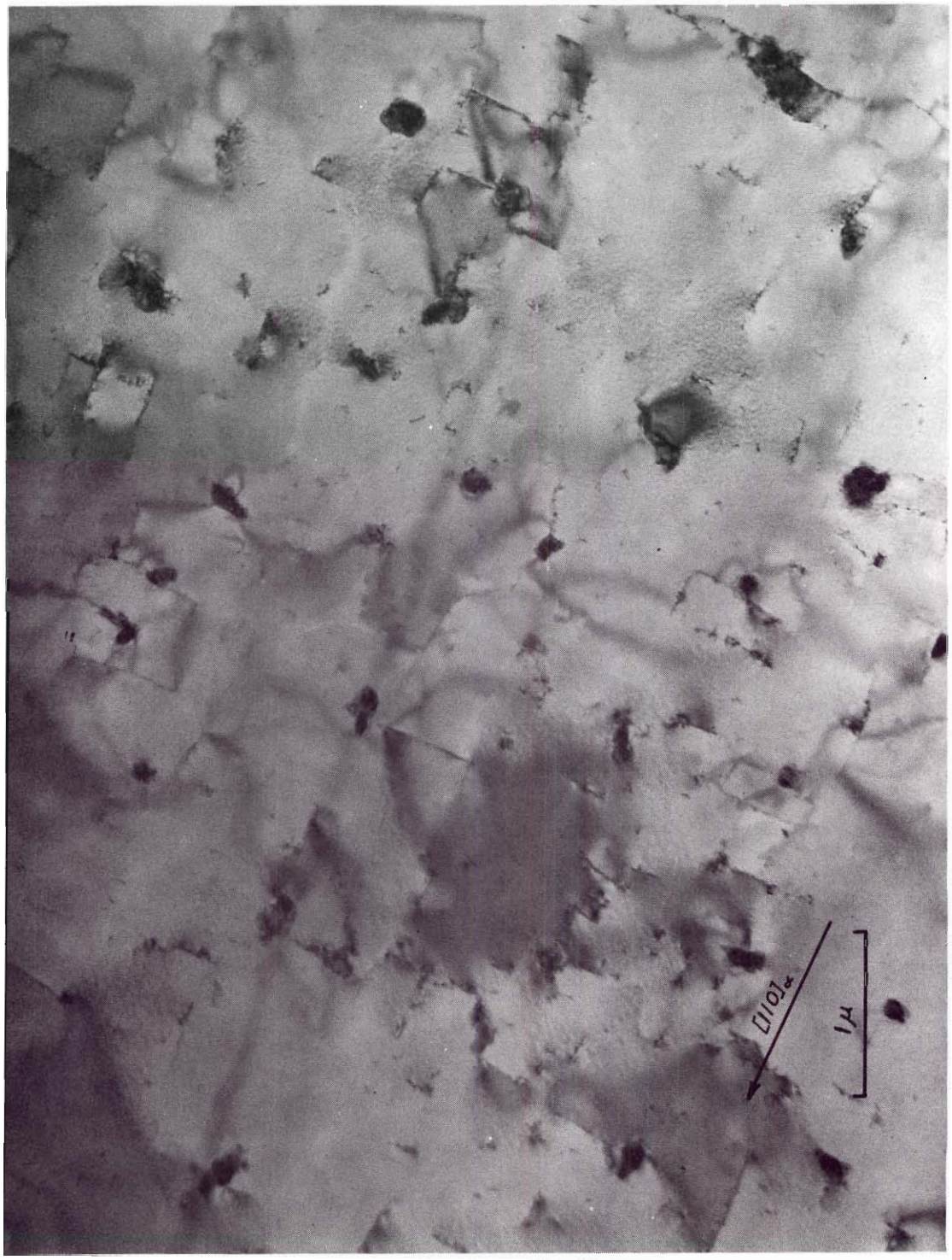

Figure 49. Cementite Nucleation Center Distribution

Table 5. Run at 250°C for Two and One-Half Hours at 1,000 μ CO (Run 61)

Plate No.	Magnification Plate	Magnification Print	1 μ (in)	1 μ^2 (in^2)	Rotation Angle (°cl/ccl)	Plate Grade	Plate Area (μ^2)	No. of Ppts.	Ppt. Density Ppts. / μ^2	Ppt. Size Range (μ^2)	Distance Range Between Ppts. (μ)
5397	SAD of 5398					C					
5398	20,000	51,000	2.0	4.0	27 ccl	A-	16	17	1.1	0.005 to 0.076	0.25 to 0.80
5399	14,000	36,000	1.4	2.0	20.5 ccl	A-	32	25	0.78	0.045 to 0.75	0.15 to 1.0
5400	16,000	41,000	1.6	2.6	23 ccl	A	25	16	0.64	0.030 to 0.040	0.25 to 2.3
5401	29,000	74,000	2.9	8.4	32.5 ccl	A	7.7	6	0.78	0.023 to 0.048	0.25 to 1.0
5402	SAD of 5403					D					
5403	20,000	51,000	2.0	4.0	27 ccl	D	16	--	--	0.010 to 0.070	0.25 to 1.0
5405	SAD of 5406					B					
5406	35,000	90,000	3.5	12	35.5 ccl	B-	5.4	2.5	0.46	0.023 to 0.037	2.0
5407	SAD of 5408					C					
5408	29,000	74,000	2.9	8.4	32.5 ccl	B	7.7	4	0.52	0.067	1.0
5409	29,000	74,000	2.9	8.4	32.5 ccl	A	7.7	4	0.52	0.023 to 0.031	0.60 to 0.80

Table 5. Run at 250°C for Two and One-Half Hours at 1,000 μ OD (Run 61) (Continued)

Plate No.	Magnification Plate	Magnification Print	1 μ (in)	1 μ^2 (in^2)	Rotation Angle (°cl/ccl)	Plate Grade	Plate Area (μ^2)	No. of Ppts.	Ppt. Density Ppts./μ^2	Ppt. Size Range (μ^2)	Distance Range Between Ppts. (μ)
5410	SAD of 5411					C+					
5411	35,000	90,000	3.5	12	35.5 ccl	B+	5.4	2	0.37	0.040 to 0.047	0.50 to 1.2
5412	SAD of 5413					C					
5413	28,000	72,000	2.8	7.8	32 ccl	A	8.3	3	0.36	0.044 to 0.073	0.90 to 1.0
5414	SAD of 5415					C					
5415	28,000	72,000	2.8	7.8	32 ccl	A	8.3	1	0.12	0.044	--
5416	12,000	31,000	1.2	1.4	17 ccl	A	46	31	0.67	--	0.25 to 1.0

Typical Precipitate Population Density = 0.60 ppts./μ^2
Average Precipitate Projected Area Size = 0.035 μ^2
Distance Range Between Precipitates = 0.15 to 2.3 μ

Reaction 3

(320°C, 1,000 μ CO, 1 hour)

Figure 50. Cementite Precipitate Particle

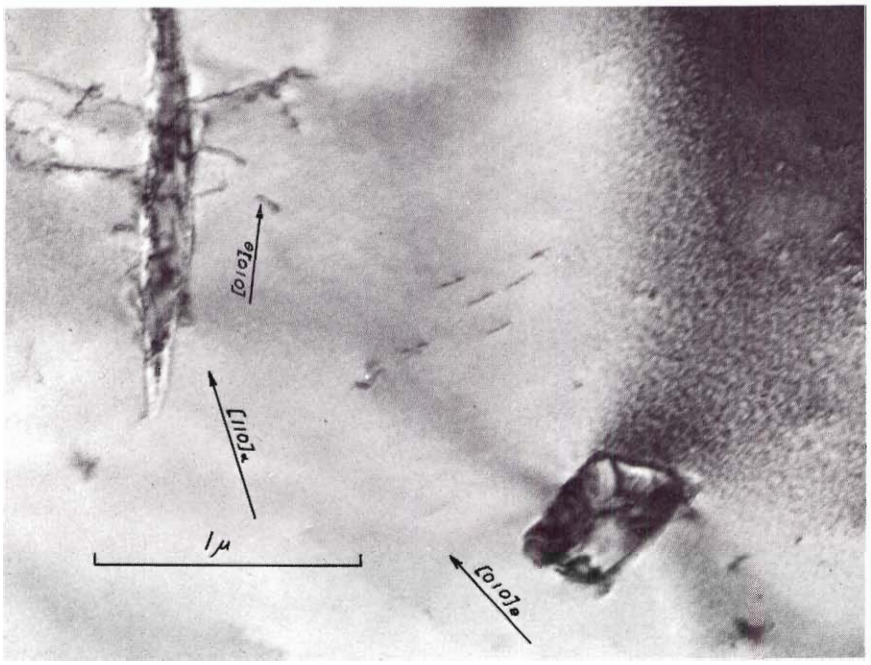

Figure 51. Cementite Precipitate Particles

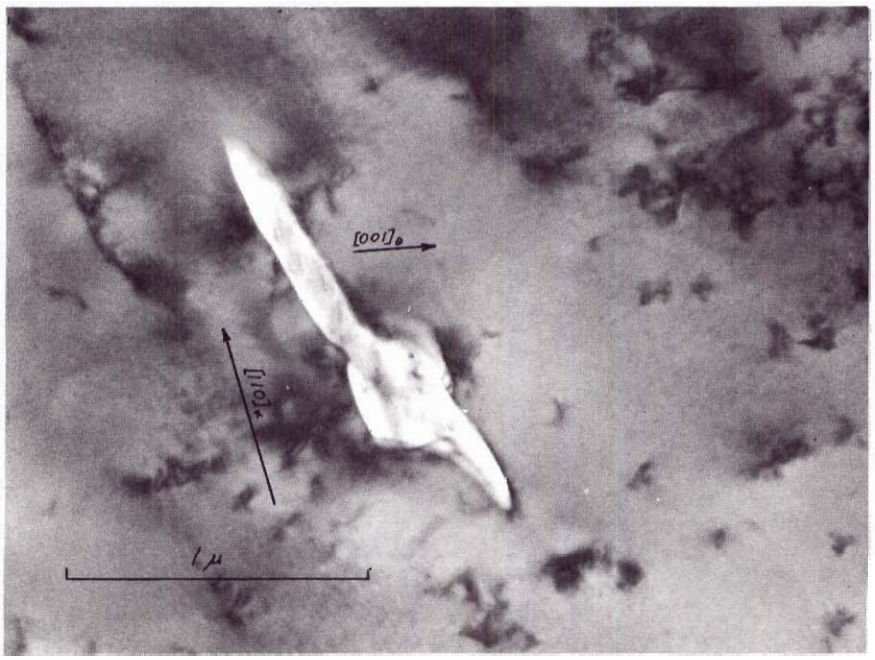

Figure 52. Faulted Cementite Precipitate Particle

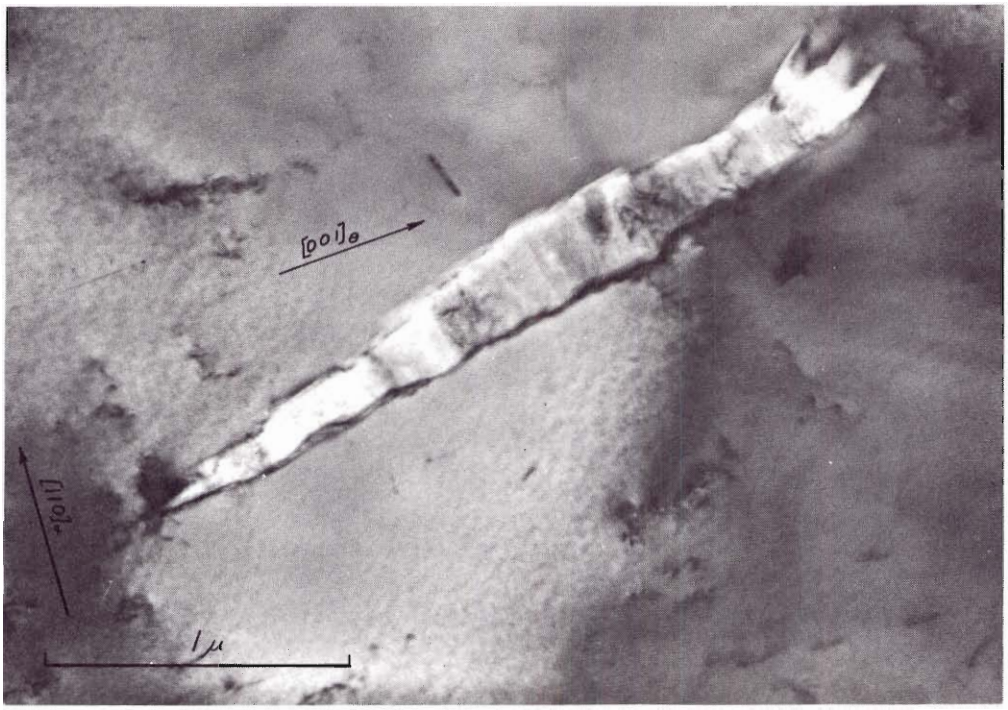

Figure 53. Faulted Cementite Precipitate Particle

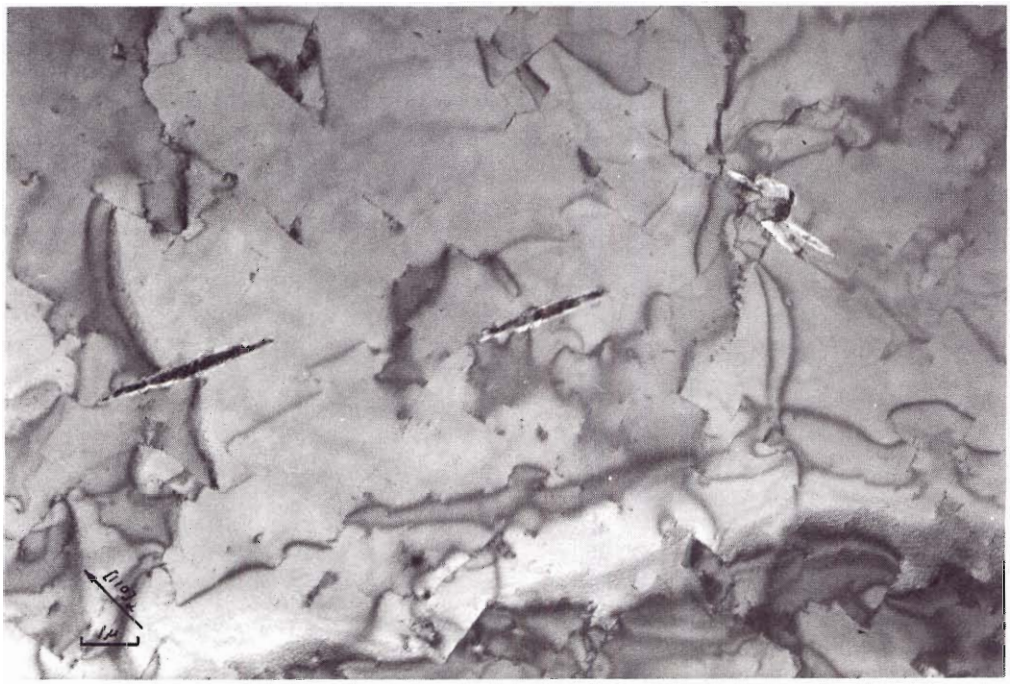

Figure 54. Cementite Precipitate Particles

Table 6. Run at 320°C for One Hour at 1,000 μ CO (Run 63)

Plate No.	Magnification Plate	Magnification Print	1μ (in)	$1\mu^2$ (in^2)	Rotation Angle (°cl/ccl)	Plate Grade	Plate Area (μ^2)	No. of Ppts.	Ppt. Density Ppts./μ^2	Ppt. Size Range (μ^2)	Distance Range Between Ppts. (μ)
5448	SAD of 5449					C-					
5449	27,000	69,000	2.7	7.8	31.5 ccl	A-	8.8	1	--	0.22	--
5450	SAD of 5451					D-					
5451	35,000	90,000	3.5	12	35.5 ccl	C-	5.4	1	--	0.31	--
5452	SAD of 5453					A					
5453	27,000	69,000	2.7	7.8	31.5 ccl	A-	8.8	1	--	0.60	--
5454	SAD of 5455					A					
5455	24,000	62,000	2.4	5.8	29.5 ccl	B	11	2	--	0.19 to 0.23	1.4
5456	SAD of 5455					B+					
5457	3,600	9,200	0.36	0.13	$\approx$0	A	500	10	0.020	0.15 to 0.45	3.5 to 6.9
5458	3,600	9,200	0.36	0.13	$\approx$0	B+	500	15	0.030	0.10 to 0.38	2.8 to 5.3
5459	SAD of 5460					A+					
5460	45,000	120,000	4.5	20	40 ccl	B+	3.2	1	--	0.41	--
5461	SAD of 5460					B					

Table 6. Run at 320°C for One Hour at 1,000 μ CO (Run 63) (Continued)

Plate No.	Magnification Plate	Magnification Print	1 μ (in)	1 μ^2 (in^2)	Rotation Angle (°cl/ccl)	Plate Grade	Plate Area (μ^2)	No. of Ppts.	Ppt. Density Ppts. / μ^2	Ppt. Size Range (μ^2)	Distance Range Between Ppts. (μ)
5462	4,700	12,000	0.47	0.22	2.2 cl	A	290	6	0.021	0.36 to .76	5 to 5.9
5463	4,700	12,000	0.47	0.22	2.2 cl	A	290	4	0.014	0.40 to 0.80	0.2 to 4
5464	27,000	69,000	2.7	7.3	31.5 ccl	B	8.8	2	--	0.40 to 0.45	0.2
5465	24,000	62,000	2.4	5.8	29.5 ccl	B+	11	1	--	0.47	--
5466	St. P.	62,000	2.4	5.8	29.5 ccl	B+	11	1	--	0.47	--

Typical Precipitate Population Density = 0.025 ppts./μ^2
Average Precipitate Projected Area Size = 0.37 μ^2
Distance Range Between Precipitates = 1.4 to 7 μ

Reaction 4

(350°C, 1,000 μ CO, 1 hour)

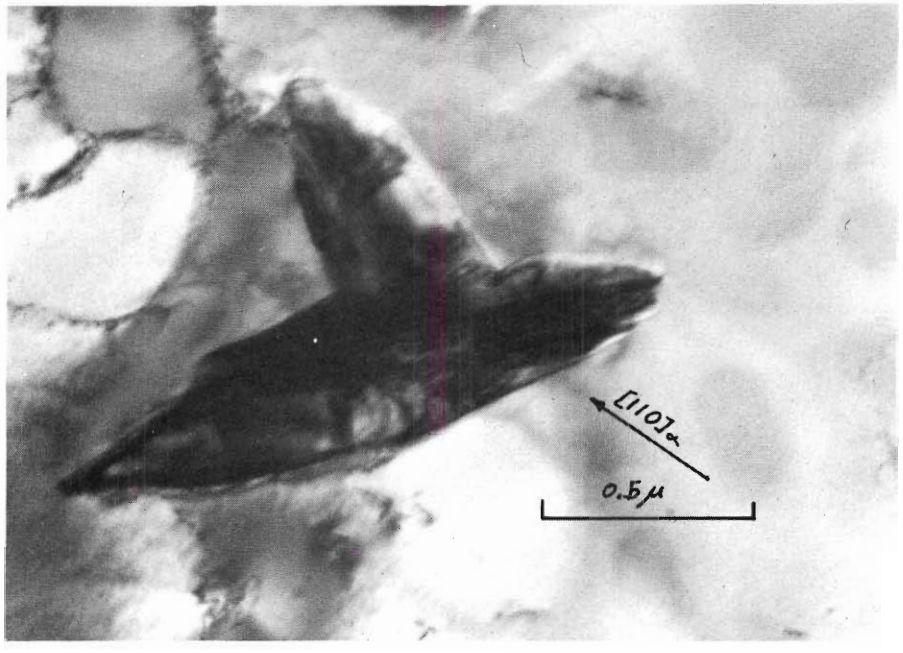

Figure 55. Faulted Cementite Precipitate Particle

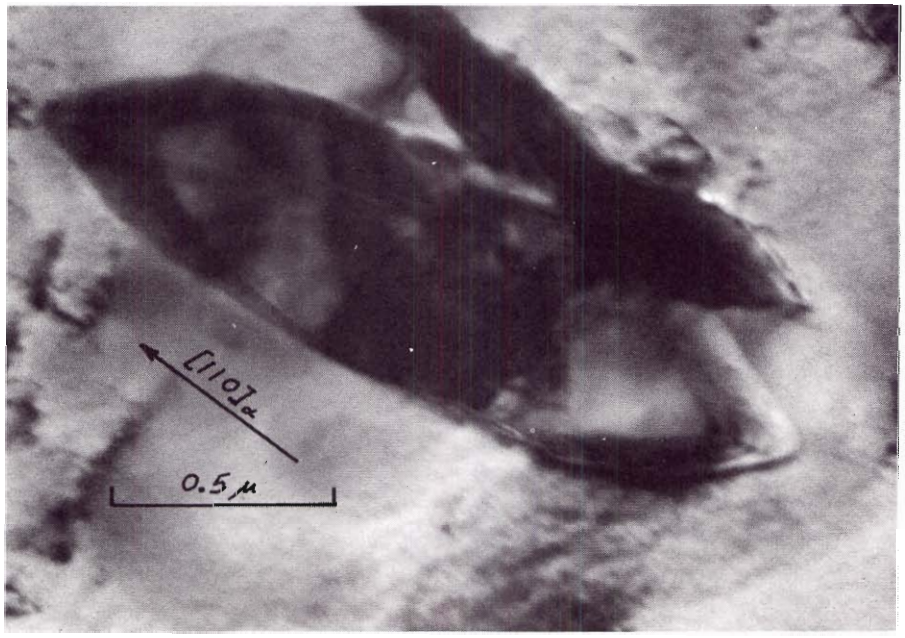

Figure 56. Cementite Precipitate Particle

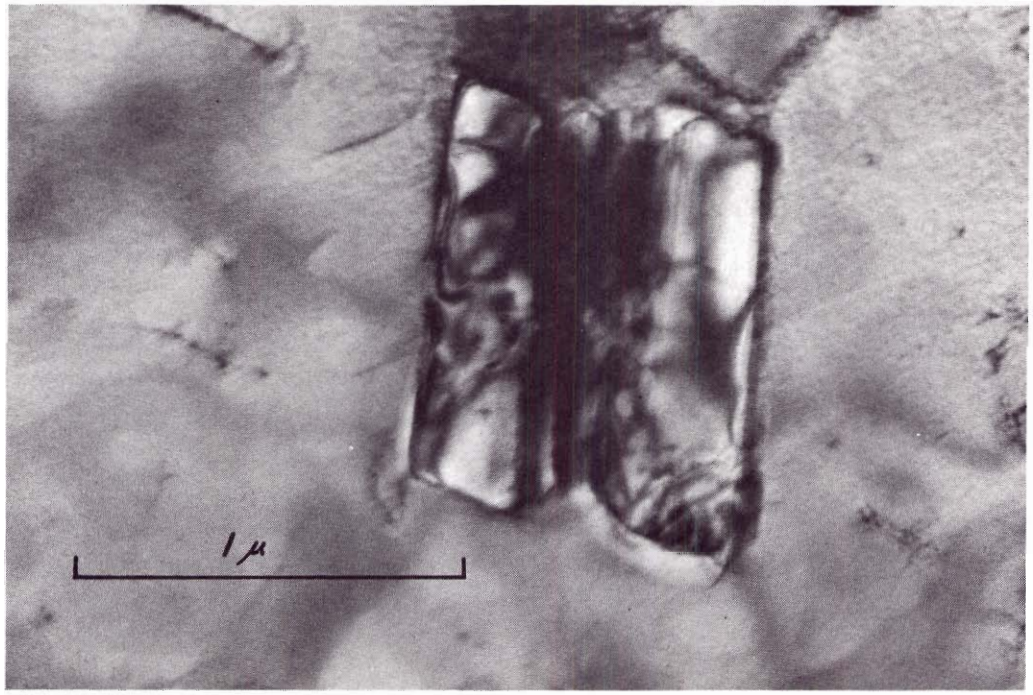

Figure 57. Faulted Cementite Precipitate Particle

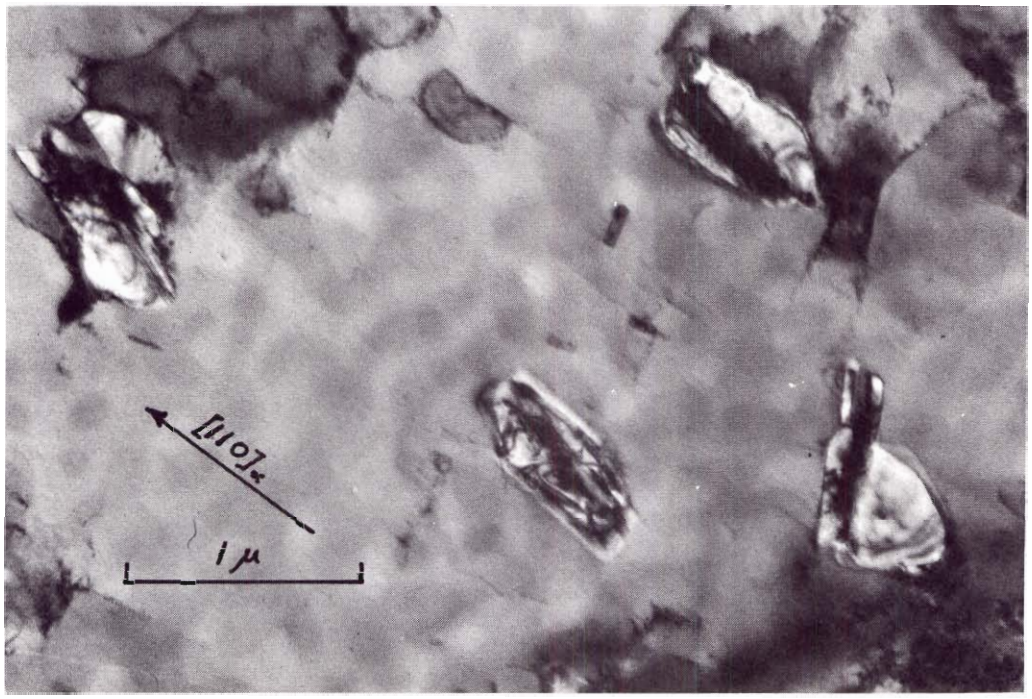

Figure 58. Cementite Precipitate Particles

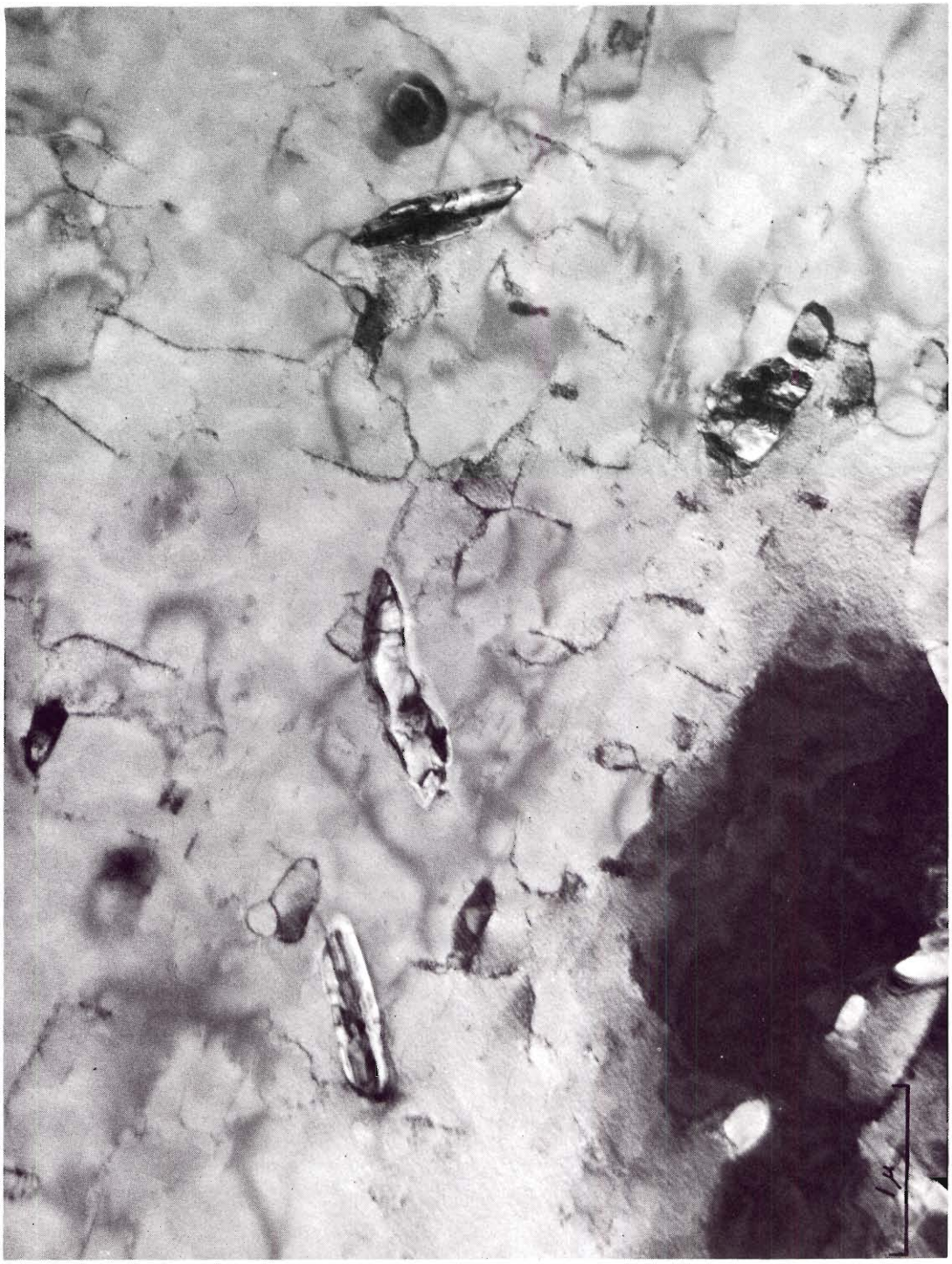

Figure 59. Distribution of Cementite Particles

Table 7. Run at 350°C for One Hour at 1,000 μ CO (Run 49)

Plate No.	Magnification Plate	Print	1 μ (in)	1 μ^2 (in^2)	Rotation Angle (°cl/ccl)	Plate Grade	Plate Area (μ^2)	No. of Ppts.	Ppt. Density Ppts. / μ^2	Ppt. Size Range (μ^2)	Distance Range Between Ppts. (μ)
5013	25,000	64,000	2.5	6.3	30.5 ccl	A	10	1	--	0.52	--
5014	SAD of 5013					C					
5015	35,000	90,000	3.5	12.0	35.5 ccl	B	5.4	1	--	--	--
5016	26,000	67,000	2.6	6.8	31 ccl	A	9.5	1	--	0.87	--
5017	SAD of 5016					D					
5018	26,000	67,000	2.6	6.8	31 ccl	C	9.5	1	--	0.98	--
5019	SAD of 5018					B+					
5020	SAD of 5021					A+					
5021	43,000	110,000	4.3	19.0	39 ccl	C	3.4	1	--	0.74	--
5022	29,000	74,000	2.9	8.4	32.5 ccl	B+	7.7	1	--	0.56	--
5023	27,000	69,000	2.7	7.3	31.5 ccl	B+	8.8	1	--	0.88	--
5024	SAD of 5023					D					
5025	23,000	59,000	2.3	5.3	29 ccl	A-	12	1	--	--	--
5026	16,000	41,000	1.6	2.6	23 ccl	A	25	1	< 0.04	0.81	--
5027	SAD of 5026					C-					
5028	16,000	41,000	1.6	2.6	23 ccl	B	25	1	< 0.04	0.56	

Table 7. Run at 350°C for One Hour at 1,000 μ CO (Run 49)
(Continued)

Plate No.	Magnification Plate	Magnification Print	1 μ (in)	1 μ^2 (in^2)	Rotation Angle (°cl/ccl)	Plate Grade	Plate Area (μ^2)	No. of Ppts.	Ppt. Density Ppts./μ^2	Ppt. Size Range (μ^2)	Distance Range Between Ppts. (μ)
5029	20,000	51,000	2.0	4.0	27 ccl	A	16	1	—	0.88	--
5030	12,000	31,000	1.2	1.4	17 ccl	A+	46	4	0.087	0.19 to 0.33	0.8 to 2.0
5031	29,000	74,000	2.9	8.4	32.5 ccl	B+	7.7	1	--	0.40	--
5032	DF of 5035		1.2	1.4	17 ccl	A	46	4.5	0.098	0.25 to 0.37	0.7 to 1.2
5033	DF of 5035		1.2	1.4	17 ccl	A	46	4.5	0.098	0.25 to 0.37	0.7 to 1.2
5034	DF of 5035		1.2	1.4	17 ccl	A	46	4.5	0.098	0.25 to 0.37	0.7 to 1.2
5035	12,000	31,000	1.2	1.4	17 ccl	A	46	4.5	0.098	0.25 to 0.37	0.7 to 1.2
5036	SAD of 5035					C+					

Typical Precipitate Population Density = 0.04 ppts./μ^2
Average Precipitate Projected Area Size = 0.53 μ^2
Distance Range Between Precipitates = 0.8 to 2 μ

Reaction 5

(350°C, 500 μ CO, 1 hour)

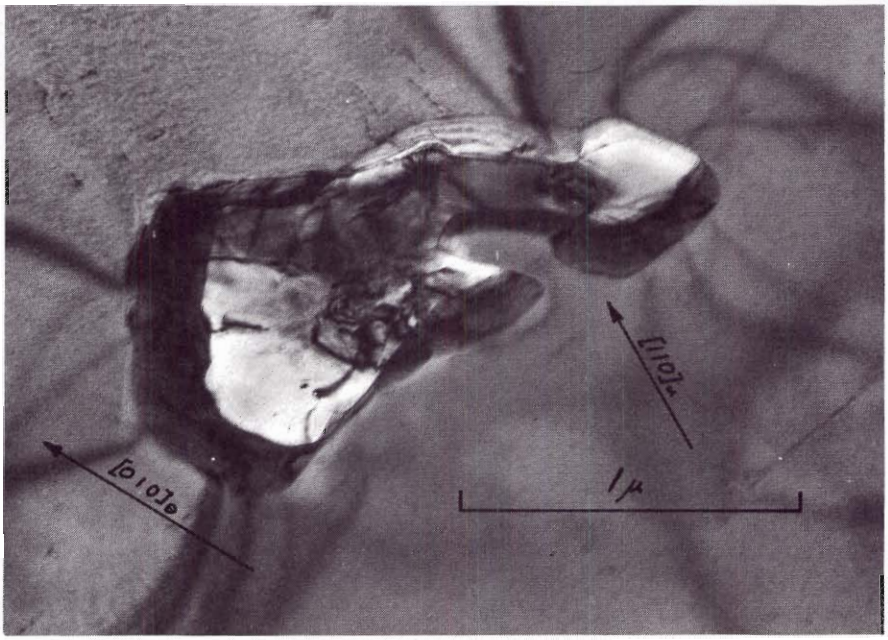

Figure 60. Cementite Precipitate Particle

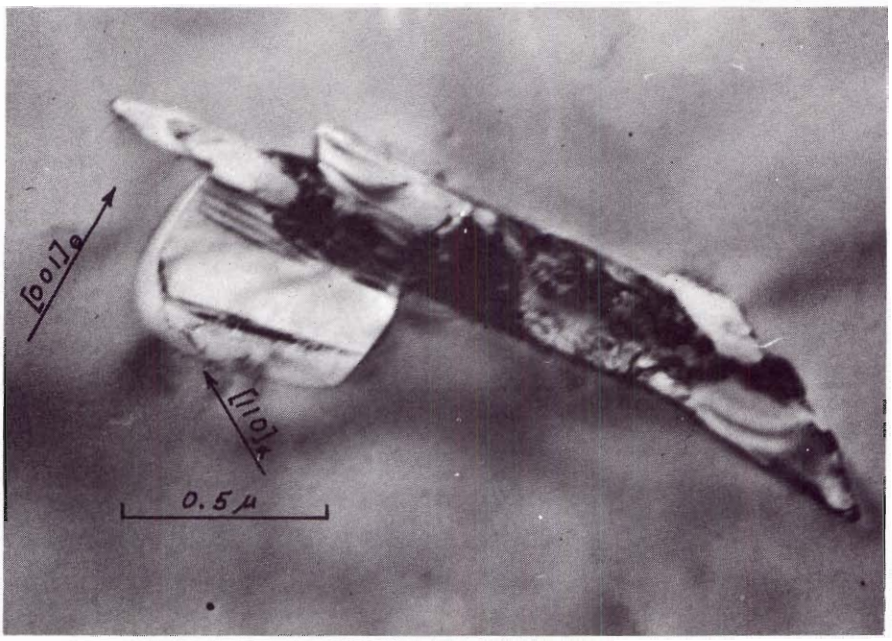

Figure 61. Cementite Precipitate Particle

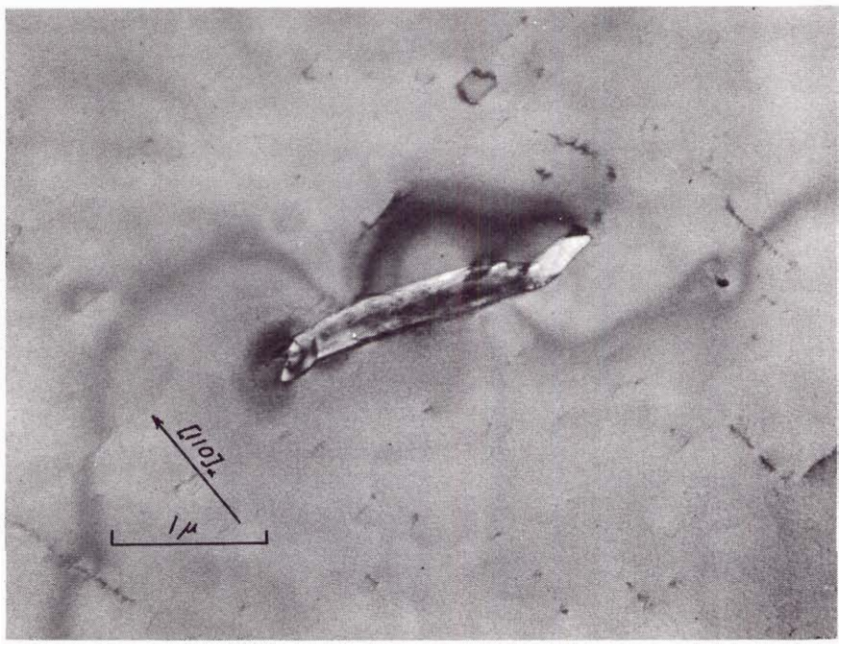

Figure 62. Cementite Precipitate Particle

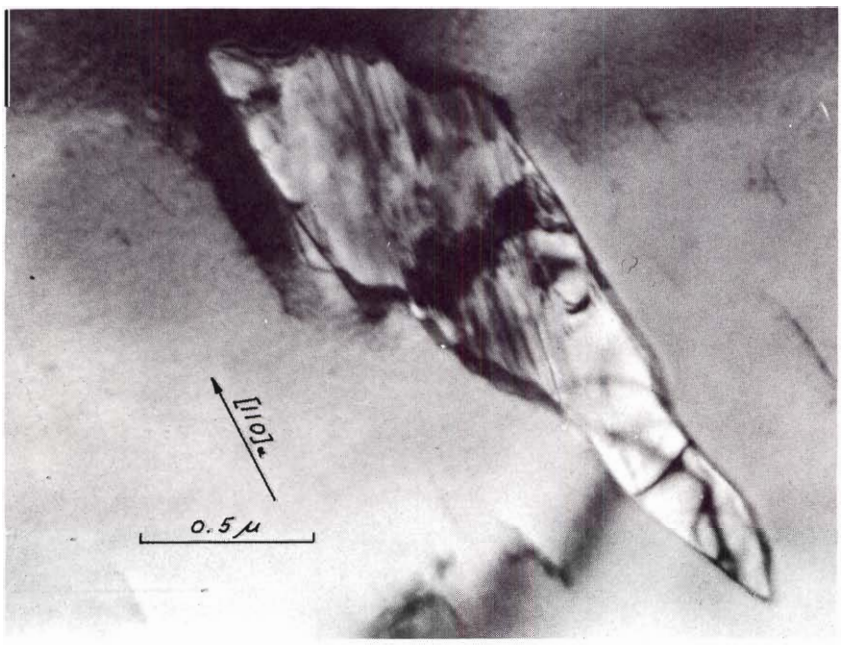

Figure 63. Striated Cementite Particle

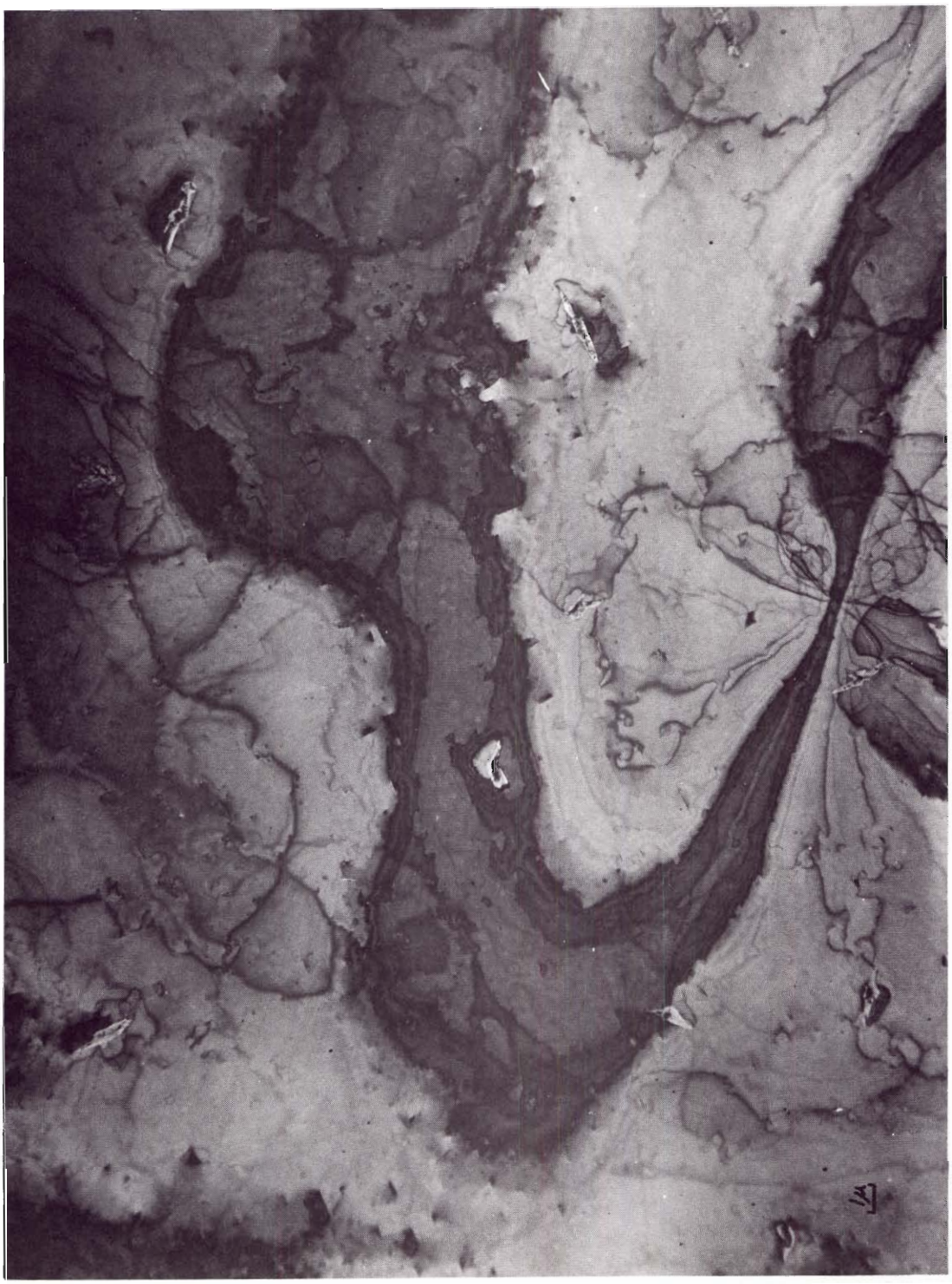

Figure 64. Cementite Particle Distribution

Table 8. Run at 350°C for One Hour at 500 μ CO (Run 62)

Plate No.	Magnification Plate	Print	1 μ (in)	1 μ^2 (in^2)	Rotation Angle (°cl/ccl)	Plate Grade	Plate Area (μ^2)	No. of Ppts.	Ppt. Density Ppts. / μ^2	Ppt. Size Range (μ^2)	Distance Range Between Ppts. (μ)
5467	12,000	31,000	1.2	1.4	17 ccl	A	46	1	--	0.46	--
5468	SAD of 5469					B					
5469	24,000	62,000	2.4	5.8	29.5 ccl	B+	11	1	--	0.70	--
5470	20,000	51,000	2.0	4.0	27 ccl	B+	16	1	--	1.17	--
5471	27,000	69,000	2.7	7.3	31.5 ccl	A	8.8	1	--	0.82	--
5472	SAD of 5473					A					
5473	20,000	51,000	2.0	4.0	27 ccl	A+	16	1	--	0.74	--
5474	20,000	51,000	2.0	4.0	27 ccl	B+	16	-	--	--	--
5475	3,600	9,200	0.36	0.13	$\approx$ 0	A-	500	6	0.012	<0.75	3.8 to 9
5476	3,600	9,200	0.36	0.13	$\approx$ 0	A-	500	7	0.014	0.20 to 0.80	1.9 to 10
5477	4,800	12,000	0.48	0.23	2.4 cl	A-	280	3	0.011	0.40 to 0.70	5.3 to 7.3
5478	4,800	12,000	0.48	0.23	2.4 cl	A	280	5	0.018	0.13 to 0.43	3.6 to 5.8
5479	4,800	12,000	0.48	0.23	2.4 cl	A-	280	4	0.014	0.30 to 0.47	2.9 to 9
5480	1,800	4,600	0.18	0.032	--	A	2,000	11	0.006	--	5.6 to 18

Table 8. Run at 350°C for One Hour at 500 μ CO (Run 62) (Continued)

Typical Precipitate Population Density	= 0.01 ppts./μ^2
Average Precipitate Projected Area Size	= 0.52 μ^2
Distance Range Between Precipitates	= 1.9 to 18 μ

Reaction 6

(350°C, 100 μ CO, 1 hour)

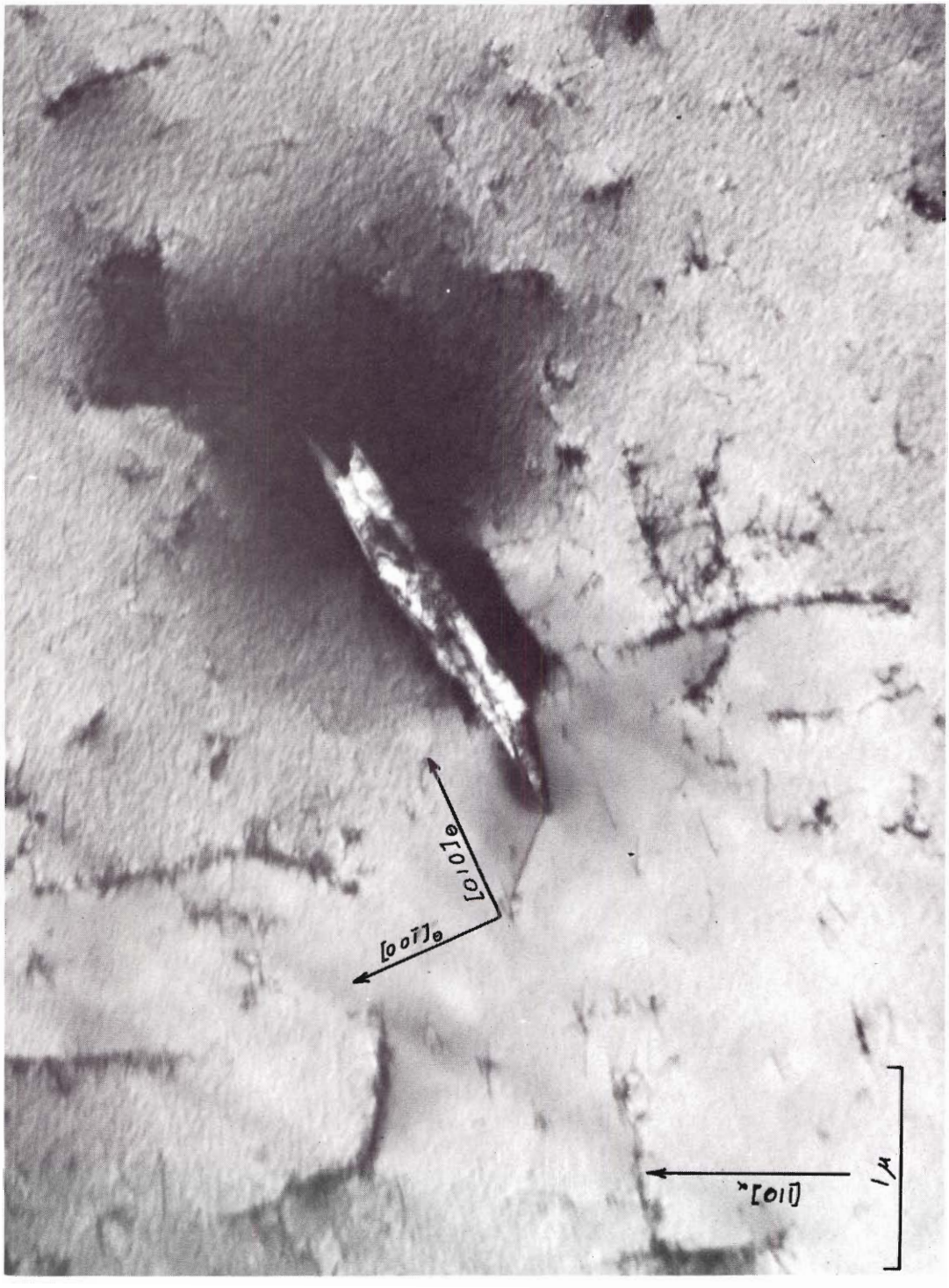

Figure 65. A Faulted Cementite Crystal

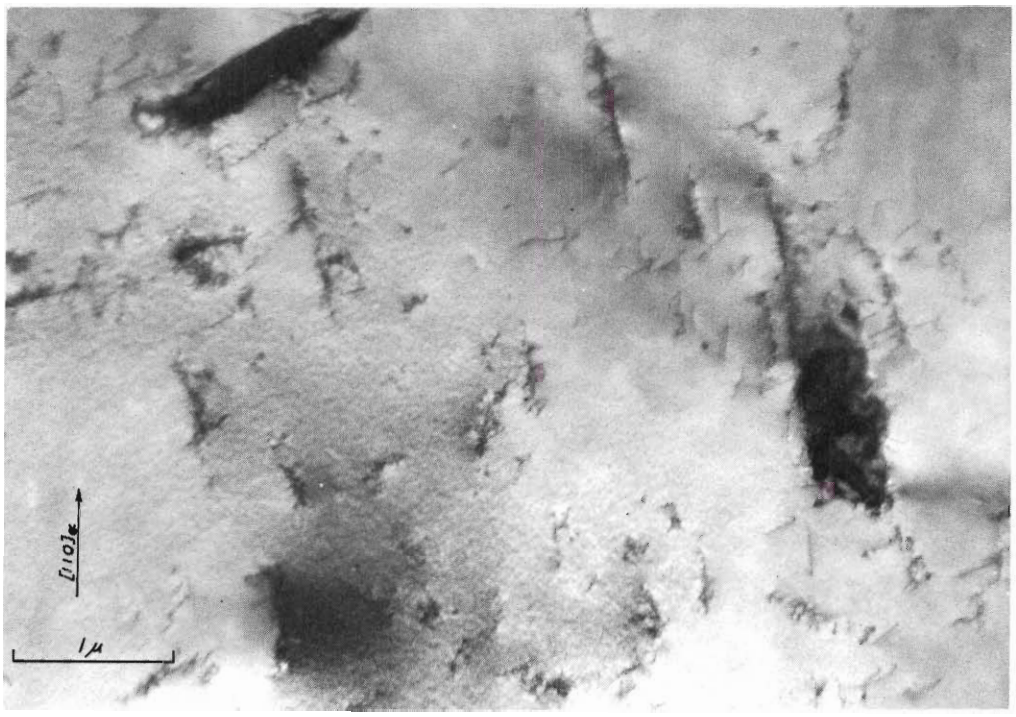

Figure 66. Cementite Formations Between Sub-boundaries

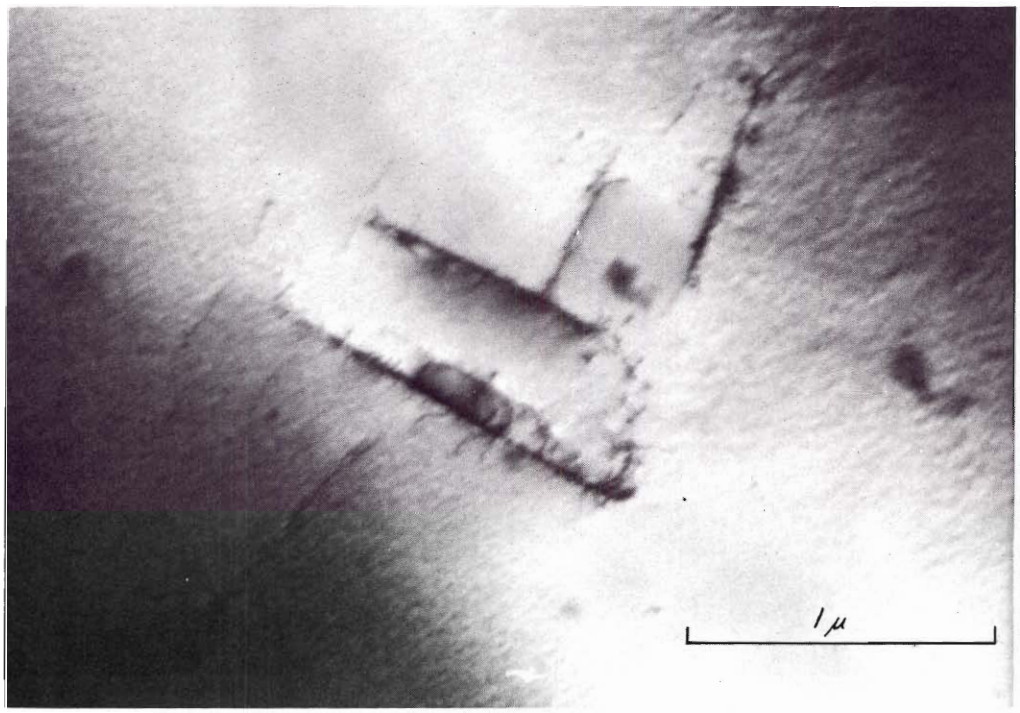

Figure 67. A Product Nucleation Site on a Dislocation Sub-boundary

Table 9. Run at 350°C for One Hour at 100 μ CO (Run 51)

Plate No.	Magnification Plate	Print	1 μ (in)	1 μ^2 (in^2)	Rotation Angle (°cl/ccl)	Plate Grade	Plate Area (μ^2)	No. of Ppts.	Ppt. Density Ppts. / μ^2	Ppt. Size Range (μ^2)	Distance Range Between Ppts. (μ)
5073	20,000	51,000	2.0	4.0	27 ccl	B-	16	1	--	0.56	--
5074	16,000	41,000	1.6	2.6	23 ccl	A	25	-	--	--	--
5075	SAD of 5076					C-					
5076	16,000	41,000	1.6	2.6	23 ccl	B	25	1	--	0.41	--
5077	12,000	31,000	1.2	1.4	17 ccl	D	46	-	--	--	--
5078	SAD - Typical					B+					
5079	13,000	33,000	1.3	1.7	19 ccl	A-	38	-	--	--	--
5084	20,000	51,000	2.0	4.0	27 ccl	B+	16	-	--	--	--
5085	35,000	90,000	3.5	12.0	35.5 ccl	A-	5.4	-	--	--	--
5086	24,000	62,000	2.4	5.8	29.5 ccl	B+	11	-	--	--	--
5087	29,000	74,000	2.9	8.4	32.5 ccl	A	7.7	-	--	--	--
5088	27,000	69,000	2.7	7.3	31.5 ccl	B	8.8	-	--	--	--
5089	SAD of 5090					B+					
5090	14,000	36,000	1.4	2.0	20.5 ccl	A	32	1	0.025	0.40	--
5091	16,000	41,000	1.6	2.6	23 ccl	B+	25	1	--	0.40	--
5092	St. P.	41,000	1.6	2.6	23 ccl	A	25	1	--	0.25	--

Table 9. Run at 350°C for One Hour at 100 μ CO (Run 51) (Continued)

Plate No.	Magnification Plate	Magnification Print	1 μ (in)	1 μ^2 (in^2)	Rotation Angle (°cl/ccl)	Plate Grade	Plate Area (μ^2)	No. of Ppts.	Ppt. Density Ppts./μ^2	Ppt. Size Range (μ^2)	Distance Range Between Ppts. (μ)
5093	14,000	36,000	1.4	2.0	20.5 ccl	A	32	2	--	0.31 to 0.52	2.4
5094	14,000	36,000	1.4	2.0	20.5 ccl	A	32	1	--	0.27	--

Typical Precipitate Population Density = < 0.025 ppts./μ^2
Average Precipitate Projected Area Size = 0.39 μ^2
Distance Between Precipitates = 2.4 μ

Reaction 7

($350^{\circ}C$, 5 μ CO, 1 hour)

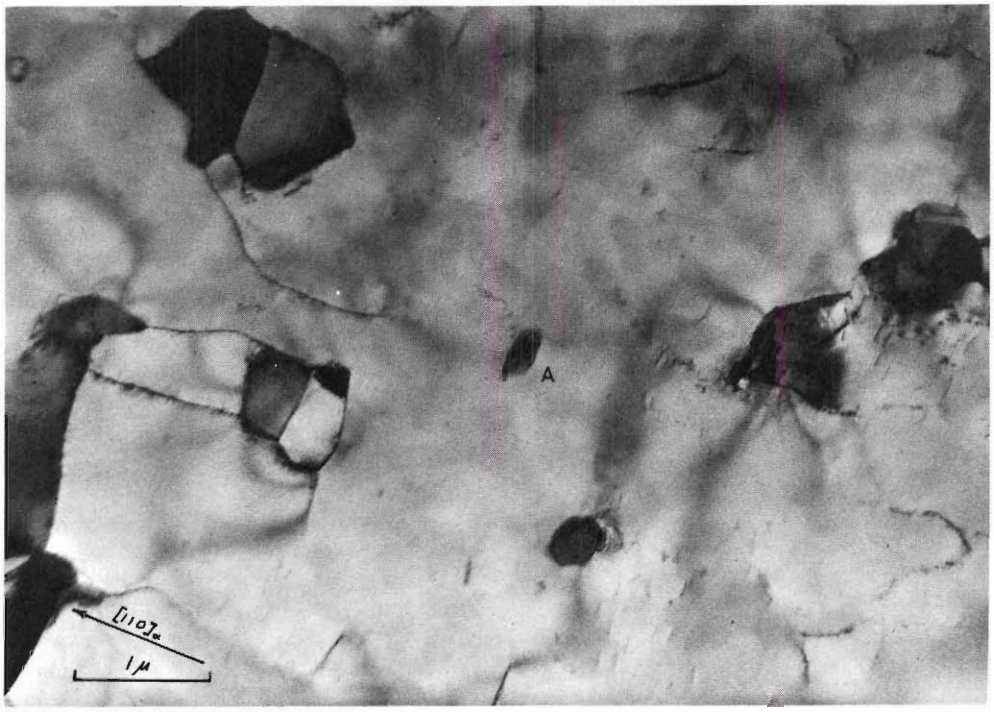

Figure 68. A Product Nucleus Produced at 350°C

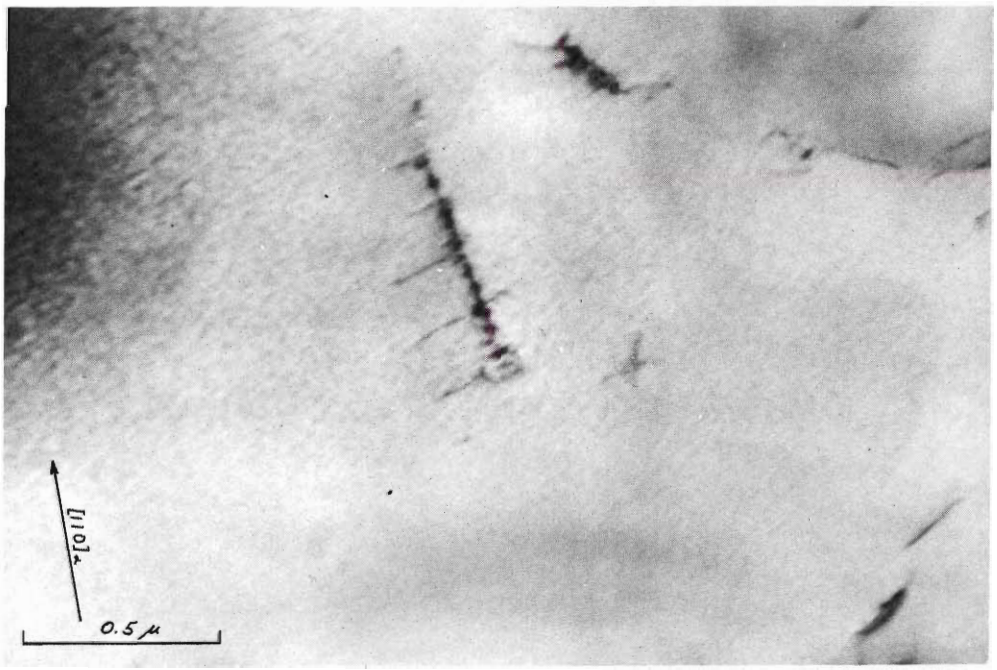

Figure 69. Sub-boundary Decoration by Product Nuclei

Table 10. Run at 350°C for One Hour at 5 μ CO (Run 48)

Plate No.	Magnification Plate	Magnification Print	1 μ (in)	1 μ^2 (in^2)	Rotation Angle (°cl/ccl)	Plate Grade	Plate Area (μ^2)	No. of Ppts.	Ppt. Density Ppts. / μ^2	Ppt. Size Range (μ^2)	Distance Range Between Ppts. (μ)
4979	12,000	31,000	1.2	1.4	17 ccl	A	46	-	--	--	--
4980	20,000	51,000	2.0	4.0	27 ccl	B+	16	-	--	--	--
4981	30,000	77,000	3.0	9.0	33 ccl	B	7.2	1	--	0.028	--
4982	SAD of 4983					B					
4983	12,000	31,000	1.2	1.4	17 ccl	A	46	1	<0.02	0.01	--
4984	30,000	77,000	3.0	9.0	33 ccl	C	7.2	1	--	--	--
4985	20,000	51,000	2.0	4.0	27 ccl	A	16	-	--	--	--
4986	SAD - Typical					C					
4988	35,000	90,000	3.5	12	35.5 ccl	F	5.4	-	--	--	--
4989	SAD of 4988					F					
4990	20,000	51,000	2.0	4.0	27 ccl	A	16	-	--	--	--
4991	SAD of 4992					F					
4992	35,000	90,000	3.5	12	35.5 ccl	B+	5.4	-	--	--	--

Precipitate Projected Area Size Range = <0.02 μ^2

Reaction 8

(350°C, 5 μ CO_2, 2 hours)

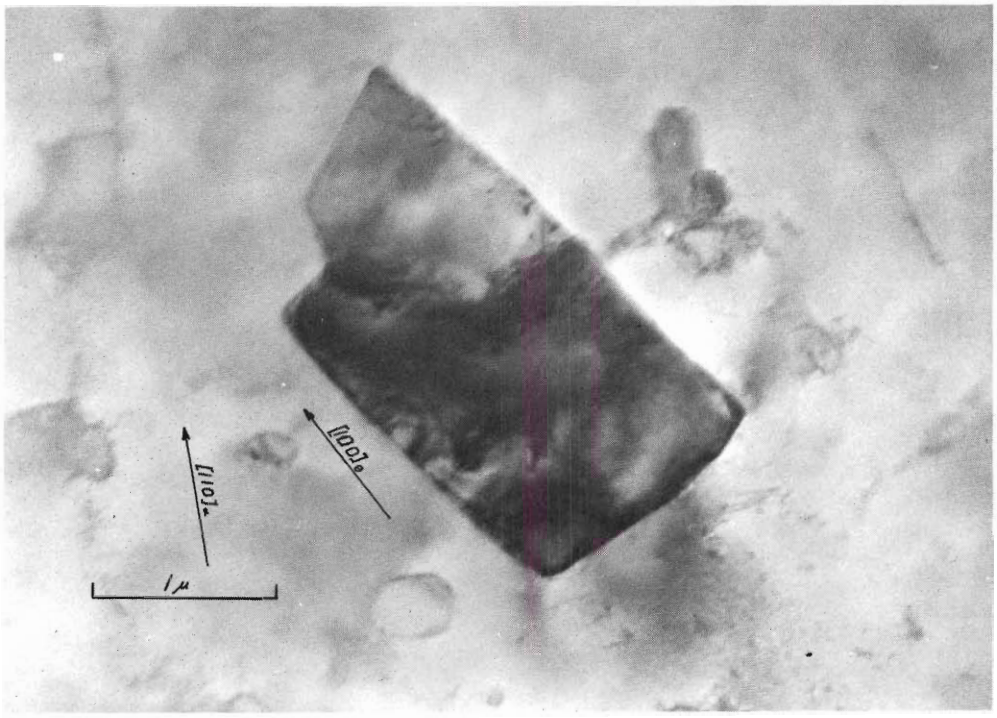

Figure 70. A Cementite Precipitate Particle

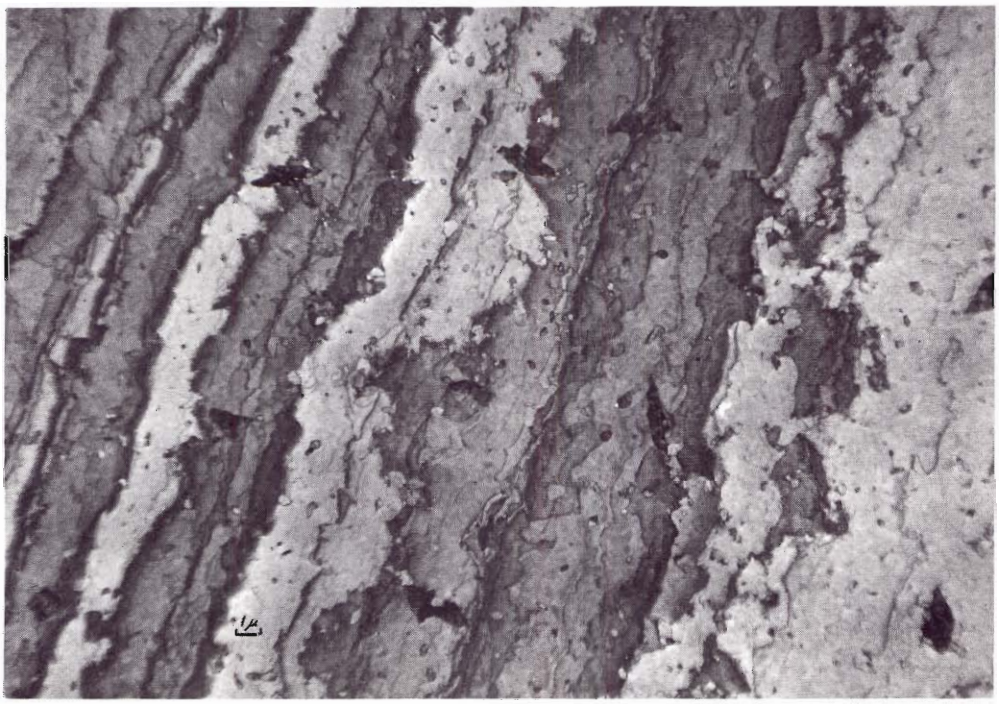

Figure 71. Cementite Precipitate Particles

Table 11. Run at 350°C for Two Hours at 5 μ CO (Run 40)

Plate No.	Magnification Plate	Magnification Print	1 μ (in)	1 μ^2 (in^2)	Rotation Angle (°cl/ccl)	Plate Grade	Plate Area (μ^2)	No. of Ppts.	Ppt. Density Ppts./μ^2	Ppt. Size Range (μ^2)	Distance Range Between Ppts. (μ)
4899	1,900	4,900	0.19	0.036	--	A	1,800	9	0.0050	1.9 to 5.4	6.1 to 20
4900	20,000	51,000	2.0	4.0	27 ccl	A+	16	--	--	--	--
5190	SAD of 5191					B-					
5191	16,000	41,000	1.6	2.6	23 ccl	B	25	1	--	1.7	--
5192	SAD of 5193					A-					
5193	16,000	41,000	1.6	2.6	23 ccl	B	25	1	--	3.5	--
5194	1,800	4,600	0.18	0.032	--	A-	2,000	10	0.0050	1.2 to 3.3	3.2 to 16

Typical Precipitate Population Density = 0.0050 ppts./μ^2
Average Precipitate Projected Area Size = 2.9 μ^2
Distance Range Between Precipitates = 3.2 to 20 μ

Reaction 9

(450°C, 1,000 μ CO, 1 hour)

Figure 72. A Cementite Precipitate of Complex Structure

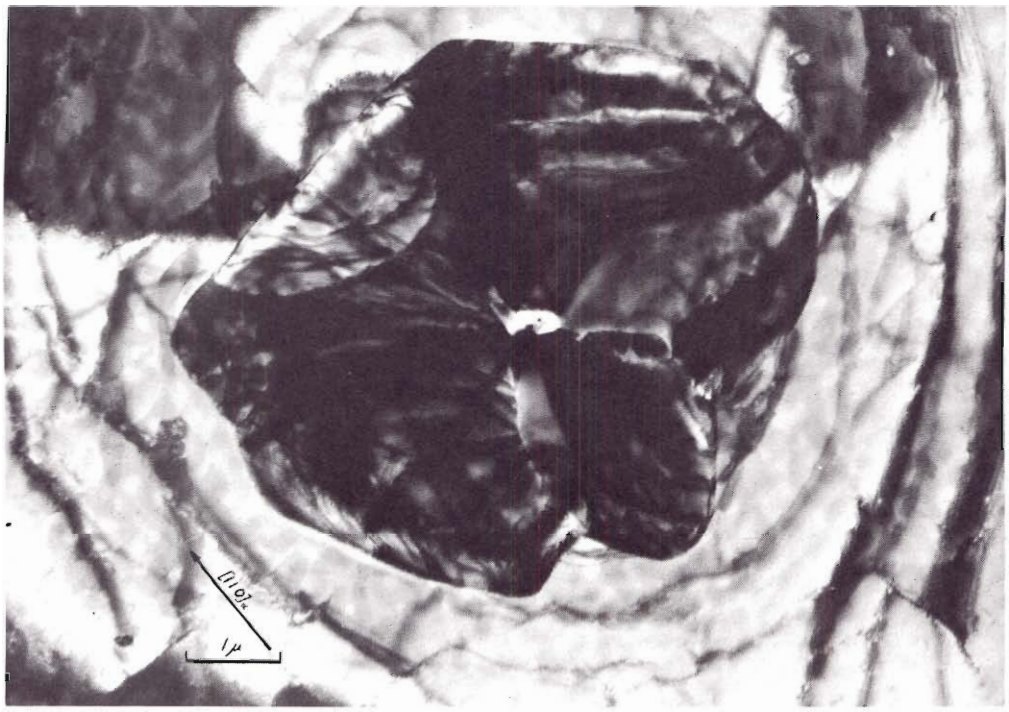

Figure 73. Precipitation at a Hole in the Iron Film

Figure 74. Precipitates Showing a Variety of Particle Shapes

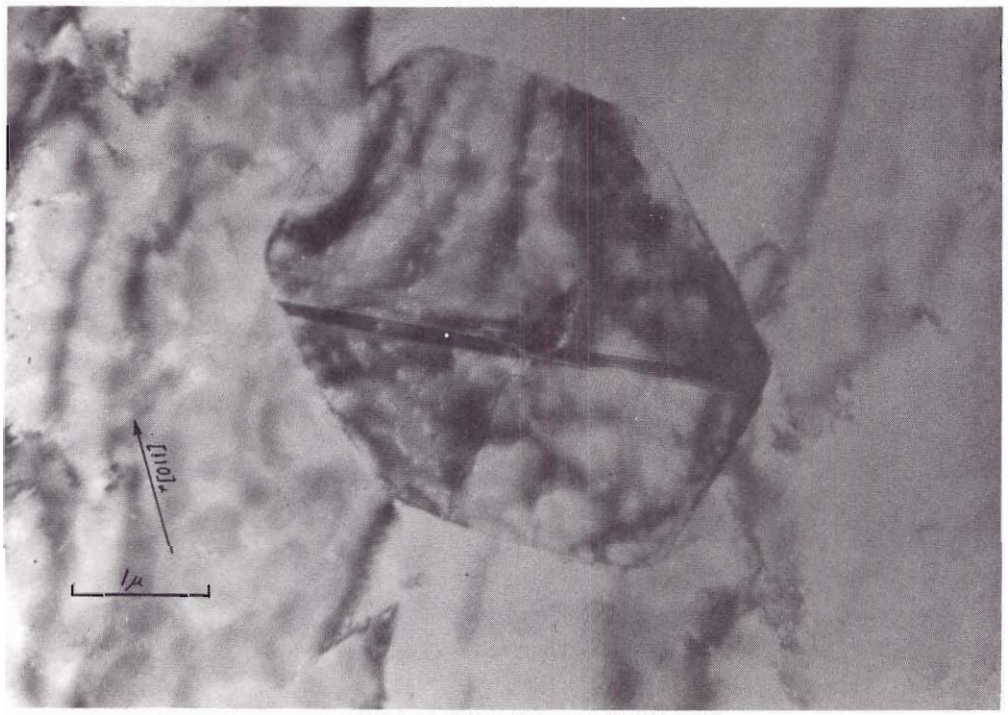

Figure 75. A Faulted Cementite Particle of Nearly Hexagonal Shape

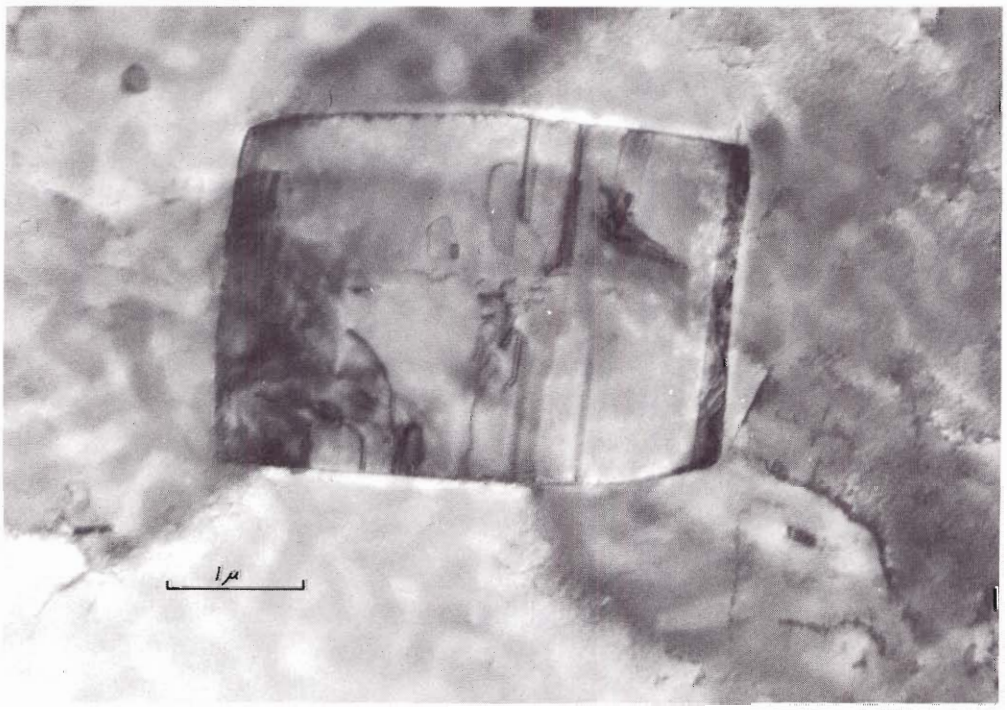

Figure 76. A Cementite Particle of Nearly Parallelepiped Configuration

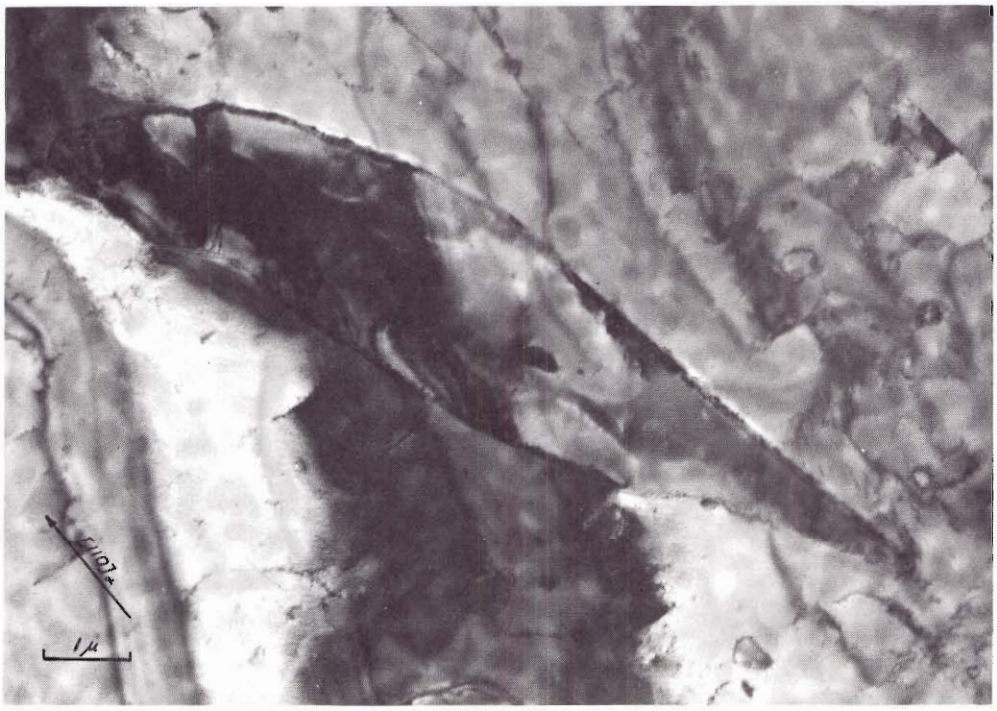

Figure 77. A Cementite Precipitate with a Lenticular Projection

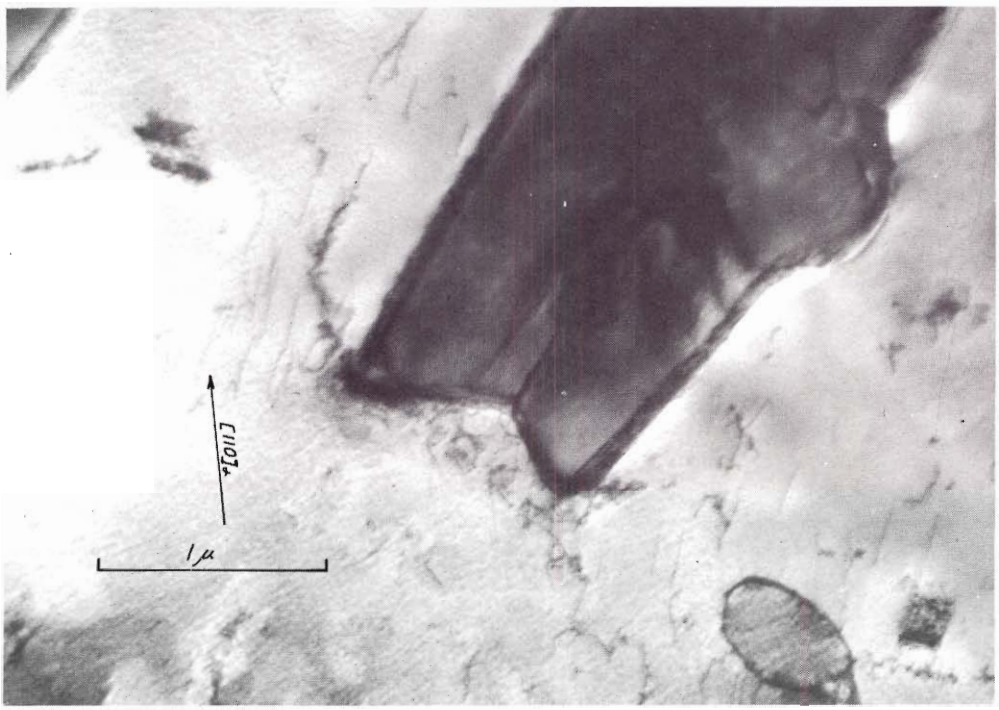

Figure 78. A View of Cementite-Ferrite Interfaces

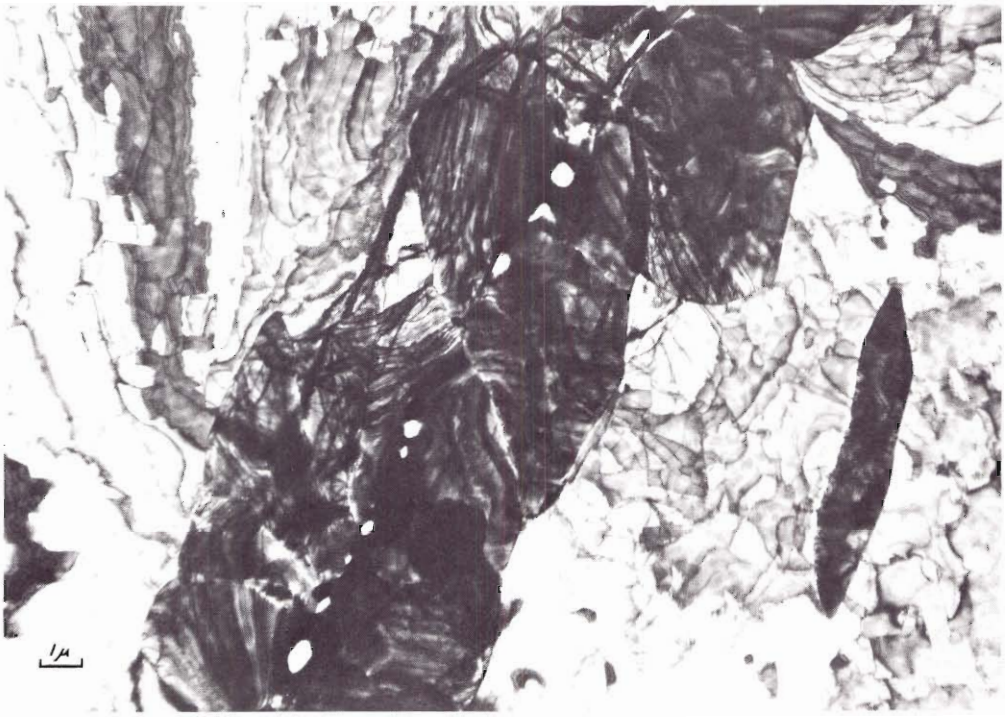

Figure 79. Cementite Grain Boundaries

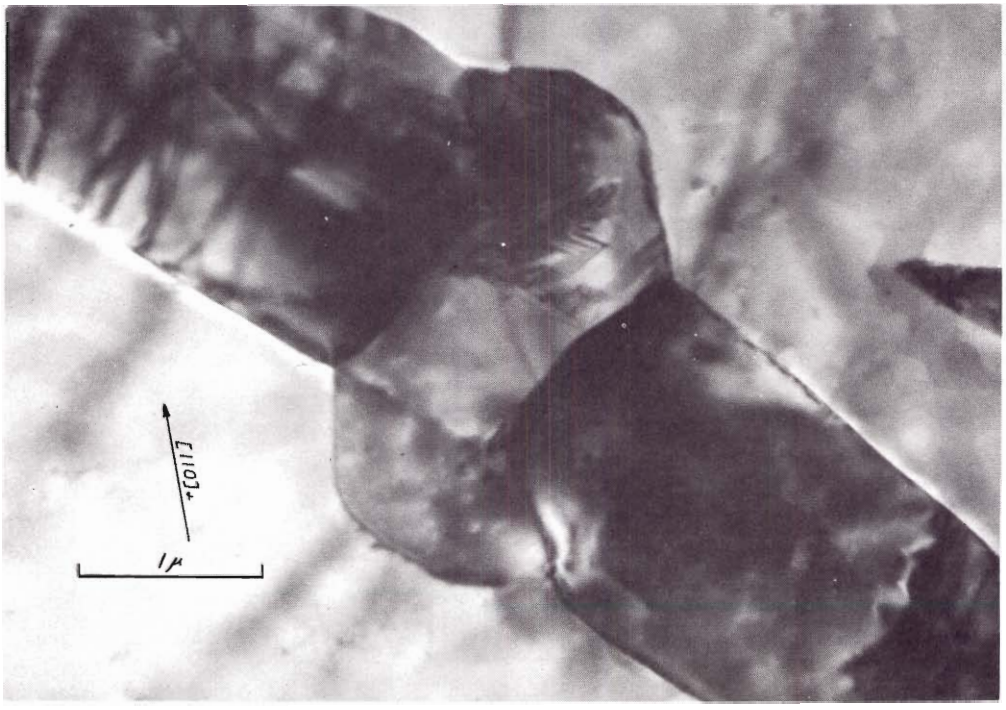

Figure 80. Cementite Formation Along a Line of Iron Film Discontinuities

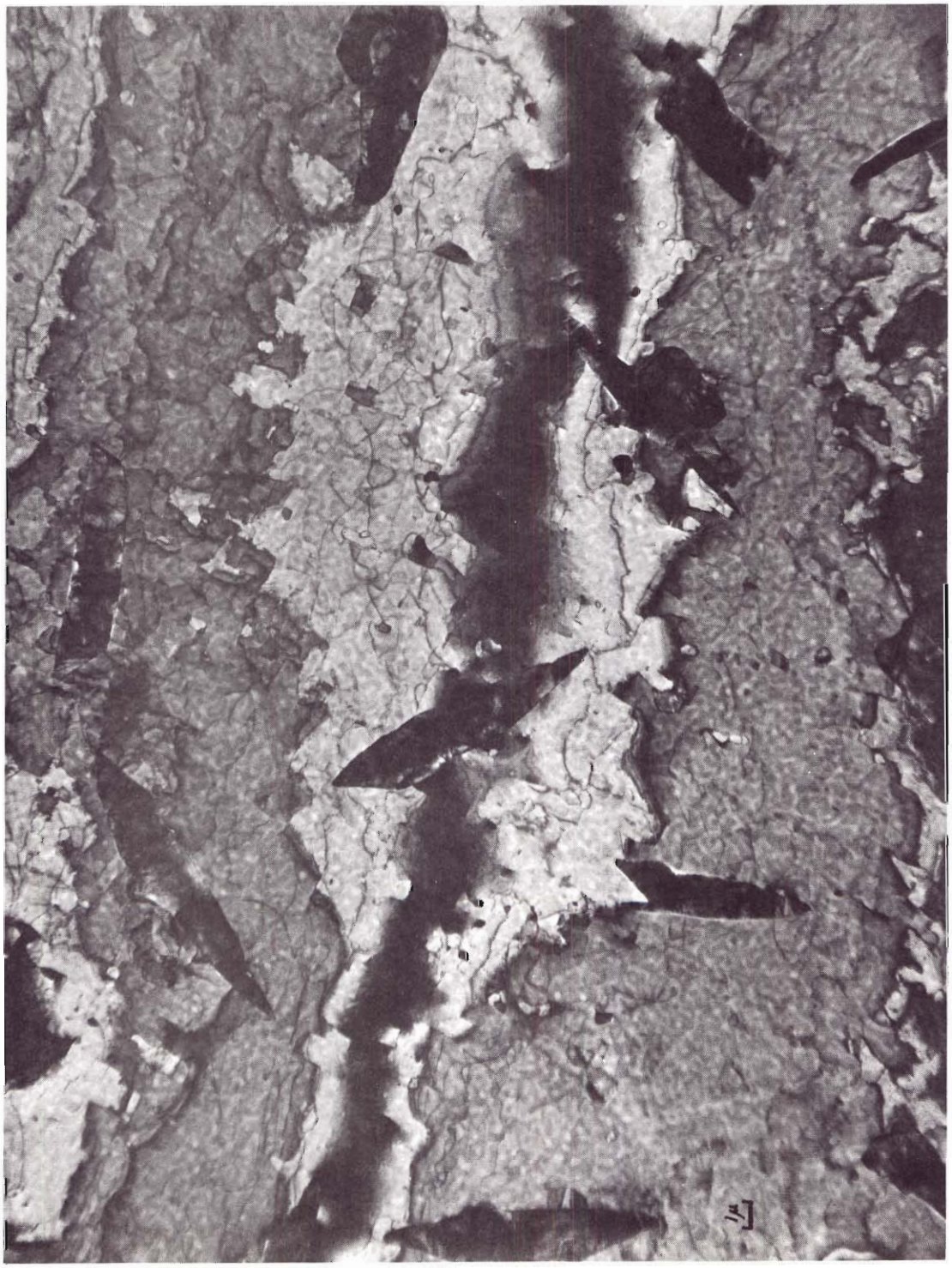

Figure 81. Cementite Particle Distribution

Table 12. Run at 450°C for One Hour at 1,000 μ CO (Run 52)

Plate No.	Magnification Plate	Magnification Print	1 μ (in)	1 μ^2 (in^2)	Rotation Angle (°cl/ccl)	Plate Grade	Plate Area (μ^2)	No. of Ppts.	Ppt. Density Ppts. / μ^2	Ppt. Size Range (μ^2)	Distance Range Between Ppts. (μ)
5125	23,000	59,000	2.3	5.3	29 ccl	B	12	1	--	--	--
5126	29,000	74,000	2.9	8.4	32.5 ccl	D	7.7	1	--	--	--
5127	SAD of 5128										
5128	7,500	19,000	0.75	0.56	6.3 cl	A	115	1	--	18	--
5129	12,000	31,000	1.2	1.4	17 ccl	B-	46	1	--	9.7	--
5130	St. P.	31,000	1.2	1.4	17 ccl	B	46	1	--	9.7	--
5131	SAD of 5129										
5132	SAD of 5134										
5134	8,000	21,000	0.8	0.64	6.8 cl	B+	100	1	--	*31	--
5133	3,600	9,200	0.36	0.13	$\approx$ 0	A	500	4.5	0.0090	3.7 to 9.3	2.9 to 7.2
5135	12,000	31,000	1.2	1.46	17 ccl	A	46	1	--	12	--
5136	7,500	19,000	0.75	0.56	6.3 cl	B+	115	1	--	18	--
5137	20,000	51,000	2.0	4.0	27 ccl	B-	16	1	--	--	--
5138	7,500	19,000	0.75	0.56	6.3 cl	A+	115	1	--	16	--
5139	16,000	41,000	1.6	2.6	23 ccl	B+	25	1	--	--	--

*Precipitate Mass on a hole in the metal foil

Table 12. Run at 450°C for One Hour at 1,000 μ CO (Run 52) (Continued)

Plate No.	Magnification Plate	Magnification Print	1 μ (in)	1 μ^2 (in^2)	Rotation Angle (°cl/ccl)	Plate Grade	Plate Area (μ^2)	No. of Ppts.	Ppt. Density Ppts./μ^2	Ppt. Size Range (μ^2)	Distance Range Between Ppts. (μ)
5140	6,200	16,000	0.62	0.38	4.7 cl	A+	170	2	--	3.3 to 13	0.72
5141	27,000	69,000	2.7	7.3	31.5 ccl	A	8.8	1	--	0.14	--
5142	20,000	51,000	2.0	4.0	27 ccl	A+	16	1	--	--	--
5143	29,000	74,000	2.9	8.4	32.5 ccl	A+	7.7	1	--	--	--
5144	1,900	4,900	0.19	0.036	--	B+	1,800	9.5	0.0053	8.1 to 21	1.8 to 15
5145	1,900	4,900	0.19	0.036	--	A-	1,800	9.5	0.0053	3.0 to 21	2.9 to 12
5146	3,600	9,200	0.36	0.13	--	B-	500	--	--	8.8	2.5
5147	12,000	31,000	1.2	1.4	17 ccl	A	46	1	--	9.2	--

Typical Precipitate Population Density = 0.005 ppts./μ^2
Average Precipitate Projected Area Size = 12 μ^2
Distance Range Between Precipitates = 0.72 to 15 μ

Reaction 10

(450°C, 1,000 μ CO, 1 hour, annealed)

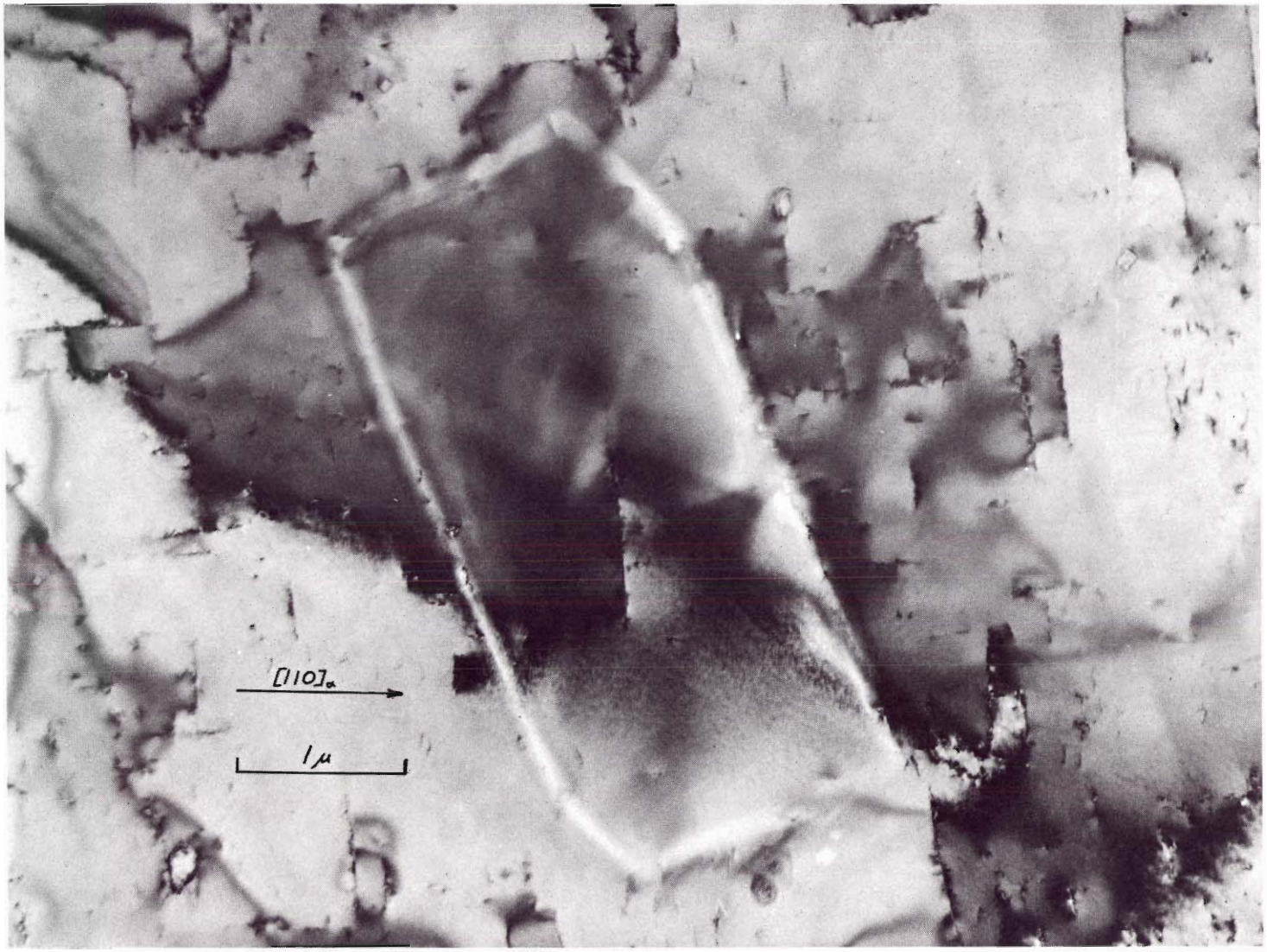

Figure 82. An Impression Left by a Decomposed Cementite Crystal - A "Ghost Crystal"

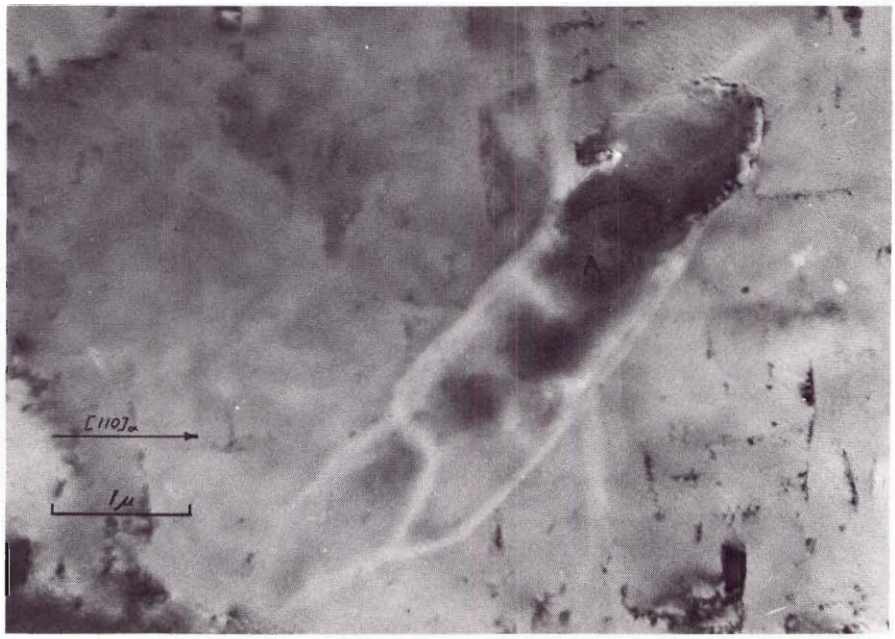

Figure 83. Graphite Nuclei in the Vicinity of a "Ghost Crystal"

Figure 84. Relative Positions of a "Plate-Button" Formation and a "Ghost Crystal"

Figure 85. A "Plate-Button" Formation

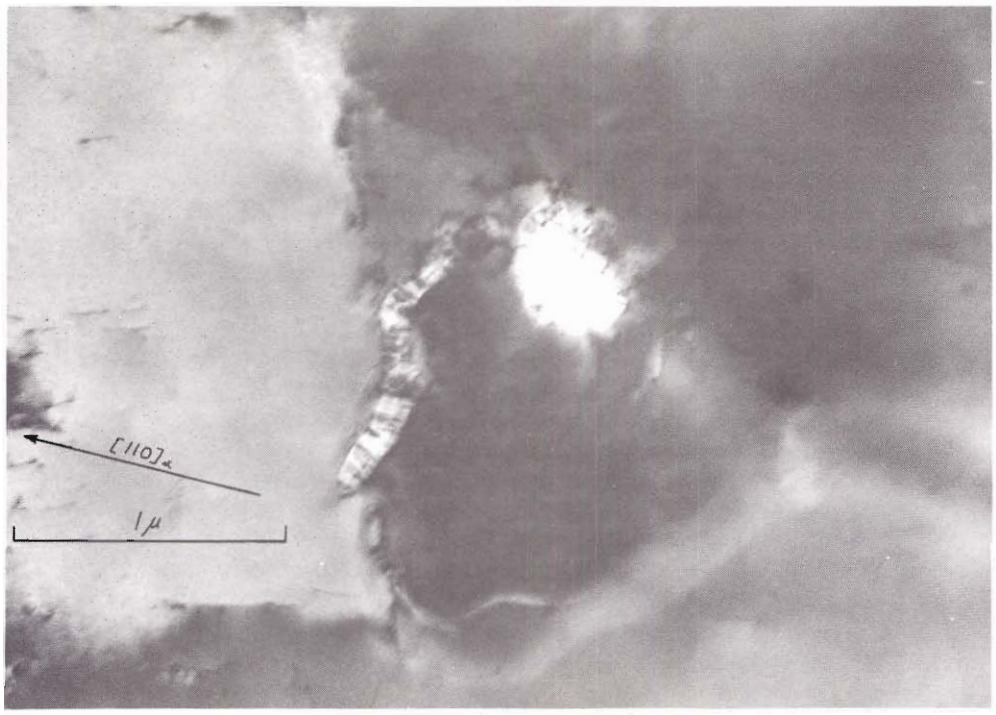

Figure 86. A Bright Field Micrograph of a Line of Specially Oriented Graphite Lamellae

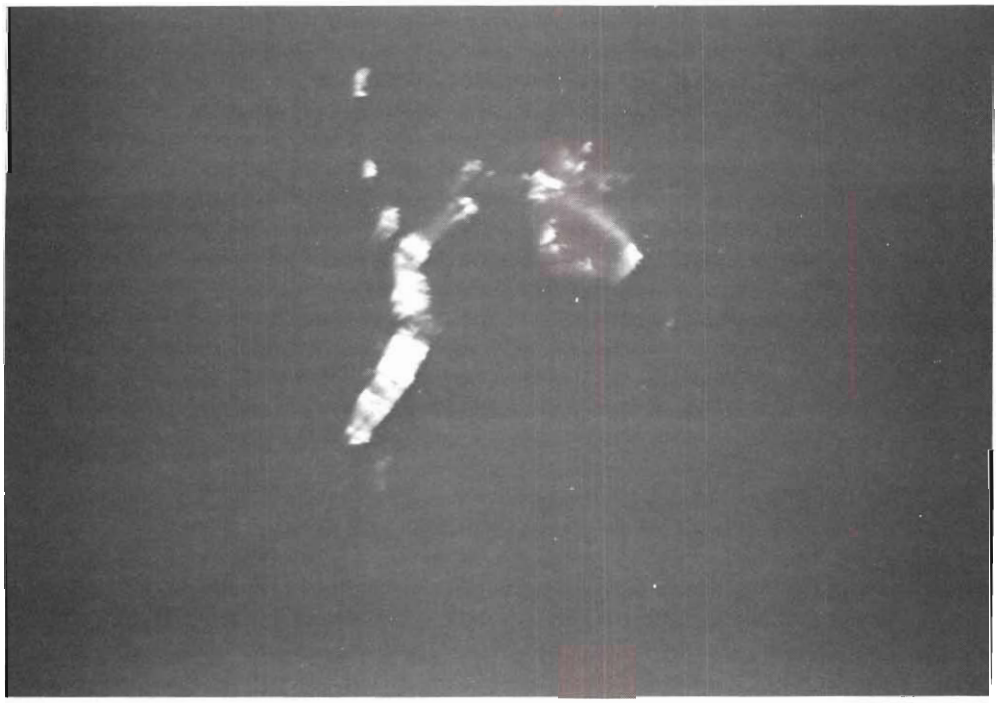

Figure 87. A Dark Field Micrograph of a Line of Graphite Lamellae

Table 13. Run at 450°C for One Hour Under 1,000 μ CO Followed by Vacuum Annealing for Eight Hours (Run 65)

Plate No.	Magnification Plate	Magnification Print	1 μ (in)	1 μ^2 (in^2)	Rotation Angle (°cl/ccl)	Plate Grade	Plate Area (μ^2)	No. of Ppts.	Ppt. Density Ppts./μ^2	Ppt. Size Range (μ^2)	Distance Range Between Ppts. (μ)
5520	24,000	62,000	2.4	5.8	29.5 ccl	A	11	1	—	B - 0.25 P - 2.10	—
5521	24,000	62,000	2.4	5.8	29.5 ccl	A	11	1	—	B - 0.25 P - 2.10	—
5522	St. P.	62,000	2.4	5.8	29.5 ccl	A	11	1	—	B - 0.25 P - 2.10	—
5523	SAD of 5520					A					
5524	DF of 5525		2.4	5.8	29.5 ccl	A	11	1	—	—	—
5525	24,000	62,000	2.4	5.8	29.5 ccl	A	11	1	—	G - 3.1 P - 2.1	—
5526	SAD of 5525					A					
5527	12,000	31,000	1.2	1.4	17 ccl	A+	46	1	—	G - 8.7	—
5528	SAD of 5527					C					
5529	SAD of 5530					C					
5530	20,000	51,000	2.0	4.0	27 ccl	A	16	1	—	B - 0.31 P - 2.5	—
5531	9,000	23,000	0.90	0.81	7.6 cl	A+	80	1	—	G - 5.8	—

Table 13. Run at 450°C for One Hour Under 1,000 μ CO Followed by Vacuum Annealing for Eight Hours (Run 65) (Continued)

Plate No.	Magnification Plate	Print	1 μ (in)	1 μ^2 (in^2)	Rotation Angle (°cl/ccl)		Plate Grade	Plate Area (μ^2)	No. of Ppts.	Ppt. Density Ppts./μ^2	Ppt. Size Range (μ^2)	Distance Range Between Ppts. (μ)
5532	SAD of 5533											
5533	11,000	28,000	1.1	1.2	15	ccl	B	54	1	—	P - 0.55	—
5534	11,000	28,000	1.1	1.2	15	ccl	A+	54	1	—	—	—
5535	11,000	28,000	1.1	1.2	15	ccl	A	54	-	—	B - 0.50 P - 1.10	—
5536	SAD of 5535						C					
5537	11,000	28,000	1.1	1.2	15	ccl	A	54	2	—	G - 4.9 P - 1.1	—
5538	SAD of 5537						D					
5539	SAD of 5540						B					
5540	16,000	41,000	1.6	2.6	23	ccl	A	25	1	—	B - 0.71 P - 2.90	—
5541	DF of 5540		1.6	2.6	23	ccl	C	25	1	—	—	—
5542	11,000	28,000	1.1	1.2	15	ccl	A	53	1	—	G - 4.0	—
5543	SAD of 5544						C					
5544	16,000	41,000	1.6	2.6	23	ccl	B+	25	1	—	G - 3.0	—
5545	16,000	41,000	1.6	2.6	23	ccl	A	25	1	—	B - 0.4 P - 2.6	—

Table 13. Run at 450°C for One Hour Under 1,000 μ CO Followed by Vacuum Annealing for Eight Hours (Run 65) (Continued)

Plate No.	Magnification Plate	Magnification Print	1 μ (in)	1 μ^2 (in^2)	Rotation Angle (°cl/ccl)	Plate Grade	Plate Area (μ^2)	No. of Ppts.	Ppt. Density Ppts./μ^2	Ppt. Size Range (μ^2)	Distance Range Between Ppts. (μ)
5546	St. P.	41,000	1.6	2.6	23 ccl	A-	25	1	--	B - 0.4 P - 2.6	--
5547	11,000	28,000	1.1	1.2	15 ccl	A	53	-	--	--	--
5548	7,500	19,000	0.75	0.56	6.3 cl	A+	115	2	--	G - 4.4 P - 3.0	2
5549	2,000	5,100	0.20	0.040	--	A	1,600	7	0.0044	G - 2.5-7.5	6 - 12
5550	2,500	6,400	0.25	0.063	--	B	1,000	5	0.0049	G - 8.5 P - 2.5	12
5551	2,100	5,400	0.21	0.044	--	B	1,500	3	0.0021	G - 6	8 - 10
5552	SAD - Typical					B					

Typical Precipitate Population Density = 0.004 ppts./μ^2
Including the impressions left in the iron film by precipitates having disappeared

Typical "Ghost Crystal" (G) Projected Area Size and Range = 5.4 (3.1 - 8.7) μ^2
"Ghost Crystal" is a name given the impression left in an iron film after the original precipitate has disappeared.

Table 13. Run at 450°C for One Hour Under 1,000 μ CO Followed by Vacuum Annealing for Eight Hours (Run 65) (Continued)

Typical "Plate" (P) Projected Area Size and Range = 2.1 (0.6 - 3) μ^2
"Plate" is a name given to the contrast effect illustrated in Figure 85 which appears to be the residue of a former carbide precipitate which has decomposed to carbon. The "Plate" carried a graphitic "Button" on its surface which apparently results from the original carbide decomposition.

Typical "Button" (B) Projected Area Size and Range = 0.38 (0.25 - 0.7) μ^2

Distance Range Between Precipitates = 2 to 12 μ

Reaction 11

(450°C, 1,000 μ CO, 6 hours)

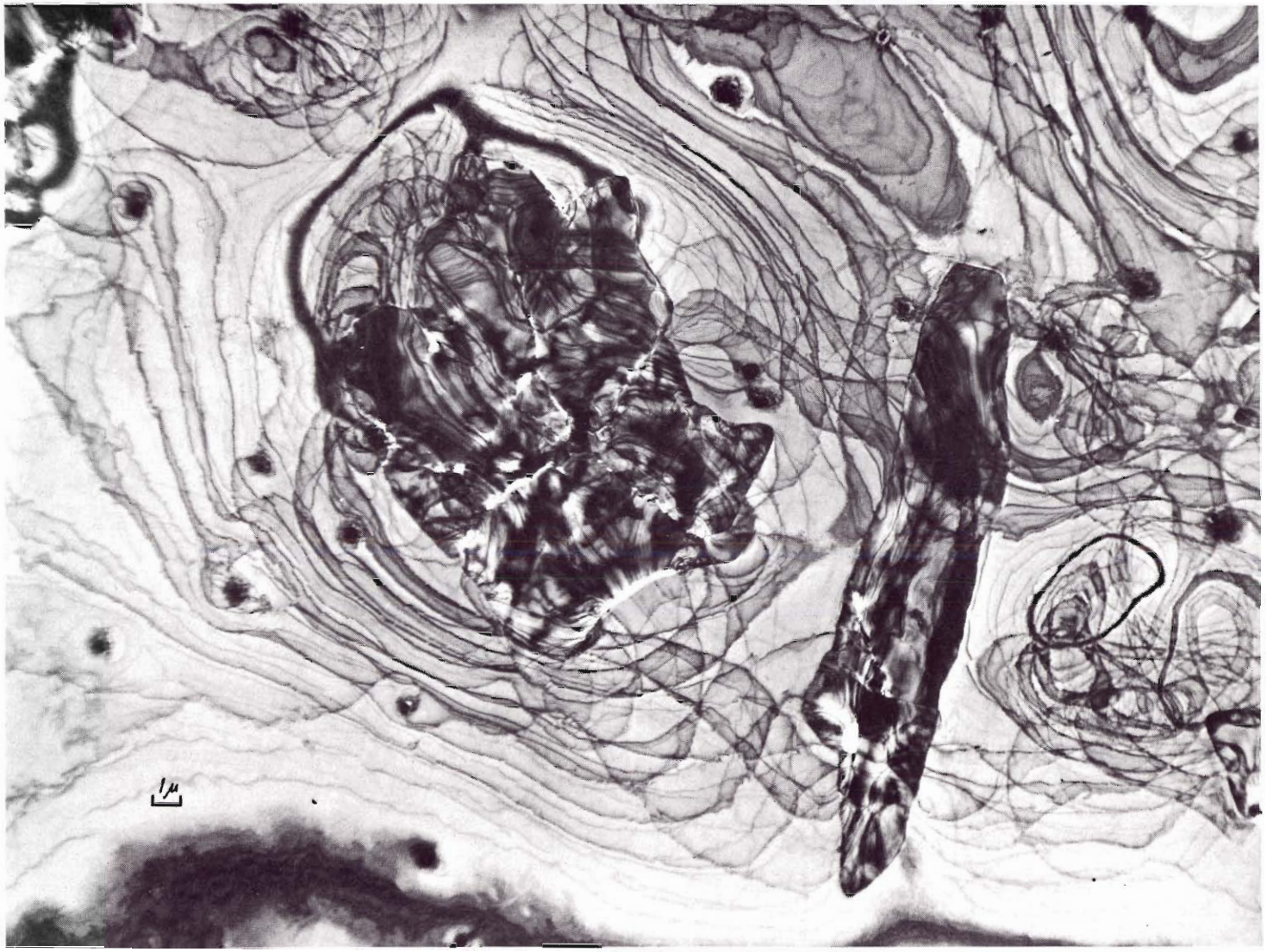

Figure 88. Distribution of Large Cementite Particles and Small Graphite Formations

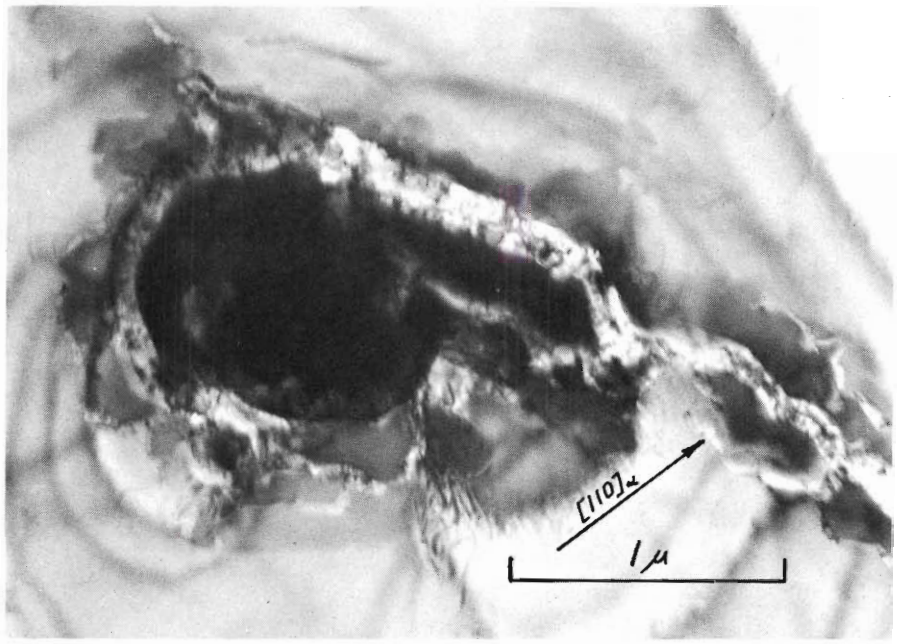

Figure 89. Graphte Formation Proximate to an Iron Film Surface Step

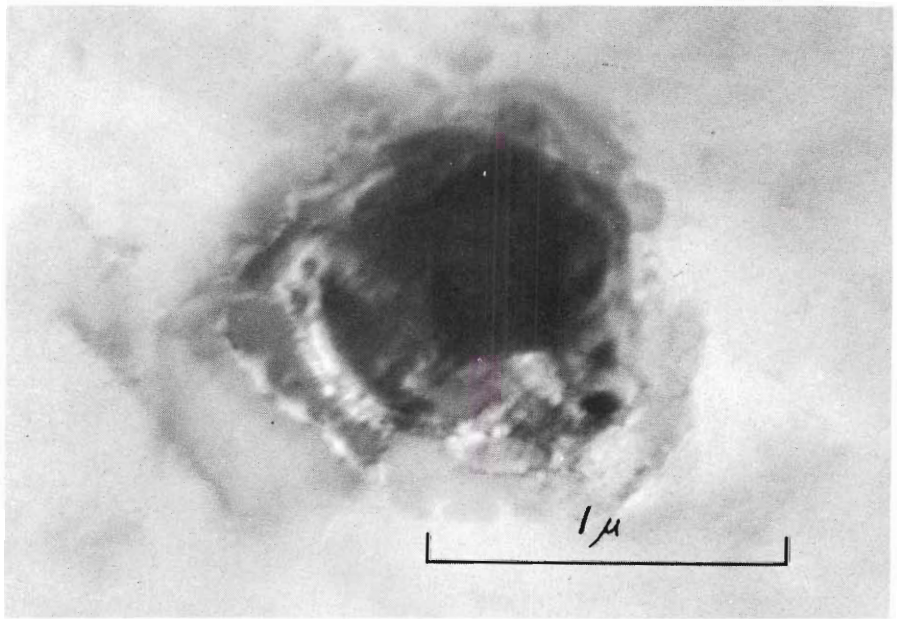

Figure 90. A "Plate-Button" Graphite Formation

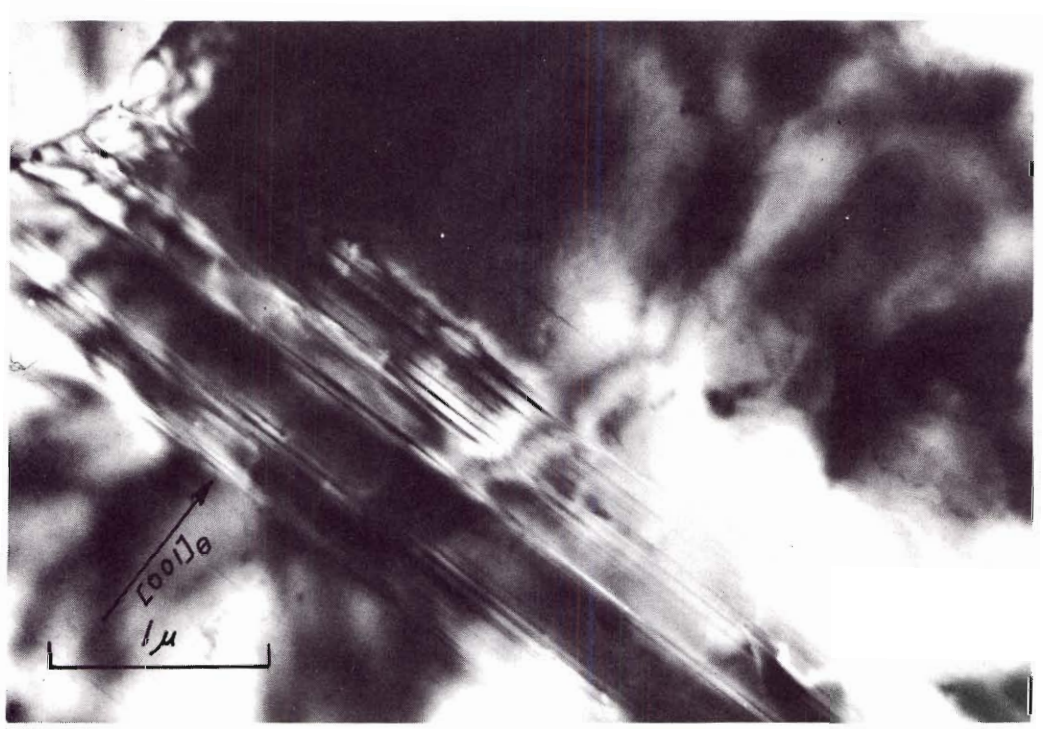

Figure 91. Cementite (001) Plane Stacking Faults

Table 14. Run at 450°C for Six Hours at 1,000 μ CO (Run 64)

Plate No.	Magnification Plate	Print	1 μ (in)	1 μ^2 (in^2)	Rotation Angle (°cl/ccl)	Plate Grade	Plate Area (μ^2)	No. of Ppts.	Ppt. Density Ppts./μ^2	Ppt. Size Range (μ^2)	Distance Range Between Ppts. (μ)
5491	24,000	62,000	2.4	5.8	29.5 ccl	C+	11	Θ - 1	--	--	--
5492	SAD of 5491					D					
5493	SAD of 5494					A+					
5494	12,000	31,000	1.2	1.4	17 ccl	A	46	Θ - 1	--	--	--
5495	26,000	67,000	2.6	6.8	31 ccl	D-	9.5	Θ - 1	--	--	--
5496	29,000	74,000	2.9	8.4	32.5 ccl	C+	7.7	Θ - 1	--	--	--
5497	SAD of 5498					B					
5498	20,000	51,000	2.0	4.0	27 ccl	A	16	P - 1	--	P - 0.90 B - 0.19	--
5499	20,000	51,000	2.0	4.0	27 ccl	B	16	P - 1	--	P - 1.20 B - 0.66	--
5500	St. P.	51,000	2.0	4.0	27 ccl	B	16	P - 1	--	P - 1.20 B - 0.66	--
5501	26,000	67,000	2.6	6.8	31 ccl	B+	9.5	P - 1	--	P - 0.98 B - 0.36	--
5502	SAD of 5503					C					
5503	16,000	41,000	1.6	2.6	23 ccl	B+	25	P - 1	--	P - 2.20 B - 0.69	--

Table 14. Run at 450°C for Six Hours at 1,000 μ CO (Run 64) (Continued)

Plate No.	Magnification Plate	Magnification Print	1μ (in)	$1\mu^2$ (in^2)	Rotation Angle (°cl/ccl)	Plate Grade	Plate Area (μ^2)	No. of Ppts.	Ppt. Density Ppts. / μ^2	Ppt. Size Range (μ^2)	Distance Range Between Ppts. (μ)
5504	DF of 5503		1.6	2.6	23 ccl	B+	25	P - 1	--	P - 2.20 B - 0.69	--
5505	2,000	5,100	0.2	0.04	--	A+	1,600	~~θ~~- 3 P- 20	~~θ~~- 0.002 P- 0.013	~~θ~~- 83-150 P- 0.25-2.0	~~θ~~- 3.8-12 P- 0.5-9
5506	1,900	4,900	0.19	0.036	--	A	1,800	~~θ~~- 4 P- 24	~~θ~~- 0.002 P- 0.013	~~θ~~- 24-280 P- 0.25-2.2	~~θ~~- 0-12 P- 0.6-12
5507	SAD of 5508					B					
5508	20,000	51,000	2.0	4.0	27 ccl	C-	16	~~θ~~ - 1	--	--	--
5509	SAD of 5510					B					
5510	24,000	62,000	2.4	5.8	29.5 ccl	C	11	~~θ~~ - 1	--	--	--
5511	SAD of 5512					C+					
5512	29,000	74,000	2.9	8.4	32.5 ccl	D-	7.7	~~θ~~ - 1	--	--	--
5513	SAD of 5514					A+					
5514	11,000	28,000	1.1	1.2	15 ccl	B+	54	~~θ~~ - 1	--	--	--
5515	SAD - Special					B-					
5516	SAD - Special					B-					

Note: ~~θ~~ - Designation for cementite precipitates
P - Designation for "Plate" type precipitates
B - Designation for "Button" outcropping on "Plate" precipitates

Reaction 12

(450°C, 5 μ CO, 1 hour)

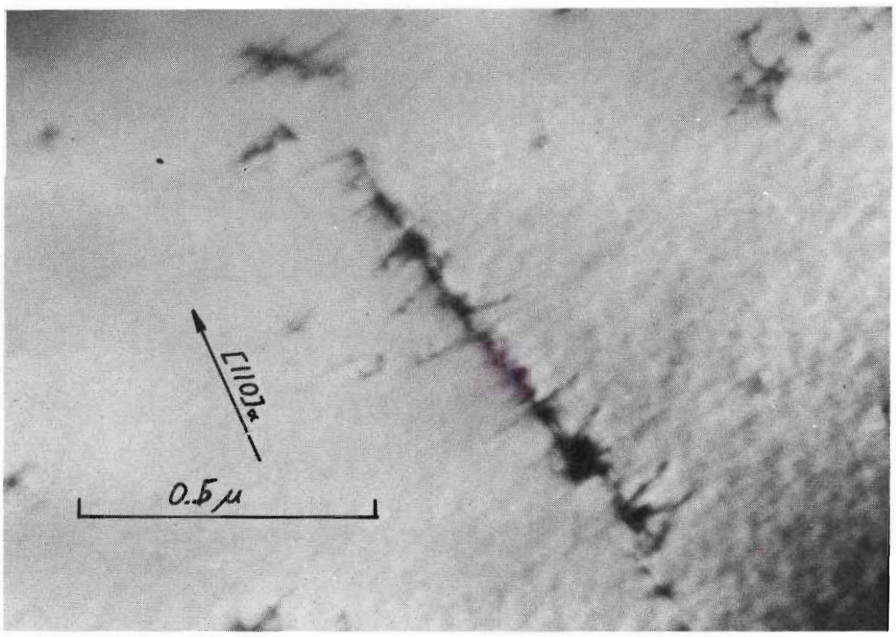

Figure 92. Sub-boundary Decoration with Product Nuclei

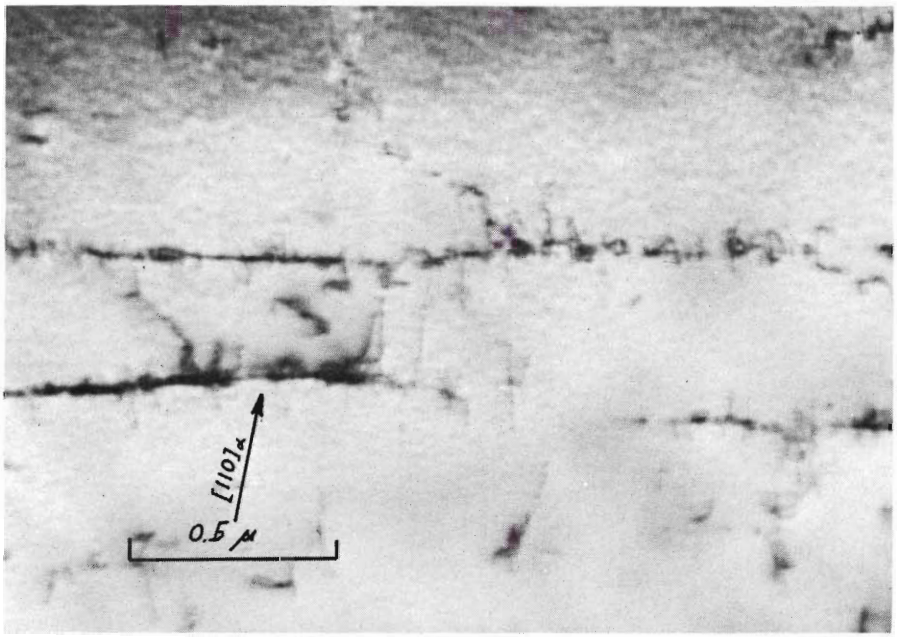

Figure 93. Sub-boundary Decoration with Product Nuclei

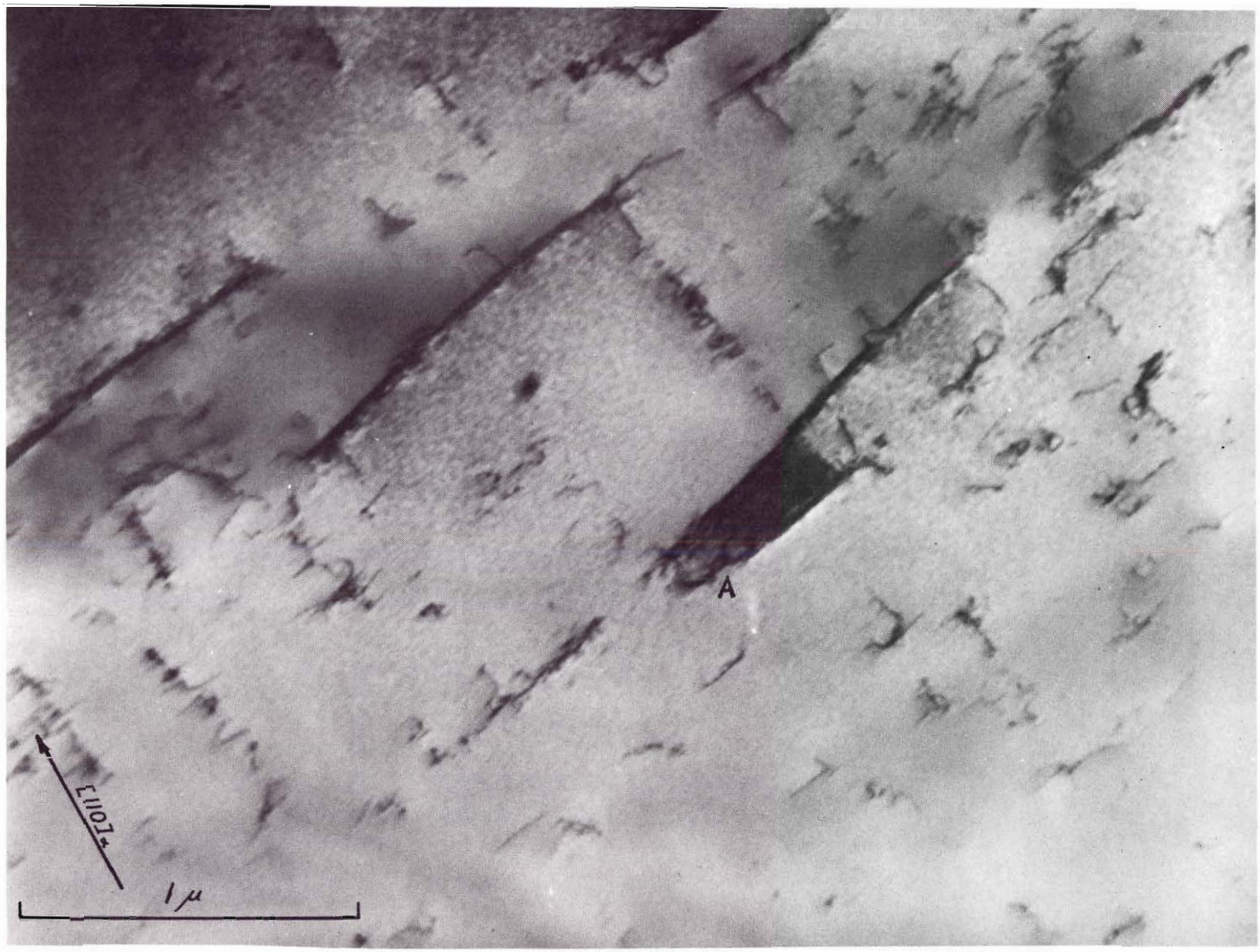

Figure 94. Concentration of Product Nuclei On and Between a Pair of Parallel Sub-boundaries

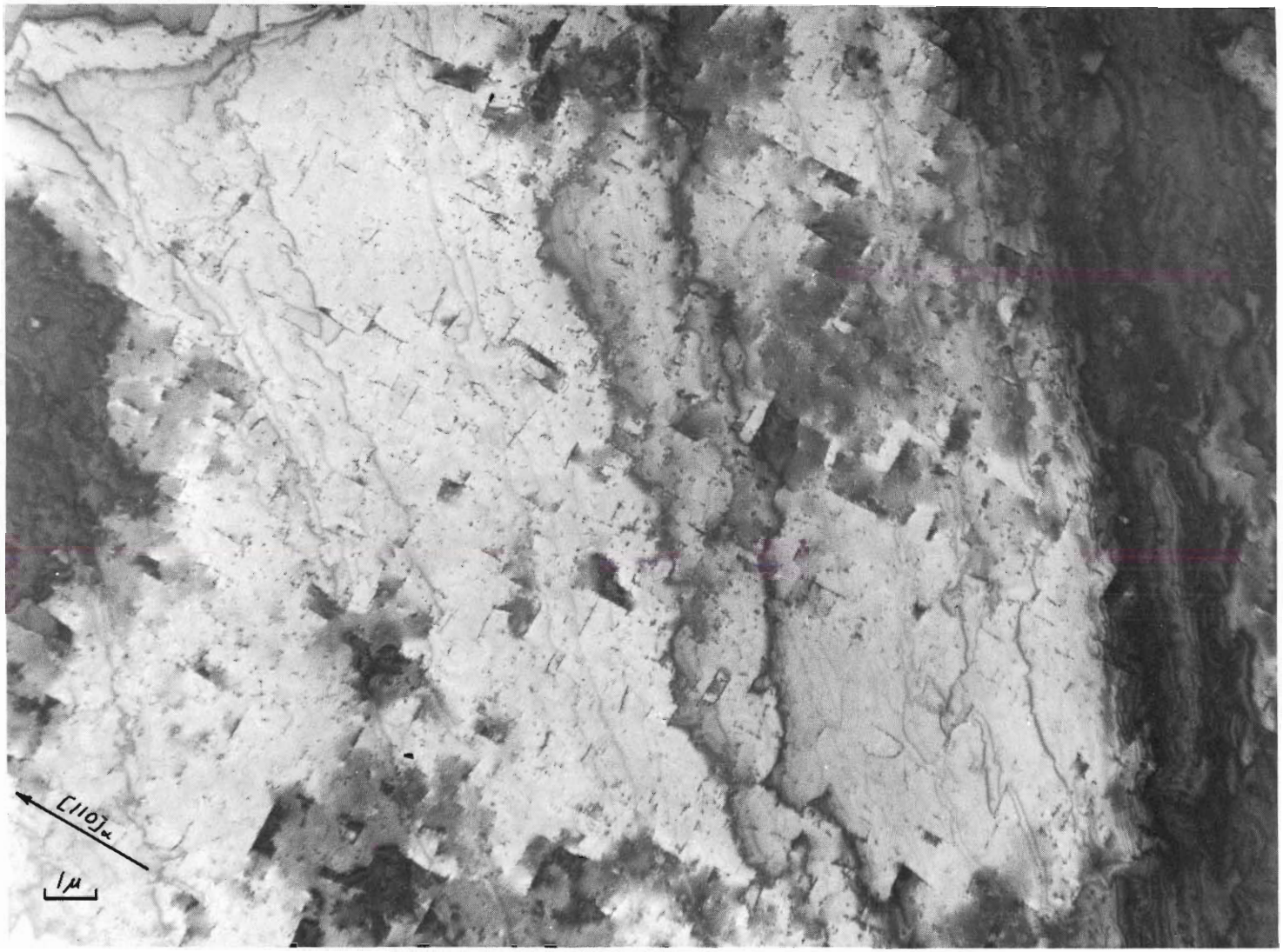

Figure 95. Distribution of Sub-boundaries and Product Nucleus Decoration

Table 15. Run at 450°C for One Hour at 5 μ CO (Run 55)

Plate No.	Magnification Plate	Magnification Print	1 μ (in)	1 μ^2 (in^2)	Rotation Angle (°cl/ccl)	Plate Grade	Plate Area (μ^2)
5264	35,000	90,000	3.5	12	35.5 ccl	B+	5.4
5265	43,000	110,000	4.3	19	39 ccl	A	3.4
5266	43,000	110,000	4.3	19	39 ccl	B+	3.4
5267	24,000	62,000	2.4	5.8	29.5 ccl	A	11
5268	43,000	110,000	4.3	19	39 ccl	B	3.4
5269	24,000	62,000	2.4	5.8	29.5 ccl	A	11
5270	29,000	74,000	2.9	8.4	32.5 ccl	B-	7.7
5271	45,000	115,000	4.5	20	40 ccl	B-	3.2
5272	24,000	62,000	2.4	5.8	29.5 ccl	A	11
5273	41,000	105,000	4.1	17	38 ccl	C+	3.8
5274	24,000	62,000	2.4	5.8	29.5 ccl	B	11
5275	3,600	9,200	0.36	0.13	0	A+	500
5276	SAD - Special					C	

Typical Precipitate Population Density = 3 to 15 nuclei/μ^2
Average Precipitate Projected Area Size = up to 0.006 μ^2
Distance Range Between Precipitates = 0.03 to 0.5 μ

Reaction 13

(450°C, No CO, 1 hour)

Figure 96. The Clean Film from Control Experiment Reaction 13

Table 16. Blank Run at 450°C for One Hour (Run 57)

Plate No.	Magnification Plate	Magnification Print	1μ (in)	$1\mu^2$ (in^2)	Rotation Angle (°cl/ccl)	Plate Grade	Plate Area (μ^2)
5253	28,000	72,000	2.8	7.8	32 ccl	B	8.3
5254	16,000	41,000	1.6	2.6	23 ccl	B	25
5255	13,000	33,000	1.3	1.7	19 ccl	A	38
5256	24,000	62,000	2.4	5.8	29.5 ccl	B+	11
5257	13,000	33,000	1.3	1.7	19 ccl	A	38
5258	SAD - Typical					B	
5259	3,600	9,200	0.36	0.13	≈0	A	500
5260	3,600	9,200	0.36	0.13	≈0	B+	500

Reaction 15

(550°C, 1,000 μ CO, 1 hour)

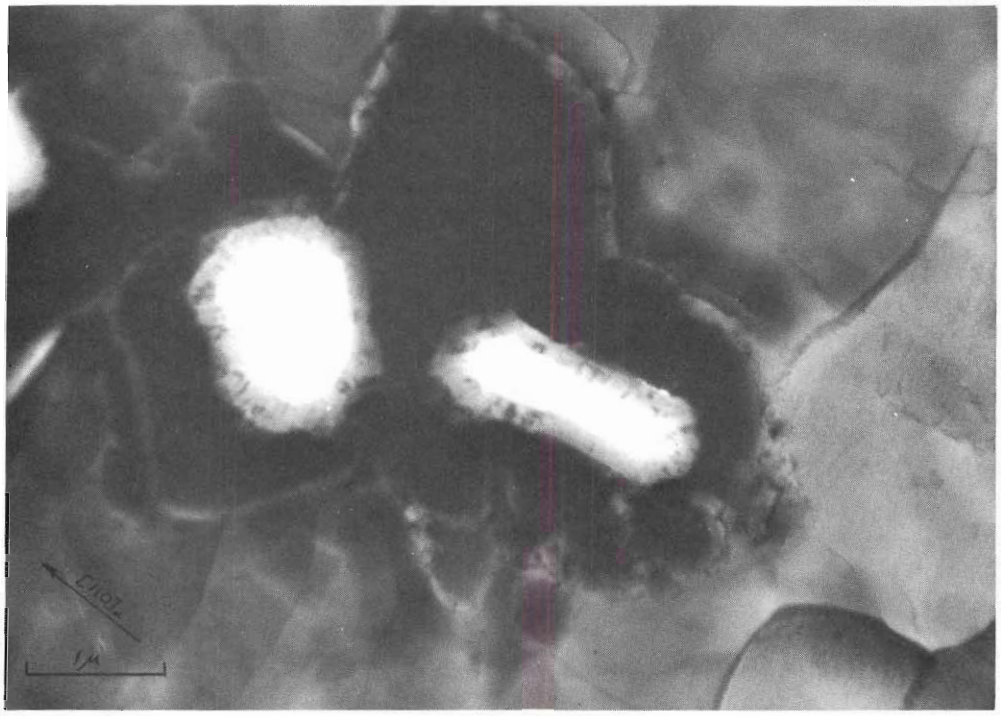

Figure 97. Decomposed Precipitate Crystals on a Hole in the Iron Film

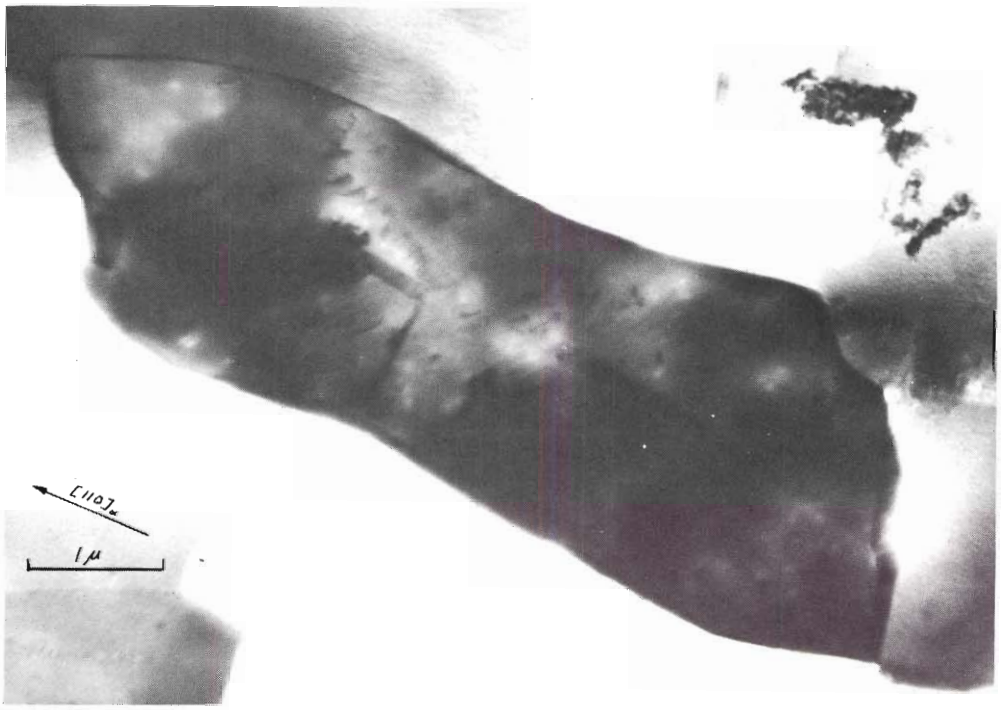

Figure 98. Faulted Cementite Precipitate Crystal

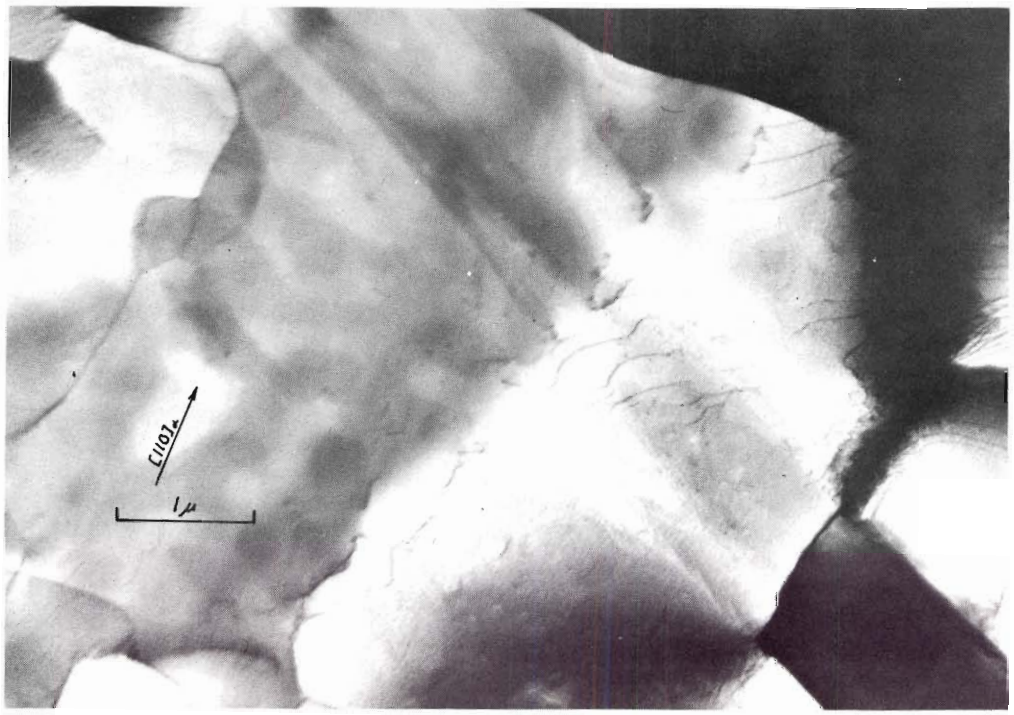

Figure 99. Partially Decomposed Cementite Particle

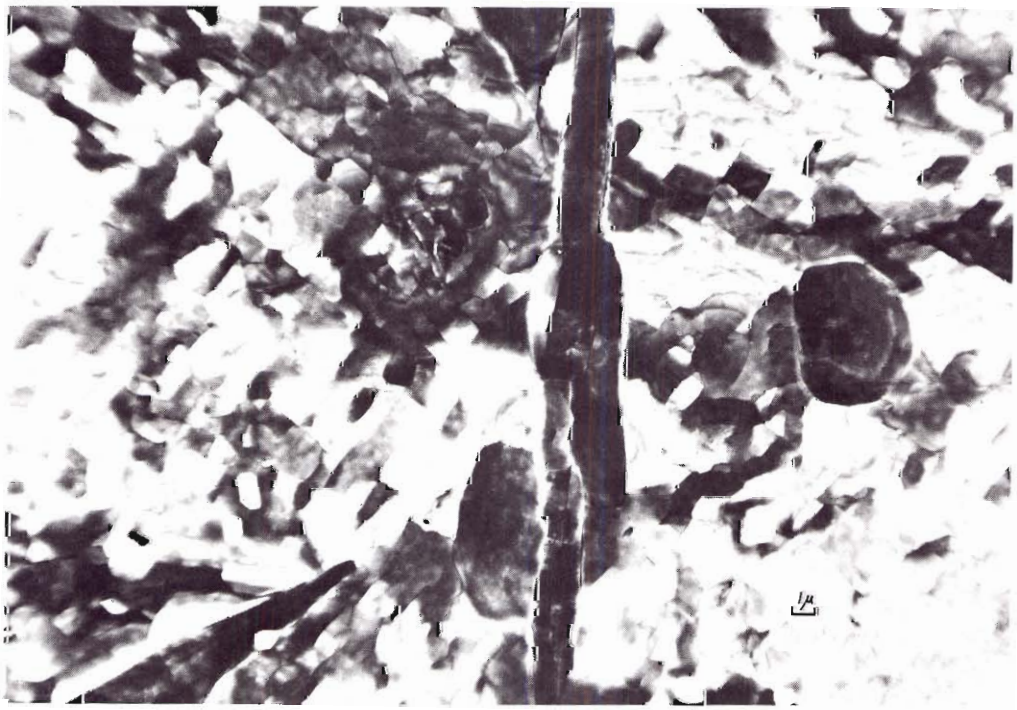

Figure 100. Product Particle Distribution

Table 17. Run at 550°C for One Hour at 1,000 μ CO (Run 54)

Plate No.	Magnification Plate	Print	1 μ (in)	1 μ^2 (in^2)	Rotation Angle (°cl/ccl)	Plate Grade	Plate Area (μ^2)	No. of Ppts.	Ppt. Density Ppts. / μ^2	Ppt. Size Range (μ^2)	Distance Range Between Ppts. (μ)
5261	DF of 5262		1.2	1.4	17 ccl	A	46	1	--	14	--
5262	12,000	31,000	1.2	1.4	17 ccl	A	46	1	--	14	--
5263	SAD of 5262					C+					
5173	SAD of 5174										
5174	16,000	41,000	1.6	2.6	23 ccl	D	25	1	--	--	--
5175	12,000	31,000	1.2	1.4	17 ccl	B+	46	-	--	--	--
5176	12,000	31,000	1.2	1.4	17 ccl	C	46	1	--	--	--
5177	5,000	13,000	0.50	0.25	2.8 cl	C+	260	1	--	--	--
5178	SAD of 5177										
5179	12,000	31,000	1.2	1.4	17 ccl	C+	46	-	--	--	--
5180	20,000	51,000	2.0	4.0	27 ccl	C	16	-	--	--	--
5181	SAD of 5182										
5182	12,000	31,000	1.2	1.4	17 ccl	B-	46	1	--	--	--
5183	SAD of 5184										
5184	1,800	4,600	0.18	0.032	--	A	2,000	4.5	0.0023	30 to 120	0.5 to 8
5185	SAD of 5186										
5186	12,000	31,000	1.2	1.4	17 ccl	B+	46	1	--	*14	--

Table 17. Run at 550°C for One Hour at 1,000 μ CO (Run 54) (Continued)

Plate No.	Magnification Plate	Magnification Print	1 μ (in)	1 μ^2 (in^2)	Rotation Angle (°cl/ccl)	Plate Grade	Plate Area (μ^2)	No. of Ppts.	Ppt. Density Ppts./μ^2	Ppt. Size Range (μ^2)	Distance Range Between Ppts. (μ)
5187	2,100	5,400	0.21	0.044	--	A+	1,500	6	0.0040	3.5 to 41	5 to 12
5188	1,900	4,900	0.19	0.036	--	--	1,800	6	0.0033	34 to 64	0 to 10
5189	3,200	8,200	0.32	0.10	≈ 0	--	640	1	--	--	--

*Partial cementite particle; the remainder apparently decomposed.

Typical Precipitate Population Density = 0.002 ppts./μ^2
Representative Precipitate Projected Area Size = 51 μ^2
Distance Range Between Precipitates = 0 to 12 μ

d. Summary Tables and Graphs. Summary tables of the reduced data presented in the preceding subsection will be found in the following pages (Tables 18 through 21). The purpose is to group the data to be used in comparative analyses in later discussions for ready reference. The temperature dependencies of precipitate particle size and precipitate particle density for experiments conducted under 1,000 μ of CO for a one-hour interval are illustrated in Figures 101 and 102.

Table 18. Summary of the Electron Micrograph Data for Experiments Capturing the Reaction in the Nucleation Stages

Reaction Number	Experimental Conditions: Temp. (°C)	Pressure (μ CO)	Time (Hrs.)	Typical Nucleus Density and Range (nuclei/μ^2)	*Average Precipitate Size (μ^2)
1	250	1,000	1	0.4 (0.13 - 0.65)	0.018
2	250	1,000	2.5	0.6 (0.37 - 1.1)	0.035
7	350	5	1	0.02	0.02
12	450	5	1	(3 - 15)	<0.006

*The precipitates were sized on the basis of their projected areas in the plane of the iron films.

Table 19. Summary of Results for Reactions Carried Out at 1,000 μ of CO for One Hour at Various Temperatures on Single Crystal Iron Films

Reaction Number	Experiment Temperature (°C)	Typical Precipitate Density and Range (ppts./μ^2)	Precipitate Projected Area Size Range and Average (μ^2)	Distance Range Between Precipitates (μ)
1	250	0.4 (0.13 - 0.65)	(0.0050 - 0.060) 0.018	0.15 - 1.8
3	320	0.02 (0.010 - 0.030)	(0.10 - 0.80) 0.37	1.4 - 7
4	350	<0.04 (<0.04 - 0.098)	(0.19 - 0.98) 0.53	0.8 - 2
9	450	0.005 (0.0050 - 0.0090)	(3.3 - 21) 12	0.72 - 15
15	550	0.002 (0.002 - 0.004)	(14 - 120) 51	0 - 12

Table 20. Summary of Results for Reactions Carried Out at 350°C for One Hour at Various Pressures of CO on Single Crystal Iron Films

Reaction Number	Pressure of CO (μ)	Typical Precipitate Density and Range (ppts./μ^2)	Precipitate Projected Area Size Range and Average (μ^2)	Distance Range Between Precipitates (μ)
7	5	$\ll$ 0.02	(0.01 - 0.07)	-
6	100	$<$ 0.02	(0.25 - 0.56) 0.39	2.4
5	500	0.01 (0.0055 - 0.018)	(0.13 - 1.2) 0.52	1.9 - 18
4	1,000	$<$0.04 ($<$0.04 - 0.098)	(0.19 - 0.98) 0.53	0.8 - 2
8*	5	0.005	(1.2 - 5.4) 2.9	3.2 - 20

*For reaction carried out at 350°C for two hours; There is reason to question results of this run.

Table 21. Summary of Results for Reactions Carried Out at 450°C for Different Pressures of CO and Reaction Periods on Single Crystal Iron Films

Reaction Number	Pressure (μ)	Time (hrs.)	Typical Precipitate Density and Range (ppts./μ^2)	Precipitate Projected Area Size Range and Average (μ^2)	Distance Range Between Precipitates (μ)
9	1,000	1	0.005 (0.005 - 0.009)	(3.0 - 21) 12	0.7 - 15
10	1,000*##@	1	0.004 (0.002 - 0.005)	(3.1 - 8.7) 5.4	2 - 12
11	1,000#	6	0.002	24 - >280	0 - 12
12	5	1	3 - 15	$\leqslant$ 0.006	0.03 - 0.5

*Reaction followed by an in-place anneal for eight hours at the temperature of the reaction

##Data refers to precipitate "Ghost Crystals" (impressions left in the Fe film after particle disappearance).

@ See Table 13 for data regarding precipitates of unusual morphology

See Table 14 for data regarding precipitates of unusual morphology

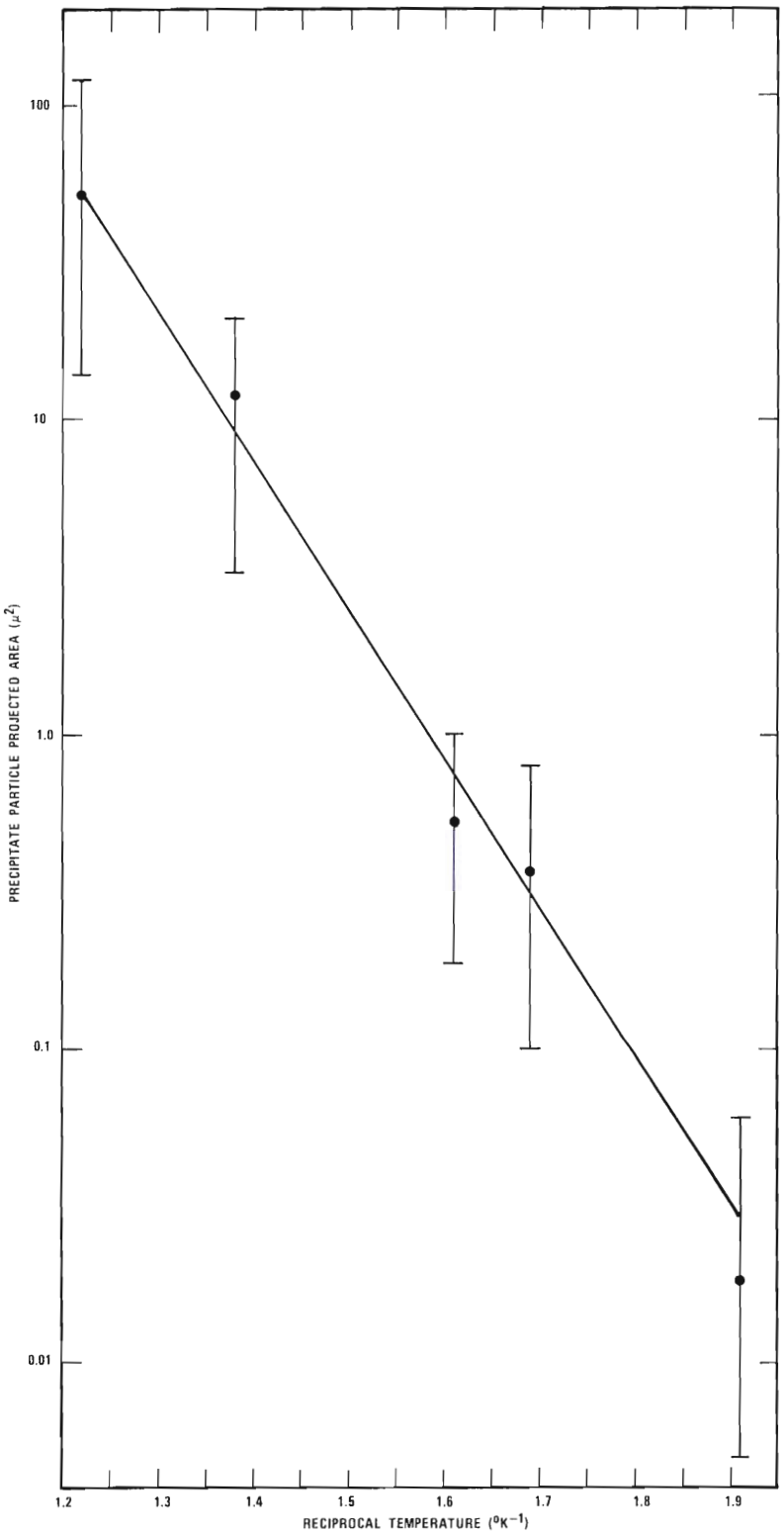

Figure 101. Precipitate Particle Size - Temperature Relation for Reactions Conducted Under 1,000 μ of CO for 1 Hour.

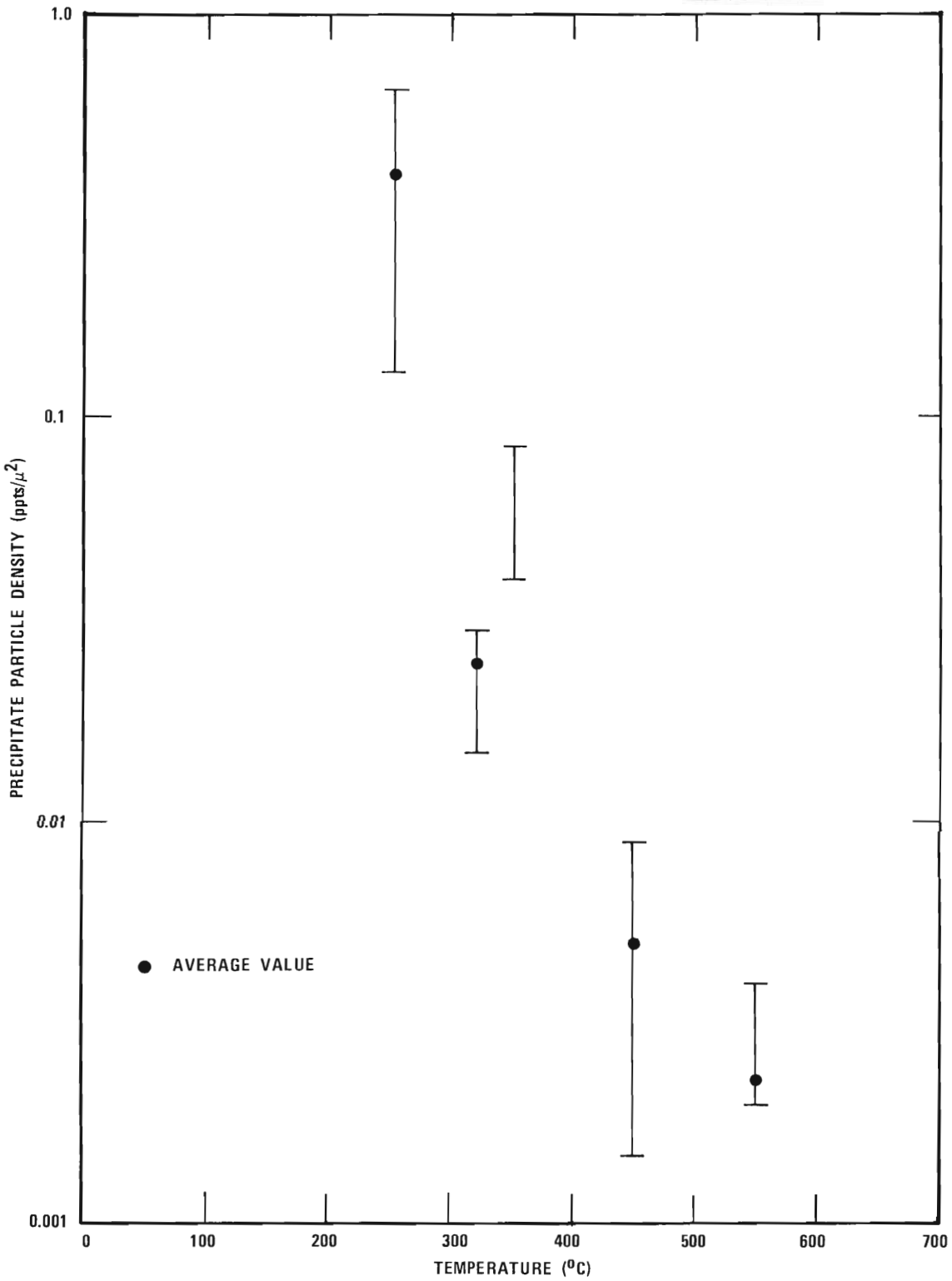

Figure 102. Precipitate Density - Temperature Relation for Reactions Conducted Under 1,000 μ of CO for 1 Hour.

2. Electron Diffraction Results and Discussion

a. General Presentation. In this section only one or two representative patterns and their solutions will be presented for each of the reactions listed in Table 3. Since the only reaction products found during the course of this research were cementite and graphite and since their identifications were straightforward, only summary remarks will be made concerning the overall results.

The standard diffraction data are presented in Appendix B. The tabulations include the data for iron, magnetite (Fe_3O_4), epsilon iron carbide, Hägg carbide, Fe_7C_3, and cementite. These compounds have been variously reported for the action of CO on iron. Accordingly, the presence of each material was considered in the analysis of every diffraction pattern of the reacted films. All the SAD patterns are listed in the summary tables in subsection C.1.c.

Not every pattern was completely solvable. However, the presence or absence of Fe_3O_4 and graphite was readily determinable in all instances due to their particularly characteristic patterns. Identification of the carbide was more complicated. For cementite there have been more than one hundred interplanar spacings or d-spacings reported between the values 0.989 and 6.948 Å. Similar conditions exist for the Hägg carbide. Epsilon carbide and Fe_7C_3 have been reported to give thirteen and seventeen different reflections, respectively between d-values of 1.04 and 4.40 Å. Within the latter range the d-spacings for either epsilon carbide or Fe_7C_3 correspond within the limit of error to reported spacings for either cementite or Hägg carbide. The problem is compounded by the fact that there is a degree of uncertainty associated with all the reported values. Distinguishing the

iron carbides must then be made on other evidence than a few d-spacings alone. In all the carbide patterns analyzed, there appeared d-values above 2.38. Above this value individual spacings are more widely separated from one material to another. In addition, Fe_7C_3 does not have spacings above this value, and the reported reflections for ϵ-carbide do not lead to confusion. Thus, either Hägg carbide or cementite was always present when a carbidic product was analyzed. Whether or not one of the other carbides was also present required further analysis. The micrographs of the areas analyzed revealed that large grains of carbide were present having the same appearance from grain to grain. The evidence thus indicated that a single carbide was present and it could only be either Hägg carbide or cementite.

The normal method for distinguishing which carbide phase is present is based on the relative ring intensities of the diffraction patterns. Since the specimens were single crystals, the rings characteristic of polycrystalline material were not present. The patterns were instead superpositions (in the complex cases) of spot patterns of relatively few grains. In this instance, the relative spot intensities are more sensitive to orientation and grain size than to structure factors. Therefore, for a completely satisfactory solution, the reflections of a single grain had to be extracted from a complex pattern. Single crystal patterns are unique. Differentiation between materials is facilitated by the crystallographic information inherent in the interplanar angles of the materials. The angles between planes producing electron diffraction pattern spots are readily measured from photographic prints.

The patterns selected for analysis in this work were photographed

with the foregoing considerations in mind. As a result, single crystal reflections were commonly determined and identified. The patterns often contained extra reflections. However, none of the extra reflections or partial patterns gave spacings which could not plausibly be attributed to cementite on iron. There were no positive identifications made of a carbide other than cementite which was identified at all temperatures investigated. There was no evidence to suggest the existence of another carbide although suspicious spots were found occasionally in the patterns. All effort to correlate these reflections with a standard single crystal pattern for another carbide failed.

In summation, cementite was the only carbide positively identified and it was identified repeatedly. The solutions to all the SAD patterns are on file in the Metallurgy Department.

Figures 103 through 117 present the typical patterns and their solutions for most of the experimental runs tabulated in Table 3. The results for Reactions 13, 14, and 16 have been omitted since they represent control experiments without CO exposure. The patterns were analogous to that illustrated in Figure 32. No SAD patterns were taken of Reaction 1 because the precipitate nuclei did not give detectable diffraction patterns. The nuclei at the stage of development depicted in the micrographs of Reaction 1 may have been coherent, as will be discussed later. Similarly, SAD patterns for Reactions 7 and 12 were not included since no characteristic diffraction effects from the precipitate nuclei were observed for these experiments.

The precipitates of Reaction 2 were in the earliest stage of development which gave rise to identification by SAD. Figures 103 and 104 show the two solvable patterns obtained in the reaction carried out for 2.5 hours

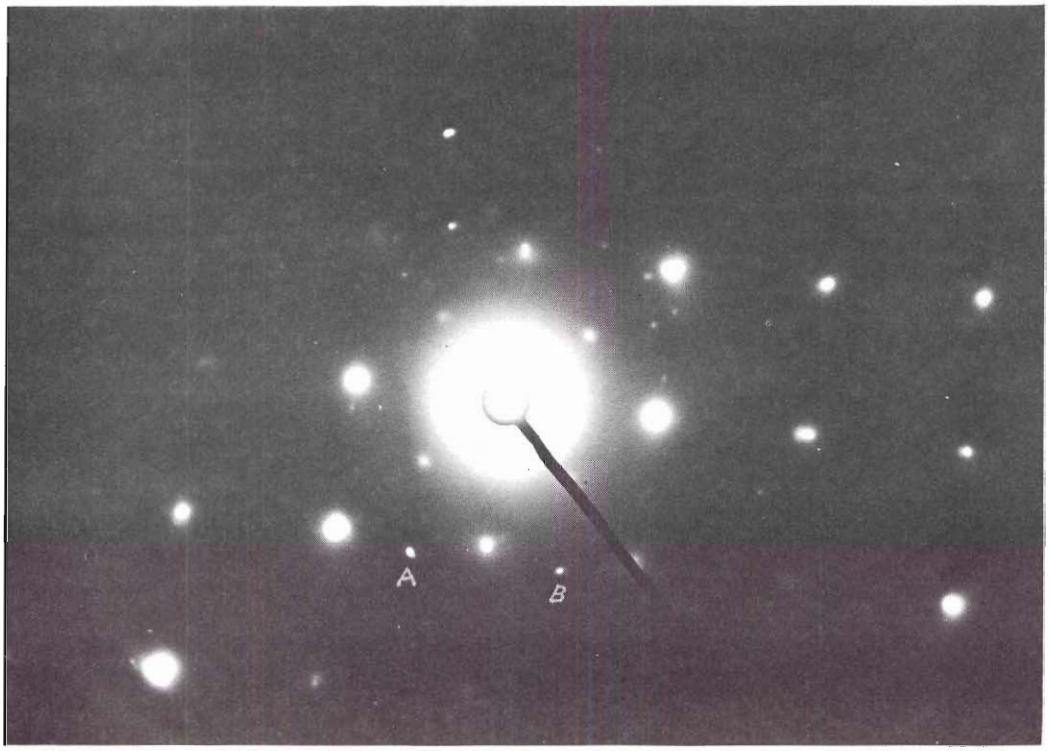

NOTES: CEMENTITE (θ) AND α-IRON WERE IDENTIFIED. THE ORIENTATION WAS $(100)_\theta \parallel (001)_\alpha$ WITH $[001]_\theta$ 4° FROM $[\bar{1}20]_\alpha$.

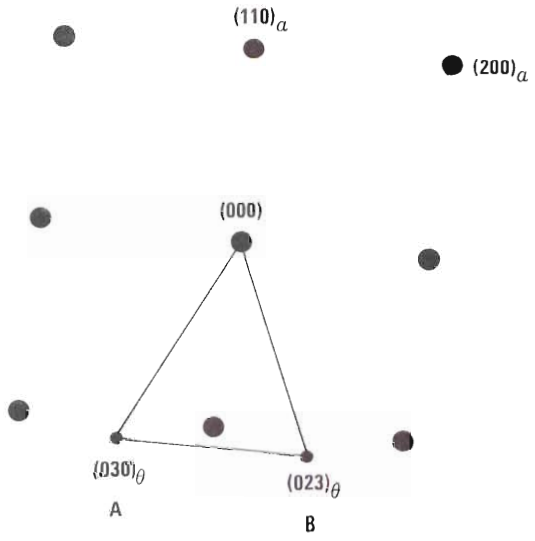

Figure 103. SAD Pattern and Solution Diagram for a Specimen from Reaction 2

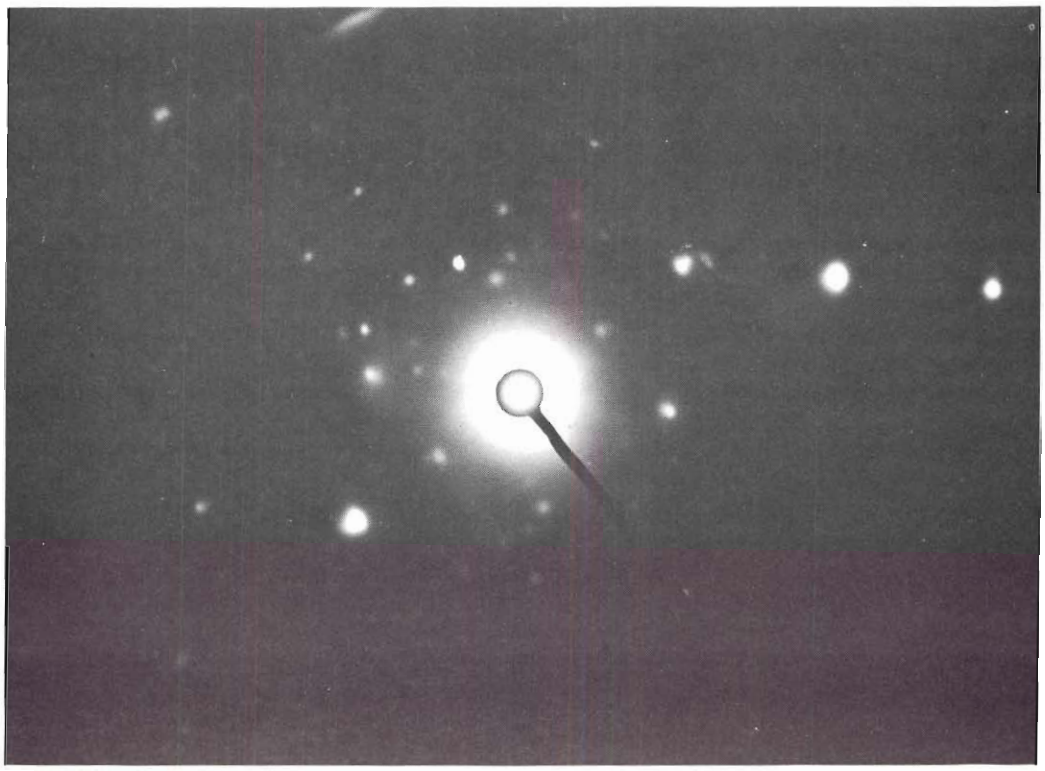

NOTES: CEMENTITE (θ) AND α-IRON WERE IDENTIFIED. THE ORIENTATION RELATION WAS $(230)_\theta \parallel (001)_\alpha$ WITH $[001]_\theta$ 13^0 $[1\bar{1}0]_\alpha$.

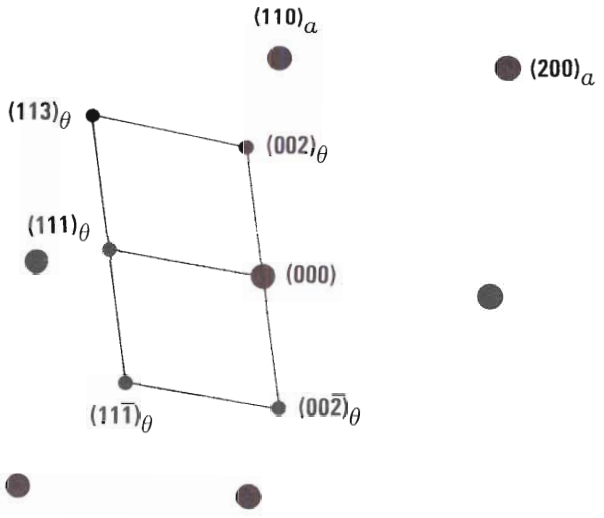

Figure 104. SAD Pattern and Solution Diagram for a Specimen from Reaction 2

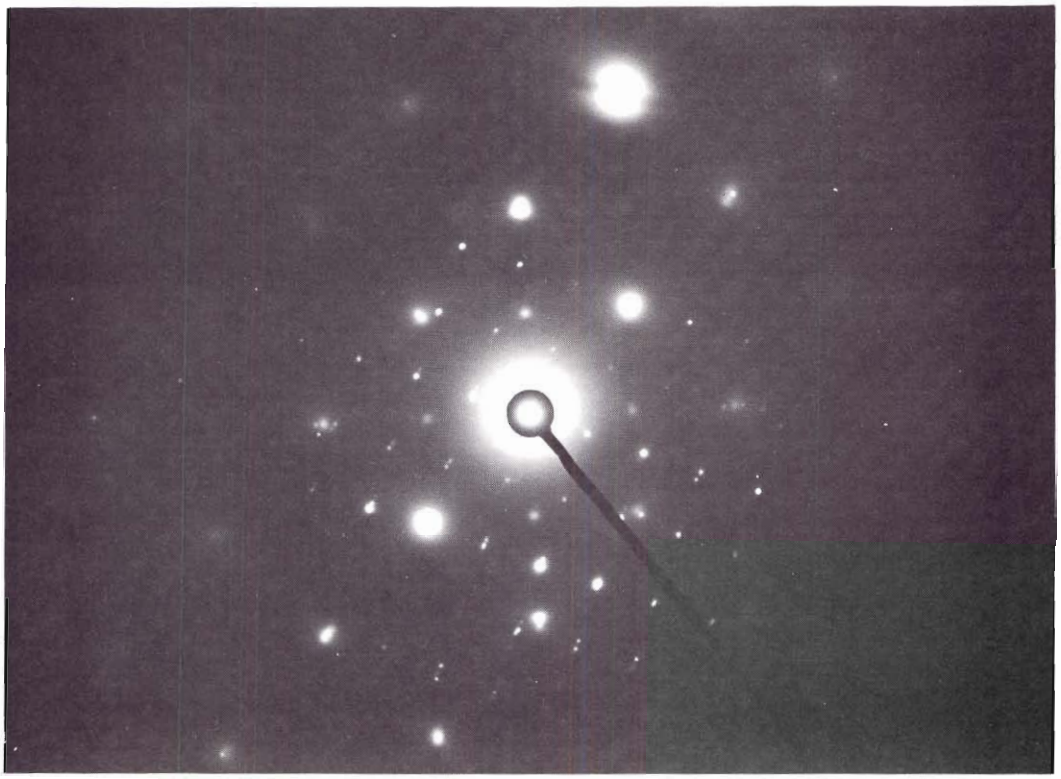

NOTES: CEMENTITE (θ) AND α-IRON WERE IDENTIFIED. THE ORIENTATION RELATION WAS $(001)_\theta \parallel (001)_\alpha$ WITH $[100]_\theta$ 23° FROM $[110]_\alpha$.

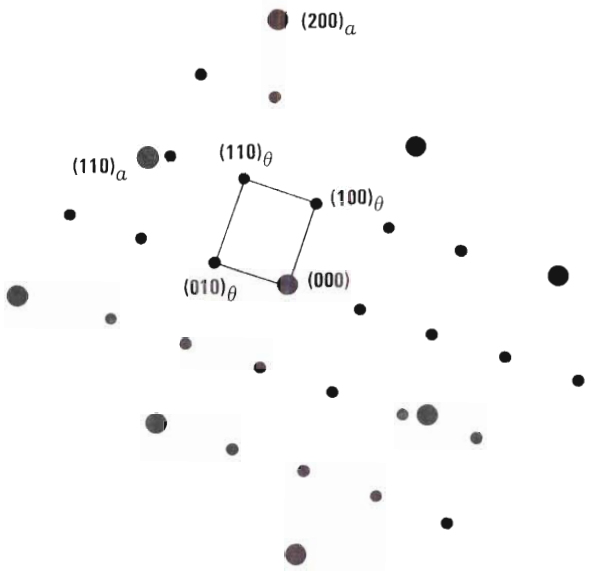

Figure 105. SAD Pattern and Solution Diagram for a Specimen from Reaction 3

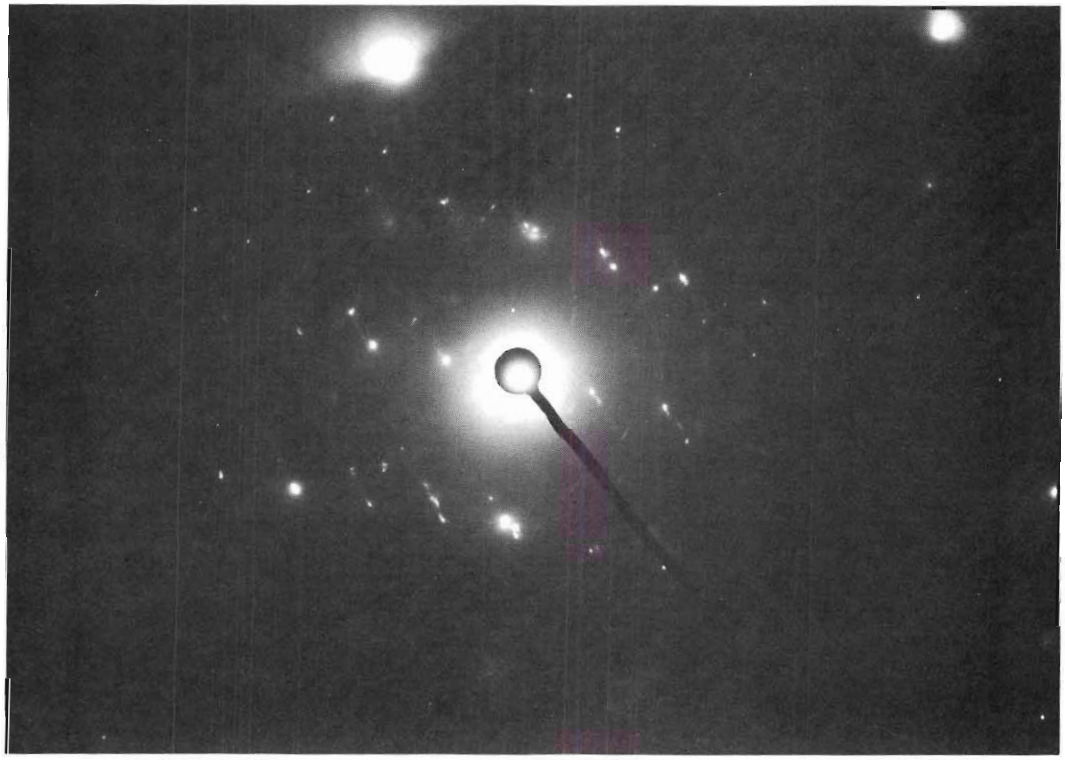

NOTES: CEMENTITE (θ) AND α-IRON WERE IDENTIFIED. THE APPROXIMATE ORIENTATION RELATION WAS $(1\bar{1}\bar{2})_\theta \parallel (001)_\alpha$ WITH $[23\bar{1}]_\theta \parallel [020]_\alpha$.

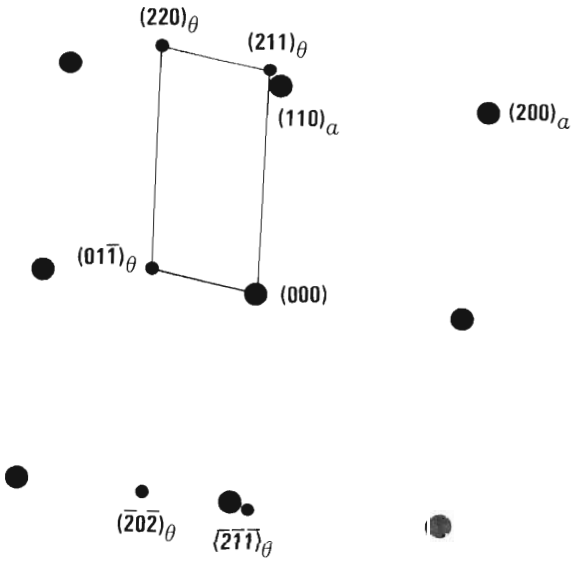

Figure 106. SAD Pattern and Solution Diagram for a Specimen from Reaction 4

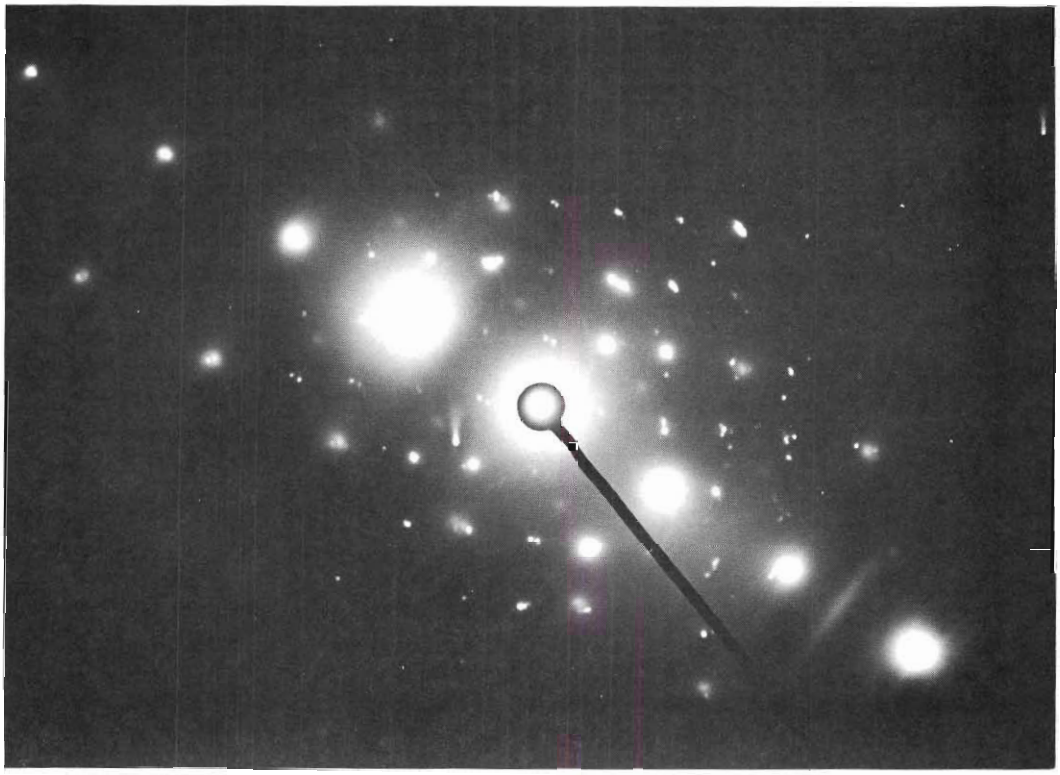

NOTES: CEMENTITE (θ) AND α-IRON WERE IDENTIFIED. THE ORIENTATION RELATION WAS $(001)_\theta \parallel (001)_\alpha$ WITH $[0\bar{1}0]_\theta \parallel [3\bar{1}0]_\alpha$.

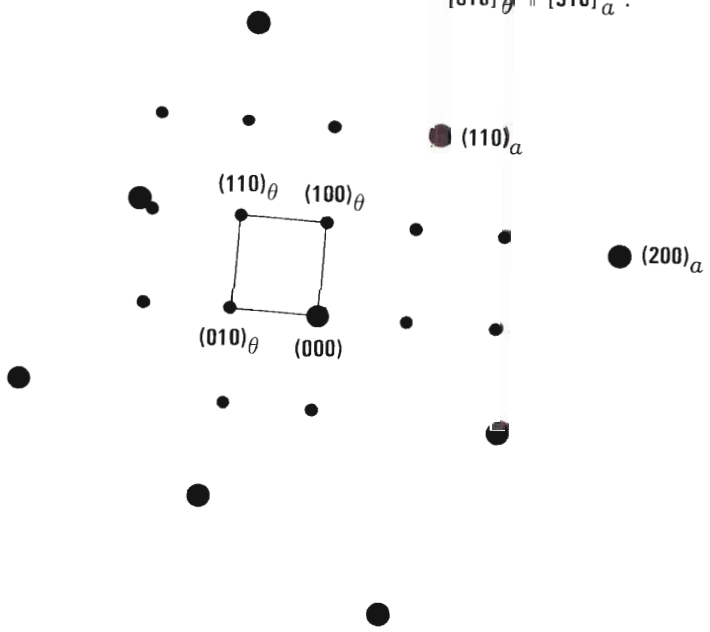

Figure 107. SAD Pattern and Solution Diagram for a Specimen from Reaction 5

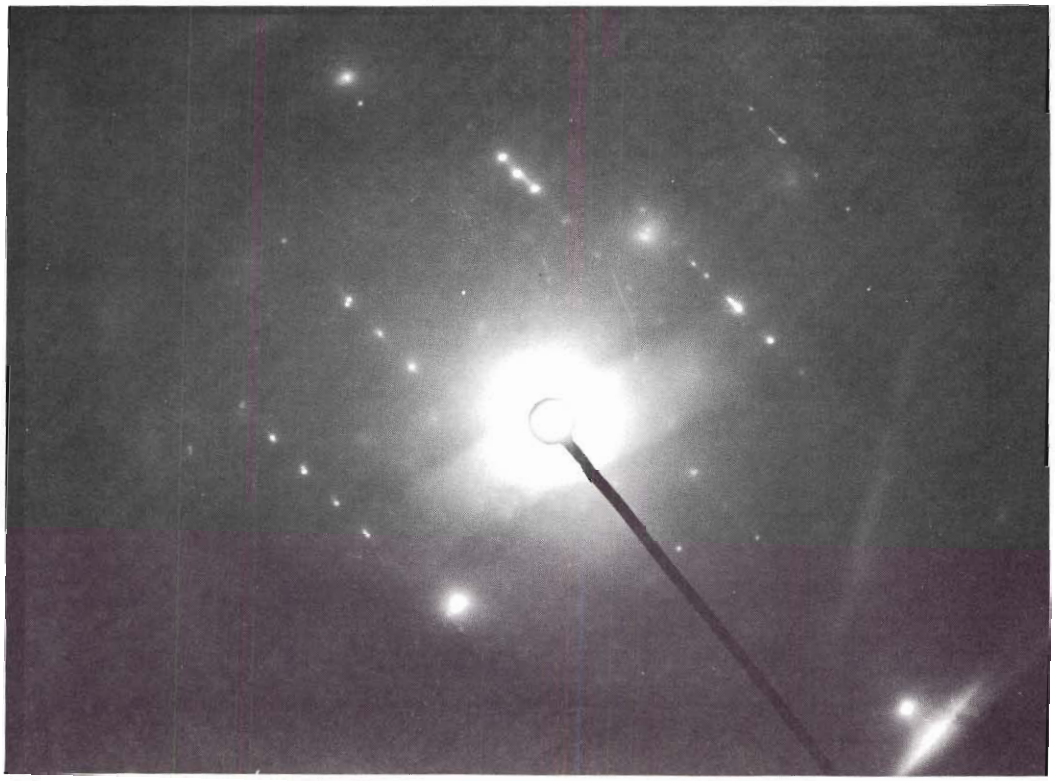

Figure 108. SAD Pattern and Solution Diagram for a Specimen from Reaction 6

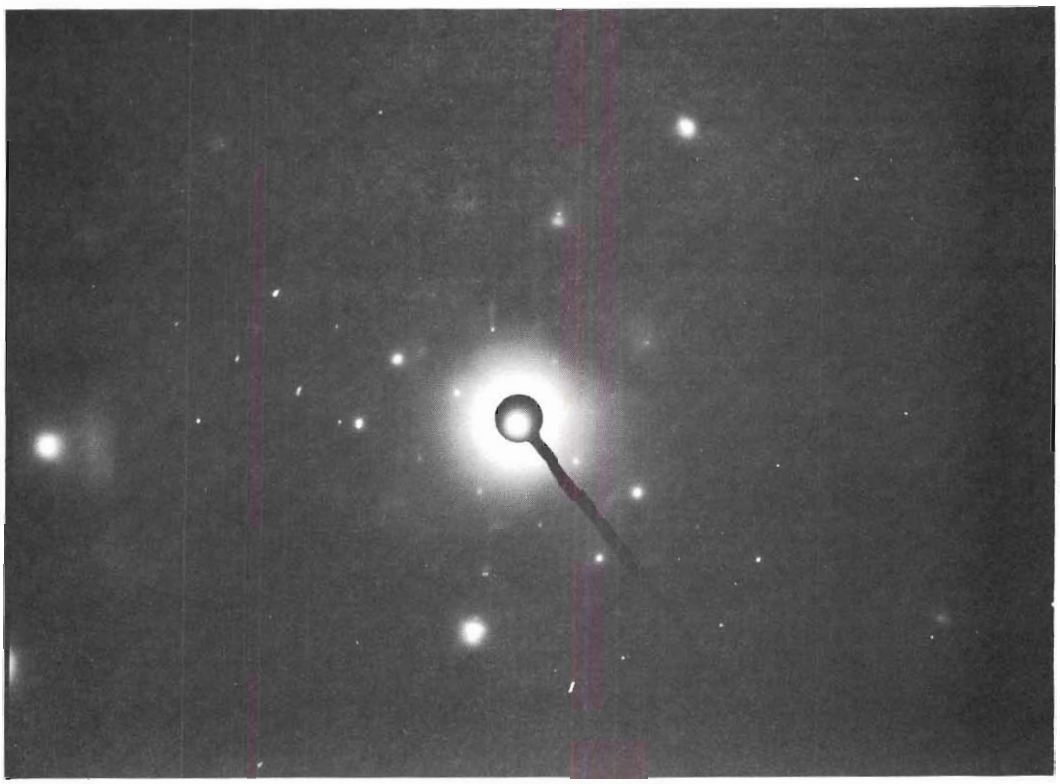

NOTES: CEMENTITE (θ) AND α-IRON WERE IDENTIFIED. THE ORIENTATION RELATION WAS $(0\bar{1}2)_\theta \parallel (001)_\alpha$ WITH $(\bar{1}22)_\theta$ WITHIN 2^0 OF $(110)_\alpha$.

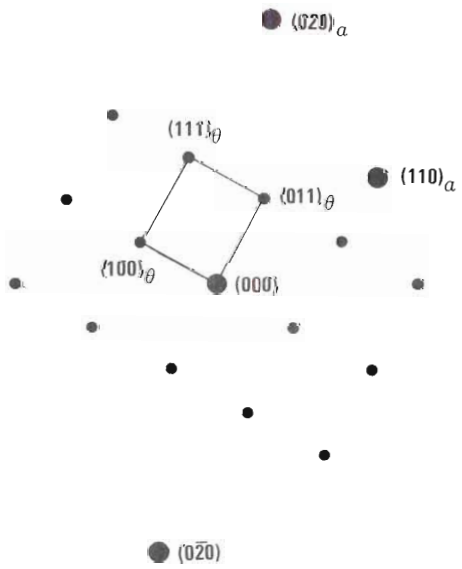

Figure 109. SAD Pattern and Solution Diagram for a Specimen from Reaction 8

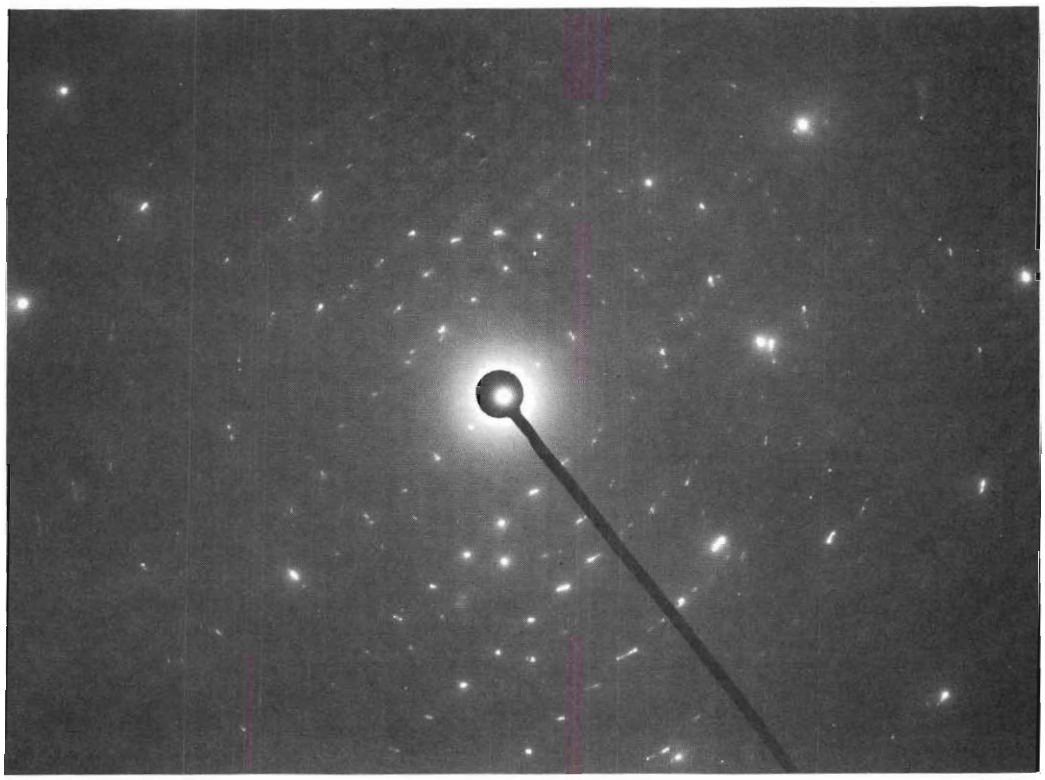

NOTES: CEMENTITE (θ) WAS IDENTIFIED.
THE PATTERN SHOWS THE $(2\bar{3}0)_\theta$
PLANE TO LIE PARALLEL TO
THE FILM PLANE.

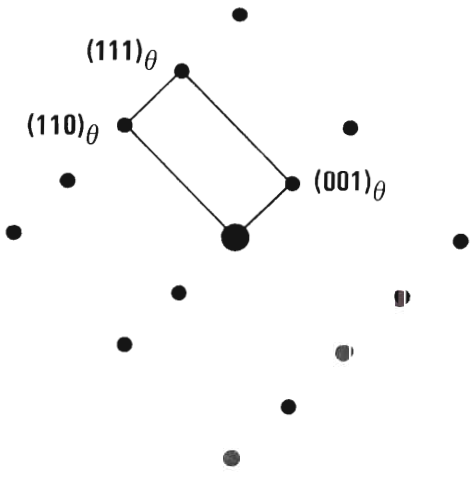

Figure 110. SAD Pattern and Solution Diagram for a Specimen from Reaction 9

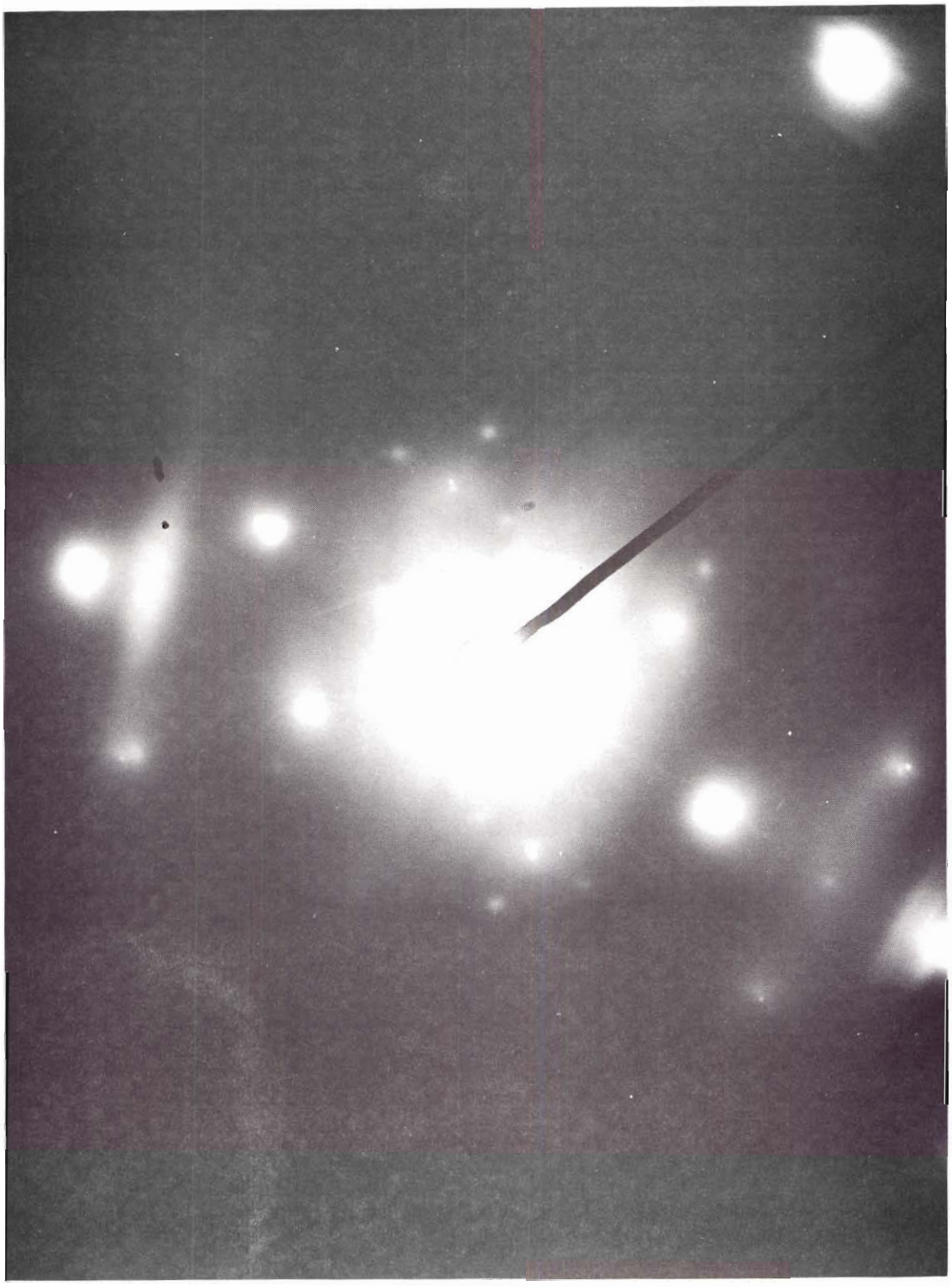

Figure 111. SAD Pattern for a Specimen from Reaction 10

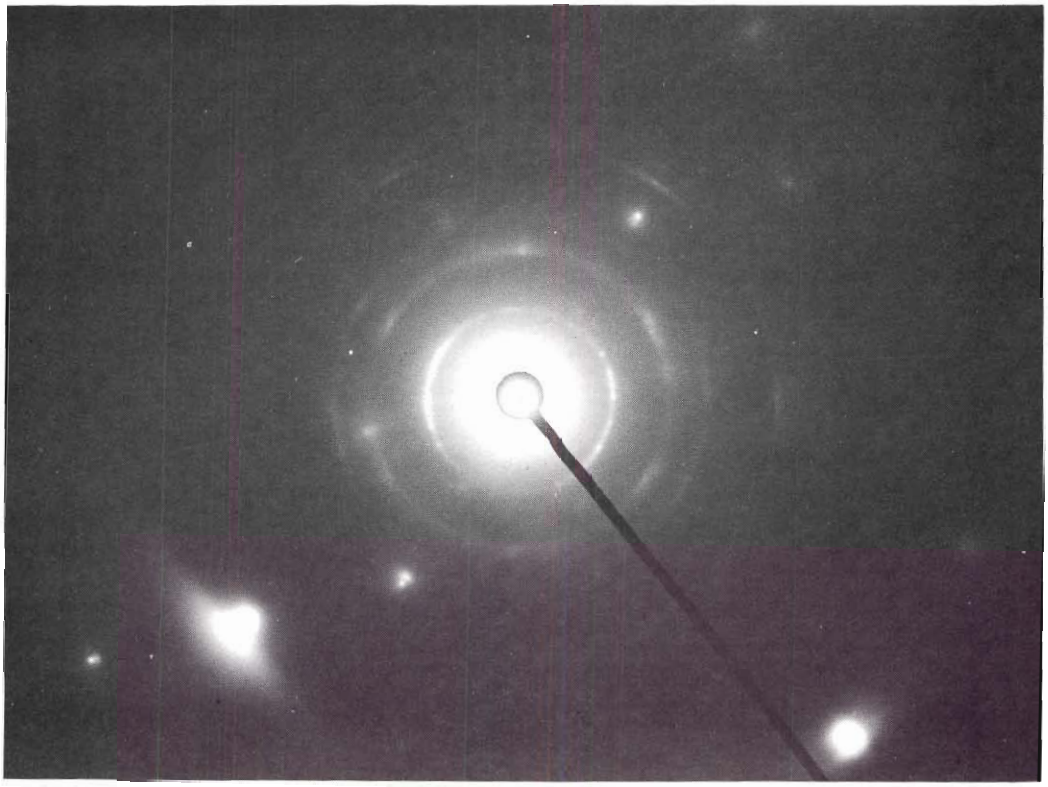

NOTE: GRAPHITE (gr) AND IRON WERE IDENTIFIED.

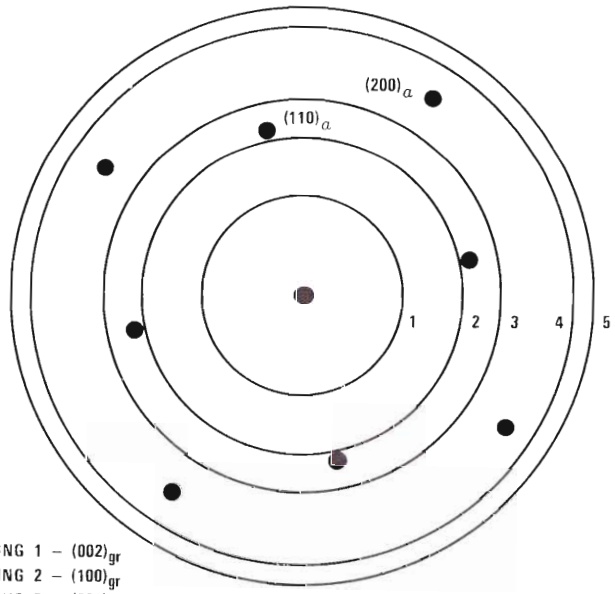

RING 1 – $(002)_{gr}$
RING 2 – $(100)_{gr}$
RING 3 – $(004)_{gr}$
RING 4 – $(110)_{gr}$
RING 5 – $(112)_{gr}$

Figure 112. SAD Pattern and Solution Diagram for a Specimen from Reaction 10

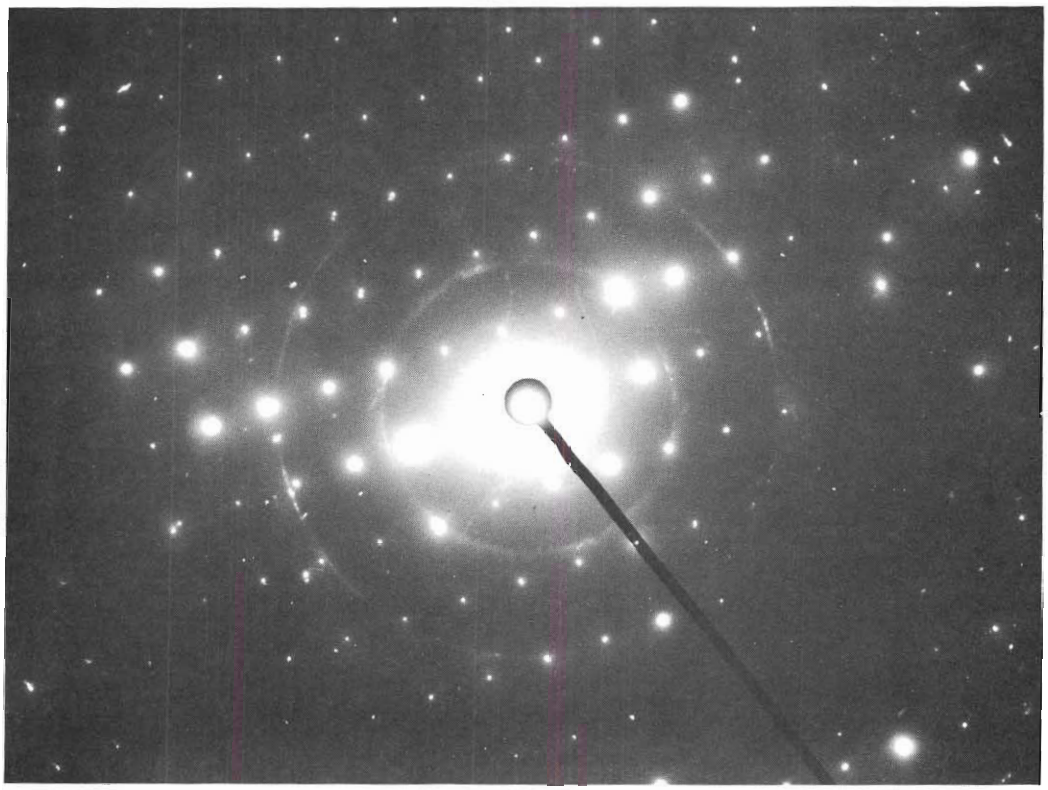

NOTES: CEMENTITE (θ) AND GRAPHITE (gr) WERE IDENTIFIED. THE ORIENTATION RELATION BETWEEN THE CEMENTITE AND IRON WAS $(10\bar{2})_\theta \parallel (001)_a$ WITH $(121)_\theta$ CLOSE TO $(110)_a$. THE BASAL PLANES OF THE GRAPHITE WERE PARALLEL TO THE FILM PLANE.

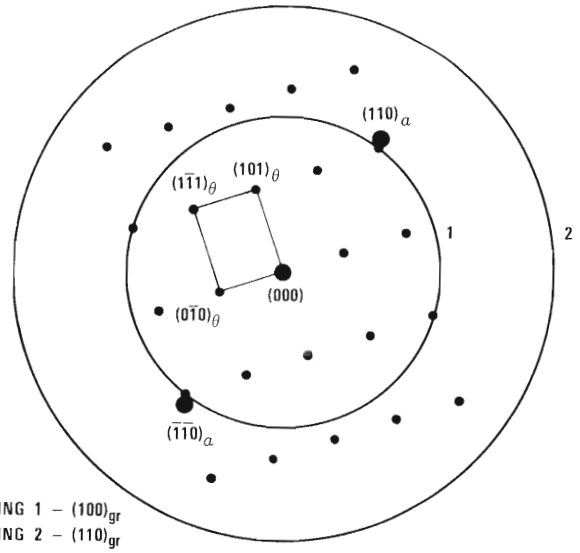

Figure 113. SAD Pattern and Solution Diagram for a Specimen from Reaction 11

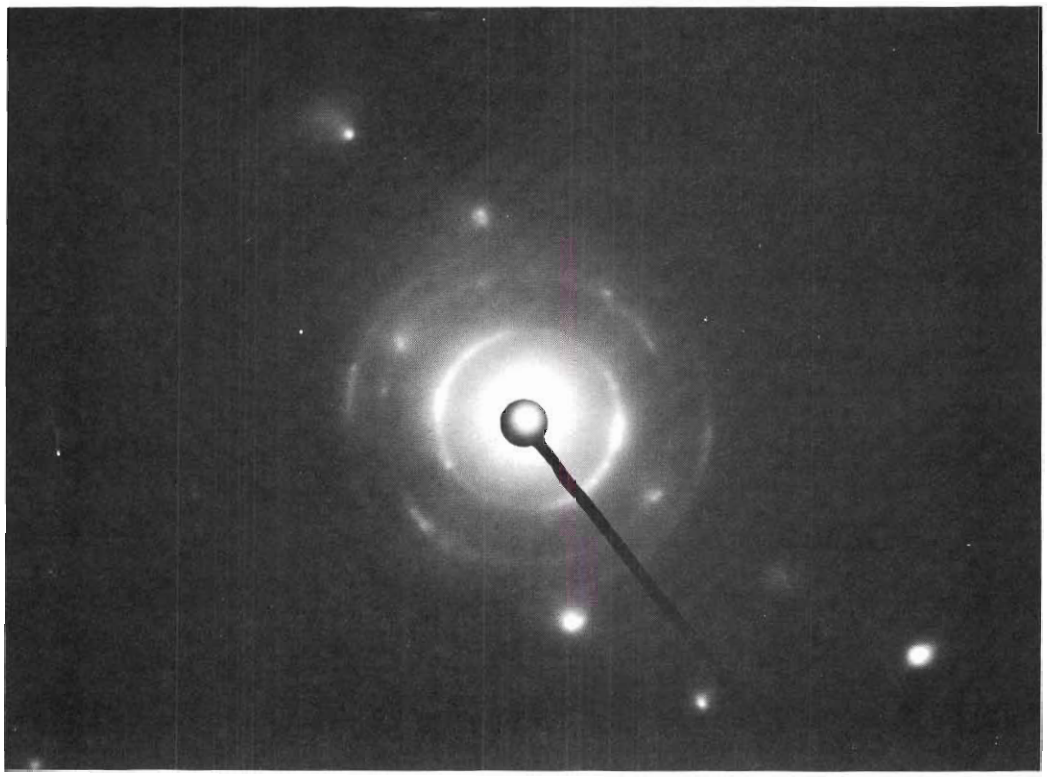

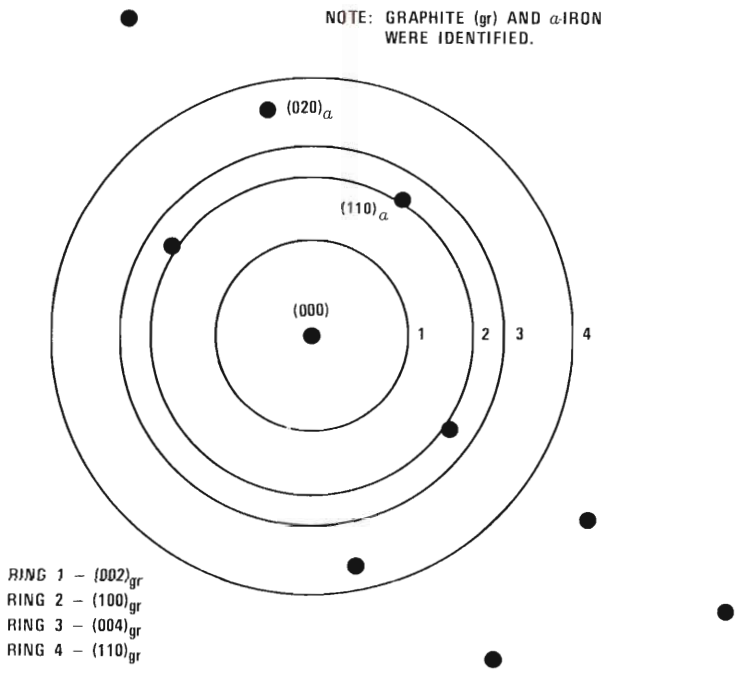

Figure 114. SAD Pattern and Solution Diagram for a Specimen from Reaction 11

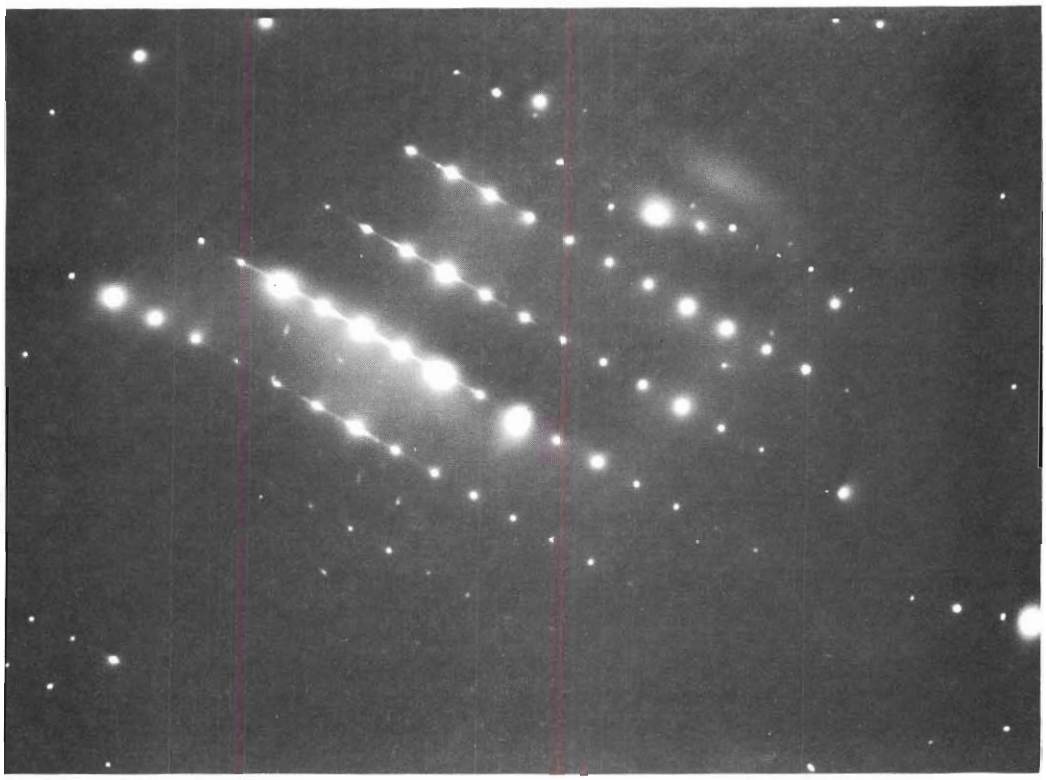

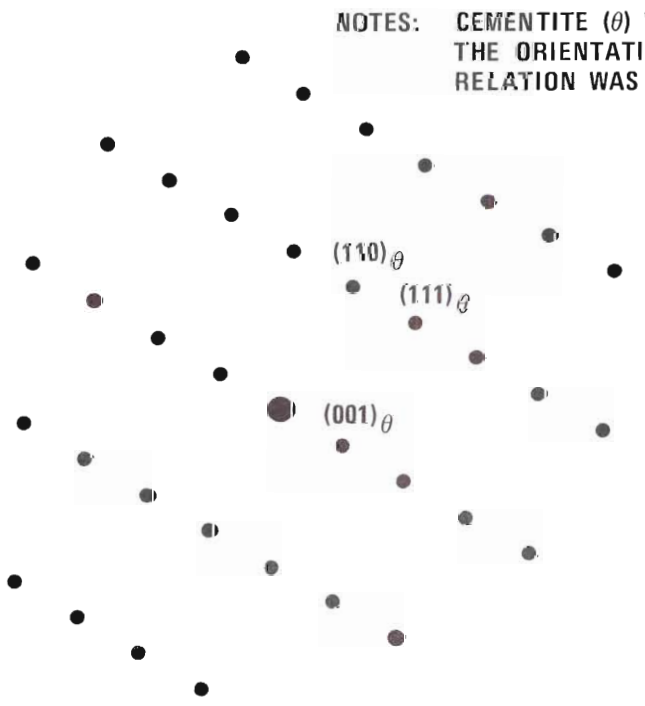

Figure 115. SAD Pattern and Solution Diagram for a Specimen from Reaction 11

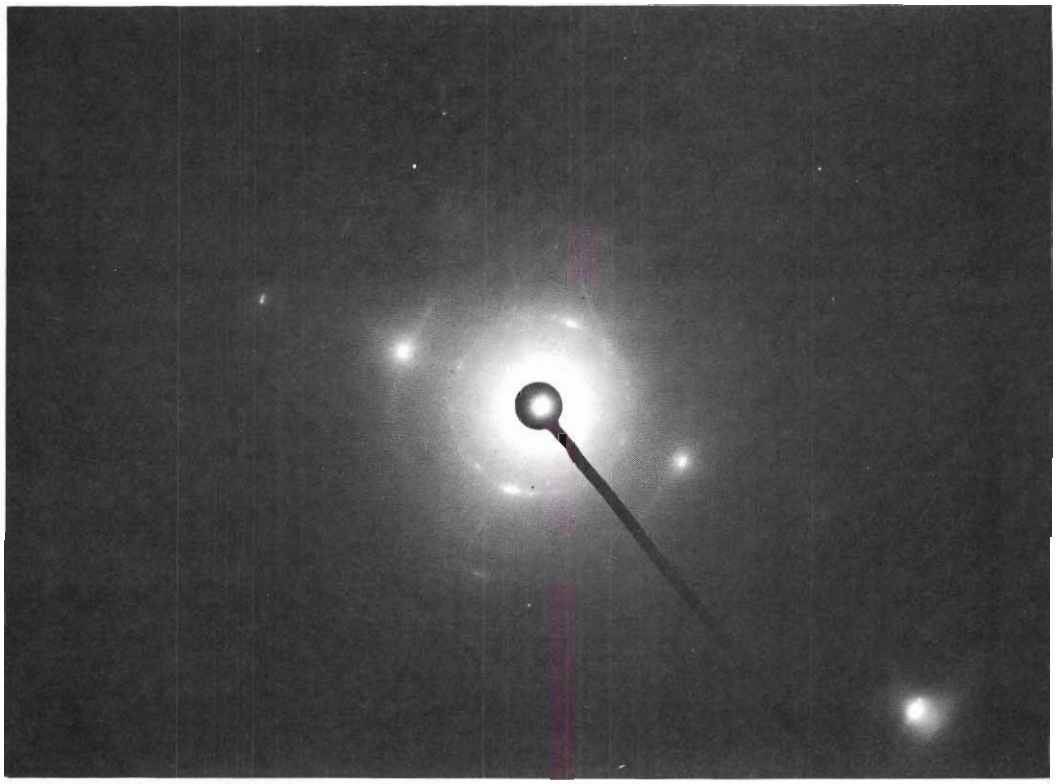

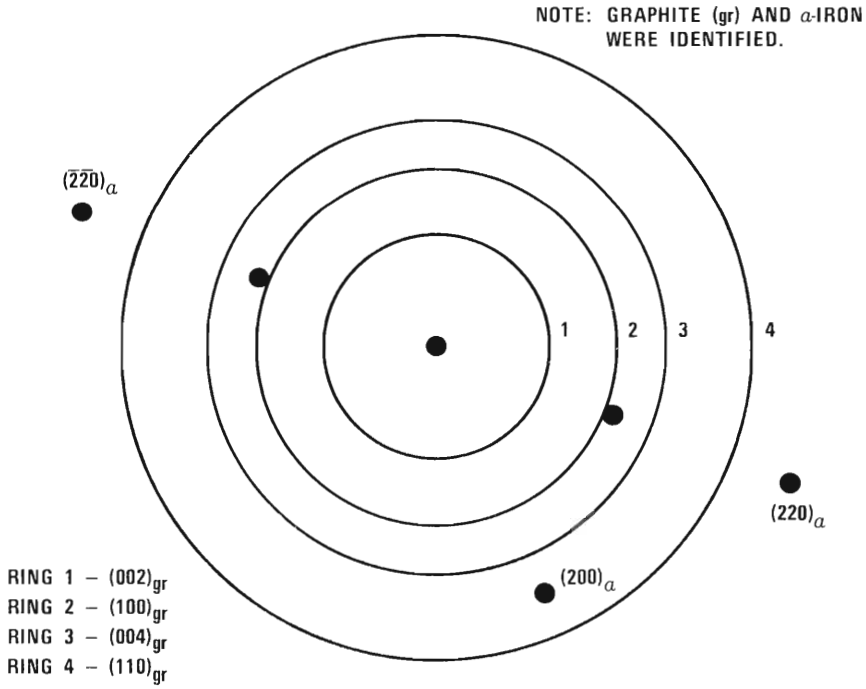

Figure 116. SAD Pattern and Solution Diagram for a Specimen from Reaction 15

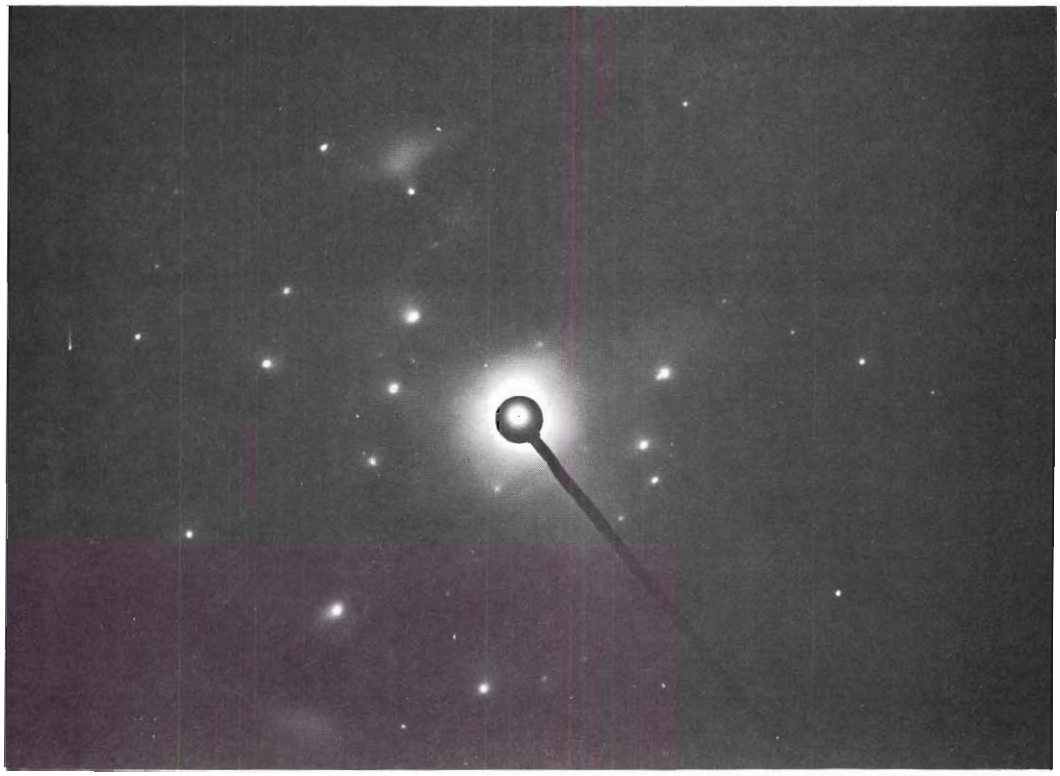

NOTES: CEMENTITE (θ) WAS IDENTIFIED.
THE ORIENTATION RELATION WAS
$(3\bar{1}\bar{2})_\theta \parallel (001)_\alpha$ WITH $(01\bar{1})_\theta$ INDICATED
TO BE 8° FROM $(110)_\alpha$.

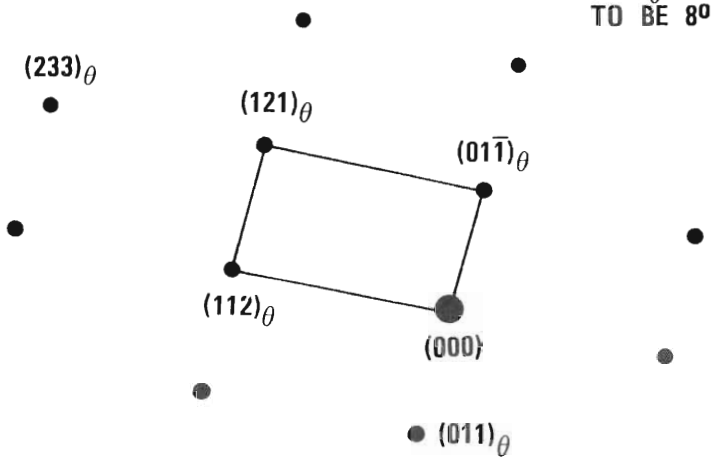

Figure 117. SAD Pattern and Solution Diagram for a Specimen from Reaction 15

at 250°C in 1,000 μ of carbon monoxide. The precipitate particles of Reaction 2 were in the nucleation stage of development, and a few had just begun transformation into incoherent particles. The two nuclei analyzed were of the latter character. Both patterns indicated the presence of cementite, but the orientation between each cementite particle and the ferrite matrix was different.

For the reaction conditions of the films represented in the other SAD patterns, refer to Table 3 under the corresponding reaction number given in each individual figure.

In summation of the information obtained from the SAD patterns in Figures 103 through 117, cementite was identified in all the films reacted for 1 hour in 1,000 μ of CO at the temperatures 320, 350, 450, and 550°C. For the 1-hour run at 250°C in 1,000 μ of CO the precipitates gave no detectable diffraction effects but after 2.5 hours of reaction (Reaction 2) cementite was identified.

Cementite was also found to be present in the reactions carried out at 350°C for 1 hour under both 500 and 100 μ of CO. However, for the reaction at 350°C and 1 hour under 5 μ of pressure, no diffraction effects were found from the precipitate nuclei. The same was true of the 1-hour reaction at 450°C and 5 μ of CO.

Cementite could not be identified in the reaction carried out at 450°C for 1 hour under 1,000 μ of CO which was followed by a vacuum annealing process at 450°C for an 8-hour duration. Only a carbon product was identified. This experiment will be fully discussed later.

Graphite as well as cementite was detected in the sample reacted for 6 hours at 450°C in 1,000 μ of CO. Under the same pressure, graphite and

cementite were identified in a film reacted only 1 hour at a temperature of 550°C.

The control experiments (Reactions 13, 14, and 16) gave no diffraction patterns other than the single-crystal reflections of a (001) iron film and the epitaxic oxide previously attributed to atmospheric oxidation. The epitaxic oxide (Fe_3O_4) film was noted to occur to some extent on every reacted sample.

In order to determine whether oxidation of the iron could take place in the CO producing the Fe_3O_4 observed, Reaction 11 was made. In this experiment the reaction time was 6 hours with 1,000 μ of CO at 450°C. For this experiment, the amount of Fe_3O_4 should have increased significantly if CO oxidation of iron had played a measurable role in the oxide film formation noted for lesser periods of exposure. Since no such increase was observed, oxidation by CO is probably stericly hindered. Carbon monoxide chemisorbs with the carbon atom attaching itself to the iron, and the carbon-oxygen bond is positioned normal to the local metal surface (129). The oxygen in this position is logically prevented from having direct interaction with the iron.

b. Orientation Relationships. Of the diffraction patterns taken from cementite precipitates, fifteen gave rise to well-developed single crystal patterns. Solution of these patterns revealed that eleven different orientations between the lattices of the cementite particles and the ferrite films existed. It is definite from the evidence that no fixed orientation exists between cementite and the (001) iron single crystal films. This is probably true for the surface of bulk iron where the strain and surface energies associated with a growing phase may more readily be accommodated.

Except to accommodate strain and surface energy, no fixed orientation relationship should exist between an incoherent precipitate and the parent matrix. Factors influencing orientation and evidence to illustrate the incoherent character of the cementite precipitate will be presented later.

The cementite planes which were found to be approximately parallel to the (001) iron film plane were: (230), $(2\bar{3}0)$, (100), (001), $(3\bar{1}2)$, (010), $(1\bar{1}\bar{2})$, $(0\bar{1}2)$, $(3\bar{1}\bar{2})$, and (323). The uncertainty in the exact coincidence of these planes with the film plane arises from some buckling of the film. The solutions for the SAD patterns indicated only the planes which were perpendicular to the electron beam. However, this is of no consequence since there was no exact orientation relation to be established.

Ralph (130) has found no fixed orientation relationship to exist between cementite and ferrite in his laboratory's investigations of steels with the Field Ion Microscope. However, the fact that preferred orientations have been proposed after certain transformations (131-135) warrants further analysis of the present results. Three different orientations have been commonly reported. No agreement was found between the present results and any of the three reported relations. However, the $(001)_\theta \parallel \{110\}_\alpha$ part of the total relationship reported by Darken and Fisher (135) for pearlite may be pertinent to the present investigation. The cementite particles observed in this work often contained plane faulting which lay parallel to the cementite (001) plane. This was determined from several micrograph and SAD pattern pairs. Excellent evidence of cementite faulting on (001) planes was illustrated in the SAD pattern of Figure 115. The streaking through the reciprocal lattice points in the $\vec{R}_{(001)}$ direction is indicative of the faulting. Numerous instances of cementite faulting were observed in

micrographs for which no SAD information was available. The faulting traces occasionally lay close to parallel to the < 110 > directions for the lower temperature experiments. This indicates a possible relation between the (001) cementite plane and the {110} ferrite planes. Jack (136) has suggested that the cementite initially forms as platelets only a few unit cells thick. Precipitates of this type in a ferrite matrix would lead to diffraction pattern streaking in the [001] cementite direction. In addition, others (137,138,139) have reported the {110} planes of ferrite to be the cementite habit planes for precipitation during quench aging. However, they did not report $(001)_\theta \parallel \{110\}_\alpha$ to exist.

From the diffraction patterns containing information regarding the relative orientations of the $(001)_\theta$ and $\{110\}_\alpha$ planes, the following was found: two cases of direct coincidence; five instances of approximately 26° of separation; two instances of approximately 11° of separation; two instances of approximately 18° of separation; and one instance of approximately 22° of separation. These angles are very close to values expected for the angular separation from $\{110\}_\alpha$ planes of the following respective planes: (110), (310), (320), (210), and (520). In other words, these planes give corresponding trace angles with (110) in the plane of the film. The corresponding < 110 >, < 210 >, < 310 >, < 320 >, and < 520 > crystallographic directions resemble the traces of the major precipitate axes, which will be discussed further later. If the $(001)_\theta \parallel (110)_\alpha$ relation does exist even during nucleation, it appears that carbide lattice rotation within the incoherent phase boundary occurs during particle growth.

Graphite formations were found to exist in three orientational forms. First, very small randomly oriented grains of graphite were required to

give rise to the diffuse continuous ring segments of Figures 112 and 114. Second, the high intensity arcs on the (002) ring illustrated in Figure 116 indicates preference for the basal plane of graphite to be oriented parallel to both {110} and {100} iron planes. Figure 112 shows a preference for the graphite basal plane to lay parallel to the $[001]_{\alpha}$ zone axis with a broad spread of orientations between $(020)_{\alpha}$ and $(110)_{\alpha}$. The third form observed indicated the basal planes of graphite to lie parallel to the film plane. The orientation of the individual graphite grains of this form was random about the basal plane normal. This observation was based on the absence of the (002) ring and the pronounced (100) and (110) rings, as shown in Figure 113.

The significance of the three graphite orientational types is not presently known, but the phenomenon is probably important to an overall understanding of graphite nucleation. More will be said on graphite nucleation and orientation in the discussions of the electron micrographs.

The orientation of the Fe_3O_4 found on the reacted specimens was the same as that observed on unreacted films.

3. Nucleation Phenomena as Observed and Related to Theory

a. Identification of the Product Nuclei. As already mentioned, trial reactions were carried out on the iron single crystal films in CO. This was necessary in order to determine the CO pressure and film temperature combinations which would yield the most pertinent information by electron microscopy. Experimental Run 49 (Reaction 4) was the first giving a recognizable and characteristic solid product. It was carried out at 350° for 1 hour under 1,000 μ of pure carbon monoxide. Typical electron micrographs for this run are shown in Figures 55 through 59. The reaction pro-

duct was observed to lie in the surface of the iron rather than upon the surface. In other words, the product carbide was surrounded by the iron matrix except for one face lying approximately in the plane of the original iron surface. This conclusion is based on the studies of interface and replica evidence. The product particles gave the appearance of being partially submerged in a translucent fluid. Figures 56, 58, and 59 give examples of cementite-ferrite boundaries inclined to the plane of the composite film. Further replica evidence will be presented later to substantiate the interpretation. The observations then indicated that a precipitation process was operative in the formation of the product crystals. As shown earlier, the product carbide was cementite.

Using Reaction 4 (Run 49) as a standard, experiments were designed to give lesser degrees of reaction by steps so that the reaction product might be traced to its nucleation. The experimental runs tabulated in Table 18 are presented as representing the reaction in the nucleation stages. Tracing the product by following the cementite particle morphology from the large precipitates (having typical projected areas of 0.5 μ^2) to the smaller ones, it was observed that the cementite definitely nucleates on dislocations and sub-boundaries. The evidence is contained in the micrographs for Reactions 1, 2, 6, 7, and 12 as presented in subsection C.1.c. Not all the nuclei pictured in the figures represent that characteristic type traced to the stages of nucleation. Many are rather nondescript. However, it is certain that these images do represent the first solid phase product to form. These nuclei were formed at the same crystallographic locations (the dislocations and sub-boundaries) as those relating to the smallest definable cementite particles. The precipitate nuclei shown in the centers of Figures 44

and 45 were of sufficient crystal development to yield diffraction patterns which were solvable and indicated the presence of cementite. Henceforth, in this discussion all precipitate particles will be classified as cementite whether a direct confirmation by a corresponding SAD pattern was obtained or not. This liberty will be taken to facilitate discussion. It is reasonable to make the assumption that all the precipitate particles (except for graphite found only in extended reaction) were cementite since it was the only carbide to be identified under any condition.

Another feature useful in linking the precipitate nuclei to the larger cementite crystals identifiable by diffraction was the striation of diffraction contrast centrally located in many of the precipitate crystals. As will be discussed in more detail later, a faulted region was often observed to traverse the cementite particles. The faults lay just off the axis of longest dimension in the plane of the film. The contrast from these faulted regions was striated. The faulted layers were characterized as lying perpendicular to the [001] cementite direction. Jack (133) has proposed that cementite initially precipitates during martensite tempering as thin platelets ($[001]_\theta$ perpendicular to the platelets). He proposed that continuation of growth was three-dimensional, giving rise to a shift from the two-dimensional layer type x-ray diffraction pattern to the normal three-dimensional cementite pattern. Evidently, an analogous precipitation effect often occurs in the process being studied here. As illustrated in Figures 47 and 48, some of the nuclei contained a similar striated or faulted appearance as might be expected for cementite from Jack's work.

b. Theory Relating to Precipitate Nucleation. As previously stated, the nucleation of the carbide phase appears to take place within the iron

matrix and not on the surface. This suggests that the process for forming the solid product phase may be one of precipitation from a supersaturated solid solution. The following discussion will illustrate the close similarity of the experimental observations to phenomena predictable by theory. Specifically, it will be shown that the present results closely resemble those of a particular type of precipitation process from supersaturated solid solutions. On this basis it is likely that the CO attack of iron in the early stages of reaction is controlled by matrix rather than surface phenomena.

Christian gives a comprehensive treatment of the subject of precipitation from supersaturated solid solutions in his book, The Theory of Transformation in Metals and Alloys (140). Much of the discussion presented in this section is based on his treatment. From the reports of all investigations of the subject, Christian found it convenient to distinguish the following modes of precipitation:

(1) Continuous (or General)

(2) Discontinuous (or Cellular)

(3) Coherent Precipitation of Metastable Phases

(4) Formation of Segregates or Guinier-Preston (G.P.) Zones

The third and fourth processes occur mainly at low temperatures and in metallic solid solutions. They describe the formation of exceedingly small coherent precipitates whereas most of the precipitates under the reaction conditions of the present work were definitely non-coherent and quite large in comparison. At best, processes (3) and (4) may describe the prenucleation phenomena for precipitating cementite. Nuclei of a precipitating phase often form directly from the solid solution by a series of small compositional

fluctuations. They may also be derived from solute atom segregates (G.P. zones) and metastable precipitates which form first within the parent matrix.

The first two precipitation processes Christian listed are adequate to define precipitation from nucleation to completion. For continuous precipitation, individual crystals of precipitate nucleate in a random distribution. This corresponds to random volume nucleation or to hetrogeneous nucleation on uniformly distributed sites. This description matches that of the cementite particles which were located on the dislocations and subboundaries of the iron film. During continuous precipitation, the process proceeds simultaneously throughout the matrix even though the process rate may vary considerably from one area to another. As growth of a precipitate crystal continues, the solute concentration in the surrounding matrix decreases uniformly until all excess solute has precipitated. Throughout the process the original matrix crystals maintain their shape and relative orientation. The single crystals of iron in the present work maintained their integrity in the experiments performed. The new phase in continuous precipitation is not necessarily the equilibrium phase and may transform, decompose, or dissolve on subsequent nucleation of the equilibrium phase. Cementite is metastable, and as will be shown later in this chapter, it decomposes to yield graphite and free iron.

Discontinuous precipitation has been described as "nucleation and growth occurring on a reaction front that moves through the metastable solution leaving a two-phase aggregate behind." (141) The concentration of solute in the parent matrix changes abruptly in the immediate vicinity of the reaction front. Christian describes the process as "requiring the nucleation and growth of duplex cells," and "involves the fragmentation and

recrystallization of the original solid solution grains." The distribution of the precipitate is not uniform and the process gives a characteristic microstructure to the affected material. It is obvious that the CO attack of the iron films in this study did not give rise to discontinuous precipitation.

Christian (140) points out that continuous precipitation generally occurs in solid solutions of low supersaturation or in systems having large energies of misfit between the phases. As will be discussed later, these conditions hinder nucleation. In solutions of this type, precipitation may be expected to begin at grain boundaries and dislocations (140). These imperfections in the crystal lattice can catalyze precipitation. The description just given is probably representative of the iron single crystal-cementite system presently being investigated. The complex orthorhombic structure of the cementite versus the body-centered-cubic structure of iron with the accompanying bulk density difference (7.87 gm/cc for iron versus 7.69 to 7.74 gm/cc for Fe_3C (72)), constitutes a reasonable basis for assuming considerable misfit energy to exist. The carbon content of the iron single crystals undergoing CO attack will shortly be shown to reach saturation early in the reaction. The degree of supersaturation attained is questionable. Before proceeding with this treatment it should be re-emphasized that precipitation does nucleate at the dislocations and sub-boundaries of the iron single crystals as expected of a continuous precipitation process. The precipitation of carbon from quench-aged steels has been studied as a continuous precipitation process (140), and the present problem is seen as a logical extension. A major difference in the experimental study made in this work from the theoretical treatment of continuous

precipitation is the complication introduced by the continuous addition of carbon to the iron matrix. Appendix F treats the question of the carbon distribution in an iron film resulting from the dissolution of the nascent carbon produced by the surface decomposition of carbon monoxide. An initial assumption was made that the surface concentration of carbon remains constant. It is shown that the time required for diffusion processes to bring the average solute concentration of carbon in the film to a minimum of 99 per cent of the surface concentration would be less than 1 second. With this being the case, it is logical to assume that the film is saturated very early in the reaction. Further, it is reasonable to consider that the iron matrix will remain saturated throughout the precipitation process. The proof of the last two statements should lie in the observations of the amount of product formed at given temperatures and times but for different pressures of carbon monoxide. In other words, at some minimum pressure it is feasible that the supply of carbon from CO decomposition may become slow enough that saturation cannot be attained for a specific reaction period. Under this assumption, the effect should become more severe with decreasing pressure. The result should show up as a decrease in precipitate particle size and population density. At pressures above this minimum the results should not vary drastically. Some variation should be expected from other causes, of course. These observations were in fact made and will be discussed in detail later.

The classical theory of homogeneous nucleation is based on the premise that random fluctuations (concentration fluctuations for solid solutions) in the assembly generate nuclei. The number of atoms in the segregate clusters and correspondingly the cluster size is critical to the forma-

tion of a stable nucleus of the new phase. The ease with which the nuclei form, plus their size, shape, orientation, and distribution are functions of the physical and chemical character of the system in question.

For the homogeneous nucleation of a new phase, the Gibbs free energy change accompanying the process is commonly formulated as

$$\Delta G = \Delta G_{st} + \Delta G_{sf} + \Delta G_{ch} \quad . \tag{2}$$

The first term, ΔG_{st}, takes account of the resistance to a volume change accompanying the creation of a nucleus and is a positive energy term for strain. The ΔG_{sf} is a positive term expressing the energy required to create a boundary associated with the nucleus. The final term, ΔG_{ch}, represents the chemical driving potential for the reaction and must be negative for precipitation to take place. All three terms increase in absolute value as the number of atoms, n, in the nucleus increases, but each is a different function of n. The result is an initial increase in ΔG as n increases until a critical value, n_c, is reached where ΔG is maximized. After a cluster of atoms reaches the size corresponding to n_c it may become a stable nucleus which grows with a corresponding decrease in Gibbs free energy.

The values ΔG_{st} and ΔG_{sf} are relatively independent of temperature in comparison with ΔG_{ch}. The latter increases in absolute value as the degree of supercooling is increased. The term ΔG_{ch} can also be increased in magnitude by using a higher solute concentration at a constant temperature. The nucleation rate I is very sensitive to the degree of supersaturation i and is schematically represented in Figure 118.

The equations used to arrive at the shape of this curve were derived

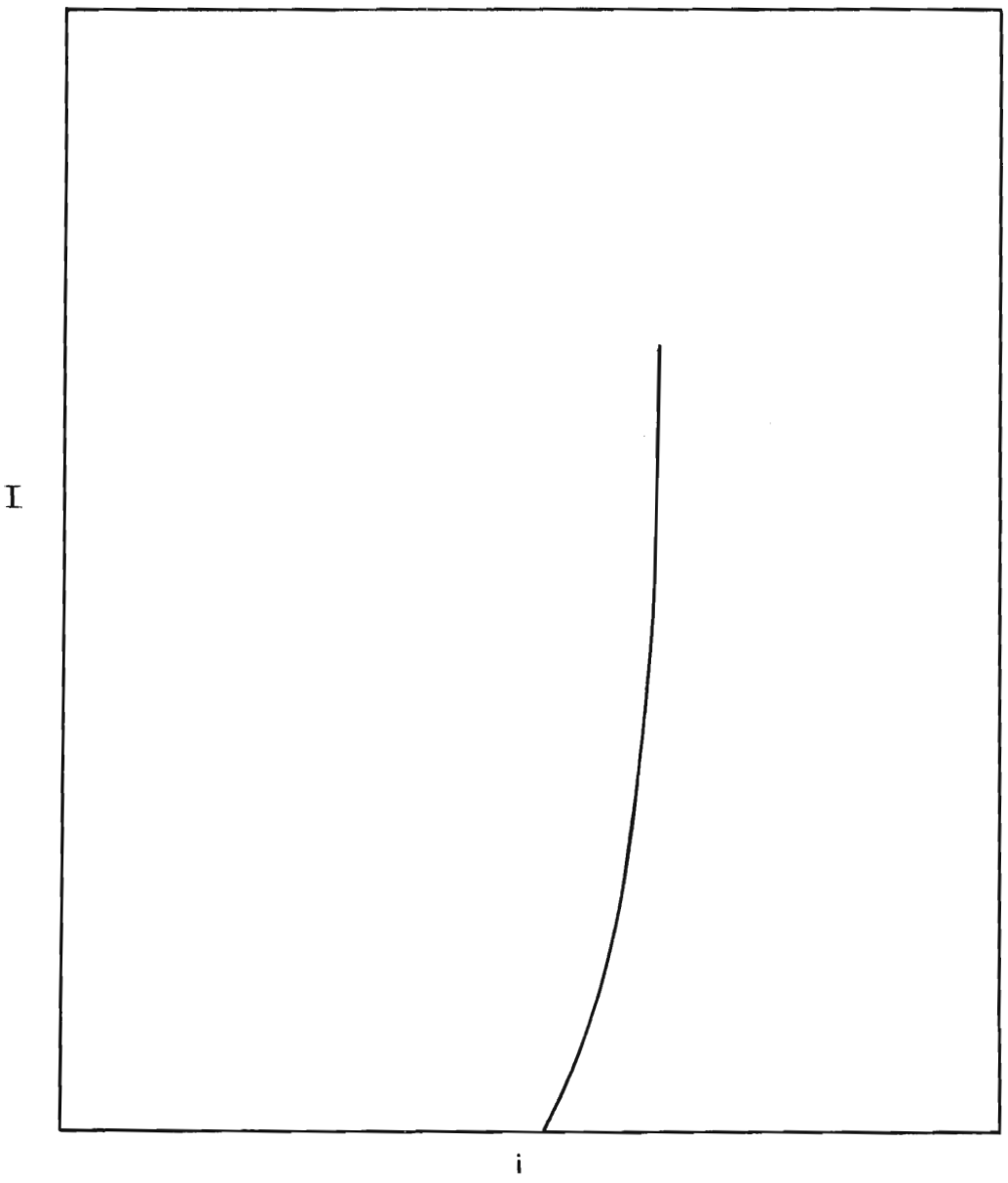

Figure 118. Schematic Form for the Variation of Nucleation Rate I with Supersaturation ï

for homogeneous nucleation from a supersaturated vapor. However, the form of the curve should be similar for solid phase nucleation.

Continuous precipitation from metal solutions are commonly heterogeneous. Mounting evidence supports the view that dislocations are often important to the nucleation of precipitates. Early work by Davenport and Bain (143), and Cottrell and Churchman (144) has shown that the precipitation of carbon from supersaturated solution in alpha-iron can be greatly accelerated by the presence of lattice distortions. This evidence led to the development of the "Dislocation Theory of Strain Aging." Strain aging is regarded as the process whereby solute atoms diffuse toward free dislocations at rest and anchor them by the formation of solute concentration atmospheres. In an early study, Nabarro (145) showed the agreement of this theory with several features of the strain aging of iron. The activation energy for strain aging and the activation energy for the diffusion of carbon in alpha-iron were determined to be the same. Also, the time for strain aging was shown to be of the same magnitude as that expected for the formation of carbon atmospheres at dislocations. Shortly after this analysis was reported, a detailed treatment was published by Cottrell and Bilby (146).

The initial condition for a treatment of strain aging places the solute atoms in a random distribution about a dislocation. An atom situated at the polar co-ordinates (r,θ) relative to a positive edge dislocation has an interaction energy $U = (A \sin \theta)/r$ associated with it. The A is a constant accounting for the rigidity modulus, Poisson's ratio, the slip distance in the dislocation, and the atomic radii of solvent and solute. Equipotential lines, U = constant, form a family of circles passing through the center of the dislocation. These are centered on the perpendicular bisector

of the slip plane which cuts the slip plane at the point of intersection of the extra half plane of atoms. The change in U from circle provides a force on each solute atom which imparts to it a drift velocity in the direction perpendicular to the local equipotential line. The paths solute atoms must take are orthogonal to the family of circles, $(\sin \theta)/_r$ = constant, and are also circles, $(\cos \theta)/_r$ = constant. These pass through the dislocation and have centers on the slip plane. Solute atoms move along these flow lines toward the dislocation until they reach the point of maximum binding, i.e., the point just below the dislocation, $(r_o, 3\pi/2)$. As the atmosphere builds up concentration differences effect the velocity of flow, but in the early stages of aging they can be neglected. In his book on dislocations and plastic flow (147), Cottrell gives a rough calculation for the early stages of the process indicating the main features of his earlier treatment with Bilby (146). In this discussion Cottrell shows that at time t every flow line with radius r less than $(ADt/kT)^{1/3}$ has been drained of solute atoms while only those lines with larger radii are still active. This radius will be used later on in this discussion to illustrate roughly the magnitude of the physical system being discribed under the experimental conditions of the present work.

Harper (142) extended the mathematical treatment of the strain aging theory to the latter stages of solute segregation. He assumed that the decrease in the precipitation rate would be proportional to the fraction previously precipitated. Incorporated with the previous theory, his results took the form:

$$f = 1 - \exp\left[-2L\left(\tfrac{1}{2}\pi\right)^{1/3}(ADt/kT)^{2/3}\right] \quad , \qquad (3)$$

where f is the fraction of the original amount of solute which has precipitated during time t, L is the total length of edge dislocations per unit volume, and D is the diffusion coefficient at the absolute temperature T. His paper substantiated this formulation and the dislocation strain aging theory by a treatment of some experimental data. Harper used the internal friction method for measuring the fraction of carbon remaining in interstitial solution as a function of strain aging time. Specimens were taken with carbon contents in the two-phase region of the iron carbon equilibrium diagram (i.e., 0.015 wt. per cent), strained 5, 10, and 15 per cent and aged at various temperatures up to 51.5°C. From his data on aging he calculated the values of L. These were found to be compatible with previous estimates. His calculated L's are notable from the standpoint of the relative agreement between the samples of different strain. Some of the experiments were carried out to a precipitation fraction as high as 0.85.

A value of $f \approx 1$ is obtained by extrapolating Harper's results with the aid of Equation (3) to a temperature of 450°C for a 1-hour aging time using $D = 5.2 \times 10^{-4} \exp -1900/T$ (148). This result implies that all the carbon in interstitial solution will either precipitate or be tied up in concentration atmospheres at dislocations under the typical conditions of the experiments performed in this work. The equation for the radius of an area completely drained of carbon atoms in the original interstitial solution was applied under the same conditions of temperature and time. The radius of depletion found was 5,000 Å or 0.5 μ. This radius is greater than the average distance between dislocation sub-boundaries in the iron films produced for this research. If this were a true picture of the physical process, it is evident that dislocation interaction with solute atoms would

be a sufficient potential to drive precipitation through to completion. The solute concentration in the vicinity of the dislocations would increase far above the ferrite solubility limit and a carbide phase would precipitate.

Shewmon (149), however, states that the period over which the interaction potential is valid is determined by the volume of matrix over which the potential $U(\theta,r)$ maintains an "appreciable" effect. He argues that when r becomes large enough for $U(\theta,r) < kT$, the driving potential will be less than the thermal energy of the solute atoms and, therefore, "inappreciable." He defines an "effective radius" R for the iron-carbon system where

$$U = kT \approx \frac{10^{-20} \text{ dynes cm}^2}{R} \quad . \qquad (4)$$

This radius is then considered to be a capture radius for the dislocation (screw and edge types being treated similarly) for solute atoms. He states that Ham (150,151,152) has given a more exact definition of the capture radius which yields a value for R 1.78 times as large as the value obtained from Equation (4). For the iron-carbon system at 450°C this radius is 51 Å.

Christian's discussion of the formula for f derived by Harper credits it with reasonable correlation of a great deal of experimental data. He suggests that this is probably fortuitous, as the theoretical basis for Harper's formulation is untenable, according to Ham (150,151,152).

It seems certain from the discussion that a dislocation will at least generate solute-rich clusters in the matrix in the immediate vicinity of the dislocation core. The concentration fluctuations requisite for nuclei formation will, therefore, have a much greater probability of forming a nucleus

of critical size at these locations.

It should be pointed out that there is no evidence for a parallel type of solute interaction potential associated with dislocation surface intercepts. The intercept of a dislocation with a surface should create no more discontinuity than a surface step. Steps are, of course, in abundance on real surfaces.

A theory for precipitate nucleation on dislocations has also been proposed by Cahn (153). In his treatment the nucleus model lies along the dislocation line and has a circular section perpendicular to it. The appearance of the nucleus is similar to that of a bead on a string. In the expression for the energy of formation for a nucleus of given size, a new term is included representing the strain energy of the dislocation within the volume of the nucleus. In effect, the energy gained by destroying the elastic energy of the dislocation during atomic rearrangement is made available to aid the nucleation process. Equation (2) takes the form

$$\Delta G = (\Delta G_{sf} + \Delta G_{st} + \Delta G_{disl}) + \Delta G_{ch} \quad .$$

The negative ΔG_{disl} term has been stated to effectively reduce the ΔG_{sf} and ΔG_{st} terms, thereby reducing n_c (141).

One of the findings of Cahn's treatment was that when the chemical free energy and dislocation energy factors are sufficiently large and negative, there is no energy barrier to nucleation on dislocations. In this event the transformation rate will be governed only by growth phenomena. Under more normal conditions the activation energy is still greatly reduced. This information was found useful in interpreting the nucleaion observed in this study, as will be shown later on.

Christian (140) gave a relevant comparison of nucleation rates for the ease of homogeneous nucleation versus heterogeneous nucleation on dislocations based on Cahn's theoretical treatment. Parameter values used in the calculations were typical of a metallic system. For homogeneous nucleation, the rate was estimated at 10^{-70} nuclei cm^{-3} sec^{-1} while the rate under the same conditions on dislocations was 10^{8} nuclei cm^{-3} sec^{-1}. This example serves to illustrate the probable importance of dislocations as sites for nucleation in solid phase precipitation processes. The experimental fact has broad support, and the quench-aging process for iron-carbon solutions is an example.

Doremus (154) has demonstrated that the number of particles precipitating in an iron-carbon system is constant throughout transformation. This finding implies that the carbide nuclei saturate the active sites within the matrix at the beginning of the aging process, and no further nucleation occurs. Only a very low activation energy for nucleation would give rise to the rapid site saturation. The locations of the precipitate nuclei for the quench-aging process are well established as matrix dislocations (138,139,155,156,157) as long as the carbon supersaturation does not exceed that required for additional precipitation at lattice sites. As a result of this finding, Doremus was able to use his kinetic data for precipitation to calculate an activation energy representative of the actual growth process taking place.

At this point one other feature of Cahn's treatment needs to be mentioned. The rate of change of dislocation nucleation with the chemical driving potential (the degree of supersaturation) is even more sensitive than that for homogeneous nucleation. This important concept will be used

in interpreting the nucleation phenomena observed in the present work. In the system studied the nuclei are expected to be generated quickly on supersaturation of the iron film.

There are two major categories into which precipitate particles can be classified, coherent and incoherent. Briefly, a coherent precipitate is one which has the same type of crystal structure as the parent matrix and maintains atomic plane co-ordination across the interface. However, there may be considerable strain in the two lattices at the interface due to lattice parameter differences. The contrast effect in the electron micrographs caused by a coherent precipitate is complex. In rather unsophisticated terms, the precipitate may appear as a region of diffuse contrast. It may also be quite small and indistinguishable in the presence of the relatively large strain fringes sometimes produced by diffraction from the surrounding matrix. Under these conditions the precipitate cannot be accurately sized from the micrographs. The precipitates in the earliest stages of formation observed in this work have such an appearance as shown in the figures for Reactions 1, 2, 6, 7, and 12. The effect is most pronounced in the micrographs of precipitates formed at 250°C. Evidently, at this low temperature the available thermal energy is small enough to allow the formation of larger precipitate structures before they break free to form incoherent particles. The fact that this process takes place is evidenced by the nuclei found for longer reaction times at 250°C, i.e., Figures 44 through 49. It is obvious from these that incoherent precipitates were to be the end result.

In incoherent precipitation the particles have a crystal structure type differing from that of the parent lattice, and there will be no cor-

respondence of atomic positions. The nature of the interface can be either sharp or diffuse. Some of the more mature precipitates produced in these studies show how complex this interface between cementite and iron can be, i.e., Figures 72, 76, 77, and 78. The micrographs reveal complex dislocation structures which can be reasonably expected to facilitate the diffusion of carbon and iron as the cementite boundary advances.

The contrast from incoherent precipitates of the size most commonly encountered in this work should result from structure factor and diffraction differences between the iron matrix and the precipitate. The distinction should be quite clear except perhaps in areas of inclined interfaces. Fringes in the vicinity of the precipitate will not be localized to the extent of coherency strain fringes but should result from extinction contours introduced by foil buckling. Fringes at inclined interfaces result from diffraction contrast effects analogous to those produced by a fault plane. These effects from two phase materials have been fully treated by Hirsch, et al. (2).

A third type of precipitate frequently encountered is the partially coherent particle. Here the requirement is the coherence of at least one of the interfaces. As a result, some orientation relation between the parent and precipitate lattices will occur. An initial stage in carbide precipitation, characterized by this type of particle, is a distinct possibility. Andrews has shown that carbon diffusion and small shifts of iron atoms in the b.c.c. lattice are all that is required to form cementite (132). Evidence for this occurrence is illustrated in the micrograph and matching SAD pattern shown in Figures 44 and 103, respectively. The micrograph shows the region of the precipitate to be made up of a combination of contrast

effects both sharp and diffuse. The diffraction pattern solution shows reflections A and B to correspond to the (030) and (023) planes, respectively. This solution indicates the relation $(100)_\theta \parallel (001)_\alpha$ to hold between the cementite and ferrite matrix with $[010]_\theta \parallel [3\bar{1}0]_\alpha$. A complete two-dimensional array was not obtainable for the SAD pattern of the precipitate shown, which could be the result of a difficiency in the three-dimensional development of the particle. This illustration is not proof of the occurrence of partial coherency, but the evidence shows that it is a distinct possibility.

The strain energy of an incoherent precipitate particle is a function of its shape. Under suitable conditions this strain can be made very small. Nabarro (145) has shown theoretically that the strain energy introduced into a system by the creation of an incoherent precipitate is least for disc shaped particles, greatest for spheres, and intermediate for needle configurations. Consequently, incoherent nuclei formed under constraint in a solid phase will always have a shape approximating a flat plate or an oblate spheroid. The strain energy for a coherent particle also varies with the shape. However, only a limited reduction in the strain can normally be achieved by changing the shape. If it were not for surface energy effects all precipitates might be expected to be incoherent.

The surface energy which opposes the strain energy factor is much larger for an incoherent boundary than for a coherent boundary. Since the strain energy is proportional to the volume of a precipitate particle, the surface energy will be the dominant energy factor for the smaller particle sizes. Thus, the nuclei may be coherent while the more mature precipitate crystals are incoherent. As the nucleus grows the strain energy will increase until it may become energetically favorable for the particle to "break

away" from the matrix. According to Christian, this breaking away should occur quite early in a nucleation and growth reaction.

Diffraction and contrast effects from two-phase materials as observed in the electron microscope are important to this work. In summary, the presence of particles of a precipitate phase can have several effects on the diffraction pattern from the parent matrix. The diffraction pattern of the second phase may be superimposed on that of the parent lattice. Precipitate shape effects on matrix reflections may also be present in the total pattern. The presence of the precipitate can produce changes in the matrix diffraction spots. Double diffraction may occur when the electron beam must pass through both phases.

In the case of small coherent particles, there are two of these effects to consider. First, the segregation of solute atoms into precipitate clusters produces centers having a different scattering power from that of the matrix. The shape of the reciprocal lattice points for the parent phase will accordingly depend on the shape of these particles. Spherical precipitates produce a diffuse shell around each reciprocal lattice point. Disc shapes produce a streak through each point perpendicular to the plane of the disc. For rod shapes there is a sheet of intensity formed through each reciprocal lattice point. The second effect on diffraction is produced by elastic distortion of the matrix. The result is displacement and streaking of the lattice points in a direction parallel to the distortion. The effect is characteristic of segregation by the solute atoms to planes parallel to parent matrix planes. Care must be taken in interpreting this particular effect because plane faulting of a pure phase may give rise to a similar diffraction pattern. This information is quite useful in ex-

plaining diffraction contrast features to be described later.

Partially coherent particles generally have crystal structures which are closely related to that of the matrix. The precipitate in this case will diffract according to its own crystal structure and the resulting compound pattern may reveal the orientation relation between the precipitate and matrix lattices. The latter effect is not a necessary result since the prominent zones for both lattices will not appear together for all sample orientations. The most distinctive feature for diffraction patterns from partially coherent precipitates is the clustering of small spots slightly displaced from matrix spots (2).

Non-coherent precipitates diffract according to their own crystal structure. Complications to the diffraction pattern arise from the superposition of patterns and double diffraction. The latter effect may lead to the repetition of the precipitate pattern around each matrix reflection. In general, non-coherent precipitates bear no specific orientation relationship to the matrix. As a result, there is no reason for a prominent zone pattern for the precipitate to appear coincident with one for the matrix. The intensity of the diffraction pattern obtained from the precipitate is partially dependent on the quantity of material present. Therefore, the presence of a second phase is not necessarily ruled out from the lack of an observable pattern. In addition, some non-coherent precipitates are amorphous and produce no extra spots in the composite pattern.

The interpretation of contrast from particles in a second phase is a complex problem. For a treatment of the subject one is referred to the book by Hirsch, et al. (2). A rigorous analysis of the contrast effects observed in this work will not be given since the subject being explored can

be more than adequately treated without it. In the present study the contrast effects to be explained were for the most part obvious effects caused by differences in the structure factor between precipitate and matrix and by diffraction contrast. Dark field techniques have been used when appropriate to identify the precipitate phase. After identifying the precipitate phase under experimental conditions which produced it in quantity, the reaction conditions were modified to reduce the amount formed and thereby to trace the reaction produced precipitate to its point of nucleation. The contrast effects referred to as carbide nuclei although not completely characterized in this work are a result of reaction and appear at defects shown to be associated with identifiable carbide particles.

Electron microscopy is also useful for determining the habit planes of precipitate phases. An observation of plate-shaped particles can arise from two causes. First, plate shapes can result in lower strain energies as mentioned earlier. However, the requirement that a plate shape be adopted still does not determine the crystallographic plane on which the particle will form. In iron, precipitates form preferentially on {100} or {110} planes (141). The {100} habit plane has been commonly observed for coherent and semi-coherent precipitates (141). This may be the result of the minimum elastic modulus in the < 100 > direction in cubic metals. If most of the strains introduced by the creation of a precipitate are accommodated in the < 100 > direction, then the strain energy has been minimized for the particle under consideration. Therefore, a precipitate plate of {100} habit is the configuration offering the lowest strain energy possible for precipitation.

A spherical shape is not always the necessary configuration for a

precipitate which introduces very little strain into the system. Certain crystallographic planes may produce a lower interfacial energy with the precipitate than others due to good matching of the precipitate and matrix lattices at the interface. The formation of a polyhedron or a plate could then lead to minimization of the surface energy. Even when appreciable strain is involved the combination of strain reduction by plate formation and surface energy accommodation by suitable habit plane precipitation can result in the configuration with the lowest possible total energy. The plane of closest packing in iron is the {110}. It is known to be the habit plane for several systems in which surface energy minimization is more important than the reduction of strain energy obtained with a {100} habit. Materials with hexagonal structures are notable examples (141). Cementite has also been reported to have {110} habit planes in iron (131,136,138) although its crystal structure is a complex orthorhombic type.

c. Character of Nucleation Sites. The crystallographic feature which was observed to act as the primary site for carbide nucleation was the dislocation sub-boundary. Individual dislocations also appeared to act in this capacity.

The sub-boundaries characteristic of the iron films tended to give < 110 > traces in the surfaces of the iron crystals. Another interesting feature of the sub-boundaries was the fact that the individual dislocations could normally not be resolved in the electron microscope. As shown earlier, this implies that the dislocation lines overlapped. The result was a tendency for formation of a {110} boundary plane perpendicular to the plane of the film. The orientation of the ferrite matrix on either side of the sub-boundary appeared to be very close as shown by electron diffraction.

Thus, the nature of this fault boundary appears to result in a lesser degree of misorientation than that often accompanying the formation of the low angle boundaries of polygonized material.

The dislocation densities of the films were not determined since it was not possible for all the dislocations in the boundaries to be resolved. The number of dislocations existing other than in the boundaries must have been extremely small since extensive annealing was conducted prior to exposure to the CO. As a result, the character of nucleation on isolated dislocations may not have been properly displayed in the micrographs of this research.

Figure 41 shows a complex structure of nuclei in an area between perpendicular sub-boundaries. There seem to be dislocations pinned in the sub-boundaries which pass into the nuclei complex. The evidence indicates that nucleation may be associated with individual dislocations as well as sub-boundary planes. Support of individual dislocations acting as nucleation centers may be found in the micrographs for Reaction 12. This run was carried out at 450°C for 1 hour at 5 μ of CO pressure. Here almost all dislocation features contain nuclei.

A reasonable picture of the dislocation density in the sub-boundaries may be obtained from Figure 43. In the micrograph a region of the iron crystal is surrounded by a dislocation sub-boundary. It is evident that some segments of the boundary are inclined to the plane of the film allowing resolution of the individual dislocations. The spacing is about 100 Å. Considerable segregation of solute to individual dislocations can therefore occur before a combined action of the dislocations at sub-boundaries could be expected to dominate the precipitation process.

Since nucleation for this reaction occurs almost exclusively at dislocations and dislocation sub-boundaries, the density of nuclei is highly heterogeneous. The nuclei may be quite closely spaced along the same defect line. However, the nuclei density taken over a relatively large area is rather uniform due to an overall uniformity of the crystallographic defects, i.e., Figure 95.

Figures 92, 93, and 94 are good examples of an effect apparently associated with the presence of small precipitates in sub-boundaries. Numerous dislocations are seen to be pinned at points in the boundaries which can be directly related to precipitate nuclei. However, to use dislocation pinning in sub-boundaries alone as evidence of the existence of small precipitates is difficult. The boundaries themselves can pin or retard the movement of dislocations, but the degree to which this occurs should be less than that arising from pinning by precipitates. The point is made because micrographs taken of reacted films showing large precipitates but low precipitate density raise the question of the character of likely nucleation sites seemingly uneffected by the reaction. In other words, might not foil supersaturation be limited to very local areas due to local CO decomposition.

Reaction 6 is a good example for initiating an explanation of this question. This run was made at 350°C under 100 μ of CO for 1 hour. The data for this reaction show that some precipitates have formed but that the precipitate density is abnormally low. This constitutes a condition where nucleation should become rapid under the assumption of uniform film supersaturation. Therefore, many potential nuclei should exist as solute clusters on the dislocation boundaries. The electron micrographs of Reaction

6 show a high degree of sub-boundary decoration by dislocations. The pictures of this effect are shown in Figures 65, 66, and 67. Considering the reaction conditions and the high incidence of dislocation decoration, it seems plausible that much of the pinning is caused by the presence of precipitate embryos. Further, justification for this supposition is derived from the relatively low incidence of decoration in unreacted films and films in which a great deal of precipitation has occurred. In the latter type of experiment, the embryos are expected to dissolve. The lowering of the degree of supersaturation coupled with the surface and strain energies associated with the nuclei will cause re-solution of nuclei after preferred growth centers are established. The effect is also associated with the sensitivity of the volume nucleation rate to the degree of supersaturation. These observations present plausible evidence that carbon saturation of the lattice resulting from CO attack is not localized.

d. The Variation of the Nuclei Density with Temperature, Pressure, and Time. The phenomena involved in the precipitation of carbon from an iron single crystal receiving carbon from a surface reaction make rigorous analysis of the density of nucleation sites a difficult problem. An objective of this study was the formulation of a plausible explanation for the observed variation of precipitate nuclei and particle population densities with temperature, pressure, and time. The variations are shown in Table 18. In retrospect, it is evident that a minimal amount of experimental data is available for this analysis. However, it is proposed on the basis of the information available that the degree of supersaturation is the parameter directly responsible for the observed variations.

The degree of supersaturation as a driving potential for precipitation

is in itself a function of both temperature and solute concentration. The sensitivity of the nucleation rate to the degree of supersaturation has already been established. In an initially saturated solution, a decrease in temperature will bring about an increase in the degree of supersaturation, while at constant temperature an increase in solute content will give a similar result. In this study temperature, CO pressure, and time were the adjustable parameters, and all three may effect the carbon content of the iron film. The solubility of carbon in iron varies with temperature but is always extremely small. The degree to which CO can supersaturate iron is unknown but may be close to constant when the temperature is varied and the CO pressure held constant. The basis for this line of reasoning is that the maximum carbon content obtainable above that for saturation may well vary with temperature in the same manner as the carbon concentration for saturated ferrite. Also, it is plausible that a maximum concentration does exist for relatively low carbon concentration. This is proposed since martensite having a carbon content of approximately 0.025 weight per cent (158) must exist as an unstable body-centered-tetragonal crystal (an expanded ferrite lattice). In other words, there must be a limit to the amount of carbon the iron matrix will accept before the lattice is significantly modified.

Pressure may effect the rate of decomposition of CO on the iron surface and thus the rate of carbon penetration into the lattice. These two phenomena may take place at the same rate or else CO decomposition is the slower process since surface carbon was not found to build up to a detectible level by analysis with the electron microscope. Surface graphite, as shown later, appeared only after a second nucleation had begun.

An effect on the rate of decomposition of CO, whether caused by temperature or pressure change, will result in a time dependence of the carbon concentration in the sample. As a result the nucleation rate may be time dependent since it is a very sensitive function of the degree of supersaturation. As previously discussed, nucleation on dislocations is expected to have little energy barrier resistence and consequently to occur rapidly in a supersaturated matrix. Therefore, a time dependence of the nucleation rate is not expected to result from the energy barrier consideration inherent in many nucleation processes. Also, it is reasonable that diffusion in such thin films will not contribute to an appreciable time dependence of the degree of supersaturation if carbon is supplied to the lattice uniformly over the surface. As was shown in the last section, saturation of the film appears to be uniform. If a large number of sites for CO decomposition exists in comparison with the number of dislocation sub-boundaries, a uniformly distributed supply of carbon to the lattice would result.

The population densities for the product nuclei of Reactions 1 and 2 are quite similar, as shown in Table 18. Both experiments were run at 250°C using 1,000 μ of CO pressure. Reaction 2 was run for 2.5 hours or more than twice the time of Reaction 1, a one-hour exposure. The nucleus densities overlap considerably for the two runs and their averages are close. Thus, no distinction can be made between the two densities. However, the average nucleus size for Reaction 2 is close to twice the value for Reaction 1. It is not unrealistic then to propose the growth rate for the nuclei to be nearly constant if a steady value for the degree of supersaturation is maintained throughout precipitation.

The implication is that CO decomposes at a rate sufficient to maintain a constant diffusion gradient for particle growth. Again, there was no evidence to suggest a surface carbon build-up.

A comparison of the average nucleus size with the corresponding size range in both reactions suggests that the majority of the nuclei were formed at the same time assuming each nucleus grew at roughly the same rate. Under the latter assumption the nuclei would have had to form very early in the reaction. As previously shown, this system would be expected to generate the growth nuclei rapidly upon supersaturation of the film. The fact that the growth per hour for both Reactions 1 and 2 are close to the same is indicative that supersaturation is developed early in both experiments.

The data for the nucleus density for Reaction 7, run at 350°C for 1 hour under 5 μ of carbon monoxide, indicate that the film is in the initial stages of precipitation. The rate of increase of carbon concentration must have been relatively slow in the experiment since the precipitate density was abnormally low for nucleation. The implication is that the maximum degree of supersaturation corresponding to the carburizing potential of the CO under the experimental conditions used could not be attained within 1 hour. Thus, the CO decomposition rate is dependent on the pressure in the region of 5 μ. Relatively extensive precipitation took place for a longer reaction run as well as for reactions at the same temperature and time of exposure but higher pressures.

For the run at 450°C with 5 μ CO for 1 hour, the density of nuclei was the largest observed. The reaction number is 12 and the data are presented in Table 18. In comparing this run with the 5 μ - 1 hour run at

350°C, it is evident that the increase in temperature brings about a much higher degree of supersaturation within 1 hour. Thus, the rate of decomposition of CO increases with temperature. For higher pressures of CO at 450°C and within 1 hour of reaction, a relatively large amount of precipitation occurs, again indicating the rate of CO decomposition to increase with increasing pressure. As will be shown later, there is an apparent limit to this increase with pressure at least in the early stages of reaction. The population density of precipitates drops off drastically for the higher pressure run at 450°C. This is attributed to the preferential growth for some nuclei and the dissolution of the others. A uniform distribution of growth nuclei or precipitate particles is the result, and the population density characterizes the rate of growth. The greater the growth rate the larger will be the area effected by the carbon draining toward the carbide particle. This characterization will be demonstrated later for the runs amenable to comparisons which were made using 1,000 μ of carbon monoxide and a 1-hour exposure.

e. Physical Character of the Carbide Nuclei. Micrographs of the nuclei formed at 250, 350, and 450°C are illustrated in the series of figures given for Reactions 1 and 2 carried out at 1,000 μ, and Reactions 7 and 12 conducted under 5 μ of CO. The morphologies of the nuclei in each individual run are quite similar. However, from one temperature to another the change in the morphology of the nuclei is striking. This observation is considered partly due to thermal energy changes which effect nucleus growth processes. Also, the stage in the nucleation captured by each reaction differs. The observations for each reaction will be treated

individually.

Reaction 1 was carried out at 250°C in 1,000 μ of CO for 1 hour. The nuclei were characterized in their film plane projections by distinct areas of diffuse contrast and of intermediate intensity. Inside these areas there did exist distinct dark features although without sharp outlines. The discriptions of the latter features range from that of a grainy texture to dense cores. The nuclei were generally elongated and lay at angles to the sub-boundaries on which they formed. The angles most often encountered were approximately 19°, 26°, 32°, 45°, 57°, 64°, 80°, and 90°. If the sub-boundaries actually lie in $< 110 >_{Fe}$ directions, then the angles observed correspond approximately to: < 210 >, < 310 >, < 320 >, < 410 >, < 100 >, and < 110 > directions in the film plane. The angles were too scattered to draw a good conclusion. The measurements could not be made with precision due to uncertainties in the particle axes.

It was not possible to rigorously define the character of the diffuse nucleus area and the dark internal features. Whether the diffuse regions constituted areas of a new but coherent phase, carbon-rich segregates, or strain fringes generated by the nucleation of coherent particles could not be directly determined. It was certain, however, that the nuclei were contained within the matrix and not on the surface of the film. Electron diffraction of the nuclei gave no new diffraction spots nor any matrix reflection distortions even on tilting the specimen in the microscope. This indicated the amount of precipitate material actually present to be less than that expected from the appearance of the micrographs.

The sizes of the nuclei are given in Table 4 and range from 0.006 to 0.065 μ^2. The smaller nuclei appear to extend from only one side of the

sub-boundaries while the larger nuclei often cross them. The smaller nuclei appear as dark knots bounded by semicircular or triangular regions of diffuse contrast. Good examples are shown in Figure 39. The nucleus character is thus indicated to be coherent or partially coherent.

Specific features in two of the electron micrographs of Reaction 1 warrant individual discussion. Figure 43 shows what appears to be a thin, perhaps coherent plate of precipitate or segregate material. This nucleus lies at an angle to the plane of the film across a sub-boundary isolating a region of crystal. The trace of the upper boundary of the nucleus lies along a < 100 > direction. The implication is that the habit plane of the nucleus intersects the (001) face of iron in an < 100 > trace. A logical plane for containing a carbon atom segregate giving rise to the stated trace is a {110} plane. Johnson (134) from a computer model of ferrite predicted that carbon atom clustering may occur on {110} type iron planes. Leslie (137) has proposed cementite to first form on {110} planes of iron in the quench-aging of iron. The work of these investigators and the present research appear to be mutually supporting. The degree of the support will be examined further in later sections of the discussion. Similar nuclei to those of Reaction 1 were captured in the process of transforming directly into definable cementite.

The second morphological feature requiring individual discussion is illustrated in Figure 42. Two nearly parallel sub-boundaries are shown which have nucleation taking place between them. A segment of one of the boundaries bordering the nucleus is invisible in the micrograph due to diffraction effects. The point to be made is that the area between two dislocation sub-boundaries of close spacing ($\approx 0.2\ \mu$ in this case) may be traversed

by a nucleus in the early stages of development. Later, it will become apparent that the area between sub-boundaries must be a preferred region for cementite growth.

Since well defined particles of cementite are incoherent with respect to the ferrite matrix, some sort of coherent solute-rich stage of development must be passed in the overall precipitation process. Only the size of the area affected is debatable. Thus, the diffuse area pictured in the region of a nucleus may be a coherent plate of solute-rich phase while the dark features may be partially coherent or incoherent cementite nucleating in the segregate. This is, of course, specious reasoning but a good deal more evidence tending to substantiate this supposition was derived from extending the CO exposure to 2.5 hours using the same temperature and pressure conditions.

The nuclei or areas of nucleation for Reaction 2 are characterized by the distinct areas of diffuse contrast and intermediate intensity as were those of Reaction 1. However, the dark internal features of the nucleation areas for Reaction 2 are often sharply defined and of definite crystal character. Reaction 2 was carried out at 250°C for 2.5 hours under 1,000 μ of CO, and the micrographs of this run are given in section C.1. The features referred to are well illustrated in Figures 44, 46, and 47. The nucleation areas may now be described as relatively large areas of coherent solute segregates in which nucleation of new crystal structures may take place at more than one point. In Figure 46 a good example of a strain fringe associated with the coherent material is shown at point A.

Figures 44 and 45 are typical examples of the nucleation areas containing nuclei which were developing into partially coherent or incoherent

crystals. This fact is demonstrated by the SAD patterns from the areas centrally located in the micrographs. Figures 103 and 104 show the corresponding patterns. There was obviously more than one product crystal present in each case. However, reflections corresponding to single carbide grains were determined and their patterns indicate cementite to be the phase which was forming. As shown earlier, the presence of a pattern for the second phase proves the partially coherent or incoherent character of the diffracting crystal. The distinction between partially coherent or incoherent character for the nuclei was not established for these crystals. Only the two solvable patterns were obtained from a total of five taken of this sample. If many others had been available the distinction probably could not have been made. Since the orientation relationships found in the two patterns were not the same, more than one possible orientation relationship would be allowed between the precipitate crystal and the matrix. In the case of incoherent precipitation, matrix-precipitate orientation relationships are not required (2). The evidence favors the latter.

Evidence contained in Figures 47 and 48 indicates an orientation relationship between cementite and ferrite may be operable at some stage in the precipitation process. The relationship was seen to occur frequently during the course of this research. The observations were striations in well-developed cementite crystals which had < 110 > traces in the b.c.c. iron. The crystals referred to are marked A in the micrographs. The significance of the striations is their analogy with a fault feature found frequently in the large precipitate crystals formed under more reactive conditions. In these instances the faulting planes were determined to be (001) cementite planes. Darken and Fisher (135) have found the (001) planes of

cementite in pearlite to lie parallel to the lamellae and parallel to the {110} ferrite planes. Therefore, the observations may be more than fortuitous.

Although the average size of the nuclei for Reaction 2 is roughly twice that for Reaction 1, the shapes and the orientations of the nuclei with respect to the nucleating sub-boundaries are quite similar. This observation indicates a continuity of nucleus and precipitate morphology under the same conditions of pressure and temperature.

Figures 68 and 69 show the typical forms of the nuclei found at 350°C and 5 μ of CO (Reaction 7). There seem to be two types. Figure 68 shows a nucleus characterized by the distinguishable but diffuse contrast region of intermediate intensity having a dark and nondescript core. Selected area diffraction of the area gave no indication that a new phase was forming. The nuclei of this run are interpreted to be in the formative stage of development and are probably still coherent.

Figure 69 shows some sub-boundary decoration by dislocations seemingly pinned at "knots" in the boundary. The "knots" are likely small precipitates and are to be expected in this form as nucleation is initiated. Nucleation was not as far advanced in Reaction 7 as it was in the two previously discussed reactions. As a result the information obtained from this run was limited.

The nuclei formed at 450°C under 5 μ of CO after 1 hour are illustrated in the micrographs for Reaction 12. These nuclei appear as dark knots along the sub-boundaries of the iron single crystal. There appeared to be a large variation in the degree of complexity associated with the dislocation sub-boundaries present. However, none of the boundaries appeared to

be free of precipitate nuclei. In fact, apparent single dislocations contained nuclei. The largest nuclei were associated with the boundaries of greatest complexity as determined by sub-boundary width. The physical picture of nuclei on dislocations presented by the micrographs of Reaction 12 supports the theoretically proposed picture by Cahn.

The sizes of the nuclei range from dots in the micrographs to knots having projected areas of only 0.006 μ^2. These small features did not yield characteristic diffraction patterns nor did they cause distortion of the matrix reflections. They were demonstrated to be distinct from the matrix by tilting experiments in the microscope in which the contrast associated with them could not be eliminated. Other contrast features associated with the matrix having the same size as the nuclei and being similarly located could be eliminated by tilting the specimens with respect to the electron beam.

Additional attention should be called to Figures 94 and 95. Figure 94 gives a good illustration of a crystallographic feature which probably is a preferred site for the development of the large precipitates formed under more reactive conditions. The feature marked A is a region located between two nearly parallel sub-boundaries $\approx 0.2\ \mu$ apart. It is evident that a high concentration of nucleation centers exists on the boundaries as well as between them. The latter lie on seemingly pinned dislocations which existed there prior to reaction.

Figure 95 was singled out for specific attention due to the excellent illustration of the overall uniformity of the distribution of sub-boundaries. The precipitate decoration of the boundaries is seen to be extensive with the nuclei being randomly distributed.

4. Morphology of the Cementite Particles

This section will be directed to the morphology of the incoherent cementite precipitates. The particles considered were formed in Reactions 2, 3, 4, 5, 6, 8, 9, and 15. Excluded from consideration in this section are the carbidic particles formed in the experiments involving prolonged specimen treatment. The results of these experiments are treated separately.

As previously established in this discussion, the precipitates have the cementite lattice structure but do not have a fixed lattice orientation relationship to the ferrite. It is then left to establish the shape and shape-matrix relation for a complete morphological definition of the carbide precipitate.

Reference to the electron micrographs of subsection C.1 for the reactions under consideration illustrates that the shapes of the cementite precipitates on the whole were irregular. Not only did the precipitate formations vary in shape from one experiment to another, but individual precipitates in a single run could differ greatly. A good illustration of the latter variation is given in the series of micrographs in Figures 50 through 54.

Many of the precipitates were made up of more than one cementite crystal. The precipitate crystal complexes had both high and low angle grain boundaries between the constituent cementite crystals. The high angle grain boundaries between two cementite crystals of a single precipitate often appeared to follow the contour of the original iron sub-boundary on which the precipitate crystals formed. Figure 79 shows an example of this formation. In the figure is pictured a cementite crystal which had formed between two closely spaced sub-boundaries. On the outside of each

of these sub-boundaries a second and third crystal of cementite had formed growing in directions directly opposite to each other. Figures 56, 61, 73, 74, 81, and 100 provide other good examples of this effect. The crystal complexes were more prevalent, and they increased in size with the experiments constituting higher degrees of reaction. The amount of reaction increased with increasing temperature and CO exposure time. The sizes of the precipitates are presented in the tables of subsection C.1.c. The significance of the precipitate sizes will be taken up in detail later. The point to be made in this instance is that the relatively large size of the cementite crystals on dislocation sub-boundaries necessitated the combination of adjacent nuclei on the same boundary to form a single crystal of cementite. Nucleation can, as observed, result in a second crystal of cementite on the opposite side of the sub-boundary.

It was not possible to determine whether the incorporation of more than one nucleus into the growth of a precipitate crystal occurred by recrystallization or if one nucleus dissolved as another grew. However, it was evident that solution of many nuclei in the vicinity of a growing precipitate does take place. This fact was noted from decreases in precipitate population of more heavily reacted samples.

The shape of the cementite precipitates and the amount formed were not independent of matrix disturbances. A few holes occurred in the single crystal films as a result of substrate irregularities. Figures 73 and 97 of Reactions 9 and 15 respectively show the results of the reaction in the vicinity of a hole. Obviously cementite precipitation has been promoted in the area of the hole in the film of Reaction 9. The hole in the film of Reaction 15 appears to have promoted cementite formation and subsequent ce-

mentite decomposition and graphite nucleation. In the area of the hole only graphite and the substrate metal matrix remained. Figure 80 of Reaction 9 shows extensive cementite formation along an underlying cleavage step in the NaCl. Apparently the iron film was thin and partially discontinuous along the step edge.

At least two basic types of particle shape were common among the precipitates from all the experiments. First is the lenticular cross-section. This shape often appeared as a wedge shape extension from a crystal complex. Reaction 2 produced cementite particles in the earliest stage of development observed, and particles of the lenticular cross-sectional shape were observed in the specimens of this run. The particle marked A in Figure 47 is a good illustration for Reaction 2, as are Figures 51, 52, 54, 56, 58, 62, 64, 65, 66, 71, 74, 77, and 100 for other runs. The thickness of these particles was, of course, limited to the film thickness (approximately 1,000 Å), but as will be indicated later, the precipitates probably did not extend completely through the films.

A second characteristic shape was also observed in Reaction 2 and is illustrated in Figure 49 by the particle marked A. This shape resembles a distorted rectangle and similar shapes are seen in the results of all the other reactions being considered in this section. The remaining precipitates can be generally described as modifications and combinations of the two types just covered.

The effect of temperature, pressure, and reaction time (all parameters of the degree of reaction) on the character of the precipitates was principally to change the precipitate size. Some change of shape was considered to accompany a size increase, i.e., the ratio of the film plane axes

of the precipitates tended toward unity as the particle sizes increased significantly.

In the discussion of product nucleation, the effect of strain energy on the geometrical shape of nuclei was presented. For the growing incoherent precipitate, the potential to minimize strain energy continues to influence the particle shape. The shape also continues to be influenced by the minimizing potential for the surface energy. Thus, the overall shape at any point in the growth process will represent an accommodation between these two potentials. This shape should approximate an oblate spheroid lying between the ideal shapes of a disc for strain effects and a sphere for surface effects. Departures from smooth boundaries may result from the anisotropic character of the crystals. The general morphology of the growing precipitates suggests the accommodation of strain and surface energies as perturbed by crystal anisotropy.

In Figures 73, 74, 75, and 76 the precipitates are observed not to have as high a length to width ratio as that typically found for precipitates in experiments constituting a lesser degree of reaction. These precipitates tend toward a circular cross-section in the plane of the foil and exhibit contrast effects indicating peripheral thinning and precipitate "surfacing." The growth of the precipitates is apparently toward the film surface where strain energies are readily accommodated. As the precipitate "surfaces" the interfacial energy of the precipitate is minimized during further growth by the development of a near circular particle cross-section in the surface of the iron. The polygonal shape of the precipitates pictured in Figures 73 and 75 is indicative of the tendency of the reaction interface to conserve singular crystal faces. The evidence for surface and

strain energy accommodation for the precipitate particles as indicated by their shapes is further support of the proposition that cementite forms within the iron matrix and not on the metal surface.

The thin blades of precipitate close to the iron surface as shown in Figures 52, 58, and 72 plus the other dendritic type features observed in this work, may plausibly be accounted for by the Gibbs-Thomson effect. According to Ham's (150,151,152) exact treatment of the equations for diffusion controlled growth, diffusion conditions themselves will not produce shape changes in precipitate particles.

The Gibbs-Thomson effect relates to the change in the local chemical potential along a curved phase boundary. Christian expresses the effect as follows: "The effective difference in pressure across the curved interface changes the concentration of solute in the matrix with which the particle is in equilibrium, and for the critical radius of curvature the particle is in equilibrium with the average composition of the matrix." Below the critical radius, growth of the particle is not possible. Zener's theory of diffusion controlled growth (159,160) takes account of the equilibrium concentration change with curvature of the interface. From his work the maximum growth rate is found to occur when $r = 2\ r_c$ where r is the radius of curvature of the interface and r_c is the critical radius of curvature. Zener's theory is not exact, but none have been presented which are more exact (140). In summation, it is reasonable that edges or projections such as occurred in many of the precipitates may have grown at annomolous rates giving rise to peculiarities in precipitate shape.

Planar faulting of the cementite precipitate crystals was commonly observed. All the experiments made, exhibiting incoherent cementite, pro-

duced cementite crystals with faults in them. Figures 115 and 91 respectively show a SAD pattern and the corresponding electron micrograph of a faulted area of cementite. The information indicates the faults to be stacking faults lying on the (001) cementite planes. Figures 52, 53, and 65 show smaller precipitate particles containing planar faults. The corresponding SAD patterns of these crystals also imply the faulting to lie on (001) cementite planes. Figures 48, 55, 56, 57, 58, 59, 62, 63, 66, 71, 79, and 98 show particles which contain planar faulting as evidenced by the characteristic striated contrast although no SAD evidence was available for proof. Since a number of the SAD patterns were taken which indicated (001) cementite faulting, it was tentatively assumed that the faulting observed in all the micrographs lay on (001) cementite planes. The angles which the faulting traces in the film surface made with the principal axes of the particles are interesting. Values of 0°, 5°, 7°, 10°, 19°, 27°, 80°, and 90° were measured. Easily the most common value was 0°. Since the faulted region of the precipitate particles predominately appeared in the central region of the particles, it is plausible that the particles may form by nucleating successive $(001)_{\theta}$ planes. The precipitates may then grow preferably by extending these planes through the ferrite lattice. At some point in the process the three-dimensional cementite lattice would begin to form along the outer surfaces of the central $(001)_{\theta}$ plane aggregate.

Faulting was seen to be less prevalent in the particles formed in the higher temperature runs. The size of these particles was larger also (due to the experimental design). It is uncertain whether the reduction in faulting incidence was due to a recrystallization accompanying precipitate growth or due to thermal energy inhibition. The faulted regions noted at

the higher temperatures were also thinner and much better defined.

As Jack (133,136) has suggested, the cementite may initially precipitate as (001) cementite platelets in the ferrite matrix. Pitsch (131) and Leslie (137) suggest that the {110} planes of iron are the habit planes of cementite for precipitation in the quench aging processes for steels. With this knowledge an attempt was made to relate the (001) planes of the precipitate faults to the {110} planes of the ferrite film. The result of trace analysis indicated that the (001) planes of cementite were rarely parallel to {110} ferrite planes. There were a few instances in which the relation may have held but the information required for proof was not available (particles marked A in Figures 47 and 48). In relatively small precipitates, measurements indicated the relation to be within 20° of that sought (Figures 52 and 53 show good examples). It is possible that the (001) cementite planes do form parallel to {110} ferrite planes at least in some instances and then lose the orientation relationship with growth.

It was previously established on the basis of electron diffraction evidence that no fixed orientation relationship existed between the incoherent precipitate particles and the ferrite matrix. From this evidence it should be expected that no simple regularity of the three-dimensional cementite particle boundaries exists. In other words, no habit plane relationship between ferrite and cementite should be expected. Figures 47, 52, 53, 56, 59, 60, 63, 64, 65, 71, 79, and 98 give clear pictures of some of the irregularities observed in the cementite-ferrite interfaces. This series of micrographs covers the range of reaction conditions used in the experimental program. It is of interest to note that the interfaces generally tend to be faceted although continuous changes in interface inclination to the

surface was evident, i.e., Figures 56 and 60. Good illustrations of interface faceting will be shown later in the section discussing extraction replicas of reacted films.

Pitsch (131) and Leslie (137) have suggested that the major growth direction for cementite precipitating from steels in the quench-aging process is the [010] cementite direction in coincidence with the [111] ferrite direction. The principal growth directions (coincident with precipitate particle extensions) for the particles observed in this work were quite varied. However, in two instances (Figures 51 and 65) the growth direction for the cementite lattice was found to lie close to the [010] cementite direction as determined from micrograph and SAD pattern pairs. The corresponding ferrite direction was not, however, [111] in either case. The film plane trace for the growth direction would have necessarily been directed along $[110]_{\alpha}$ for the relation to have held, and this was not the case.

The [010] direction may then be a preferred direction of cementite growth. However, since the particles of cementite observed in the iron single crystals of this work were variously oriented, only those particles oriented such that the [010] cementite direction was parallel to the plane of the film could be used to check the phenomenon. The square-shaped precipitate of Figure 51 reveals an apparent contridiction.

It is interesting to note at this point that the [010] cementite direction lies in the (001) cementite plane. This plane was shown earlier to be the faulting plane which was demonstrated to commonly extend through the particle close to parallel with the growth direction. Figure 65 pictures a particle in which the fault plane lies parallel to the major growth axis. The growth axis in this instance also corresponds to the [010] cemen-

tite direction. Thus, the growth of cementite may be particularly favorable along the $[010]_\theta$ direction at the edges of $(001)_\theta$ plane lamellae. This constitutes only specious reasoning as there were no unequivocal observations to be made concerning the cementite morphology.

The possibility of a directional relation between the major axis of a cementite particle and the [110] iron lattice direction was investigated. Angles commonly encountered approximate 0°, 12°, 18°, 22°, 26°, 33°, and 45°. These angles are close to the angles between the [110] ferrite direction and the following respective directions: [110], [320], [210], [520], [410], and [100]. In light of the obvious uncertainty of establishing the growth direction of the complex particles, the orientation could be considered nearly random. However, micrographs picturing sizable areas of the film containing several precipitates indicate the distribution is not random, i.e., Figures 54, 59, 64, 71, 81, and 100. The general appearance of these micrographs indicate the precipitates to grow at 0°, 45°, and 90° to one another. Closer inspection reveals this to be only a tendency. In the absence of a general trend for precipitates to grow in [110] or [100] directions, no ready crystallographic explanation exists for the growth direction of cementite in the single crystal iron films. It is, however, apparent that shapes and directions are predominantly controlled by strain and surface energy accommodation.

Several attempts were made in the foregoing discussion to relate the morphology of the cementite precipitated in the iron single crystal films to that of cementite precipitated during quench-aging experiments in iron. This was done for obvious reasons. The failure to establish rigid correlations should not, however, be alarming. Precipitation in the bulk takes

place under more uniform three-dimensional constraint than precipitation near the metal surface. Also, the phenomena taking place in the bulk have not been fully explained nor explored. From the present discussion it is obvious that the factors effecting the morphology of cementite in the surface of iron single crystal films are quite complex.

5. Growth Mechanism of the Cementite Particles

Five reactions (1, 3, 4, 9, and 15) were made using the same pressure of CO (1,000 μ) and the same exposure interval (1 hour). These reactions constitute a basis for comparing the effect of temperature on the reaction products. The temperatures for these reactions were 250°, 320°, 350°, 450°, and 550°C, respectively. It has already been established that cementite precipitates in the matrix of the iron specimens of all five reactions considered and is accompanied by graphite as a reaction product in Reaction 15. From inspection of the micrographs, temperature variation was found to influence the size and population density of the cementite precipitates and the rate of carbide decomposition. As exhibited by Reaction 15, the higher temperatures aid graphite formation.

To obtain a quantitative basis for comparing the precipitate sizes, the projected area of each individual particle pictured in the micrographs was measured. The cementite particle sizes for each experiment were summarized in Table 19. The data is presented as the Projected Area Size Range and Average. The projected area of a precipitate particle is considered an adequate basis for comparing the relative sizes of the precipitates.

The average particle size, together with the ranges of size distribution for Reactions 1, 3, 4, 9, and 15, were plotted versus 1/T on semi-logarithmic paper. The plot (Figure 101) shows a straight line correlation.

The information contained in Figure 101 relates to the growth mechanism of the cementite particles and requires explanation.

The kinetics of a continuous precipitation process depends on the growth rate of an individual precipitate crystal (140). This growth rate, according to the theories of continuous precipitation, is diffusion controlled. The process presently being discussed has many features in common with a continuous precipitation process. With the aid of Figure 101 the relation between the two processes can be tested further.

First, it was assumed that the formation of the cementite particles constituted a continuous precipitation process. Under this assumption it is reasonable that a particle grows by two-dimensional diffusion since the film plane dimensions dwarf the particle thickness. Ham's exact treatment of the diffusion problem for particle growth shows that the volume of irregular particles (approximate to oblate spheroids) varies as $t^{3/2}$, just as for spheres. He also shows that plates which remain highly eccentric during diffusion growth increase in volume as t^{1}. In analogy with his results, it is expected that plates although irregular will grow as discs. This assumption permits the following analysis.

It has been well established that the linear dimension of a particle growing by a diffusion controlled process increases as $(Dt)^{1/2}$. If the area A is represented by

$$A = \pi r^2$$

and the linear dimension r by

$$r = a(Dt)^{1/2} \quad ,$$

it is readily found that for constant temperature

$$\frac{dA}{dt} = \pi a^2 D = k \quad ,$$

where D is the diffusion coefficient and a is a constant of proportionality. The area A and roughly the volume (for an essentially constant plate thickness) varies as t^1. The results of Reactions 1 and 2 as shown previously do indicate the particles to grow in approximately a linear fashion.

The growth rate k incorporates the temperature dependent diffusion coefficient to the power one. The diffusion coefficient can be expressed as

$$D = D_o \, e^{-Q/RT} \quad .$$

Therefore, if legitimate values of k for different temperatures can be calculated, a value for the activation energy of the growth process can be determined. This value should correspond to the activation energy for diffusion of carbon in iron.

For an individual experiment, the average particle size divided by 1 hour represents the instantaneous growth rate, k, at some intermediate time under certain restrictive conditions.

The instantaneous growth rates calculated at different temperatures after 1 hour of reaction will correspond to the same intermediate time if the functions governing growth for the different temperatures belong to the same family. It is reasonable to assume that this is true. Therefore, a plot of ln k versus 1/T should permit the calculation of the activation energy from the slope of the straight line. Figure 101 is such a plot.

The restrictive conditions referred to above relate to the singularity

of the diffusion process to govern the rate at which the precipitates grow. Specifically, all precipitate nuclei must exist from the outset of precipitation. This is a reasonable assumption for the process investigated. The mean diffusion distance between precipitate particles must remain constant from one experiment to another. This condition is also satisfied since carbon is continuously being added to the film. The rate of carbon addition is sufficient to maintain supersaturation between the precipitates or else CO decomposition would be rate controlling. From evidence to be presented in the next sub-section, CO decomposition as the rate controlling step does not appear to be possible for the present investigation. It should also be pointed out that diffusion will continue to occur after pumping the system of CO. However, the amount of precipitate growth occurring during the time required to drain the film to the equilibrium carbon content should be small relative to that during reaction. The effect on the k values from one temperature to another should then be small and would not effect their relative values significantly in view of the other errors inherent in the analysis.

From the slope of the straight line in Figure 101 an activation energy of Q = 21.4 kcal/mole was calculated. This value corresponds well to the 20.1 kcal/mole determined by Wert (161,162) for the activation energy for volume diffusion of carbon in iron. Therefore, it is quite plausible that the diffusion of carbon in iron controls the growth of the cementite particles, and the process during the early stages of CO attack of iron is simply a continuous precipitation process.

Table 19 also summarizes the precipitate population densities for Reactions 1, 3, 4, 9, and 15. Figure 102 illustrates a plot of the population densities versus temperature on semi-logarithmic paper. The trend is

toward a decreasing number of precipitates with increasing temperature. This illustrates the variation in the size of the diffusion field for precipitates as a function of temperature.

The evidence of the change in diffusion field size shown in Figure 102 should not be interpreted as showing hard impingement of the diffusion fields of adjacent precipitates. Rather, only small mutual perturbations probably exist. The observed effect should illustrate the sensitivity of volume nucleation to the degree of supersaturation. A very small amount of precipitation will change the mean concentration of solute in the matrix sufficiently to decrease the volume nucleation rate by one or more orders of magnitude (140). Therefore, it is reasonable that volume nucleation or the precipitate density can reflect the change in diffusion field size without a significant change occurring in the growth character of the precipitates.

6. Effect of Pressure on the CO Attack of the Films

The data on precipitate size and population density for reactions carried out under different pressures at constant temperature (350°C) and time (1 hour) are given in Table 20. The data indicate that the precipitation reaction is dependent on the pressure of CO.

The values of precipitate size and population density for Reactions 4 and 5 (carried out at 1,000 μ and 500 μ, respectively) are quite similar. The implication is that the degree of carbon supersaturation in the iron (causing cementite precipitation) is close to the same value in both experiments. Also, the time to reach this degree of supersaturation must have been essentially the same. Only under these conditions would the precipitate densities have been equal. The precipitate particles must have formed at

essentially the same time and must have grown at nearly the same rate. There was no continuous distribution of precipitate particle size from near zero to the maximum observed in either case. The close grouping of precipitate size was characteristic of all the experiments except the extended reaction run. It has already been shown that precipitation from a supersaturated solution can reasonably begin almost instantly on dislocations and that all the active nucleation sites will be operating from the outset of the process. Therefore, little, if any, additional nucleation would be expected with time. For Reactions 4 and 5 it may be assumed that the maximum supersaturation attained was reached early in the process and that the average size of the precipitates at the end of the experiment is representative of their growth rate. Similar assumptions can be made for all the other reactions carried out at 1,000 μ of CO.

The data for Reaction 6 carried out at 100 μ of CO is very similar to that of Reactions 4 and 5. The values of precipitate size and population density for Reaction 7 (the 350°C, 5 μ, 1-hour run) differ greatly from those obtained from the runs made at 500 μ and 1,000 μ. The implication is that at 5 μ of CO the rate of decomposition of CO supplying carbon to the lattice becomes insufficient to supersaturate the film within an hour to a level comparable to that achieved in Reactions 4 and 5.

The fact that the precipitation of carbide is dependent on CO pressure below 100 μ and that it is insensitive to CO pressure in the 500 to 1,000 μ range, indicate the existence of a maximum degree of carbon supersaturation in iron and the independence of the carbide formation rate on CO pressure greater than 500 μ.

Also, since there was no build-up of detectable carbon on the surface

of the iron in the early stages of the reactions studied, the overall rate of decomposition of CO must be controlled by the processes in the matrix. In other words, CO decomposes only at a rate sufficient to maintain the supersaturation of the lattice during the carbide precipitation.

7. Extended Film Treatments

The results of Reactions 10, 11, 13, 14, and 15 will be treated in this section. Reaction 10 was carried out under the same conditions of CO exposure as Reaction 9 (450°C, 1,000 μ of CO; 1 hour of exposure), but the reaction portion of the experiment was followed immediately by an 8-hour vacuum annealing process at the same temperature as the reaction. Reaction 11 made use of the same temperature and pressure conditions as Reactions 9 and 10 but the duration of the exposure was extended to 6 hours. Reactions 13 and 14 were control runs simulating reactions in the absence of CO. Reaction 15 was an experiment carried out at the highest temperature (550°C) employed in the experimental program.

Reaction 10 was conducted to determine whether cementite could be decomposed by annealing it at a temperature as low as 450°C. Specifically, cementite particles of the size formed after 1 hour of reaction at 450°C in 1,000 μ of CO were of interest. The SAD patterns from the specimens of this reaction were presented in Figures 111 and 112 (Section C.2) and the electron micrographs in Figures 82 through 87. It is evident from these that the cementite was no longer present after the 8-hour annealing treatment. Figures 82, 83, and 84 show distinctly where the cementite particles existed before decomposition. A bright outline encompasses the area of ferrite matrix which was formerly covered by the cementite particle. The areas outlined together with their bright borders will henceforth be referred

to as "Ghost Crystals." The areas of the ghost crystals were comparable to the precipitate projected area sizes of the corresponding run, Reaction 9, as illustrated in Table 21. SAD patterns from the interior regions of ghost crystals exhibited only the reflections characteristic of (001) iron single crystal films, i.e., Figure 111. The whereabouts of the carbon and the iron released upon the decomposition of the carbide was not evident in the SAD or micrograph of the area pictured in Figure 82. The black specks in the upper end of the ghost crystal of Figure 83 were graphite. Also, contrast effects were visible in the areas marked A in Figures 83 and 84 which were indicative of interfacial features between the ferrite matrix and an essentially transparent film overgrowth. This film was considered to consist of graphite lamellae. Extraction replicas substantiate this interpretation.

The growth in the upper right of Figure 84 is difficult to explain. It appears as a dark region or irregular "Plate" in the film on which rests a protrusion or "Button" of material. SAD indicated nothing but the iron matrix to exist in the interior portions of the plate-like formation remote from the button. However, graphite was observed at the periphery of the protrusion. The central portion of the button showed no diffraction, evidently as a result of high diffuse scattering and absorption of electrons. The button, therefore, was considered to be a thick, dense carbon growth and not a carbide or ferrite crystal. Positive identification was not possible. Figures 85 and 86 are other illustrations of these features. The diffraction effects were similar to those previously observed except that graphite was found at the peripheries of the plates. This graphite was of a partially oriented nature.

The corresponding SAD pattern from the area pictured in Figure 86 was given in Figure 112. The arcing of the interior ring indicates a preference for the graphite basal planes to lie parallel to the $[001]_\alpha$ zone axis and at angles between a $(0\bar{2}0)_\alpha$ and $(1\bar{1}0)_\alpha$ plane pair. Selecting a portion of the arced reflection ring (basal reflections of graphite) for dark field imaging, the micrograph of Figure 87 was obtained. This micrograph shows that the striated regions at the periphery of the plate-like formation in Figure 86 contains a great deal of the oriented graphite. The appearance indicates that the basal planes of the graphite lie in lamellae perpendicular to the film plane giving surface traces tending toward $[110]_\alpha$ and $[100]_\alpha$ directions. It is also clear that the plate-like region cannot contain more than a small amount of graphite with basal planes inclined to the surface. The graphite at the periphery of the button in Figure 85 was found to be of the oriented form. All graphite found in the corresponding positions in other instances was of the same type.

The origin of the plate and button formation combinations is uncertain. The areas covered by the plates were significantly smaller on the average than the areas of the ghost crystals,as shown in Table 13. It is, therefore, unlikely that the plates coincide with decomposed cementite crystals. In some instances the plate type formations were, however, seen to intersect a ghost crystal, and Figure 83 seems to show this occurrence although not a good example due to the absence of the button feature. In most cases the plate-button combinations were remote from ghost crystals, as illustrated in Figure 84. This micrograph suggests that the carbide dissolved and the carbon diffused too and formed graphite at the plate-button site.

Either of the explanations, cementite decomposition or cementite solution and subsequent precipitation of graphite, are consistent with the theories of continuous precipitation.

The purpose of Reaction 11 was to determine if secondary products form under extended reaction conditions. Graphite and cementite were identified and Figure 88 displays the relative quantities of each. The large particles were cementite and the small, randomly spaced nodules were graphite. Cementite was in much greater abundance than the graphite. The graphite nodules while generally positioned on the iron film surface were often found on the cementite surface.

The appearance of the isolated nodules is illustrated in Figures 89 and 90. These are similar to the plate-button formations observed in Reaction 10. The selected area diffraction characteristics were similar in that the plate interiors showed only iron single crystal reflections while the plate and button peripheries often showed oriented graphite to be present, i.e., Figure 89. The sizes of the formations were also comparable. Since reaction was being conducted during the entire 6 hours of Reaction 11 and since the plate-button type formations were apparently the same for the two runs, the growth mechanisms were probably the same and independent of the surface reaction. The formation of the graphite plate-button structures is considered to result from nucleation and growth by diffusion of carbon through the ferrite lattice to active sites. Figure 89 shows graphite formation at a surface step which resulted from the existence of a cleavage step in the NaCl substrate. Figure 90 indicates sub-boundaries to be active in the nucleation of graphite since one of the plate boundaries coincides with a sub-boundary in the ferrite. It is suspected that the

active sites in the ferrite generate nuclei of graphite of oriented character. The remaining graphite forms layers which are evident in Figure 90. Apparently the layers are autonucleated from the first formed graphite.

Another mechanism of graphite formation is suggested from the results of Reaction 11. Figure 113 illustrates a SAD pattern taken within the confines of a large cementite particle. The rings denote graphite of special orientation. The graphite was present on the surface of the cementite having the basal planes oriented parallel to the film plane. This observation is based on the absence of the (002) graphite reflection. The continuous rings show the graphite to be polycrystalline with the individual graphite crystallites oriented randomly around the basal plane normal. This suggests that the cementite may decompose to give graphite lamellae parallel to the original cementite surface.

It is important to note that the cementite formed in these reactions had an unusually good crystalline integrity. The particles would be ideal for a basic study of cementite. Figure 91 shows an area of a cementite grain in which an excellent representation of faulting was found. This observation was not uncommon. The SAD pattern given in Figure 115 indicates the faulting to be a stacking fault type which occurred on the (001) cementite plants.

In the light of any consideration of cementite decomposition, it is pertinent to reconsider the results of Reaction 15. Figures 97 and 99 give evidence of cementite decomposition after only 1 hour of reaction at 450°C in 1,000 μ of CO. Figure 97 shows the decomposition of cementite platelets in the vicinity of a hole leaving a residue of graphite. Figure 99 illustrates the partial decomposition of a cementite particle as evidenced by the

partly real, partly ghost crystal portions of the particle. Figure 100 shows the existence of a plate-button formation as well as cementite particles. The overall results suggest that the state of graphite formation in Reaction 15 is approximately the same as that displayed by Reaction 11.

From the three runs considered in this section, a time-temperature dependency appears to exist for the nucleation of the equilibrium graphite phase. In nucleation and growth processes a plot of the time t_x for some definite fraction of the transformation to occur versus temperature shows that the precipitation rate first increases and then decreases again with falling temperature. This results in the C-curve characteristic of nucleation and growth processes (140). At sufficiently low temperatures, the relation between $\ln t_x$ and $1/T$ approximates to a straight line. The straight line slope indicates a temperature independent activation energy is rate controlling, and "it is natural to identify this with the energy for diffusion."(140)

Several investigators have observed an incubation period associated with the CO decomposition on iron (35,47). The most recent and thorough treatment of incubations was made by Westerman (35). In his work kinetic studies were made using a thermobalance to measure continuous weight gain of iron wire as a function of time. The purity of the iron wire used in his investigations was the same as that of the iron used for the present work. The pertinent temperature range of the incubation studies ran from 475 to 700°C. It is reasonable because of the limit of accuracy of the thermobalance that the incubation periods he reported did not refer to the exact point of product nucleation but to some other point in the development of reaction products. Westerman found that a plot of the incubation time

versus 1/T resulted in a straight line. He also found the rate of product formation to decrease with decreasing temperature in analogy to the C-curve. This would place his study in the low temperature straight line portion of the C-curve if it is assumed that a nucleation and growth process was taking place. On the basis of this assumption, he has postulated that the creation of critical nuclei of cementite is the process giving rise to the incubation period. The only products reported in his work were cementite and graphite. Graphite was the major contributor to the weight gain during the course of an experiment. The incubation periods Westerman reported for reaction in one atmosphere of CO at 475° and 550°C were approximately 7.5 and 2.5 hours, respectively.

In view of the present work in which considerable cementite was formed at a temperature as low as 350°C after 1 hour of reaction in 1,000 μ of CO, it is suggested that Westerman's interpretation of the incubation data was erroneous in attributing the phenomena to the creation of cementite nuclei. Rather, it is suggested that the nucleation and growth process for graphite was responsible for the incubation periods observed. The present work proves that cementite precipitation takes place early in the CO attack of iron and precedes the nucleation and growth of graphite. The time required to nucleate and grow graphite to the proportions observed in Reaction 11 was 6 hours. Approximately the same state of graphite precipitation was observed after 1 hour at 550°C on Reaction 15. These times correspond reasonably well to those observed by Westerman for incubation periods in the same approximate temperature range.

The times observed for this work would, of course, be less than those observed by Westerman because the electron microscope is much more sensitive for the early detection of a new phase.

Assuming that the phenomena being observed were the same, the activation energies calculated from both sets of data were compared. Since the temperatures investigated in both Reactions 11 and 15 correspond to the lower temperature region investigated by Westerman, it was reasonable to assume that the straight line approximation applied to the data of this work. From a calculation of the slope between the two points, [6 hours, $1/(450^{\circ} + 273^{\circ})$] and [1 hour, $1/(550^{\circ} + 273^{\circ})$], using the relation, $\ln t_x = Q/RT + \ln A$, a value of $Q = 22.2$ kcal/mole was obtained. The value calculated by Westerman was 19.0 kcal/mole and is comparable to that calculated above. These values are also close to the activation energy for the diffusion of carbon in ferrite, 20.1 kcal/mole. In fact, the kinetic data of Westerman at the time of incubation plus 3 hours gave an overall activation energy of 18.5 kcal/mole for the temperature range 500 to 570°C which is also close to the activation energy for diffusion of carbon. It seems reasonable then that the diffusion of carbon in iron may be the rate controlling step for the formation of all the solid phase products. In addition, CO decomposition may be completely controlled by solid-state phenomena at sufficiently high pressures.

Reactions 13 and 14 of this work were conducted to insure that the previous results were due solely to reaction with CO and not to anomolous system contamination. Reaction 13 was a blank run (no CO) simulating a 1-hour reaction at 450°C. Figure 96 is a typical electron micrograph of the iron single crystal specimen treated. The specimen was clean of any of the fea-

tures characteristic of a reacted film. Reaction 14 was also a blank run and was conducted at 450°C for 6 hours and 55 minutes. This run was particularly important not only because of the length of the treatment but also because it followed the last experimental reaction conducted. Examination of the film of Reaction 14 showed it to be clean. Therefore, all the experiments reported are considered to be free from any artifacts due to system contamination.

8. Replicas of Reacted Films

Surface replicas were made of the single crystal films treated in Reactions 9 and 10. The purpose of this study was to increase knowledge of the physical nature of the cementite particles and to better establish the location of the graphite formed as a result of the cementite decomposition. In the micrographs of these replicas the character of the iron surface was very well illustrated, as shown previously in Figure 33.

Figures 119 and 120 are micrographs of the replica made of the specimen reacted for 1 hour in 1,000 μ of CO at 450°C (Reaction 9). The micrographs reveal a variety of cementite surface textures and features. In some instances the cementite surfaces appear generally smooth except for frequent small holes, i.e., Figure 119. These holes were evidenced by white specks in the transmission electron micrographs of the cementite particles, i.e., Figures 75 through 77. The holes appear to be a more typical feature of the runs made at 450°C and above, and it is suspected that the holes are related to graphite nucleation during Fe_3C decomposition.

In Figure 119 some of the precipitates have the appearance of double edge blades. The particles did not appear to protrude from the surface but gave the impression of being embedded in the matrix. Cementite grain bound-

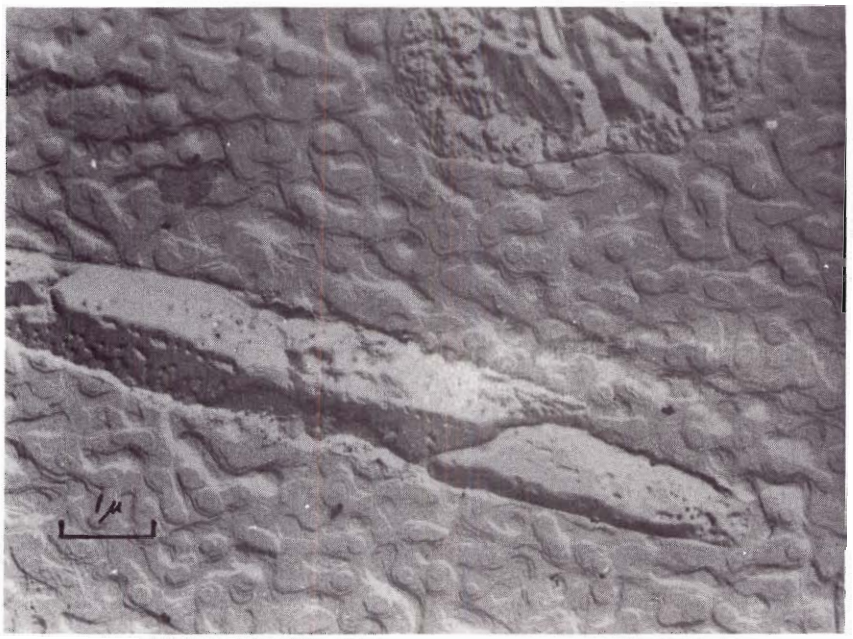

Figure 119. Replica of Cementite Precipitate Particle

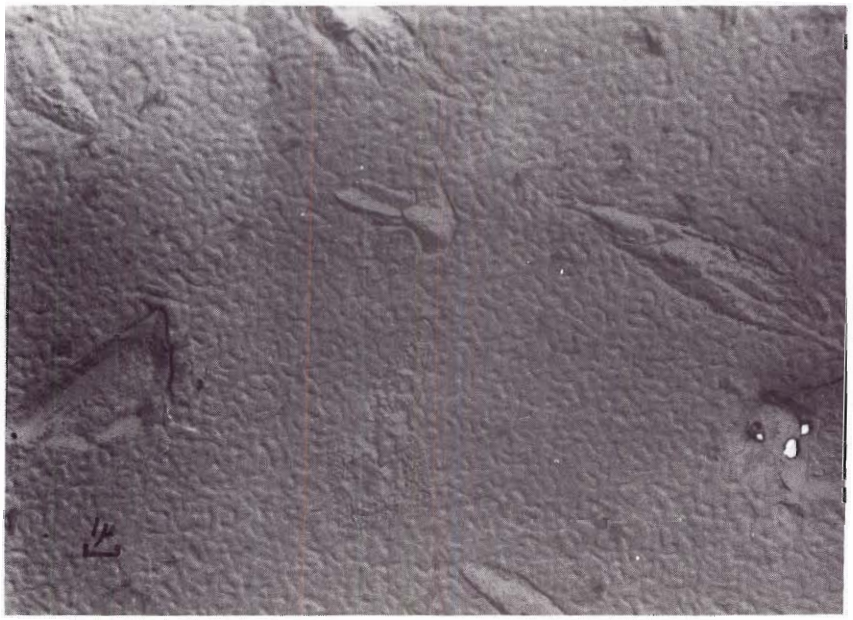

Figure 120. Replica of Cementite Precipitate Particles

aries in a precipitate particle were generally grooved, as illustrated in Figure 119.

The replicas of Reaction 10 illustrate the features of the decomposed cementite particles. The particles for this experiment were formed after 1 hour of reaction in 1,000 μ of CO at 450°C and decomposed during an 8-hour vacuum anneal at 450°C. The micrographs of Reaction 10 in effect show the result of decomposing the particles characterized in Reaction 9.

Figures 121, 122, and 123 reveal the topography of both the iron surface and the original iron-cementite interface as well as the relative placement of graphite flakes. The features of the iron surface are seen to be essentially the same as those of the film from Reaction 9. A variety of cementite-ferrite interface textures were found and are illustrated in Figures 121 and 122. Some faceting is evident. It is apparent from the micrographs that the particles did not go completely through the films except in places where a film discontinuity existed. The latter is pictured in the micrograph shown in Figure 123. Considering the micrographs of both the cementite surfaces and the cementite-ferrite interfaces, the overall picture of the cementite particles is that of irregularly shaped platelets embedded in the surface of the ferrite.

Figure 121 shows that preferred points for graphite nucleation were cementite-ferrite boundaries at the film surface and particularly surface step-particle intercepts. The points of nucleation for the graphite lamellae located in the central regions of the cementite particles are not certain. They may have nucleated at the cementite-ferrite interface underneath the particle or on the cementite surface. The latter seems more probable from strain energy considerations. The holes in the cementite preci-

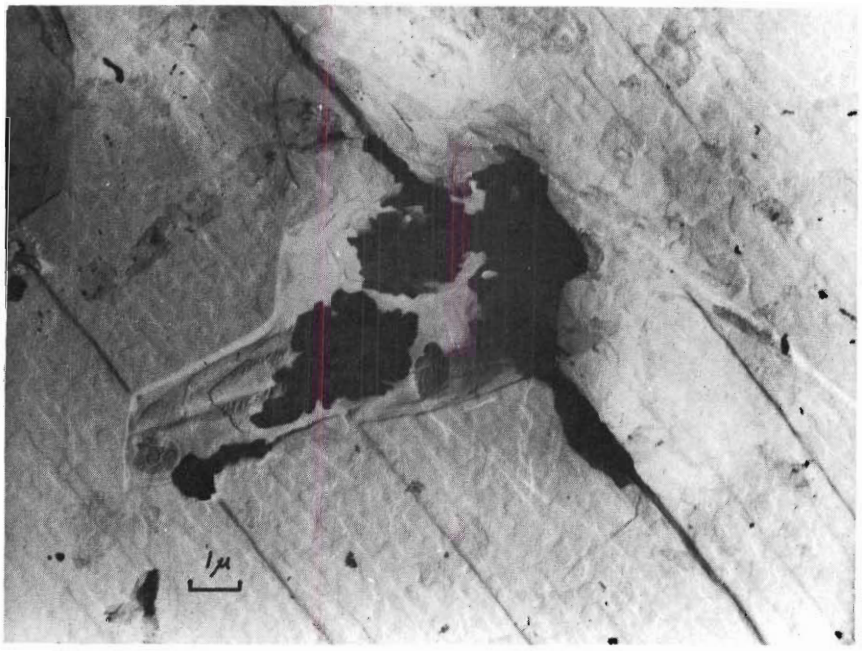

Figure 121. Replica of Decomposed Cementite Precipitate

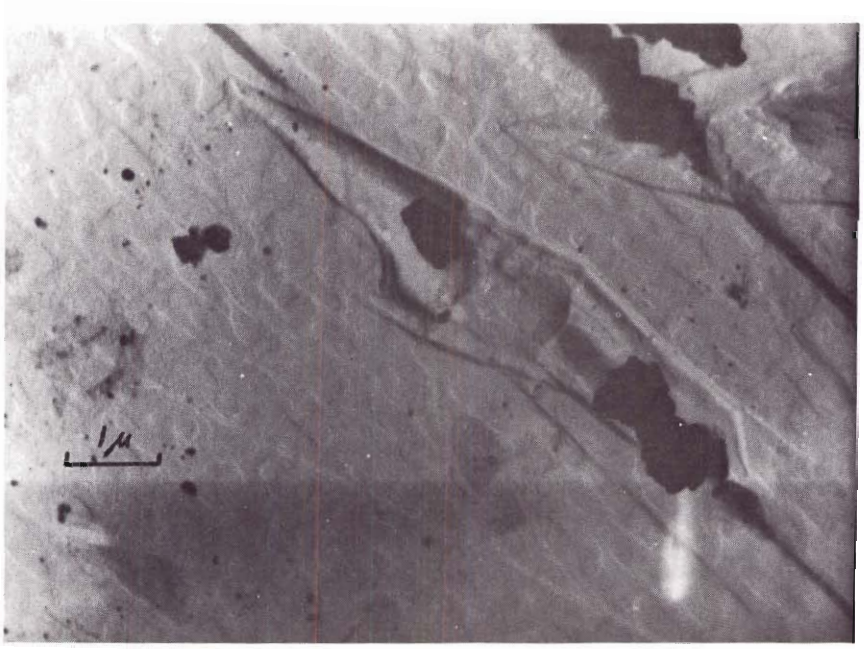

Figure 122. Replica of Decomposed Cementite Precipitates

Figure 123. Graphite Lamellae on a Replica of Decomposed Cementite Formations

pitates are the most likely points for the nucleation. Support for this suggestion comes from the spoty contrast associated with a number of the thinner graphite layers shown in Figure 123.

Although not illustrated, the plate and button type product formations discussed in subsection C.7 have platelets of carbon covering the entire area. The button portion of the formations were also carbon, but it is not certain whether the material was carbidic prior to the chemical treatment in the extraction process. The shape of the plate-button formations are suspiciously similar to some of the flat-topped mounds of iron in the film surface. Examples of the mounds are shown in Figure 119.

D. Applicability of the Results for Predicting the Behavior of Bulk Iron

Are the results and conclusions drawn from a study of thin single crystals of iron applicable to the behavior or bulk iron, or the surface of bulk iron? This question is very logical since many properties of films are not representative of those corresponding to bulk materials. In the present investigation, however, the chemistry of the surface region is of major importance in the study. The precipitation process observed in the iron films does not have to be identical with that occurring deep within bulk iron but only in the surface region. Since the CO decomposition reaction was carried out from a single face and since the films were approximately 400 unit cells thick, it is logical to consider the chemical effects observed in the surface regions of the films to be representative of those in the surface of bulk materials. The precipitation observed in the films has been demonstrated not to penetrate the film in a majority of instances, and thus the film thickness is sufficient to contain all the information of

interest.

From the observation that the films will support the continuous precipitation process, it is obvious that the surface regions of a bulk material can also. All that would be required for the bulk material would be the supersaturation of the surface. The supersaturation of bulk metal surfaces during CO attack is an obvious experimental fact since cementite has been observed in the surface regions of bulk iron repeatedly (24,26,35). It remains to correlate the morphology of cementite in the surface of bulk iron to that of iron films.

In an effort to relate single crystal film results with the results of in situ studies of CO decomposition on bulk materials, a series of experiments was conducted in a metioscope. As a courtesy, time was granted for some experiments using a metioscope by the Hardco Scientific Division of the Fieldstone Corporation of Cincinatti, Ohio. The experiments were limited in scope and duration. As a result, the information obtained was quite general and did not represent the true worth of the instrument for surface reaction investigation.

A metioscope is a secondary emission electron microscope. An image of a sample surface is produced by knocking electrons from the surface with an iron beam impinging on the specimen at grazing incidence. By accelerating the emitted electrons through an electron optics system analogous to that in an electron microscope, a relief image of the surface is produced on a fluorescent screen. Some distinction can be made between different compounds present at the specimen surface due to differences in work functions. The advantages of using this instrument are (1) bulk material investigations, (2) at temperature studies, and (3) in situ reaction

studies can be conducted under moderate vacuum conditions.

The experiments carried out in the metioscope were made prior to developing the techniques of reaction carried out on the thin single crystal films. As a result, the temperatures studied were generally 100° higher than those used for the single crystal film studies. Therefore, few direct correlations can be made between the two works. However, it is interesting to note that the overall shapes of the particles formed in the surface of the bulk specimens reacted in the metioscope are quite similar to those of the cementite particles formed in the single crystal films. Extraction replicas of the bulk samples contained the precipitate particles which gave the cementite diffraction pattern. The cementite particles were formed in the surface of a bulk polycrystalline specimen in less than 1 hour of reaction at 500°C under a CO pressure of a few mm Hg. For both (001) and (111) plane faces of bulk single crystal specimens, identifiable cementite formed in approximately 15 minutes of reaction at 650°C under similar pressure conditions. The shapes of the particles appeared to be quite similar from one specimen to another.

Kehrer and Leidheiser (24) as well as Ruston, et al. (26) reported cementite formations to grow in the surface of iron. The precipitates appear to be quite similar in morphology to those found in the iron single crystal films. The temperature range of their observations was from 350 to 550°C.

An additional observation by Ruston is significant in linking bulk iron reaction phenomena to the thin film results. The "little crystals" (described in Chapter I) observed by Ruston to form on the ferrite surface between cementite out-croppings are of the same size and shape as the button formations observed in Reactions 10 and 11. His sightings were made after

1 hour of attack in an atmosphere of 0.5 atm CO at a temperature of 550°C. In a less than convincing analysis, he proposed that these crystals were Fe_7C_3. No confirmation experiments identifying this material were made in the present work. As previously stated, the only material which could be identified in the vicinity of a button was graphite. Had a crystal of carbide been present, some diffraction evidence should have occurred even if it did not result in a complete and solvable SAD pattern. However, no such evidence was observed.

The lack of an increase in cementite formation rate for CO pressures above 500 μ for the iron films (implying a sharp decrease in CO decomposition rate) is not inconsistent with results in the literature showing the CO decomposition rate to be proportional to the CO pressure (19). The report referred to was made for reaction occurring well beyond the initial stages of metal attack. Also, more rapid decomposition of CO can be supported by bulk materials since the interior of the metal will be continuously taking carbon away from the surface. The effect will oppose the attainment of the degree of carbon supersaturation in the surface required to stop CO decomposition.

In summation, the information obtained from the studies of the CO attack on thin iron films is directly related to the processes occurring in the presence of bulk iron.

E. Relation of the Results to the Metal Dusting Problem

The decomposition of carbon monoxide as catalyzed by a metal surface is the most prominent of all the metal dusting reactions. However, the reactions for most carbonaceous gases are similar in their ultimate effect

on the metal. This fact indicates that the solid phase phenomena is basically the same from one case to another. Accordingly, the observations and postulates made in the present research have general significance.

It is proposed that metal dusting initiates by the solution of carbon into the metal matrix. Nacent carbon in the general case is liberated from the carbon bearing molecules of the environment by catalytic cracking processes at the metal surface.

The metal is proposed to act as a catalyst only if (1) it can adsorb the carbon-bearing species; (2) the specific carbon atom ultimately to be incorporated into the lattice from a molecule forms a chemisorption bond with the metal (a prior step would be required for free radial formation in the case of saturated carbon compounds); (3) the metal is capable of establishing carbide type bonds; (4) the metal is unsaturated with carbon or is actively supporting continuous precipitation. Thus, iron, cobalt, nickel, and chromium are metals which fulfill the requirements for a metal dusting type catalyst by this scheme.

As the reaction progresses, the region close to the surface becomes supersaturated with carbon, and continuous precipitation is initiated. In the case of iron, cementite nucleation occurs at dislocations, sub-boundaries, and grain boundaries. For iron the cementite nuclei grow to form distinct incoherent particles which increase in size with continuing precipitation. Later in the process graphite, the equilibrium phase, nucleates and cementite begins to decompose. Preferred sites for graphite nucleation exist at the cementite-ferrite interface at points along the surface intercepts. Other nucleation sites for graphite also exist in the ferrite surface. Continuing reaction promotes both cementite growth (concurrent with cementite

decomposition) as well as growth of the graphite deposits. These occur at accommodating rates. Cementite particles are more easily formed initially than graphite, and the carbide may act as intermediate storage centers for carbon in the early stages of the reaction. All these phenomena are common to the general theory of continuous precipitation and should be rate-controlled by the diffusion of carbon in iron. The increasing reactivity reported for iron with increasing temperature up to approximately 550°C appears to result from the corresponding increase in the diffusion rate for carbon in iron. In retrospect, a study for determining the mechanism for the decline in reactivity above 550°C would require more experiments at both 450°C and 550°C in which the time of reaction would be extended for a series of values. Westerman (35) has attributed the decrease to the increasing thermodynamic stability of cementite with increasing temperature.

Analogous precipitation processes probably control the reaction in the other metals with differences arising from differences in the stability of both the metal-carbon solutions and the carbide phases characteristic of the metal involved.

Once decomposition of the carbide (especially cementite) begins, the character of the surface product formation may be altered. If the iron, for example, is liberated in fine dispersion, obviously the great increase in the iron surface to mass ratio will increase the sites for CO decomposition. In the fine particle form, the iron may be better able to accept nacent carbon and subsequently generate graphite. In this form the iron may be more easily visualized as promoting the filamentary formation of graphite which is generally found with the reaction. The finely divided iron may also be transformed to the higher iron carbides which have been

reported to play important roles in CO decomposition and filament formation. The latter stages of this reaction obviously require further study.

In view of the proposed character of the initial stages of metal dusting, the catalytic action of the iron matrix is expected to change during the course of the reaction. The pure metal would be expected to decompose CO at a decreasing rate as the carbon content of the iron surface increased. From the present study, CO decomposition does appear to slow to a rate sufficient only to maintain supersaturation of the iron films during reaction.

For bulk materials decreasing CO decomposition may not easily be demonstrated since the interior of the metal will continuously remove carbon from the surface. In addition, once cementite decomposition begins, increasing quantities of fresh ferrite will be available for CO chemisorption and the rate of decomposition should increase. The increased CO decomposition should then be self-propagating as cementite is continuously formed and decomposed, producing more of the fine ferrite dispersion. The CO pressure curves of Hui and Boulle (56) for the reaction on iron follow the pattern expected for this type of reaction.

If precipitation of a carbide or of graphite were stopped, CO decomposition would be expected to stop when a maximum degree of supersaturation of the lattice had been achieved. Decomposition of CO would also be expected to stop if the surface of the catalyst were completely converted to a stable carbide.

In view of the proposed continuous precipitation mechanism for the phenomena taking place in the solid phase during CO attack, it is obvious that the rate and degree of attack can be varied by changing the activity of

the carbon in the system. Alloying elements are known to effect the stability of cementite in iron (and steels). The metallic elements to the left of iron in the Periodic Table, Mn, Cr, V, and Ti, are known to stabilize cementite. According to the proposed mechanism, addition of these elements to iron would retard metal dusting since the carbide would not break down as readily to nucleate the graphite nor produce more active metal. Silicon, on the other hand, lowers the solubility of carbon in iron, does not stabilize cementite, and may aid graphite formation. The ultimate effect on metal dusting by Si is not exactly known since on first thought the decrease in solubility of carbon in iron may be interpreted as an inhibiting effect. However, if Si promotes graphite formation and decreases the stability of cementite, the effect may be the reverse. An added consideration of an SiO-rich region previously formed proximate to the surface is pertinent also. Such a stable layer has been demonstrated to retard attack.

Pretreatments of iron with compounds containing divalent sulfur (i.e., H_2S) have been reported to inhibit metal dusting. According to the present scheme, this effect is understandable. Sulfur in cast iron, for example, is known to retard cementite formation and to hinder graphite nucleation and/or growth. Therefore, the propagation of the metal dusting reaction should be inhibited since cementite formation and subsequent nucleation and growth of graphite are required.

The inhibition of metal dusting by a NH_3 pretreatment is of uncertain origin. The treatment should nitride the steel. Since such treatments have been characterized as only temporary, perhaps the inhibiting effect is only kinetic in nature since a double diffusional process would be required in the matrix. In other words, not only would carbon have to diffuse into

the metal to precipitate at active sites, but nitrogen would probably have to be replaced at these sites and subsequently diffuse from the metal.

Accounting for the effects of impurities in either gas or metal is obviously a complex problem. It is, however, quite clear that the purity of the system may have profound influences on metal dusting reactions in general.

As previously shown in this chapter, the only compounds identified on or in the iron films reacted in the present program were cementite (Fe_3C), graphite (C), and magnetite (Fe_3O_4). Magnetite was found to occur upon exposure of the films to the atmosphere. No magnetite formation could be attributed to result from the exposure to CO. It is proposed that the appearance of magnetite in metal dusting reactions occurs as a result of an oxidizing impurity in the carbonaceous environment. Carbon dioxide concentrations above specific levels can also definitely lead to oxidation. A number of the oxide observations appearing in the literature were described in Chapter I.

Graphite has been observed as the primary product of metal dusting in all instances of sufficient duration. Cementite, on the other hand, was not the only carbide phase reported in the literature to result from the CO attack of iron. It is proposed on the basis of the present investigation and the background obtained from the literature that cementite is the first new product phase formed in the CO attack of iron masses of sufficient size to support a continuous precipitation process. The temperature range of applicability for the proposal runs from 250°C to 550°C. Predominantly, the reported observations of the higher carbides of iron were for CO attack of iron powder (often the promoted NH_3 synthesis type catalyst) under 350°C.

It has been suggested in the literature that very small grains of bulk iron can be directly transformed to a higher carbide. Since the present investigation deals with only the initial stages of reaction and only overlaps a small portion of the temperature range of these observations, it cannot be used to support nor contradict this evidence. Once cementite begins to decompose to produce fine iron particles, it may be possible that the higher carbides form in the CO attack of bulk iron.

CHAPTER IV

CONCLUSIONS

The research described in the preceding chapters led to the following conclusions.

1. Good quality iron single crystal films can be grown reproducibly on the (001) cleavage faces of NaCl. The (001) films form from the vapor by the growth of small nuclei which impinge to form complex networks. Upon closure of the networks crystallographic defects are trapped. A good quality crystal is formed by annealing most of the lattice defects out of the film. The primary crystallographic defect of iron single crystal films is the dislocation sub-boundary.

2. Iron surfaces of very high purity are a sufficient catalyst for the decomposition of carbon monoxide.

3. The iron lattice becomes supersaturated with the nascent carbon from the surface decomposition of carbon monoxide. No carbon deposit nucleates on the iron surface during the early stages of the reaction.

4. The first electron microscopic evidence of the ensuing formation of a solid phase product is the decoration of dislocations and dislocation sub-boundaries within the iron matrix. The first discernable decorations are coherent carbon-rich atom clusters.

5. The population density of product nuclei is very sensitive to the degree of supersaturation of the iron lattice with carbon.

6. Cementite, the first identifiable product in the temperature

range 250° to 550°C, nucleates from coherent carbon-rich atom segregates observable in the electron microscope.

7. The population density of carbide particles after 1 hour of reaction under 1,000 μ of CO tends to decrease with increasing temperature.

8. The only other solid phase product to form is graphite which appears when the cementite begins decomposing. Graphite nucleates and grows in more than one form. Specially oriented graphite flakes exist at lattice discontinuities such as relatively large surface steps and holes in the iron films. The (002) graphite planes tend to lie parallel to {110} and {200} iron planes. Graphite lamellae with the basal planes parallel to the film plane form on the cementite surfaces. Significant quantities of apparently amorphous carbon are often left at the sites of cementite particle decomposition.

9. Magnetite (Fe_3O_4) is not a product of the CO attack of iron. Magnetite as an epitaxic film is formed on the iron foil upon subjecting it to analysis. The satellite spots around iron {110} reflections are caused by the {311} and {511} reflections from the surface oxide. The oxide is oriented Fe_3O_4 (001) [400] || (001) [110] Fe. These findings clarify a number of observations of iron oxidation reported in the literature.

10. Cementite will decompose at a temperature at least as low as 450°C.

11. Cementite particle shapes give evidence of the accommodation of surface energy and strain energy associated with their nucleation and growth. This evidence together with that from surface replicas establish that the cementite forms and grows in the metal matrix and not on the surface. The particles have shapes corresponding to irregular platelets.

12. Cementite particle growth is controlled by the diffusion of carbon in the iron. The growth rate data for the cementite particles was used to calculate the activation energy for growth. The value was 21.4 kcal/mole corresponding well with the accepted value for the activation energy for carbon diffusion in alpha-iron.

13. All features observed for the nucleation and growth of the product particles correspond to the theory of continuous precipitation.

14. A fixed orientation relationship does not exist between the lattices of cementite and the iron single-crystal films.

15. Large crystals of cementite can be formed by reacting iron single crystal films with CO. Stacking faults on the (001) cementite planes do occur.

16. Pressure variation of the CO does not change the order of product formation in the 5 to 1,000 μ range. Temperature and pressure do effect the CO decomposition rate. The rate of CO decomposition is also a function of the carbon content of the iron phase. The CO decomposition rate is equal to the rate of carbon precipitation (in the form of cementite) from the ferrite matrix when the pressure is sufficient and saturation of the iron has been attained. The evidence indicates a maximum exists for the degree of supersaturation attained at a given temperature.

CHAPTER V

RECOMMENDATIONS FOR FUTURE STUDIES

The research described in the foregoing chapters immediately suggests many new programs as well as extensions of the studies presently treated. The development of techniques for reproducibly growing iron single crystal films affords many new investigations of iron systems because of the exceptional versatility of transmission electron microscopy. Of immediate value, the possibility of stacking fault formation in the body-centered-cubic iron lattice could be investigated and the fault characterized. Some evidence for their existence was observed in the deposited iron films although no proof of the character of the phenomenon was obtained. Also, investigation of the heat treatment of iron single crystal films coated with evaporated carbon should be made to check the results of Schenck (95). Schenck's studies of the time-temperature range of existence of the iron carbides are very interesting, but there is reason to believe that the films used in his work were discontinuous. Therefore, extension of the investigations using the high quality single-crystal iron films produced for the present studies would be very worthwhile and readily accomplishable.

The single crystal iron films will also allow basic studies of the properties of pure iron. Magnetic and mechanical properties are two of the more obvious subjects. Also, the very large cementite particles which form in the iron after extended exposure to carbon monoxide are excellent specimens for basic studies of cementite crystallography. Other logical

extensions of the present investigation could contribute much information to the basic knowledge of the iron-carbon system.

Of significance to metal dusting, the methods of investigation used in this work can be extended to study the influence of gaseous impurities on iron as a catalyst. The mechanism of acceleration or inhibition of CO decomposition induced by the impurities could well be the end result.

Also of great interest are fundamental oxidation studies using the single crystal films as specimens. Once the oxidation of the films is characterized, the additional study of the CO attack of iron supporting an oxide film can be conducted.

In addition to more drastic experimental modifications, the present type of investigation should be expanded to include more intensive studies of the carbon-rich atom clusters from which cementite is nucleated. The temperature range investigated should be extended to include temperatures as low as 100°C in order to determine whether a carbide of higher carbon content is formed. The pressure range should be increased to include carbon monoxide pressures at and above 1 atmosphere in order to more fully investigate the pressure dependence of the solid phase product formation. Time as a single reaction variable should be extensively studied to better define the overall kinetics of the process. The time of reaction should also be extended and varied for a series of experiments at both 450° and 550°C to allow investigation of the phenomena causing the decline in reactivity above 550°C.

The orientation relation observed between the graphite formations and the iron matrix warrants further investigation. There appeared to be no other feature which might logically be expected to give rise to the

filament formations found in other studies of CO decomposition on iron.

A very important approach for future studies appears to be the combination of internal friction measurements and thin foil electron microscopy of iron sheets undergoing carbon monoxide attack. From such studies the maximum degrees of carbon supersaturation at fixed temperatures and pressures may be determined. The point of initial carbon precipitation might also be related to the micrographic picture of precipitate development.

In order to determine the exact sites of molecular CO adsorption and decomposition, it is apparent that low energy electron diffraction or possibly field emission microscopy are the only techniques applicable. The continuous precipitation process observed in this study suggests that the decomposition site density is very large with respect to the product density in the surface plane.

While the individual procedures developed for producing, reacting, and analyzing specimens are certainly not new in concept, their combination as a program approach to specific problems has not often been used. The quality of the results presented in this work is quite indicative of the soundness of the approach for use in studying many surface reactions under quite varied conditions. It is not practical to list all the problems for which similar and extended studies are applicable. The intent is to stimulate further development of these techniques in their application to surface reaction studies.

APPENDICES

APPENDIX A

THERMODYNAMIC CONSIDERATIONS

Preparatory to the experimental portion of this research, a thermodynamic study was made concerning the formation of a variety of compounds in the iron-carbon-oxygen system. The study was made to aid the planning of experiments for determining the reaction products resulting from the action of carbon monoxide on iron.

The free energy changes of twelve reaction equations as functions of temperature were investigated. Standard Gibbs free energy of formation data (163) were calculated at 400°, 700°, 800°, 900°, $1{,}000^{\circ}$, and $1{,}400^{\circ}$K to obtain the information for plotting the thermodynamic relations. The equations for CO decomposition and cementite formation as well as those for reactions involving direct oxidation of iron by both CO and CO_2 were included. The reactions were formulated as follows:

1) $2\ CO = CO_2 + C$

2) $3\ Fe + C = Fe_3C$

3) $Fe + CO = FeO + C$

4) $3\ FeO + CO = Fe_3O_4 + C$

5) $2\ Fe_3O_4 + CO = 3\ Fe_2O_3 + C$

6) $Fe + CO_2 = FeO + CO$

7) $3\ FeO + CO_2 = Fe_3O_4 + CO$

8) $2\ Fe_3O_4 + CO_2 = 3\ Fe_2O_3 + CO$

9) $3\ Fe + 4\ CO = Fe_3O_4 + 4\ C$

10) $2\ Fe + 3\ CO = Fe_2O_3 + 3\ C$

11) $3\ Fe + 4\ CO_2 = Fe_3O_4 + 4\ CO$

12) $2\ Fe + 3\ CO_2 = Fe_2O_3 + 3\ CO$

The results are illustrated in Figure 124. The direct reaction of iron with CO to form iron pentacarbonyl was not included since it has an equilibrium content of $K = 1 \times 10^{-13}$ (from $\log K = 8940/T - 30.09$ (164)) at a temperature as low as 250°C.

The simple analysis afforded by the plots of Figure 124 provided no significant information to clarify the problem. The compounds FeO, Fe_3O_4, and Fe_2O_3 are indicated to possibly form by direct oxidation of the iron by carbon monoxide in the temperature range of interest (250° to 550°C). These same oxides by other reaction formulations can be reduced by the carbon monoxide. Both FeO and Fe_2O_3 can also be converted to Fe_3O_4. As expected, carbon and cementite are likely products of the CO interaction with iron. It is evident that the system offers many possibilities for complications.

Since the experiments were to be conducted at reduced pressures and high temperatures, the question of oxide stability arose. The decomposition pressures of the iron oxides were, therefore, calculated. The results and the reactions considered for a temperature of 900°K were as follows:

$$2\ FeO(s) = 2\ Fe(s) + O_2(g),\ p_{O_2} = 1.58 \times 10^{-24}\ atm$$

$$Fe_3O_4(s) = 3\ Fe(s) + 2O_2(g),\ p_{O_2} = 1.26 \times 10^{-24}\ atm$$

$$2\ Fe_3O_4(s) = 6\ FeO(s) + O_2(g),\ p_{O_2} = 3.98 \times 10^{-25}\ atm$$

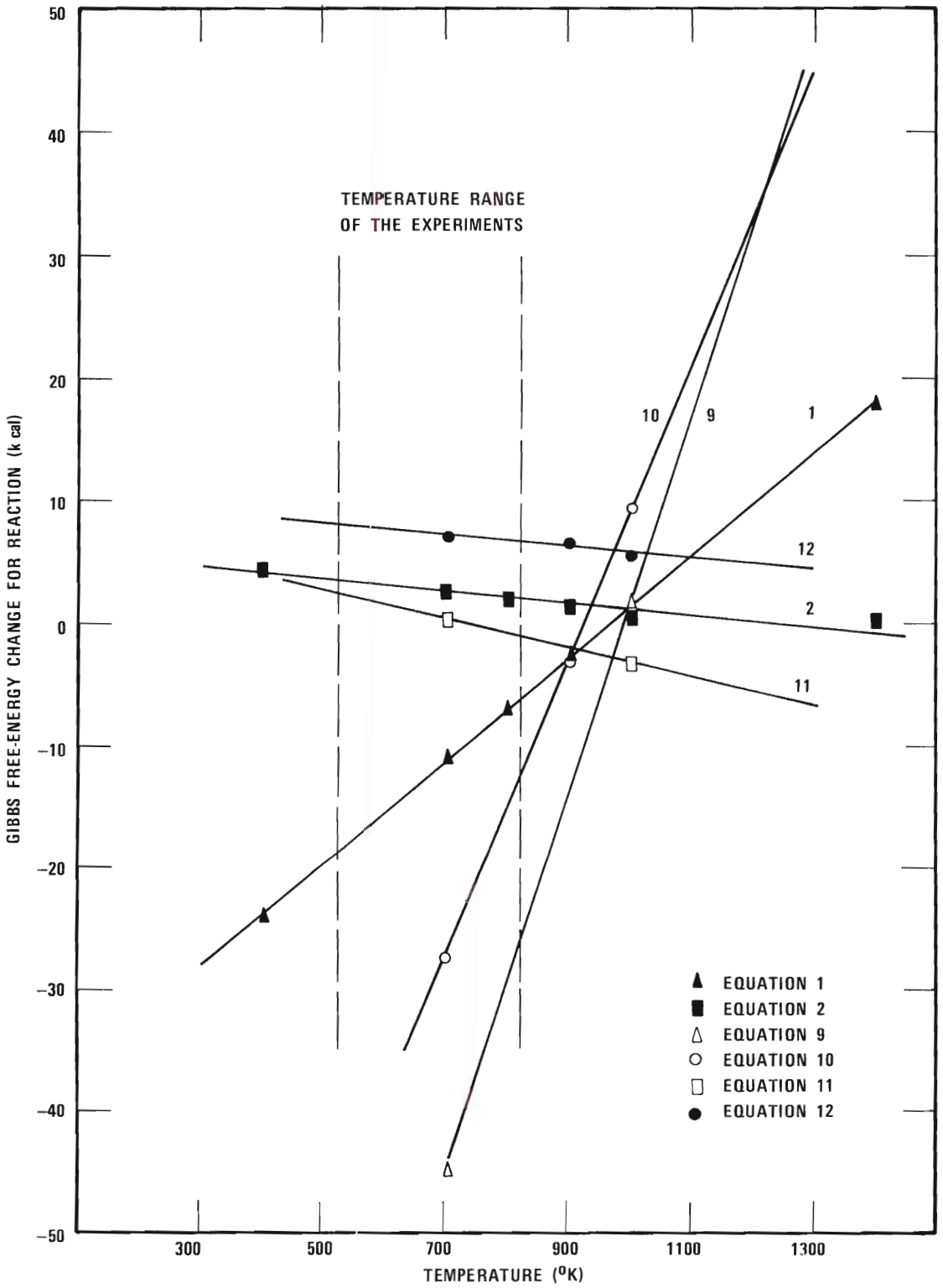

Figure 124. Gibbs Free-Energy Change for Reaction Versus Temperature for Several Reaction Formulations

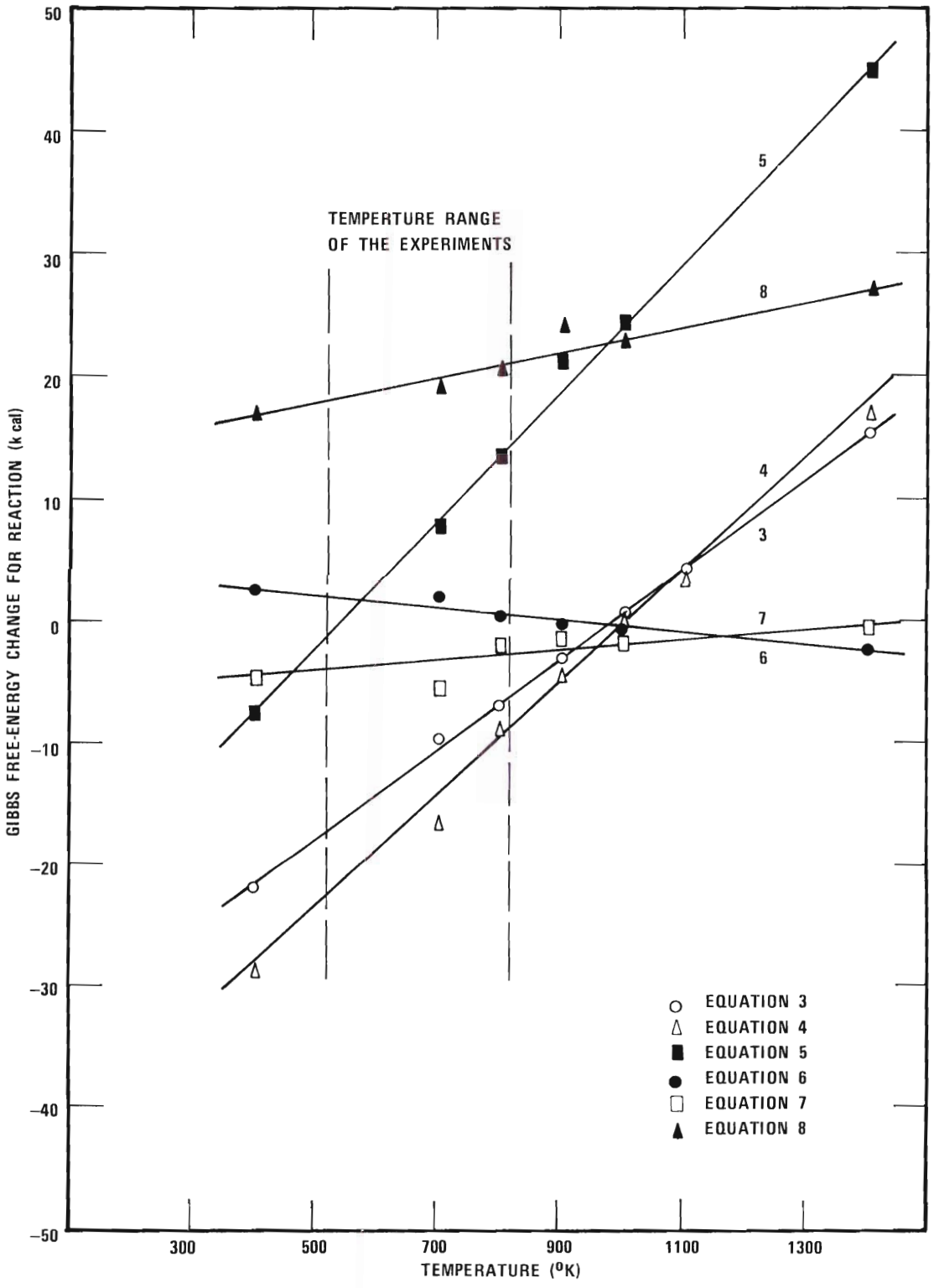

Figure 124 (Continued). Gibbs Free-Energy Change for Reaction Versus Temperature for Several Reaction Formulations

$$2\ Fe_2O_3(s) = 4\ Fe(s) + 3O_2(g);\ p_{O_2} = 2.51 \times 10^{-23}\ atm$$

$$6\ Fe_2O_3(s) = 4\ Fe_3O_4(s) + O_2(g),\ p_{O_2} = 1.26 \times 10^{-12}\ atm$$

$$2\ Fe_2O_3(s) = 4\ FeO(s) + O_2(g),\ p_{O_2} = 6.31 \times 10^{-21}\ atm$$

The relation $K = \exp(-\Delta G^{\circ}/RT)$ for the reactions was the basis for the calculations. Approximating the activities of the solids by unity and the activity of oxygen by its partial pressure, the relation used takes the form $\ln p_{O_2} = -\Delta G^{\circ}/aRT$ (where a is the coefficient of the oxygen term in the reaction being considered). The standard Gibbs free energies of formation used in the calculations were obtained from Bulletin 605 of the Bureau of Mines (163). The magnitudes of the various decomposition pressures preclude the possibility of simple oxide decomposition in the vacuum system at the temperatures used throughout the experiments.

APPENDIX B

DIFFRACTION DATA

In this appendix are tabulated the interplanar spacing data found useful for solving the electron diffraction patterns encountered. Iron, the iron carbides, magnetite, and graphite are the materials considered. Listings from multiple sources are included for the common carbides.

Table 22. X-Ray Diffraction Data for Iron (165)

hkl	d_{obs} (Å)	I/I_0 x 100
110	2.0268	100
200	1.4332	19
211	1.1702	30
220	1.0134	9
310	0.9064	12
222	0.8275	6
321	0.768	6

Table 23. Cementite Lattice Spacings and Reciprocal Lattice Spacings*

hkℓ	d	$\frac{1}{(d)}$	hkℓ	d	$\frac{1}{(d)}$
001	6.7297	0.1486	222	1.5081	0.6631
010	5.0787	0.1969	114	1.5056	0.6642
100	4.5144	0.2215	300	1.5048	0.6645
011	4.0539	0.2467	301	1.4685	0.6809
101	3.7490	0.2667	310	1.4428	0.6931
110	3.3741	0.2964	132	1.4340	0.6974
002	3.3649	0.2972	311	1.4107	0.7088
111	3.0162	0.3315	024	1.4025	0.7130
012	2.8051	0.3565	302	1.3737	0.7280
102	2.6979	0.3707	230	1.3543	0.7384
020	2.5393	0.3938	033	1.3513	0.7400
112	2.3826	0.4197	204	1.3489	0.7413
021	2.3758	0.4209	223	1.3483	0.7417
200	2.2572	0.4430	124	1.3394	0.7466
003	2.2432	0.4458	231	1.3277	0.7532
120	2.2132	0.4518	312	1.3260	0.7541
201	2.1400	0.4673	214	1.3037	0.7670
121	2.1025	0.4756	320	1.2946	0.7725
210	2.0627	0.4848	133	1.2945	0.7725
013	2.0520	0.4873	321	1.2713	0.7866
022	2.0269	0.4934	040	1.2697	0.7876
103	2.0089	0.4978	232	1.2564	0.7959
211	1.9721	0.5071	303	1.2497	0.8002
202	1.8745	0.5335	041	1.2477	0.8015
113	1.8681	0.5353	140	1.2223	0.8182
122	1.8491	0.5408	313	1.2135	0.8241
212	1.7585	0.5687	322	1.2082	0.8277
030	1.6929	0.5907	141	1.2026	0.8315
220	1.6871	0.5927	034	1.1933	0.8380
004	1.6824	0.5944	224	1.1913	0.8394
023	1.6812	0.5948	042	1.1879	0.8418
031	1.6417	0.6091	233	1.1594	0.8625
221	1.6364	0.6111	134	1.1537	0.8668
014	1.5971	0.6261	142	1.1488	0.8705
203	1.5911	0.6285	400	1.1286	0.8861
130	1.5851	0.6309	330	1.1247	0.8891
104	1.5765	0.6343	304	1.1216	0.8916
123	1.5755	0.6347	323	1.1213	0.8919
131	1.5429	0.6481	401	1.1131	0.8984
213	1.5184	0.6586	331	1.1093	0.9015
032	1.5123	0.6613	240	1.1066	0.9037

(continued)

Table 23. Cementite Lattice Spacings and Reciprocal Lattice Spacings* (continued)

hkℓ	d	$\frac{1}{(d)}$	hkℓ	d	$\frac{1}{(d)}$
043	1.1050	0.9050	344	0.8406	1.1896
410	1.1017	0.9077	441	0.8370	1.1948
314	1.0952	0.9131	434	0.8200	1.2196
241	1.0920	0.9158	442	0.8182	1.2222
411	1.0873	0.9197	443	0.7896	1.2665
143	1.0733	0.9317	444	0.7541	1.3262
402	1.0700	0.9346			
332	1.0667	0.9375			
234	1.0550	0.9479			
242	1.0512	0.9513			
412	1.0470	0.9551			
420	1.0313	0.9696			
324	1.0260	0.9747			
421	1.0194	0.9809			
044	1.0135	0.9867			
403	1.0082	0.9919			
333	1.0054	0.9946			
243	0.9924	1.0076			
413	0.9889	1.0112			
144	0.9889	1.0113			
422	0.9861	1.0141			
340	0.9704	1.0305			
341	0.9605	1.0412			
430	0.9391	1.0649			
404	0.9373	1.0669			
423	0.9370	1.0672			
334	0.9350	1.0695			
342	0.9324	1.0725			
431	0.9300	1.0752			
244	0.9245	1.0816			
414	0.9217	1.0850			
432	0.9045	1.1056			
343	0.8906	1.1228			
424	0.8793	1.1373			
433	0.8662	1.1544			
440	0.8435	1.1855			

* Calculated from lattice parameters obtained from x-ray diffraction data (166).

Table 24. Electron Diffraction Data of Cementite

Line No.	Nagakura (93) hkl*	Nagakura (93) d_{obs} (Å)	Nagakura (93) I/I_0 x 100	Schenck (95) d_{obs} (Å)	Schenck (95) I/I_0 x 100
1	(001)	6.948	s	-	-
2	(010)	5.086	w	-	-
3	(100)	4.543	vw	-	-
4	(011)	4.055	vw	-	-
5	101	3.771	w	-	-
6	110	3.386	m	3.367	20
7	002	3.386	m	-	-
8	111	3.015	w	3.020	5
9	(012)	2.810	w	2.806	5
10	(102)	2.685	w	-	-
11	020	2.543	w	2.529	20
12	112	2.384	vs	2.382	60
13	021	2.384	vs	-	-
14	200	2.258	s	2.259	30
15	(003)	-	vw	-	-
16	120	2.212	m	2.210	40
17	(201)	2.144	vw	-	-
18	121	2.106	m	2.100	80
19	210	2.063	s	2.064	80
20	(013)	-	-	-	-
21	022	2.031	m	-	-
22	103	2.015	vs	2.021	100
23	211	1.977	s	1.976	80
24	202	1.871	vs	1.863	80
25	113	1.871	vs	-	-
26	122	1.851	s	1.853	30
27	212	1.758	m	1.759	40

Table 24. Electron Diffraction Data of Cementite (Continued)

Line No.	Nagakura (93) hkl*	Nagakura (93) d_{obs} (Å)	Nagakura (93) I/I_0 x 100	Schenck (95) d_{obs} (Å)	Schenck (95) I/I_0 x 100
28	(030)	-	-	-	-
29	220	1.685	m	-	-
30	004	1.685	m	1.682	55
31	023	1.685	m	-	-
32	(031)	1.641	vw	1.640	20
33	221	1.639	m	-	-
34	(014)	1.599	vw	-	-
35	(203)	1.599	vw	-	-
36	130	1.583	w	1.585	45
37	(104)	1.576	vvw	-	-
38	123	1.576	vvw	-	-
39	131	1.544	w	1.541	20
40	213	1.514	vw	-	-
41	(032)	1.514	vw	-	-
42	222	1.508	m	-	-
43	(300)	1.508	m	1.510	30
44	114	1.508	m	-	-
45	301	1.463	vvw	-	-
46	310	1.447	vvw	-	-
47	132	1.437	vvw	-	-
48	311	1.410	w	1.407	20
49	024	1.400	w	-	-
50	(302)	-	-	-	-
51	230	-	vvw	-	-
52	(033)	-	vvw	-	-
53	204	1.348	w	-	-
54	223	1.348	w	-	-

Table 24. Electron Diffraction Data of Cementite (Continued)

Line No.	Nagakura (93)			Schenck (95)	
	hkl*	d_{obs} (Å)	I/I_0 x 100	d_{obs} (Å)	I/I_0 x 100
55	(005)	1.348	w	-	-
56	124	1.339	w	-	-
57	231	1.331	m	1.335	25
58	312	1.331	m	1.328	45
59	214	1.303	w	-	-
60	320	1.303	w	-	-
61	(015)	-	-	-	-
62	133	1.290	w	1.293	15
63	105	1.283	vvw	-	-
64	321	1.271	vvw	-	-
65	040	1.271	vvw	-	-
66	232	1.256	vw	1.254	15
67	303	1.249	w	-	-
68	115	1.249	w	-	-
69	041	1.249	w	-	-
70	140	1.221	w	1.218	55
71	313	1.212	m	-	-
72	322	1.212	m	-	-
73	141	1.201	vvw	-	-
74	(034)	1.189	m	-	-
75	224	1.189	m	-	-
76	025	1.189	m	-	-
77	042	1.189	m	-	-
78	215	1.167	vw	1.161	45
79	233	1.157	m	-	-
80	(205)	-	-	-	-
81	134	1.150	m	1.153	15

Table 24. Electron Diffraction Data of Cementite (Continued)

Line No.	Nagakura (93) hkl*	Nagakura (93) d_{obs} (Å)	Nagakura (93) I/I_0 x 100	Schenck (95) d_{obs} (Å)	Schenck (95) I/I_0 x 100
82	125	1.150	m	-	-
83	142	1.150	m	-	-
84	400	1.127	s	1.128	50
85	330	1.127	s	-	-
86	(304)	1.121	m	-	-
87	323	1.121	m	-	-
88	006	1.121	m	-	-
89	(401)	-	-	-	-
90	331	1.109	w	-	-
91	240	1.109	w	1.106	35
92	043	1.102	vw		
93	410	1.102	vw	-	-
94	314	1.102	vw	-	-
95	(016)	1.095	vw	-	-
96	241	1.095	vw	-	-
97	(106)	1.087	vw	-	-
98	411	1.082	vvw	-	-
99	143	1.072	vvw	-	-
100	402	1.072	vvw	1.069	10
101	-	-	-	1.054	20
102	-	-	-	1.028	10
103	-	-	-	1.009	10
104	-	-	-	0.989	35

*(hkl) is the forbidden reflection

Table 25. Lattice Spacings of Hägg Carbide (Fe_5C_2)

	X-Ray Diffraction Data		Electron Diffraction Data			
	Duggin and Hofer (167)		Nagakura (93)		Schenck (95)	
Line No.	hkl	d_{obs} (Å)	d_{obs} (Å)	I	d_{obs} (Å)	I/I_0 x 100
1	-	-	5.37	w	-	-
2	-	-	5.05	w	-	-
3	-	-	4.25	w	-	-
4	-	-	3.98	vw	-	-
5	-	-	3.34	w, br	-	-
6	-	-	3.25	w	-	-
7	-	-	2.90	vw, br	-	-
8	$31\bar{1}$	2.62	2.63	vw	2.640	10
9	002	2.48	2.499	m	2.511	40
10	$311/20\bar{2}$	2.39	2.413	m	2.410	35
11	-	-	2.38	vw	-	-
12	$02\bar{0}$	2.26	2.275	w	2.271	35
13	$11\bar{2}/202$	2.18	2.205	s, br	2.197	55
14	-	-	2.100	m	2.103	45
15	$51\bar{0}/02\bar{1}$	2.06	2.071	vs	-	-
16	312/402	2.03	2.033	s	2.030	100
17	-	-	2.016	s	-	-
18	$51\bar{1}/22\bar{1}$	1.98	1.976	s	-	-
19	221	1.91	1.918	m	1.928	30
20	312/511	1.80	1.815	s	1.825	50
21	$40\bar{2}$	1.76	1.765	w	1.761	15
22	$42\bar{1}$	1.72	1.725	w	-	-
23	$51\bar{2}$	1.67	1.674	w	1.684	10

Table 25. Lattice Spacings of Hägg Carbide (Fe_5C_2) (Continued)

	X-Ray Diffraction Data		Electron Diffraction Data			
	Duggin and Hofer (167)		Nagakura (93)		Schenck (95)	
Line No.	hkl	d_{obs}(Å)	d_{obs}(Å)	I	d_{obs}(Å)	I/I_0 x 100
24	-	-	1.658	w	1.650	10
25	$60\bar{2}$	1.62	1.626	w	-	-
26	$11\bar{3}$	1.57	1.571	s	1.580	60
27	-	-	1.529	m	-	-
28	$42\bar{2}$	1.50	1.514	m	1.516	20
29	-	-	1.450	vw	-	-
30	-	-	1.430	vw	-	-
31	$33\bar{1}$	1.37	1.375	w	1.373	10
32	$33\underline{1}$	1.34	1.336	w	1.338	45
33	$80\underline{2}$	1.32	1.322	w	-	-
34	$53\bar{1}$	1.27	1.275	vw	-	-
35	$71\underline{2}$	1.25	1.234	w	1.242	20
36	$11\underline{4}/82\bar{1}$	1.21	1.216	s, br	1.217	70
37	-	-	1.204	vw	-	-
38	$62\bar{3}/91\bar{2}$	1.17	1.162	vw	1.168	70
39	$42\bar{3}/80\underline{2}$	1.16	1.158	w	-	-
40	$82\underline{1}/04\underline{0}/100\bar{0}$	1.14	1.139	w	1.139	30
41	$13\bar{3}/60\underline{4}$	1.13	1.126	w	1.128	35
42	041	1.11	1.111	w	1.109	55
43	404	1.09	1.086	w	-	-
44	-	-	1.063	vw	-	-
45	-	-	1.042	w, br	1.050	25
46	-	-	1.022	vw	1.014	40

Table 25. Lattice Spacings of Hägg Carbide (Fe_5C_2) (Continued)

	X-Ray Diffraction Data		Electron Diffraction Data			
	Duggin and Hofer (167)		Nagakura (93)		Schenck (95)	
Line No.	hkl	d_{obs} (Å)	d_{obs} (Å)	I	d_{obs} (Å)	I/I_0 x 100
47	-	-	1.003	vw	0.989	40
48	-	-	0.982	w	-	-
49	-	-	0.971	w	-	-
50	-	-	0.938	vw	-	-
51	-	-	0.926	vw	-	-
52	-	-	0.912	w	-	-
53	-	-	0.904	vw	-	-
54	-	-	0.887	vw, br	-	-
55	-	-	0.868	w, br	-	-
56	-	-	0.840	w	-	-
57	-	-	0.823	vw	-	-
58	-	-	0.805	vw	-	-
59	-	-	0.785	vw	-	-
60	-	-	0.774	vw	-	-
61	-	-	0.759	vw	-	-

Table 26. Lattice Spacings for Epsilon Carbide

	X-Ray Diffraction Data			Electron Diffraction Data			
	Hoffer (68)			Nagakura (93)		Schenck (95)	
Line No.	hkl	d_{obs}(Å)	I/I_0 x 100	d_{obs}(Å)	I/I_0 x 100	d_{obs}(Å)	I/I_0 x 100
1	-	-	-	4.0 - 4.4	vw, br	-	-
2	-	-	-	2.8 - 3.2	vw, br	-	-
3	100	2.38	40	2.384	15	2.365	25
4	002	2.16	60	2.172	18	2.160	40
5	101	2.08	100	2.084	87	2.078	100
6	102	1.60	60	1.607	13	1.600	50
7	110	1.37	60	1.378	10	1.370	60
8	103	1.24	60	1.234	9	1.237	40
9	-	-	-	-	-	1.185	10
10	112 201	1.16	60	1.161	18	1.158	40
11	-	-	-	-	-	1.140	20
12	-	-	-	-	-	1.087	20
13	-	-	-	-	-	1.044	20

Table 27. X-Ray Diffraction Data for Fe_7C_3 (74)

hkl	d_{obs} (Å)	I/I_0 x 100
002	2.270	7
120	2.255	31
012	2.122	41
121	2.019	100
300	1.989	13
112	1.895	5
301	1.820	11
022	1.807	22
220	1.720	13
401	1.417	4
023	1.349	8
303 500	1.204	14
322	1.171	15
501	1.153	11
330	1.146	13
004 142	1.131	5
133 014	1.117	6

Table 28. X-Ray Diffraction Data for Fe_3O_4 (165)

hkl	d_{obs} (Å)	I/I_0 x 100
111	4.86	30
220	2.97	60
311	2.530	100
222	2.425	10
400	2.097	50
422	1.714	40
333, 511	1.615	60
440	1.484	70
620	1.326	10
533	1.279	30
622	1.266	10
444	1.209	20
642	1.120	20
553, 731	1.091	50
800	1.048	20
660, 822	0.988	10
751, 555	0.968	40
840	0.938	30

Table 29. Electron Diffraction Data of Graphite (47)

hkl	d_{obs}(Å)	I
002	3.39	vs
100	2.12	s
101	2.02	m
004	1.69	m
110	1.228	s
112	1.150	m diffuse
006	1.120	m diffuse
201	1.049	w
106	0.991	w

APPENDIX C

MATERIAL PURITIES

Table 30. Carbon Monoxide Gas Analysis
Provided by The Matheson Company

Components	Volume Per Cent
CO_2	0.0005
O_2	0.0005
H_2	0.01
Ar	0.001
N_2	0.08
CO	>99.9

Note: Carbon Monoxide Obtained From The Matheson Company

Table 31. Iron Wire Analysis Provided by the Materials Research Corporation

Impurity	Content (ppm)	Impurity	Content (ppm)
Li	0.004	Rh	<0.03
Be	0.005	Pd	<0.08
B	<0.0008	Ag	<0.04
C	8.0	Cd	<0.08
N_2	7.0	In	<0.06
O_2	7.2	Sn	<0.02
H_2	< .1	Sb	<0.02
F^2	Interference	Te	<0.07
Na	0.8	I	<0.007
Mg	8.0	Cs	<0.006
Al	Interference	Ba	0.04
Si	<0.5	La	<0.006
P	0.3	Ce	<0.006
S	1.2	Pr	<0.006
Cl	3.0	Nd	<0.02
K	0.2	Sm	<0.025
Ca	2.0	Eu	<0.012
Sc	<0.025	Gd	<0.025
Ti	0.5	Tb	<0.006
V	<0.1	Dy	<0.03
Cr	0.6	Ho	<0.01
Mn	<0.1	Er	<0.4
Fe	-	Tm	<0.3
Co	0.3	Yb	<0.02
Ni	1.2	Lu	<0.006
Cu	<0.2	Hf	<0.025
Zn	<0.8	Ta	<1.0
Ga	<0.5	Re	<0.012
Ge	<1.0	Os	<0.02
As	<0.1	Ir	<0.012
Se	<1.0	Pt	<0.025
Br	<0.15	Au	0.4
Rb	<0.08	Hg	<0.03
Sr	<0.08	Tl	<0.012
Y	<0.04	Pb	<0.015
Zr	<0.06	Bi	<0.008
Nb	0.03	Th	<0.008
Mo	0.2	U	<0.008
Ru	<0.1		

Notes: Iron wire obtained from the Materials Research Corporation. Analysis typical as determined by mass spectrometry by the Battelle Memorial Institute for MRC.

APPENDIX D

EXPERIMENTAL RUN DATA

For completeness, the experimental data for the runs included in the Reaction Schedule of Table 3 are presented in Tables 32 through 46. This information should also be helpful for extending the application of the equipment and techniques developed.

Table 32. Data on the Experimental Conditions for Run 60 (Reaction 1)

Film Temperature		Copper Block Temperature		System Pressure	Remarks
T.C. Output (mV)	Temp. (°C)	T.C. Output (mV)	Temp. (°C)		
13.66	252	18.35	446	5×10^{-8} torr	t_e^o = 0 min.
		17.68	430	6×10^{-8} torr	t_e = 1 min. 30 sec.
					t_e^f = 2 min. 25 sec.
24.58	450	22.46	543		t_a^f = 30 min.
13.64	251	10.11	249	1×10^{-7} torr	t_r^o = 0 min.
13.56	250	10.24	252	1,000 μ CO	t_r = 5 min.
13.52	249	10.11	249	1,000 μ CO	t_r = 10 min.
13.60	251	10.08	248	1,000 μ CO	t_r = 15 min.
13.58	250	10.18	251	1,000 μ CO	t_r = 20 min.
13.60	251	10.23	252	1,000 μ CO	t_r = 30 min.
13.48	248	10.14	250	1,000 μ CO	t_r = 35 min.
13.45	248	10.02	247	1,000 μ CO	t_r = 40 min.
13.70	253	10.18	251	1,000 μ CO	t_r = 45 min.
13.60	251	10.22	252	1,000 μ CO	t_r = 50 min.

Table 32. Data on the Experimental Conditions for Run 60 (Reaction 1) (Continued)

Film Temperature		Copper Block Temperature		System Pressure	Remarks
T.C. Output (mV)	Temp. (°C)	T.C. Output (mV)	Temp. (°C)		
13.54	250	10.18	251	1,000 μ CO	t_r = 55 min.
13.52	249	10.16	250	1,000 μ CO	t_r^f = 60 min.; Termination
				1×10^{-6} torr	t_r^f + 8 min.

Variable Power Supply Settings
Substrate Heater Circuit: During Evaporation 59; Final for Film Anneal 68; Final for Reaction 28
Radiant Heater Circuit: During Evaporation 0; Final for Film Anneal 54; Final for Reaction 28

Table 33. Data on the Experimental Conditions for Run 61 (Reaction 2)

Film Temperature		Copper Block Temperature		System Pressure	Remarks
T.C. Output (mV)	Temp. (°C)	T.C. Output (mV)	Temp. (°C)		
14.42	266	18.44	448	8×10^{-8} torr	t_e^o = 0 min.
		17.70	431	2×10^{-7} torr	t_e = 1 min. 30 sec.
					t_e^f = 2 min. 10 sec.
24.61	450	22.22	537		t_a^f = 40 min.
13.54	250	10.18	251	2×10^{-7} torr	t_r^o = 0 min.
13.60	251	10.00	246	1,000 μ CO	t_r = 0+ min.
13.56	250	10.10	249	1,000 μ CO	t_r = 5 min.
13.45	248	10.12	249	1,000 μ CO	t_r = 10 min.
13.50	249	10.11	249	1,000 μ CO	t_r = 15 min.
13.56	250	10.16	250	1,000 μ CO	t_r = 20 min.
13.56	250	10.16	250	1,000 μ CO	t_r = 25 min.
13.72	253	10.28	253	1,000 μ CO	t_r = 30 min.
13.62	251	10.26	253	1,000 μ CO	t_r = 35 min.
13.54	250	10.20	251	1,000 μ CO	t_r = 40 min.

Table 33. Data on the Experimental Conditions for Run 61 (Reaction 2) (Continued)

Film Temperature		Copper Block Temperature		System Pressure	Remarks
T.C. Output (mV)	Temp. (°C)	T.C. Output (mV)	Temp. (°C)		
13.50	249	10.16	250	1,000 μ CO	t_r = 45 min.
13.50	249	10.14	250	1,000 μ CO	t_r = 50 min.
13.50	249	10.12	249	1,000 μ CO	t_r = 55 min.
13.56	250	10.18	251	1,000 μ CO	t_r = 60 min.
13.50	249	10.14	250	1,000 μ CO	t_r = 70 min.
13.50	249	10.08	248	1,000 μ CO	t_r = 80 min.
13.48	248	10.08	248	1,000 μ CO	t_r = 90 min.
13.52	249	10.11	249	1,000 μ CO	t_r = 100 min.
13.52	249	10.11	249	1,000 μ CO	t_r = 110 min.
13.60	251	10.25	252	1,000 μ CO	t_r = 120 min.
13.62	251	10.20	251	1,000 μ CO	t_r = 130 min.
13.54	250	10.20	251	1,000 μ CO	t_r = 140 min.
13.30	245	9.90	244	1,000 μ CO	t_r^f = 150 min.; Termination
				5×10^{-7} torr	t_r^f + 10 min.

Table 33. Data on the Experimental Conditions for Run 61 (Reaction 2) (Continued)

Variable Power Supply Settings

Substrate Heater Circuit:	During Evaporation 59;	Final for Film Anneal 68;	Final for Reaction 28
Radiant Heater Circuit:	During Evaporation 0;	Final for Film Anneal 54;	Final for Reaction 28

Table 34. Data on the Experimental Conditions for Run 63 (Reaction 3)

Film Temperature		Copper Block Temperature		System Pressure	Remarks
T.C. Output (mV)	Temp. (°C)	T.C. Output (mV)	Temp. (°C)		
14.52	267	18.66	454	1×10^{-8} torr	t_e^o = 0 min.
		18.22	443		t_e = 1 min.
				4×10^{-8} torr	t_e^f = 2 min. 10 sec.
24.50	248	22.50	544		t_a^f = 27 min.
17.32	318	13.02	320	4×10^{-8} torr	t_r^o = 0 min.
17.63	324	12.61	310	1,000 μ CO	t_r = 0+ min.
17.43	320	13.25	325	1,000 μ CO	t_r = 5 min.
16.94	311	13.00	319	1,000 μ CO	t_r = 10 min.
17.44	320	13.18	323	1,000 μ CO	t_r = 15 min.
17.00	312	12.94	318	1,000 μ CO	t_r = 30 min.
17.60	323	12.78	314	1,000 μ CO	t_r = 35 min.
17.28	317	13.07	321	1,000 μ CO	t_r = 40 min.
17.42	320	13.28	326	1,000 μ CO	t_r = 45 min.
17.42	320	12.90	317	1,000 μ CO	t_r = 50 min.

Table 34. Data on the Experimental Conditions for Run 63 (Reaction 3) (Continued)

Film Temperature		Copper Block Temperature		System Pressure	Remarks
T.C. Output (mV)	Temp. (°C)	T.C. Output (mV)	Temp. (°C)		
17.49	321	12.84	315	1,000 μ CO	t_r = 55 min.
17.44	320	13.05	320	1,000 μ CO	t_r^f = 60 min.; Termination
				6×10^{-7} torr	t_r^f + 5 min.

Variable Power Supply Settings
Substrate Heater Circuit: During Evaporation 58.5; Final for Film Anneal 68; Final for Reaction 30
Radiant Heater Circuit: During Evaporation 0; Final for Film Anneal 54; Final for Reaction 37

Table 35. Data on the Experimental Conditions for Run 49 (Reaction 4)

Film Temperature		Copper Block Temperature		System Pressure	Remarks
T.C. Output (mV)	Temp. (°C)	T.C. Output (mV)	Temp. (°C)		
12.10	224	18.34	446	1.5×10^{-8} torr	t_e^o = 0 min.
		18.06	439	9×10^{-8} torr	t_e = 1 min.
					t_e^f = $\approx$ 2 min.
24.62	450	21.82	528	2×10^{-8} torr	t_a^f = 30 min.
19.07	350	14.32	351	0 μ CO	t_r^o = 0 min.
19.14	351	13.84	339	1,000 μ CO	t_r = 1 min.
19.62	360	14.27	350	1,000 μ CO	t_r = 5 min.
19.42	356	14.36	352	1,000 μ CO	t_r = 8 min.
19.05	349	14.35	351	1,000 μ CO	t_r = 10 min.
18.96	348	14.10	345	1,000 μ CO	t_r = 15 min.
19.09	350	14.10	345	1,000 μ CO	t_r = 20 min.
19.14	351	14.16	347	1,000 μ CO	t_r = 25 min.
19.15	351	14.16	347	1,000 μ CO	t_r = 30 min.
19.29	354	14.35	351	1,000 μ CO	t_r = 40 min.

Table 35. Data on the Experimental Conditions for Run 49 (Reaction 4) (Continued)

Film Temperature		Copper Block Temperature		System Pressure	Remarks
T.C. Output (mV)	Temp. (°C)	T.C. Output (mV)	Temp. (°C)		
19.04	349	14.13	346	1,000 μ CO	t_r = 50 min.
19.08	350	14.18	347	1,000 μ CO	t_r^f = 60 min.; Termination
				4×10^{-7} torr	t_r^f + 5 min.

Variable Power Supply Settings
Substrate Heater Circuit: During Evaporation 62.5; Final for Film Anneal 68; Final for Reaction 37
Radiant Heater Circuit: During Evaporation 0; Final for Film Anneal 59; Final for Reaction 49

Table 36. Data on the Experimental Conditions for Run 62 (Reaction 5)

Film Temperature		Copper Block Temperature		System Pressure	Remarks
T.C. Output (mV)	Temp. (°C)	T.C. Output (mV)	Temp. (°C)		
14.18	261	18.46	449	6×10^{-9} torr	t_e^o = 0 min.
		18.10	440		t_e^f = 2 min. 5 sec.
24.61	450	22.42	542	1×10^{-8} torr	t_a^f = 35 min.
19.10	350	14.35	351	0 μ CO	t_r^o = 0 min.
19.20	352	13.86	340	500 μ CO	t_r = 0+ min.
19.02	349	14.68	359	500 μ CO	t_r = 5 min.
19.00	348	14.18	347	500 μ CO	t_r = 10 min.
19.28	353	14.30	350	500 μ CO	t_r = 15 min.
19.01	349	14.35	351	500 μ CO	t_r = 20 min.
19.09	350	14.29	350	500 μ CO	t_r = 25 min.
19.04	349	14.29	350	500 μ CO	t_r = 30 min.
19.04	349	14.27	349	500 μ CO	t_r = 35 min.
19.03	349	14.27	349	500 μ CO	t_r = 40 min.
19.08	350	14.29	350	500 μ CO	t_r = 45 min.

Table 36. Data on the Experimental Conditions for Run 62 (Reaction 5) (Continued)

Film Temperature		Copper Block Temperature		System Pressure	Remarks
T.C. Output (mV)	Temp. (°C)	T.C. Output (mV)	Temp. (°C)		
19.16	351	14.32	351	500 μ CO	t_r = 50 min.
19.13	351	14.31	350	500 μ CO	t_r = 55 min.
19.06	350	14.27	350	500 μ CO	t_r^f = 60 min.; Termination
				2×10^{-6} torr	t_r^f + 5 min.
				8×10^{-8} torr	t_r^f + 10 min.

Variable Power Supply Settings
Substrate Heater Circuit: During Evaporation 58.5; Final for Film Anneal 68; Final for Reaction 28
Radiant Heater Circuit: During Evaporation 0; Final for Film Anneal 54; Final for Reaction 47

Table 37. Data on the Experimental Conditions for Run 51 (Reaction 6)

Film Temperature		Copper Block Temperature		System Pressure	Remarks
T.C. Output (mV)	Temp. (°C)	T.C. Output (mV)	Temp. (°C)		
14.25	262	18.35	446	2×10^{-8} torr	t_e^o = 0 min.
		17.50	426	1×10^{-7} torr	t_e = 1 min.
		17.50	426	9×10^{-8} torr	t_e^f = 2 min. 30 sec.
24.70	452	21.95	531		t_a^f = 30 min
19.05	349	14.29	350	0 μ CO	t_r^o = 0 min.
				100 μ CO	t_r = 0+ min.
18.94	347	14.07	345	95 μ CO	t_r = 1 min.
19.05	349	14.05	344	98 μ CO	t_r = 5 min.
19.15	351	14.23	349	100 μ CO	t_r = 10 min.
19.06	350	14.23	349	97 μ CO	t_r = 15 min.
19.02	349	14.20	348	100 μ CO	t_r = 20 min.
19.22	352	14.20	348	100 μ CO	t_r = 25 min.
19.18	352	14.26	349	100 μ CO	t_r = 30 min.
19.23	353	14.28	350	98 μ CO	t_r = 35 min.

Table 37. Data on the Experimental Conditions for Run 51 (Reaction 6) (Continued)

Film Temperature		Copper Block Temperature		System Pressure	Remarks
T.C. Output (mV)	Temp. (°C)	T.C. Output (mV)	Temp. (°C)		
19.11	350	14.28	350	100 μ CO	t_r = 40 min.
19.18	352	14.26	349	100 μ CO	t_r = 45 min.
19.09	350	14.27	350	100 μ CO	t_r = 50 min.
19.08	350	14.27	350	99 μ CO	t_r = 55 min.
19.05	349	14.25	349	99 μ CO	t_r^f = 60 min.; Termination
				5×10^{-7} torr	t_r^f + 6 min.

Variable Power Supply Settings
Substrate Heater Circuit: During Evaporation 58.5; Final for Film Anneal 68; Final for Reaction 35.5
Radiant Heater Circuit: During Evaporation 0; Final for Film Anneal 54; Final for Reaction 45.5

Table 38. Data on the Experimental Conditions for Run 48 (Reaction 7)

Film Temperature		Copper Block Temperature		System Pressure	Remarks
T.C. Output (mV)	Temp. (°C)	T.C. Output (mV)	Temp. (°C)		
14.52	267	18.56	451	6×10^{-8} torr	t_e^o = 0 min.
		18.05	439	1×10^{-7} torr	t_e = 30 sec.
					t_e^f = 2 min. 45 sec.
23.53	431	21.44	519	1.5×10^{-7} torr	t_a^f = 40 min.
19.04	349	14.33	351	1×10^{-7} torr	t_r^o = 0 min.
18.92	347	14.29	350	6 μ CO	t_r = 4 min.
19.01	349	14.34	351	5.5 μ CO	t_r = 10 min.
18.96	348	14.27	350	6.5 μ CO	t_r = 15 min.
19.14	351	14.22	348	6.5 μ CO	t_r = 20 min.
19.18	352	14.23	349	6 μ CO	t_r = 25 min.
19.14	351	14.26	349	5 μ CO	t_r = 30 min.
19.10	350	14.28	350	5 μ CO	t_r = 35 min.
19.20	352	14.31	350	5 μ CO	t_r = 40 min.
19.28	353	14.34	351	5 μ CO	t_r = 45 min.

Table 38. Data on the Experimental Conditions for Run 48 (Reaction 7) (Continued)

Film Temperature		Copper Block Temperature		System Pressure	Remarks
T.C. Output (mV)	Temp. (°C)	T.C. Output (mV)	Temp. (°C)		
19.16	351	14.31	350	5 μ CO	t_r = 50 min.
19.13	351	14.26	349	5 μ CO	t_r = 55 min.
19.20	352			5 μ CO	t_r^f = 60 min.; Termination
				5 x 10^{-7} torr	t_r^f + 3 min.

Variable Power Supply Settings
Substrate Heater Circuit: During Evaporation 60; Final for Film Anneal 68; Final for Reaction --
Radiant Heater Circuit: During Evaporation 0; Final for Film Anneal 54; Final for Reaction --

Table 39. Data on the Experimental Conditions for Run 40 (Reaction 8)

Film Temperature		Copper Block Temperature		System Pressure	Remarks
T.C. Output (mV)	Temp. (°C)	T.C. Output (mV)	Temp. (°C)		
13.70	253	18.85	458	3.5×10^{-9} torr	t_e^o = 0 min.
				1.5×10^{-8} torr	t_e^f = 3 min. 15 sec.
22.50	412	20.96	507		t_a = 30 min.
23.30	426	21.30	516	3×10^{-8} torr	t_a^f = 45 min.
19.12	351	14.20	348	1.5×10^{-8} torr	t_r^o = 0 min.
19.04	349	14.20	348	6 μ CO	t_r = 1 min.
19.06	350	14.25	349	4 μ CO	t_r = 2 min.
19.09	350	14.25	349	6 μ CO	t_r = 3 min.
19.09	350	14.29	350	6 μ CO	t_r = 4 min.
19.19	352	14.29	350	4.5 μ CO	t_r = 5 min.
19.17	352	14.34	351	4.5 μ CO	t_r = 6 min.
19.16	351	14.32	351	4.5 μ CO	t_r = 8 min.
19.17	352	14.30	350	5 μ CO	t_r = 10 min.
19.13	351	14.29	350	5 μ CO	t_r = 12 min.

Table 39. Data on the Experimental Conditions for Run 40 (Reaction 8) (Continued)

Film Temperature		Copper Block Temperature		System Pressure	Remarks
T.C. Output (mV)	Temp. (°C)	T.C. Output (mV)	Temp. (°C)		
19.00	348	14.26	349	6 μ CO	t_r = 15 min.
19.07	350	14.23	349	5 μ CO	t_r = 20 min.
19.16	351	14.29	350	4 μ CO	t_r = 30 min.
19.22	352	14.32	351	6 μ CO	t_r = 40 min.
19.00	348	14.27	350	8 μ CO	t_r = 50 min.
19.10	350	14.22	348	4.5 μ CO	t_r = 60 min.
19.30	354	14.34	351	4 μ CO	t_r = 70 min.
19.12	351	14.34	351	4 μ CO	t_r = 80 min.
18.96	348	14.02	344	4 μ CO	t_r = 90 min.
19.16	351	14.18	347	5 μ CO	t_r = 100 min.
19.16	351	14.25	349	5.5 μ CO	t_r = 110 min.
19.22	352	14.29	350	5 μ CO	t_r^f = 120 min.; Termination
				2×10^{-7} torr	t_r^f + 2 min.

Table 39. Data on the Experimental Conditions for Run 40 (Reaction 8) (Continued)

Variable Power Supply Settings
Substrate Heater Circuit: During Evaporation 59; Final for Film Anneal 68; Final for Reaction 35
Radiant Heater Circuit: During Evaporation 0; Final for Film Anneal --; Final for Reaction --

Table 40. Data on the Experimental Conditions for Run 52 (Reaction 9)

Film Temperature		Copper Block Temperature		System Pressure	Remarks
T.C. Output (mV)	Temp. (°C)	T.C. Output (mV)	Temp. (°C)		
14.27	263	18.25	444	4×10^{-8} torr	t_e^o = 0 min.
		17.70	431	1×10^{-7} torr	t_e = 2 min. 10 sec.
					t_e^f = 3 min.
24.59	450	21.98	531	2×10^{-7} torr	t_a^f = 30 min.
24.72	452	18.43	448	0 μ CO	t_r^o = 0 min.
		17.88	435	950 μ CO	t_r = 1 min.
24.78	453	17.85	434	1,000 μ CO	t_r = 2 min.
25.23	461	18.04	439	1,000 μ CO	t_r = 5 min.
24.86	455	18.69	454	1,000 μ CO	t_r = 10 min.
24.76	453	18.48	449	1,000 μ CO	t_r = 11 min.
24.54	449	18.30	445	1,000 μ CO	t_r = 12 min.
24.70	452	18.46	449	1,000 μ CO	t_r = 15 min.
		18.40	447	1,000 μ CO	t_r = 20 min.
24.62	450	18.32	446	1,000 μ CO	t_r = 25 min.

Table 40. Data on the Experimental Conditions for Run 52 (Reaction 9) (Continued)

Film Temperature		Copper Block Temperature		System Pressure	Remarks
T.C. Output (mV)	Temp. (°C)	T.C. Output (mV)	Temp. (°C)		
24.69	452	18.46	449	1,000 μ CO	t_r = 30 min.
24.60	450	18.36	446	1,000 μ CO	t_r = 35 min.
24.75	453	18.56	451	1,000 μ CO	t_r = 40 min.
24.72	452	18.60	452	1,000 μ CO	t_r = 45 min.
24.57	449	18.60	452	1,000 μ CO	t_r = 50 min.
24.54	449	18.53	451	1,000 μ CO	t_r = 55 min.
24.62	450	18.51	450	1,000 μ CO	t_r^f = 60 min.; Termination

Variable Power Supply Settings
Substrate Heater Circuit: During Evaporation 57.5; Final for Film Anneal 68; Final for Reaction 53
Radiant Heater Circuit: During Evaporation 0; Final for Film Anneal 54; Final for Reaction 54

Table 41. Data on the Experimental Conditions for Run 65 (Reaction 10)

Film Temperature		Copper Block Temperature		System Pressure	Remarks
T.C. Output (mV)	Temp. (°C)	T.C. Output (mV)	Temp. (°C)		
13.87	256	18.44	448	3×10^{-8} torr	t_e^o = 0 min.
		17.75	432	4×10^{-8} torr	t_e = 2 min.
					t_e^f = 3 min.
24.42	447	22.41	541		t_a^f = 30 min.
24.61	450	18.51	450	0 μ CO	t_r^o = 0 min.
24.08	440	18.10	440	1,000 μ CO	t_r = 0+ min.
24.61	450	18.40	447	1,000 μ CO	t_r = 5 min.
24.62	450	18.64	453	1,000 μ CO	t_r = 10 min.
24.36	446	18.44	448	1,000 μ CO	t_r = 25 min.
24.49	448	18.44	448	1,000 μ CO	t_r = 30 min.
24.58	449	18.50	450	1,000 μ CO	t_r = 35 min.
24.57	449	18.49	450	1,000 μ CO	t_r = 45 min.
24.60	450	18.48	449	1,000 μ CO	t_r^f = 60 min.; Termination
24.38	446	18.43	448	1×10^{-6} torr	t_a = 10 min.; t_r^f + 10 min.

Table 41. Data on the Experimental Conditions for Run 65 (Reaction 10) (Continued)

Film Temperature		Copper Block Temperature		System Pressure	Remarks
T.C. Output (mV)	Temp. (°C)	T.C. Output (mV)	Temp. (°C)		
24.76	453	18.60	452	1×10^{-6} torr	t_a = 1 hr.
24.74	452	18.56	451	1×10^{-6} torr	t_a = 2 hr.
24.68	451	18.51	450	1×10^{-6} torr	t_a = 3 hr.
24.44	447	18.42	448	1×10^{-6} torr	t_a = 4 hr.
24.87	455	18.75	456	1×10^{-6} torr	t_a^f = 8 hr. 30 min.

Variable Power Supply Settings
Substrate Heater Circuit: During Evaporation 60; Final for Film Anneal 68; Final for Reaction 53
Radiant Heater Circuit: During Evaporation 0; Final for Film Anneal 54; Final for Reaction 57

Table 42. Data on the Experimental Conditions for Run 64 (Reaction 11)

Film Temperature		Copper Block Temperature		System Pressure	Remarks
T.C. Output (mV)	Temp. (°C)	T.C. Output (mV)	Temp. (°C)		
		18.10	440	2×10^{-8} torr	t_e^o = 0 min.
					t_e^f = 3 min.
24.66	451	18.50	450		t_a^f = 2 hr.
24.66	451	18.50	450	0 μ CO	t_r^o = 0 min.
		18.00	438	1,000 μ CO	t_r = 0+ min.
24.50	448	18.41	448	1,000 μ CO	t_r = 5 min.
24.70	452	18.49	449	1,000 μ CO	t_r = 10 min.
24.60	450	18.51	450	1,000 μ CO	t_r = 15 min.
24.58	450	18.51	450	1,000 μ CO	t_r = 20 min.
24.52	448	18.52	450	1,000 μ CO	t_r = 30 min.
24.67	451	18.42	448	1,000 μ CO	t_r = 45 min.
24.66	451	18.63	453	1,000 μ CO	t_r = 1 hr.
24.66	451	18.51	450	1,000 μ CO	t_r = 1 hr. 45 min.
24.66	451	18.51	450	1,000 μ CO	t_r = 2 hr.

Table 42. Data on the Experimental Conditions for Run 64 (Reaction 11) (Continued)

Film Temperature		Copper Block Temperature		System Pressure	Remarks
T.C. Output (mV)	Temp. (°C)	T.C. Output (mV)	Temp. (°C)		
		18.56	451	1,000 μ CO	t_r = 2 hr. 15 min.
		18.51	450	1,000 μ CO	t_r = 3 hr.
24.61	450	18.38	447	1,000 μ CO	t_r = 4 hr.
24.61	450	18.55	451	1,000 μ CO	t_r = 5 hr.
24.61	450	18.44	448	1,000 μ CO	t_r^f = 6 hr.; Termination
				1×10^{-6} torr	t_r^f + 10 min.

Variable Power Supply Settings
Substrate Heater Circuit: During Evaporation 58; Final for Film Anneal 44; Final for Reaction 54
Radiant Heater Circuit: During Evaporation 0; Final for Film Anneal 60; Final for Reaction 56

Table 43. Data on the Experimental Conditions for Run 55 (Reaction 12)

Film Temperature		Copper Block Temperature		System Pressure	Remarks
T.C. Output (mV)	Temp. (°C)	T.C. Output (mV)	Temp. (°C)		
14.00	258	18.35	446	6×10^{-8} torr	t_e^o = 0 min.
					t_e^f = 2 min. 15 sec.
24.75	453	22.15	535		t_a^f = 30 min.
24.70	452	18.48	449	0 μ CO	t_r^o = 0 min.
24.62	450	18.50	450	5 μ CO	t_r = 0+ min.
24.60	450	18.51	450	5 μ CO	t_r = 1 min.
24.52	448	18.50	450	5 μ CO	t_r = 5 min.
24.62	450	18.52	450	5 μ CO	t_r = 10 min.
24.52	448	18.48	449	8 μ CO	t_r = 15 min.
24.54	449	18.50	450	5 μ CO	t_r = 20 min.
24.69	452	18.54	451	5 μ CO	t_r = 25 min.
24.72	452	18.57	451	5 μ CO	t_r = 30 min.
24.66	451	18.56	451	5 μ CO	t_r = 35 min.
24.56	449	18.52	450	5 μ CO	t_r = 40 min.

Table 43. Data on the Experimental Conditions for Run 55 (Reaction 12) (Continued)

Film Temperature		Copper Block Temperature		System Pressure	Remarks
T.C. Output (mV)	Temp. (°C)	T.C. Output (mV)	Temp. (°C)		
24.49	448	18.51	450	5 μ CO	t_r = 45 min.
24.58	450	18.45	449	5 μ CO	t_r = 50 min.
24.61	450	18.48	449	5 μ CO	t_r = 55 min.
24.61	450	18.50	450	5 μ CO	t_r^f = 60 min.; Termination
24.61	450	18.50	450	9×10^{-7} torr	t_r^f + 3 min.

Variable Power Supply Settings
Substrate Heater Circuit: During Evaporation 59; Final for Film Anneal 68; Final for Reaction 45
Radiant Heater Circuit: During Evaporation 0; Final for Film Anneal 54; Final for Reaction 58

Table 44. Data on the Experimental Conditions for Run 57 (Reaction 13)

Film Temperature		Copper Block Temperature		System Pressure	Remarks
T.C. Output (mV)	Temp. (°C)	T.C. Output (mV)	Temp. (°C)		
13.70	253	18.42	448	9×10^{-8} torr	t_e^o = 0 min.
		17.40	424		t_e = 1 min. 30 sec.
					t_e^f = 2 min. 15 sec.
24.61	450	18.40	447		t_a^f = 1 hr.; Termination of Mock Run

Variable Power Supply Settings

Substrate Heater Circuit: During Evaporation 59; Final for Film Anneal 45; Final for Reaction --

Radiant Heater Circuit: During Evaporation 0; Final for Film Anneal 58; Final for Reaction --

Table 45. Data on the Experimental Conditions for Run 66 (Reaction 14)

Film Temperature		Copper Block Temperature		System Pressure	Remarks
T.C. Output (mV)	Temp. (°C)	T.C. Output (mV)	Temp. (°C)		
13.93	257	18.22	443	1×10^{-6} torr	t_e^o = 0 min.
		17.44	425	3×10^{-6} torr	t_e = 2 min. 30 sec.
					t_e^f = 3 min.
24.50	448	18.15	442		t_a = 15 min.
24.60	450	18.46	449		t_a = 1 hr. 15 min.
24.42	447	18.20	443		t_a = 2 hr. 10 min.
24.93	456	18.53	451		t_a^f = 6 hr. 55 min.; Termination of Mock Run

Variable Power Supply Settings
Substrate Heater Circuit: During Evaporation 59; Final for Film Anneal 45 ; Final for Reaction --
Radiant Heater Circuit: During Evaporation 0; Final for Film Anneal 60.5; Final for Reaction --

Table 46. Data on the Experimental Conditions for Run 54 (Reaction 15)

Film Temperature		Copper Block Temperature		System Pressure	Remarks
T.C. Output (mV)	Temp. (°C)	T.C. Output (mV)	Temp. (°C)		
14.53	268	18.46	449	2×10^{-8} torr	t_e^o = 0 min.
					t_e^f = 3 min.
24.50	448	21.58	522		t_a^f = 30 min.
29.98	546	22.78	550	0 μ CO	t_r^o = 0 min.
30.28	551	21.84	528	1,000 μ CO	t_r = 1 min.
30.28	551	21.70	525	1,000 μ CO	t_r = 5 min.
30.32	552	22.28	538	1,000 μ CO	t_r = 10 min.
30.36	552	22.20	537	1,000 μ CO	t_r = 20 min.
30.38	553	22.50	544	1,000 μ CO	t_r = 25 min.
30.30	551	22.54	545	1,000 μ CO	t_r = 30 min.
30.32	552	22.60	546	1,000 μ CO	t_r = 35 min.
30.28	551	22.70	548	1,000 μ CO	t_r = 40 min.
30.29	551	22.61	546	1,000 μ CO	t_r = 50 min.
30.35	552	22.62	546	1,000 μ CO	t_r = 55 min.

Table 46. Data on the Experimental Conditions for Run 54 (Reaction 15) (Continued)

Film Temperature		Copper Block Temperature		System Pressure	Remarks
T.C. Output (mV)	Temp. (°C)	T.C. Output (mV)	Temp. (°C)		
30.30	551	23.52	568	1,000 μ CO	t_r^f = 65 min.; Termination
				1 x 10^{-5} torr	t_r^f + 5 min.

Variable Power Supply Settings
Substrate Heater Circuit: During Evaporation 59; Final for Film Anneal 68; Final for Reaction 79
Radiant Heater Circuit: During Evaporation 0; Final for Film Anneal 54; Final for Reaction 64

APPENDIX E

COOLING CURVES FOR THE SUBSTRATE ASSEMBLY

In an experiment simulating the cooling of a film specimen following reaction at 450°C, the temperature data was recorded for both substrate assembly thermocouples. This information has been graphed and is presented in Figure 125.

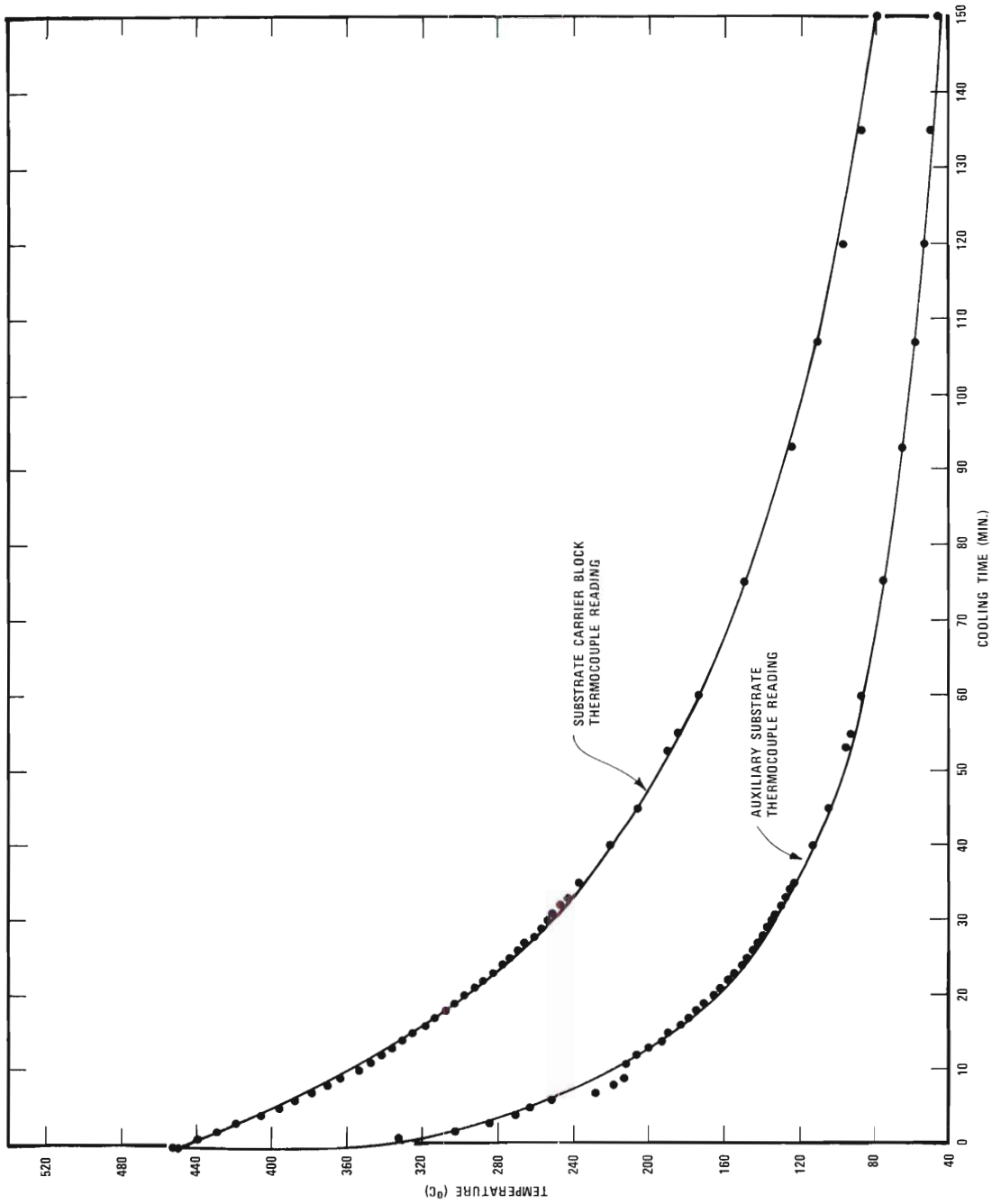

Figure 125. Cooling Curves for the Thermocouples Measuring the Temperatures of the Iron Film and Substrate Carrier Block

APPENDIX F

TIME REQUIRED TO SATURATE THE IRON FILMS WITH CARBON

The physical system may be described as follows. Carbon monoxide is assumed to decompose uniformly over the iron film surface at a temperature T. For a first approximation the concentration of surface carbon will be assumed constant, C_s. The film thickness b used for this analysis will be taken as 1,000 Å. The dimensions of the specimens in the film plane are 1 cm by 0.5 cm. With these dimensions the film will be treated as an infinite slab reducing the problem to one-dimensional diffusion. The diffusion co-ordinate x will have its origin at the surface and will run through the film perpendicular to the surface. For this case Fick's second law for non-steady-state diffusion is reduced to the following formulation:

$$\frac{\partial C(x,t)}{\partial t} = D \frac{\partial^2 C(x,t)}{\partial x^2} \quad ,$$

where t = time and D = diffusivity for carbon in iron. For constant T and the carbon-alpha-iron system, it is a reasonable approximation and commonly accepted practice to assume D constant. The flux of carbon at the interface of the iron film and NaCl substrate will be zero. Thus, the boundary conditions for the problem are:

$$C(x,0) = 0$$
$$C(0,t) = C_s$$
$$\frac{\partial C(L,t)}{\partial x} = 0$$

where L = the film thickness.

A number of solutions to Fick's partial differential equation are available in the literature. The results to a similar problem to the one formulated here are available in tabular form (168) where Dt/L^2 is tabulated against $(C_m-C_o)/(C_s-C_o)$. Here L = the half-thickness of a slab sustaining diffusion from both surfaces and C_s, C_m and C_o represent the concentrations of solute at the surface, the average concentration, and the initial slab concentration, respectively. The concentration ratio has been termed the "Fractional Saturation." The problem for the present investigation leads to the same result in terms of the fractional saturation if the total thickness of the iron film is used for L. This is true in view of the fact that at the center of the slab for which the problem solution has been given, the value of $\frac{\partial C}{\partial X}$ is zero just as if a diffusion barrier were placed there. Therefore, the solution to the partial differential equation is symmetrical about the center of the slab. The solution for one-half the slab will adequately describe the solution for the whole and vice versa.

Dt/L^2 may be calculated as follows:

$$D = D_o^{-Q/RT} \text{ where } D_o = 0.0079 \text{ cm}^2/\text{sec and } Q = 18{,}100 \text{ cal/g-mol} \quad (169)$$
$$= 0.0079\ e^{-18{,}100/RT}\ \text{cm}^2/\text{sec}$$
$$= 0.0079\ e^{-9{,}120/T}\ \text{cm}^2/\text{sec}$$

at the lowest temperature studied, 250°C or 523°K

$$D = 0.0079\ e^{-17.45}\ \text{cm}^2/\text{sec}$$
$$= 1.19 \times 10^{-6}\ \text{cm}^2/\text{sec}$$

For L = film thickness = 1,000 Å = 1×10^{-5} cm

$$\frac{Dt}{L^2} = \frac{(1.19 \times 10^{-6})(t)}{(1 \times 10^{-5})^2}$$

$$= 1.19 \times 10^{4}\ t \quad .$$

Therefore, $Dt/L^2 \gg 3$ for very short reaction intervals (t in seconds).

The value three corresponds to a fractional saturation of 0.9995. This means that whatever the concentration of carbon produced at the surface happens to be, the average concentration of the foil will approach this value very quickly, i.e., t much less than 1 second. For still higher temperatures in the alpha-iron region, the end result would be similar since D increases with increasing temperature. It would seem reasonable to assume then that the surface concentration and the average foil concentration of carbon will increase with reaction until the iron is supersaturated. The rate at which the film is saturated should then be dependent on the CO decomposition rate.

BIBLIOGRAPHY

1. Gareth Thomas, Transmission Electron Microscopy of Metals, John Wiley & Sons, Inc., New York, (1962).

2. P. B. Hirsch, A. Howie, R. B. Nicholson, D. W. Pashley, M. J. Whelan, Electron Microscopy of Thin Crystals, Butterworths, Washington, (1965).

3. R. D. Heidenreich, Fundamentals of Transmission Electron Microscopy, John Wiley & Sons, Inc., New York, (1964).

4. F. A. Prange, "Corrosion in a Hydrocarbon Conversion System," Corrosion 15, 619t(1959).

5. F. Eberle, R. D. Wylie, "Attack on Metals by Synthesis Gas from Methane--Oxygen Combustion," Corrosion 15, 622t(1959).

6. G. A. Works, "A Case History Involving Intergranular Failure of Stainless Steel Heater Tubes," Corrosion 8, 217(1952).

7. John Pattinson, "On Carbon and Other Deposits from the Gases of Blast Furnaces in Cleveland," Journal of the Iron and Steel Institute 10, 85(1876).

8. Kurt Pukall, "The Destruction of Refractory Materials by Gases Containing CO," Berichte der Deutschen Keramischen Gesellschaft 22, 430(1941).

9. W. R. Davis, R. J. Slawson, and G. R. Rigby, "An Unusual Form of Carbon," Nature 171, 756(1953).

10. T. F. Berry, R. N. Ames, R. B. Snow, "Influence of Impurities and Role of Iron Carbides in Deposition of Carbon from Carbon Monoxide," Journal of the American Ceramic Society 39, 308(1956).

11. I. L. Bell, "The Chemistry of the Blastfurnace," Journal of the Chemical Society 22, 203(1869).

12. M. D. Boudouard, "Research on Chemical Equilibria," Annales de Chimie et de Physique 24, 5(1901).

13. H. Tropsch and J. A. Von Philippovich, "Comparative Experiments on the Decomposition of Carbon Monoxide by Contract Substances," Gesammelte Abhandlungen zur Kenntnis der Kohle 7, 44(1925).

14. W. Baukloh and G. Hieber, "Influence of Various Metals and Metallic Oxides Upon Carbon Monoxide Decomposition," Zeitschrift für Anorganische und Allgemeine Chemie 226, 321(1936).

15. W. Baukloh and G. Henke, "Effect of Metals and Metal Oxides on the Decomposition of Carbon Monoxide and its Technical Significance," Metallwirtschaft 19, 463(1940).

16. W. Bauklow, "The Destructive Action of CO and of Gases Containing It," Chemische Fabrik 13, 101(1940).

17. F. Olmer, "Decomposition of Carbon Monoxide by Ferromagnetic Metals," Journal of Physical Chemistry 46, 405(1942).

18. A. R. McKinney, "The Decomposition of Ethylene and Carbon Monoxide on Metallic Catalysts," Journal of Physical Chemistry 47, 152(1943).

19. G. I. Chufarov and M. F. Antonova, "The Retardation of the Bell Reaction $2CO = C+CO_2$," Academie des sciences de l' U.R.S.S. classe des sciences techniques. Bulletin, 381(1947).

20. W. Baukloh, B. Chaterjee, and P. P. Das, "Decomposition of Carbon Monoxide in the Presence of Iron, Cobalt and Nickel as Catalysts," Indian Institute of Metals. Transactions 4, 271(1950).

21. L. J. E. Hofer, W. C. Peebles, and E. H. Bean, "X-ray Diffraction Studies of the Action of Carbon Monoxide on Cobalt-thoria-kieselguhr Catalysts," Journal of the American Chemical Society 72, 2698(1950).

22. B. Fleureau and A. Sancelme, "Catalytic Decomposition of Carbon Monoxide on Iron Reduced Electrolytically at Low Temperature," Academie des sciences, Paris. Comptes rendus hebdomadaires des seances 235, 801(1952).

23. B. Fleureau, "The Formation of Graphite by the Catalytic Decomposition of Carbon Monoxide," Academie des sciences, Paris. Comptes rendus hebdomadaires des seances 237, 330(1953).

24. V. J. Kehrer and H. Leidheiser, "The Catalytic Decomposition of Carbon Monoxide on Large Metallic Single Crystals," Journal of Physical Chemistry 58, 550(1954).

25. L. J. E. Hofer, E. Sterling, and J. T. McCartney, "Structure of the Carbon Deposited from Carbon Monoxide on Iron, Cobalt, and Nickel," Journal of Physical Chemistry 59, 1153(1955).

26. W. R. Ruston, M. Warzee, J. Hennaut, and J. Waty, Internal Dragon Project Reports (1966) and (1967).

27. M. R. Everett, Internal Dragon Project Report (1967).

28. J. J. Moran, E. N. Skinner, and F. L. LaQue, "Materials for Anti-Smog Devices," Metals Engineering Quarterly 2, 35(1952).

29. R. F. Hochman, Metal Deterioration in High Temperature Carbonaceous Environments, Project Reports, Project No. A-753, Engineering Experiment Station, Georgia Institute of Technology, Atlanta (1965-1968).

30. R. F. Hochman, "Metal Deterioration in High Temperature Carbonaceous Environments," Presented at the 20th Annual N.A.C.E. Conference in St. Louis, Missouri, March 11, 1965.

31. R. F. Hochman and J. Burson, "The Fundamentals of Metal Dusting," Division of Refining 46, 331(1966).

32. R. F. Hochman, "Survey of Metal Dusting at Elevated Temperature," Presented at the Regional Meeting of the National Association of Corrosion Engineers, Kansas City, October 2, 1963.

33. R. F. Hochman, "Metal Deterioration in Carbon Monoxide and Hydrocarbon Atmospheres at Elevated Temperatures," Presented at the Third International Conference on Corrosion, Moscow, U.S.S.R., May 15-25, 1966. To be published in the Conference Proceedings.

34. J. T. Ratliff, R. V. Westerman, and R. F. Hochman, "An Annotated Bibliography for Metal Dusting," to be published.

35. R. V. Westerman, "Mechanism and Kinetics of Iron Deterioration in Carbon Monoxide," Ph.D. Thesis, Georgia Institute of Technology (1967).

36. R. Schenck, "Equilibrium Relations Between Iron, Oxygen and Carbon," Stahl und Eisen 46, 665(1926).

37. A. Johansson and R. Von Seth, "The Equilibria of the Carburisation and Decarburisation of Iron," Journal of the Iron and Steel Institute 64, 295(1926).

38. F. Korber, H. Wiemer, and W. A. Fischer, "The Thermal Disintegration of Carbon Monoxide on Iron and its Alloys and in Mixtures with Carbon," Archiv für das Eisenhuttenwesen 17, 43(1943).

39. J. Taylor, "The Carbon Deposition Reaction Over Iron Catalysts," Journal of the Iron and Steel Institute 184, 1(1956).

40. P. L. Walker, Jr., J. F. Rakszawski, and G. R. Imperial, "Carbon Formation Over Iron Catalysts: I. Properties of Iron Formed, and II. Rates of Carbon Formation," Journal of Physical Chemistry 63, 133, 140(1959).

41. A. Stoffel, "The Reaction Between Carbon Monoxide and Iron," Zeitschrift für Anorganische Chemie 84, 56(1914).

42. S. Hilpert and T. Dieckmann, "Iron Carbides and Their Catalytic Action on the Decomposition of Carbon Monoxide," Berichte 48, 1281(1915).

43. U. Hofmann, "The Deposition of Carbon from Carbon Monoxide and Benzene in the Presence of Iron," Chemische Berichte 61B, 1180(1928).

44. U. Hofmann and E. Groll, "The Formation of Iron Oxides and Carbides in the Solid Phase," Zeitschrift für Anorganische und Allgemeine Chemie 191, 414(1930).

45. H. Tutiya, "Catalytic Decomposition of Carbon Monoxide. III. The Behavior of Iron Carbides," Institute of Physical and Chemical Research (Tokyo). Bulletin 10, 556(1931).

46. H. A. Bahr and V. Jessen, "Fission of Carbon Monoxide on Iron Oxide and Iron," Berichte der Deutschen Chemischen Gesellschaft 66B, 1238(1933).

47. H. Akamatsu and K. Sato, "Catalytic Decomposition of Carbon Monoxide by Iron," Chemical Society of Japan. Bulletin 22, 127(1949).

48. J. J. Trillat and S. Oketani, "Electron Diffraction Study of the Cementation of Iron. I. Action of Pure Carbon Monoxide," Academie des sciences, Paris. Comptes rendus hebdomadaires des seances 230, 2203(1950).

49. J. J. Trillat and S. Oketani, "Electron Diffraction Study of the Cementation of Iron. II. Action of CO + H_2 Mixtures," Academie des sciences, Paris. Comptes rendus hebdomadaires des seances 232, 1116(1951).

50. J. J. Trillat and S. Oketani, "Cementation of Single Crystals of Iron," Academie des sciences, Paris. Comptes rendus hebdomadaires des seances 233, 51(1951).

51. L. V. Radushkevich and V. M. Luk'yanovich, "Structure of the Carbon Produced in the Thermal Decomposition of Carbon Monoxide on an Iron Catalyst," Zurnal Fizicheskoi Khimii 26, 88(1952).

52. D. S. MacIver and P. H. Emmett, "Surface-area Measurements on Carbon Black Produced by the Catalytic Decomposition of Carbon Monoxide Over Iron," Journal of Physical Chemistry 59, 1109(1955).

53. P. Royen and W. Blumrich, "Catalytic Properties of Iron and Binary Systems of Iron. I. Disproportionation of Carbon Monoxide on Iron, ε-iron Nitride, and Iron Phosphides," Zeitschrift für Anorganische und Allgemeine Chemie 280, 294(1955).

54. S. R. Billington and B. C. Woodfine, "The Catastrophic Corrosion of a Flake Graphite Cast Iron in Carbon Dioxide Containing a Small Amount of Carbon Monoxide," Metallurgia 55, 213(1957).

55. Y. B. Kagan, A. N. Bashkirov, E. V. Kamzolkina, and A. Y. Rozovskii, "Kinetics for the Conversion of Carbon Monoxide in the Presence of Iron Catalysts," Zhurnal Fizicheskoi Khimii 33, 2706(1959).

56. J. Hui and A. Boulle, "Catalytic Decomposition of Carbon Monoxide in the Presence of Iron," Academie des sciences, Paris. Comptes rendus hebdomadaires des seances 254, 1806(1962).

57. A. R. Cox, "The High Temperature Reactions of Carbon Monoxide with Iron, Nickel and Austenitic Stainless Steel," M.S. Thesis, Georgia Institute of Technology, (1962).

58. B. Schmitt, "Apparatus for Measuring the Catalytic Activity of Iron-Carbon Alloys in the Decomposition of Carbon Monoxide," Centre de Documentation Siderurgique, Circulaire d'Informations Techniques No. 6, 1477(1964).

59. G. Hägg, "Powder Photographs of a New Iron Carbide," Zeitschrift Kristallographic 89, 92(1934).

60. J. F. Shultz, L. J. E. Hofer, K. C. Stein, and R. B. Anderson, "Carbides, Nitrides, and Carbonitrides of Iron as Catalysts in the Fischer-Tropsch Synthesis," U. S. Bureau of Mines Bulletin 612 (1963).

61. T. Watanabe, "Poisoning Effect of Certain Substances on the Iron Catalyzer in the Decomposition of Carbon Monoxide," Institute of Physical and Chemical Research (Tokyo). Bulletin 7, 1078(1928).

62. S. Klemantaski, "Action of Inhibitors of Carbon Deposition in Iron-Ore Reduction," The Journal of the Iron and Steel Institute 171, 176(1952).

63. B. Chatterjee and P. P. Das, "Inhibition of Iron-Catalyzed Decomposition of Carbon Monoxide," Journal of Scientific and Industrial Research (India). 15B, 412(1956).

64. W. A. Bone, H. L. Saunders, and H. J. Tress, "An Experimental Inquiry into the Interactions of Gases and Ore in the Blast-Furnace," The Journal of the Iron and Steel Institute 137, 85(1938).

65. W. Baukloh and E. Spetzler, "Effect of Gaseous Additions of the Disintegration of Carbon Monoxide," Archiv für das Eisenhuettenwesen 13, 223(1939).

66. P. Pingault, "Formation and Decomposition of Cementite," Academie des sciences, Paris. Comptes rendus hebdomadaires des seances 191, 1007(1930).

67. S. B. Hendricks, "Crystal Structure of Cementite," Zeitschrift Kristallographic 74, 534(1930).

68. L. J. E. Hofer, E. M. Cohn, and W. C. Peebles, "The Modifications of the Carbide, Fe_2C; Their Properties and Identifications," Journal of the American Chemical Society 71, 189(1949).

69. K. H. Jack and S. Wild, "Nature of χ-carbide and its Possible Occurrence in Steels," Nature 212, 248(1966).

70. E. M. Cohn and L. J. E. Hofer, "Some Thermal Reactions of the Higher Iron Carbides," Journal of Chemistry and Physics 21, 354(1953).

71. L. J. E. Hofer and E. M. Cohn, "Saturation Magnetizations of Iron Carbides," Journal of the American Chemical Society 81, 1576(1959).

72. L. J. E. Hofer, "Nature of the Carbides of Iron," U. S. Bureau of Mines Bulletin 631, (1966).

73. H. C. Eckstrom and W. A. Adcock, "A New Iron Carbide in the Hydrocarbon Synthesis Catalysts," Journal of the American Chemical Society 72, 1042(1950).

74. F. H. Herbstein and J. A. Snyman, "Identification of Eckstrom-Adcock Iron Carbide as Fe_7C_3," Inorganic Chemistry 3, 894(1964).

75. R. Schenck, "Equilibrium Relations in the Reduction, Oxidation and Carburization of Iron. IV. Iron Carbide, Iron Oxides and Iron Under an Atmosphere of Carbon Monoxide and Carbon Dioxide," Zeitschrift für Anorganische und Allgemeine Chemie 167, 254(1927).

76. H. Tutiya, "Is the So-called χ-Carbide Really Formed in the Iron Catalyst?," Institute of Physical and Chemical Research (Tokyo). Bulletin 8, 609(1929).

77. H. Tutiya, "Catalytic Decomposition of Carbon Monoxide I. Iron as Catalyst," Institute of Physical and Chemical Research (Tokyo). Scientific Papers 10, 69(1929).

78. W. Baukloh, "Destruction of Cast Iron by Carbon Monoxide Gas Mixtures at High Temperature," Metallwirtschaft 18, 47(1939).

79. P. P. Das and B. Chatterjee, "Iron as a Catalyst in the Decomposition of Carbon Monoxide," Indian Institute of Metals. Transactions 6, 279(1952).

80. B. Chatterjee and P. P. Das, "Nature of the Catalyst in the Decomposition of Carbon Monoxide in Presence of Iron," Nature 173, 1046(1954).

81. P. P. Das and B. Chatterjee, "The Nature of the Catalyst in the Decomposition of Carbon Monoxide in Presence of Iron," Indian Institute of Metals. Transactions 7, 189(1955).

82. A. Juliard, R. Rayet, and A. Lude, "A Kinetic Study of the Dissociation of Carbon Monoxide Accompanying the Reduction of Metallic Oxides," Discussions Faraday Society No. 4, 193(1948).

83. J. T. Kummer, T. W. DeWitt, and P. H. Emmett, "C^{14} Studies of Fischer-Tropsch Synthesis Mechanism," Journal of the American Chemical Society 70, 3632(1948).

84. H. Podgurski, J. T. Kummer, T. W. DeWitt, and P. H. Emmett, "Preparation, Stability, and Adsorptive Properties of Carbides of Iron," Journal of the American Chemical Society 72, 5382(1950).

85. C. Wert, "Precipitation Out of Dual Solid Solutions of Carbon and Nitrogen in Alpha-Iron," Acta Metallurgica 2, 361(1954).

86. C. S. Roberts, B. L. Averbach, and M. Cohen, "The Mechanism and Kinetics of the First Stage of Tempering," American Society for Metals 45, 576(1953).

87. J. J. Trillat and S. Oketani, "Electron Diffraction Study of Cementation of Iron by Carbon Monoxide," Metaux et corrosion 25, 263(1950).

88. J. J. Trillat and S. Oketani, "The Orientation Relations Between Cementite and α-Iron," Acta Crystallographica 5, 469(1952).

89. J. J. Trillat, L. Tertian, and M. Bonnett-Gros, "Microscopic and Electron Diffraction Study of the Carburization of Iron and of Aluminum," Academie des sciences, Paris. Comptes rendus hebdomadaires des seances 249, 1299(1959).

90. S. Oketani and S. Nagakura, "The ϵ-Phase of Iron Carbide," Kagaku 25, 638(1955).

91. S. Oketani and S. Nagakura, "Study of Iron Carbides by Electron Diffraction. I. Genesis of Carbides," Nippon Kinzoku Gakkaishi 20, 460(1956).

92. S. Nagakura, "Study of Iron Carbides by Electron Diffraction. II. Phase Transition of the Carbides," Nippon Kinzoku Gakkaishi 20, 465(1956).

93. S. Nagakura, "Study of Metallic Carbides by Electron Diffraction. III. Iron Carbides," Journal of the Physical Society of Japan 14, 186(1959).

94. S. Oketani and S. Nagakura, "Electron-Diffraction Studies on the Crystal Structures of Carbides of Iron, Cobalt and Nickel," Journal of the Physical Society of Japan 17, Supplement B-II, 235(1961).

95. H. Schenck, M. Nacken, and E. Potthast, "Investigations of the Existence Ranges of the Iron Carbides with the Aid of Electron Microscopic and Electron Diffraction," Archiv für das Eisenhuttenwesen 37, 341(1966).

96. R. B. Marcus and L. O. Brockway, "Oxidation of Thin Single Crystals of Copper," Inorganic Chemistry 2, 489(1963).

97. J. T. Ratliff and R. F. Hochman, "Thin Film Studies; A Probe into the Metal Dusting Reaction," presented at the Southeast Region Conference of the National Association of Corrosion Engineers, November 3, 1965 in Richmond, Virginia. Unpublished work. Paper on file in the Department of Metallurgy, Georgia Institute of Technology.

98. J. T. Ratliff and R. F. Hochman, "A Study of the Deterioration of Thin Metal Films in Carbonaceous Gases," presented at the South Central Region Conference of the National Association of Corrosion Engineers, October 19, 1966 in Shreveport, Louisiana. Unpublished work. Paper on file in the Department of Metallurgy, Georgia Institute of Technology.

99. W. B. Segraves, "Corrosion of Nickel Containing Materials by Carbon Monoxide at Elevated Temperatures," Ph.D. Thesis, Georgia Institute of Technology, (1960).

100. H. E. Grenga, "Active Sites for the Catalytic Decomposition of Carbon Monoxide on Nickel," Ph.D. Thesis, University of Virginia, (1967).

101. D. W. Pashley, "The Study of Epitaxy in Thin Surface Films," Advances in Physics 5, 173(1956).

102. K. H. Behrndt, "Preparation of Thin Films," Thin Films, American Soceity for Metals, Metals Park, Ohio, 1-43(1964).

103. D. W. Pashley, "The Nucleation, Growth, Structure and Epitaxy of Thin Surface Films," Advances in Physics 14, 327(1965).

104. J. W. Matthews, "Evaporated Single-Crystal Films," Physics of Thin Films, Vol. 4, Ed. by G. Hass and R. E. Thun, Academic Press, New York, 137-190(1967).

105. O. S. Heavens, Optical Properties of Thin Solid Films, Academic Press, Inc., New York (1955).

106. L. Holland, Vacuum Deposition of Thin Films, John Wiley & Sons, Inc., New York (1958).

107. Papers presented at a Seminar of the American Society for Metals, October 19 and 20, 1963. Thin Films, American Society for Metals, Metals Park, Ohio (1964).

108. M. H. Francombe and H. Sato (Editors), Single-Crystal Films, Pergamon Press, Ltd., Oxford (1964).

109. G. Hass and R. E. Thun (Editors), Physics of Thin Films, Vol. 4, Academic Press, New York (1967).

110. J. P. Hirth and K. L. Moazed, "Nucleation Processes in Thin Film Formation," Physics of Thin Films, Vol. 4, Ed. by G. Hass and R. E. Thun, Academic Press, New York, 97-136(1967).

111. S. Sakata and S. Funaki, "Evaporated Iron Film," Journal of Electron-microscopy 12, 138(1963).

112. L. E. Collins and O. S. Heavens, "The Epitaxial Growth and Oxidation of Nickel, Cobalt and Iron on Rocksalt," Physical Society (London) Proceedings 70 B, 265(1957).

113. D. Watanabe and S. Ogawa, "Epitaxial Growth of Metals on Rocksalt Faces Cleaved in Vacuum," Journal of the Physical Society of Japan 19, 881(1964).

114. A. J. Pignocco and G. E. Pellissier, "Low-Energy Electron Diffraction Studies of Oxygen Adsorption and Oxide Formation on a (001) Iron Surface," Journal of the Electrochemical Society 112, 1188(1965).

115. L. Brück, "Structure of Thin Evaporated Metal Films on Rock Salt," Annalen der Physik 26, 233(1936).

116. S. Shirai, "Structures of Iron Films Deposited on Annealed Rock Salt," Physico-Mathematical Society of Japan. Proceedings 20, 855(1938).

117. O. S. Heavens, M. M. Brown, and V. Hinton, "The Structure and Density of Iron Films Formed by Thermal Evaporation," Vacuum 9, 17(1959).

118. R. B. Belser and W. E. Woolf, "Research on Vacuum-evaporated and Cathode-spattered Thin Films," Report Number WADD-TR-60-381, Engineering Experiment Station, Georgia Institute of Technology, (1962).

119. O. S. Heavens, "The Structure and Magnetic Properties of Single-Crystal Films of Ferromagnetic Materials," Single Crystal Films, Ed. by M. H. Francombe and H. Sato, Pergamon Press, Ltd., Oxford, 383-394(1964).

120. M. Cahoreau and M. Gillet, "The Epitaxy of Thin Layers of Iron and Thin Oxidation," Journal de Microscopie 4, 207(1965).

121. S. Shimozaki and H. Sato, "Need of Contamination for the Epitaxial Growth of Iron on Rocksalt," Journal of Applied Physics 36, 2320 (1965).

122. J. W. Matthews, "Technique for Preparing Single-Crystal Films of Iron on Clean Sodium Chloride Substrates," Applied Physics Letters 7, 255(1965).

123. J. W. Matthews, "Technique for Growing Single-Crystal Films of Gold on Clean Sodium Chloride Substrates," Applied Physics Letters 7, No. 5, 131(1965).

124. O. S. Heavens, "Epitaxic Growth of Iron on Alkali Halides," Acta Crystallographica 20, 288(1966).

125. S. Tagawa, S. Ino and Ogawa, "Epitaxy of Body-Centered Cubic Metals Evaporated onto Cleavage Faces of Rocksalt," Japanese Journal of Applied Physics 5, 846(1966).

126. G. Rasigni, "Evolution des proprietes optiques de couches minces de fer etudies sous vide, puis dans l'air," Academie des sciences, Paris. Comptes rendus hebdomadaires des seances 252, 3794(1961).

127. M. Cahorean and M. Gillet, "Etude De L'Epitaxie Des Couches Minces De Fer Et De Leur Oxydation," Journal De Microscopie 4, 207(1965).

128. J. B. Wagner, K. R. Lawless, and A. T. Gwathmey, "The Rates of Formation and Structure of Oxide Films Formed on a Single Crystal of Iron," Metallurgical Society of AIME. Transactions 221, 257(1961).

129. R. P. Eischens and W. A. Pliskin, "Infrared Spectra of Adsorbed Molecules," Advances in Catalysis 10, 1(1958).

130. B. Ralph and D. M. Schwartz, "Field Ion Microscopy Applied to Studies of Steels," presented to the Symposium on Field Ion Microscopy in Physical Metallurgy and Corrosion, Georgia Institute of Technology, Atlanta, Georgia (1968).

131. W. Pitsch and A. Schrader, "Die Ausscheidungs form des Zementits im Ferrit," Archiv für das Eisenhuttenwesen 29, 485(1958).

132. K. W. Andrews, "The Structure of Cementite and Its Relation to Ferrite and Epsilon Carbide - II," Acta Metallurgica 12, 921(1964).

133. K. H. Jack, "Structural Transformations in the Tempering of High-Carbon Martensitic Steels," Journal of the Iron and Steel Institute, 169, 26(1951).

134. R. A. Johnson, "Clustering of Carbon Atoms in α-Iron," Acta Metallurgica 15, 513(1967).

135. L. S. Darken and R. M. Fisher, "Some Observations on the Growth of Pearlite," Decomposition of Austenite by Diffusional Processes, Ed. by V. F. Zackay and H. I. Aaronson, Interscience Publishers, New York, 249-288(1962).

136. K. H. Jack, "Structural Transformations in the Tempering of High-Carbon Martensitic Steels," Journal of the Iron and Steel Institute 169, 26(1951).

137. W. C. Leslie, R. M. Fisher, and N. Sen, "Morphology and Crystal Structure of Carbides Precipitated from Solid Solution in Alpha Iron," Acta Metallurgica 7, 632(1959).

138. W. C. Leslie, "The Quench-Aging of Low-Carbon Iron and Iron-Manganese Alloys; An Electron Transmission Study," Acta Metallurgica 9, 1004 (1961).

139. E. Smith, "The Role of Lattice Defects in the Precipitation of Carbon from Alpha Iron," Direct Observations of Imperfections in Crystals, Ed. by J. B. Newkirk and J. H. Wernick, Interscience Publishers, New York, 203-211(1962).

140. J. W. Christian, The Theory of Transformations in Metals and Alloys, Pergamon Press, New York (1965).

141. E. Hornbogen, "Solid Solutions of Alpha Iron," Metallurgical Society Conferences 28, 1(1965).

142. S. Harper, "Precipitation of Carbon and Nitrogen in Cold-Worked Alpha-Iron," Physical Review 83, 709(1951).

143. E. W. Davenport and E. C. Bain, "The Aging of Steel," American Society for Metals. Transactions 23, 1047(1935).

144. A. H. Cottrell and A. T. Churchman, "Change of Electrical Resistance During the Strain Aging of Iron," Journal of the Iron and Steel Institute 162, 271(1949).

145. F. R. N. Nabarro, "The Influence of Elastic Strain on the Shape of Particles Segregating in an Alloy," Physical Society. Proceedings 52, 90(1940).

146. A. H. Cottrell and B. A. Bilby, "Dislocation Theory of Yielding and Strain Aging of Iron," Physical Society. Proceedings 62, 49(1949).

147. A. H. Cottrell, Dislocations and Plastic Flow in Crystals, Oxford University Press, London (1961).

148. J. L. Snoek, "Effect of Small Quantities of Carbon and Nitrogen on the Elastic and Plastic Properties of Iron," Physica 8, 711(1941).

149. P. G. Shewmon, Diffusion in Solids, McGraw-Hill Book Company, Inc., New York, (1963).

150. F. S. Ham, "Theory of Diffusion-Limited Precipitation," Journal of the Physics and Chemistry of Solids 6, 335(1958).

151. F. S. Ham, "Stress-Assisted Precipitation on Dislocations," Journal of Applied Physics 30, 915(1959).

152. F. S. Ham, "Diffusion-Limited Growth of Precipitate Particles," Journal of Applied Physics 30, 1518(1959).

153. J. W. Cahn, "Nucleation on Dislocations," Acta Metallurgica 5, 169 (1957).

154. R. H. Doremus, "The Diffusion of Carbon During Precipitation in Alpha-Iron," Acta Metallurgica 7, 399(1959).

155. K. F. Hale and D. McLean, "Structure of Quench-Aged Iron-Carbon and Iron-Nitrogen Alloys," Journal of the Iron and Steel Institute 201, 337(1963).

156. D. Hull and I. L. Mogford, "Precipitation and Irradiation Hardening in Iron," Philosophical Magazine 6, 535(1961).

157. R. H. Doremus and E. F. Koch, "The Precipitation of Carbon from Alpha-Iron," Metallurgical Society of AIME. Transactions 218, 591(1960).

158. K. H. Jack, "Discussion: Autumn General Meeting," Journal of the Iron and Steel Institute 170, 248(1952).

159. C. Zener, "Theory of Growth of Spherical Precipitates from Solid Solution," Journal of Applied Physics 20, 950(1949).

160. C. Zener, "Kinetics of the Decomposition of Austenite," Metallurgical Society of AIME. Transactions 167, 550(1946).

161. C. Wert, "Diffusion Coefficient of Carbon in Alpha-Iron," Physical Review 79, 60(1950).

162. C. Wert, "Precipitation from Solid Solutions of Carbon and Nitrogen in Alpha-Iron," Journal of Applied Physics 20, 943(1949).

163. C. E. Wicks and F. E. Block, "Thermodynamic Properties of 65 Elements--Their Oxides, Halides, Carbides, and Nitrides," U. S. Bureau of Mines Bulletin 605, (1963).

164. L. W. Ross, F. H. Haynie, and R. F. Hochman, "Thermodynamic Functions of Nickel Carbonyl and Iron Pentacarbonyl," Journal of Chemical and Engineering Data 9, 339(1964).

165. Cumulative Alphabetical and Grouped Numerical Index of X-Ray Diffraction Data, American Society for Testing Materials, Philadelphia, Pennsylvania, (1955).

166. P. R. Swann, H. Warlimont, and R. W. Whitmore, "Lattic Spacings and Angles Between Planes in the Cementite Lattice," Memorandum No. 965, Research Center, U. S. Steel Corporation, Monroeville, Pennsylvania, (1961).

167. M. J. Duggin and L. J. E. Hofer, "Nature of χ-Iron Carbide," Nature 212, 248(1966).

168. L. S. Darken and R. W. Gurry, Physical Chemistry of Metals, McGraw-Hill Book Company, Inc., New York, (1953).

169. A. G. Guy, Elements of Physical Metallurgy, Second Edition, Addison-Wesley Publishing Company, Inc., Reading, Massachusetts, (1959).

VITA

James Titus Ratliff was born in Lyerly, Georgia on July 14, 1940. He attended public schools in Oak Ridge, Tennessee and graduated from Oak Ridge High School in 1958 as a member of the National Honor Society. In the fall of 1958, he entered the Georgia Institute of Technology as a co-operative student majoring in Chemical Engineering. He was employed by the Union Carbide Nuclear Company at the Y-12 Plant in Oak Ridge, Tennessee. With this company he received a variety of experience working three quarters in the Engineering Division, two quarters in the Development Division and two quarters in the Production Division. While an undergraduate member of Phi Sigma Kappa social fraternity, he held a number of offices as well as being voted the Outstanding Senior. In September, 1963 he was awarded the degree of Bachelor of Chemical Engineering Co-operative Plan.

In September, 1963 he was enrolled in the Graduate Division of the Georgia Institute of Technology and received the degree of Master of Science in Chemical Engineering in September, 1964. During this year he was employed by the Engineering Experiment Station as a research assistant.

In September, 1964 he enrolled again in the Graduate Division of the Georgia Institute of Technology to pursue the degree of Doctor of Philosophy in Chemical Engineering. He received a graduate fellowship from the Gulf Oil Company and was awarded a scholarship from the National Association of Corrosion Engineers. While working on his research program he was a guest speaker at two of the regional meetings of the National Association of Corrosion Engineers.

In 1964 he was married to the former Elaine Sue Murphy of Atlanta, Georgia. They are the parents of a daughter, Erin Elaine, and a son, James Scott. He and his family now live in Camden, South Carolina where he is employed by the E. I. du Pont de Nemours and Company, Incorporated.